EJA
European Journal of Anatomy
Volume 25 - Number 3 May 2021

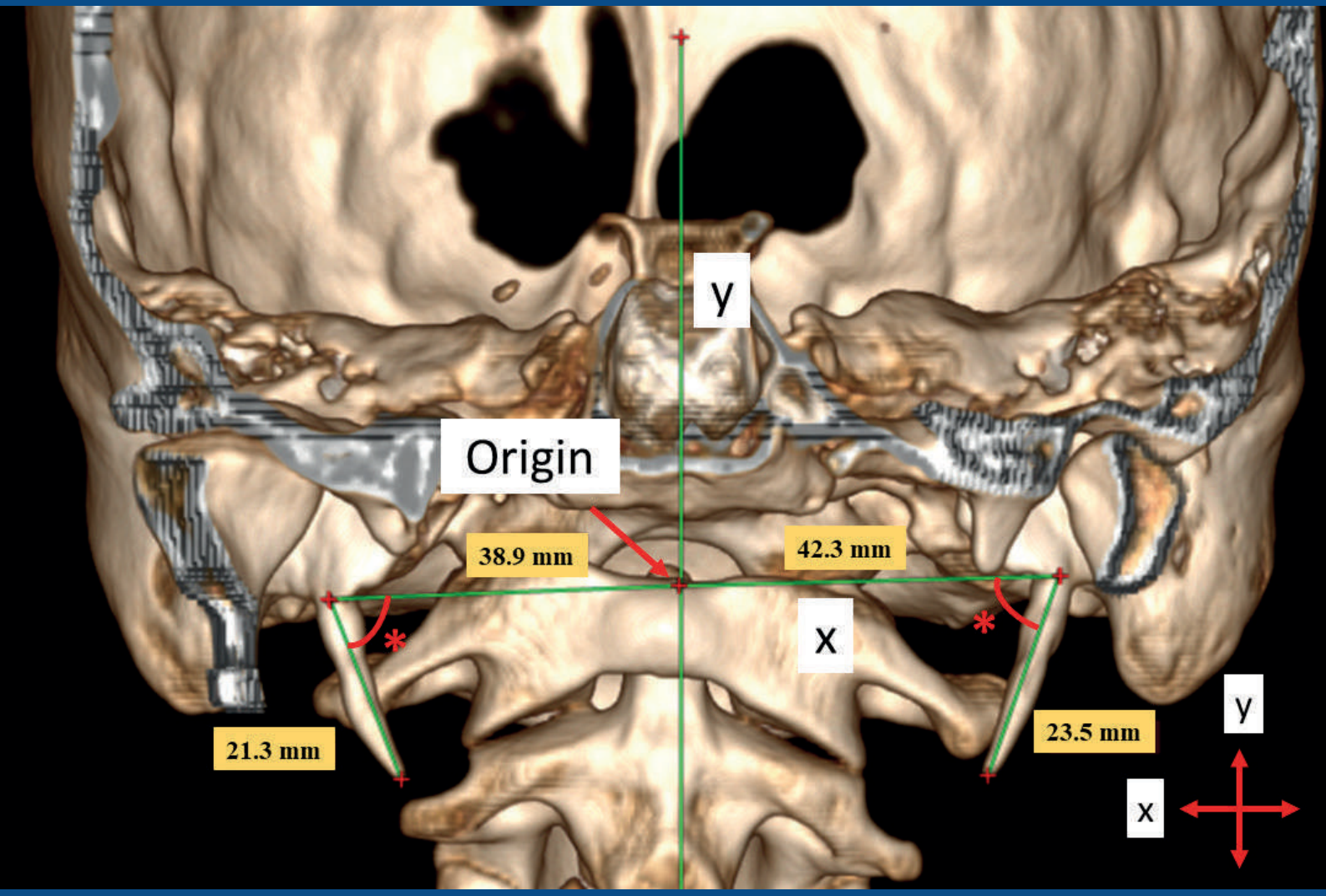

Indexed in:
DIALNET
EMBASE / Excerpta Medica
Emerging Sources Citation Index
LATINDEX. Catálogo v1.0 (2002-2017)
SCOPUS

Official Journal of the Spanish Society of Anatomy

www.eurjanat.com

EJA
European Journal of Anatomy

Volume 25 - Number 3 May 2021

CONTENTS

Original Articles

Case Report

Letter to the Editor

Growth of radius and estimation of crown-rump length and crown-heel length based on osteometry on the diaphysis of human fetal radius

Dhason Simon[1], Don Varghese[2], Annie Varghese[3], Biswajit Bhowmick[4], Monie Simon[5]

[1] *College of Health Sciences, Arsi University, Asella, Ethiopia*
[2] *Specialist Oral and Maxillofacial Surgeon, Saudi German Hospital, Dubai, UA*
[3] *IBN SINA Medical Centre, Dubai, UAE*
[4] *Senior Medical Officer, Army Medical Core, India*
[5] *Chellaram Hospital (Diabetes Care & Multispeciality), Pune - 411021, India*

SUMMARY

Earlier studies on growth and estimation of age from fetal bones were analyzed from photographs, radiographs, ultrasonographs and bones from chemically preserved fetuses. The earlier findings might not be applicable when information about growth and age estimation are sought from the naturally macerated fetal bones. The present study was undertaken in the Department of Anatomy, BJ Medical College, Pune, India with the aim to study the growth of fetal radius and also to estimate the CRL (crown-rump length) and CHL (crown-heel length) of fetuses based on osteometry on fetal radius. A natural process of maceration technique was adopted to prepare the bones. Osteometry was taken directly on fetal radius. CRL and CHL were taken from fresh fetuses. There were seven osteometric measurements (five measurements were newly introduced) taken on 912 fetal radii (right and left) from 456 fetuses (244 males and 212 females) from Indian population. The fetuses had the age range between 11 weeks to 40 weeks of intrauterine life. It was observed that 8.04% showed significant side differences and 12.5% showed significant sex differences based on the osteometry. There was positive growth trend found in fetal radius on the basis all the osteometric measurements. The Maximum Length of Radius (r-ml) showed the fastest rate of growth in females during weeks 11 to 16 of intrauterine life. For every 1 mm in the CRL, the r-ml was increased by .235 mm. Regression equations were calculated to estimate the CRL and CHL from the osteometry done on fetal radius. Growth study of the fetal radius has its anatomical significance. Age estimation is a crucial factor in dealing with forensic and archaeological anthropology.

Key words: Human fetus – Radius – Osteometry – Radius growth – Fetal age estimation

Corresponding author:
Dr. Dhason Simon. Associate Professor of Anatomy, Department of Biomedical Sciences, College of Health Sciences, Arsi University, Asella, Ethiopia. Phone: +251-912807610. E-mail: dhasonsimon@yahoo.com

Submitted: September 13, 2020. **Accepted:** November 19, 2020

INTRODUCTION

Somatometric and osteometric studies on the human fetus help understand the anatomical growth pattern and development of the human fetus. This paper presents a study on fetal skeletal growth of the radius based on a new fetal skeletal collection obtained by natural maceration.

That means maceration in fresh water. The study is important because it is based on both a good skeletal sample of fetuses (244 males and 212 females) and on Indian population. It is difficult to construct fetus skeletal collections of this size and, because of this, there is a great lack of documented (known sex and age) skeletal collections of individuals at this stage of development. In turn, this lack of fetus skeletal documented collections makes it difficult to develop skeletal growth studies on this age group, which are extremely necessary in forensic and archaeological anthropology, because they help us to estimate fetal age in cases where a perinatal or fetal individual is involved. The paper presents a new documented fetal skeletal collection, an Indian collection, and furnishes information on skeletal growth of Indian fetuses, which is extremely important for osteological research, and population variability.

Very extensive studies have been carried out, in respect of growth on infants and children (Tsuzaki et al., 1990; Shimura et al., 2005; Smith, 2007; Cardosa et al., 2014; Irurita et al., 2017), children through adolescence (Kulkarni, 1985; Padmanathan et al., 1990; Beunen et al., 1990), and also adults (Munoz et al., 2001; Mahakkanukrauh et al., 2011; Wang et al., 2012). Studies are also available on the growth aspects of human in their intrauterine life on the basis of osteometric analysis (Simon et al., 1984; Huxley, 1998; Loughna et al., 2009; Carneiro et al., 2013; Bartosch et al., 2019). Although various studies are available on fetal growth and development, the aims of these studies vary from one another. More studies aimed to concentrate on developmental aspects rather than growth aspects based on osteometry (O'Rahilly, 1973; Kulkarni et al., 1981; Mahon et al., 2009). Several studies have established an association between gestational age and the diaphyseal length fetal long bones (Fazekas and Kosa, 1978; Carneiro, 2019). Studies are available to estimate fetal age from the diaphyses of long bones (Mehta and Singh, 1972; Vare and Bansal, 1977; Kosa, 1997; Shirley, 2009). The estimation of fetal age is applicable in clinical, forensic and archaeological contexts (Butt and Lim, 2014; Carneiro et al., 2013).

The methodology adopted in the earlier studies to prepare the fetal material in dealing with prenatal growth and development was not uniform. In some studies (Ford, 1956; Mehta and Singh, 1972), fetal bones were dissected from preserved fetuses and measured. In the case of measurements taken on the dissected bones, not only would there be every chance of tender fetal long bones getting damaged, but also the removal of soft tissues from the bones might not be that perfect, which might result in distorted measurements. Moore and Persaud (1993) measured human fetuses which were preserved in formalin. Moss et al. (1955) studied fetal bones prepared with alizarin staining. Measurements on long bones, which were obtained from chemically preserved fetuses, definitely differ from that of original long bones.

Therefore, it is necessary to prepare original bone and take measurements directly on the bone to get accurate results. In various studies, observations and measurements were taken from just photographs (Burdi, 1969), radiographs (Piercecchi-Marti et al., 2002; Khan and Faruqui, 2006; Carneiro et al., 2019) and ultrasonographs (Chitty and Altman, 2002; Loughna et al., 2009; Butt and Lim, 2014). The methodology adopted by the earlier workers to measure fetal bones from photographs, radiographs and ultrasonographs might not be accurate, as there was every chance of bones being oblique in their exhibits. Moreover, the bone measurements taken from these graphs showed only a one-dimensional approach, while the bone itself exhibited a multi-dimensional form. While commenting on measurements taken from the ultrasonographs, Chitty and Altman (2002) pointed out that the measurements would vary over a wide range due to differences in fetal position, and difficulties would occur in taking correct linear measurements because of variation of objective

planes due to the movements of the fetuses. Moss et al. (1955) studied fetal bones prepared with alizarin staining. In some other studies (Ford, 1956; Mehta and Singh, 1972), fetal bones were dissected from chemically preserved fetuses and got measured. Chemical preservation results to shrinkage of specimens to some extent. Mehta and Singh (1972) measured the crown-rump length of fetuses, after fixing them in 10% formalin for 4 to 6 months. Thus, it is revealed that no uniform method has been adopted in the earlier studies in preparing the fetal specimens.

The number of fetal specimens considered in the earlier studies also varied from one another. It has been noted that in many cases the number has been found to be quite inadequate. Gray and Gardner (1969), and Gardner and Gray (1970) studied a series of only 40 embryos and fetuses. Mehta and Singh (1972) measured the diaphyseal lengths of only 50 fetuses. Dhawan et al. (2014) measured femur bones from 45 human fetuses. Carneiro et al. (2019) measured fetal bones from only 17 fetuses. Because of the inadequacy as well as variability in the sample size, no proper comparison could be made between studies. Most of the earlier studies, which were aimed to estimate age from fetal long bones, did not include all the long bones (Feltz, 1954; Moss et al., 1955; Gray and Gardner, 1969; Gardner and Gray, 1970; Mehta and Singh, 1972).

Going through the literature, it was revealed that there were different aims for the earlier studies. There were variations in methodology adopted to make the availability of the human specimens and also to measure them. There was a lesser number of parameters reported on small sample size. Thus, the whole scenario showed an incomplete picture. Thus, it was felt necessary that a systematic study be undertaken to rectify the pitfalls highlighted above. The present work aimed to study the growth pattern and the rate of growth of the fetal radius with side and sex differences, and to estimate crown-rump length (CRL) and crown-heel length (CHL) from the radius, and also to examine the applied significance based on the osteometry on fetal radius.

MATERIAL AND METHODS

Source of fetus

The principal author "(D.S.)" of the paper was an Anatomy staff member in the Department of Anatomy, B.J. Medical College (BJMC) with its attached Sassoon General Hospitals, Pune, India during 1978 to 2011. The Deans of the BJMC and Sassoon General Hospitals, and the Heads of the Department of Anatomy, BJMC were supportive for the collection of human fetuses from the Sassoon General Hospitals. The Professors and Heads of the Departments of Obstetrics and Gynaecology and Forensic Medicine, BJMC, were also cooperative to supply the human fetuses from their respective departments. The fetuses were collected during the above period. The fetuses were from abortions of Medical Termination of Pregnancies (MTPs)/ Still Births. Fetus collections procedures include such as anatomy departmental assistants to be allotted to collect fetuses, proper labeling of particulars on the fetus containers, issue and receipt of related documents of fetus, etc. The study was conducted in the Department of Anatomy, BJMC. Required approval was obtained from the Ethical Committee of BJMC.

Population base

Anatomical study on humans is both on an individual basis and population-oriented. In the present study, name of the parents of the fetuses and their place of living indicated that all the parents of the fetuses belonged within the geographical area of Maharashtra, India. This broad population base of Maharashtra provided a vital significance, indicating that the fetuses belonged to the Maharashtra population of India.

In all, there were 912 (left- and right-side bones) diaphyses of fetal radius bones from 456 normal human fetuses included for the present study. Among the 456 fetuses, 244 (53.51%) fetuses were males and 212 (46.49%) fetuses were females. The fetuses which were selected for the present study were of varying sizes ranging from 51mm to 394mm in crown-rump length (CRL) with 70 mm to 577 mm in crown-heel length (CHL). The exact gestational age (GA) of the fetuses was not known. Some of the details, such as regarding the

LMP (last menstrual period), given by the mothers of the fetuses could be misleading, as many of them want to keep their anonymity, as abortions do not enjoy much social acceptance. Therefore, in the present study, the fetuses were categorized on the basis of the CRL and CHL. As there is earlier literature available to estimate fetal age from the CRL as well as the CHL, this study adopted the already established scales, (Davies 1967; Okajima 1975; Williams and Warwick 1980), to estimate fetal age based on the CRL and CHL. Osteometry was carried out on all the 912 radius bones.

In spite of such a large collection of 456 fetuses, there existed obvious biases in the distribution of samples when individual group and sex were considered. Ideally, a trimester-wise grouping would have given better room for tracking the growth pattern. However, that would leave with only two such trimesters with meaningful sample sizes for comparison, leaving quite a few sample sizes in the remaining groups. Further, the results would provide us room only for a broad growth pattern or generalization. As a via media, an eight-week grouping was adopted, to make a total of four groups. In this way, we can justify the sample size under each group. Here too, although there existed an internal biasness in the distribution of sex-wise sample size in the group I, the remaining three groups showed good consistency in the sex-wise distribution of sample. For the purposes of discussion, the assigned group numbers, i.e. I, II, III and IV, would be used throughout this paper. All the 456 fetuses were categorized into four age groups, each group having eight weeks of duration of age range, except for the first group (Table 1). The first group had only a six-week range, because fetal bones would be available for manual measurements only after the period of 11 weeks of the intrauterine development.

Somatometry

When a fetus was brought to the Department of Anatomy, it was to be prepared for somatometric measurements. Only those fetuses that appeared normal were selected for the purpose of the present study. Firstly, the umbilical cord of the fetus was tied tightly with the help of a thread, near the umbilicus. The purpose of the tying up was to stop oozing out of the fetal blood from the fetus. The part of the umbilical cord along with the placenta was cut off and removed. The fetus was then cleaned with running water for about few minutes and kept ready for observation and taking somatometric measurements. The sex of the fetus was noted down. There were two somatometric measurements, CRL and CHL, selected for the present study. After the completion of the somatometry, the fetuses were kept for natural maceration process for the preparation of the fetal bones. No chemical was used in the maceration process.

Osteometry

There were seven osteometric measurements (Table 2) taken on the diaphyses of the fetal radii (Fig. 1) for this study. All the seven osteometric measurements were measured on both right and left bones. The maximum length of the radius is the maximum straight-line distance between the highest point on the proximal end and the lowest point on the distal end of the radius. The remaining measurements were taken at the proximal/distal/middle part of the radius from the maximum straight-line distance from anterior/posterior/medial/lateral-most points as per the

Table 1. Distribution of human fetuses for the present metric study.

Group	Weeks	CRL (mm)	CHL (mm)	Osteometry (456)		
				Male	Female	Total
I	11-16	51-100	Up to 150	18	4	22
II	17-24	101-200	151-300	159	152	311
III	25-32	-	301-400	49	42	91
IV	33-40	-	401-550	18	14	32
Total				244	212	456

(Source: Davies, 1967; Okajima, 1975; Williams and Warwick, 1980)

name of the measurement. Except the length of the radius (in this study called r-ml) and the midshaft transverse diameter (in this study called r-mml), the remaining five measurements were newly introduced in this study.

Table 2. Osteometric measurements on fetal radius.

S.No.	Osteometric Measurement	Abbreviation
1	Radius-Maximum Length	r-ml
2	Radius-Proximal Antero-Posterior Diameter	r-pap
3	Radius-Proximal Medio-Lateral Diameter	r-pml
4	Radius-Distal Antero-Posterior Diameter	r-dap
5	Radius-Distal Medio-Lateral Diameter	r-dml
6	Radius-Middle Antero-Posterior Diameter	r-map
7	Radius-Middle Medio-Lateral Diameter	r-mml

Statistical considerations

Regression coefficient

It was calculated using the following formula.

$$b_{yx} = \frac{\Sigma XY - \frac{\Sigma X \Sigma Y}{N}}{\Sigma X^2 - \frac{(\Sigma X)^2}{N}}$$

Where, b_{yx} = regression coefficient of dependent variable Y (e.g., r-ml) on independent variable X (CRL/CHL). In the present study b0 and b1 were used in places of b_y and b_x.

Tests of significance

t-test: The computation of values of 't' was according to the given formula.

$$t = \frac{\overline{X_1} - \overline{X_2}}{\sqrt{(S.E.\overline{X_1})^2 + (S.E.\overline{X_2})^2}}$$

Where, X_1 and X_2 = mean of sample 1 and 2 respectively, and

S.E. X_1 and S.E. X_2 = standard error of mean of sample 1 and 2, respectively. The value of 't' obtained was checked against the total degrees of freedom to get the level of significance (Singh and Bhasin, 1989).

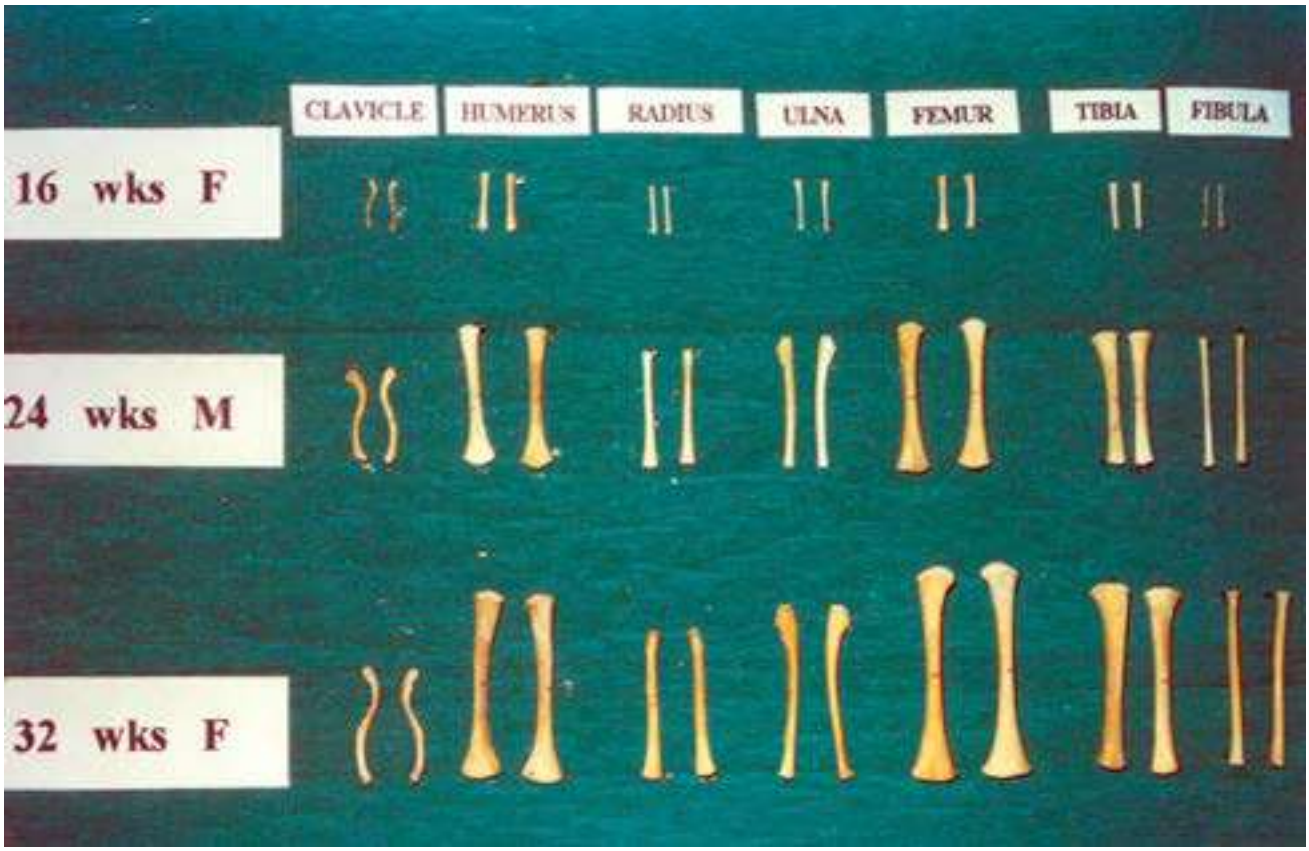

Fig. 1.- Shafts of fetal long bones (16 to 32 weeks) (Sample).

The degrees of freedom used were obtained by using the following formula.

$$d.f = (N_1 + N_2) - 2$$

where, N_1 and N_2 = total number of sample 1 and 2, respectively.

Absolute growth rate calculation

For calculating the absolute growth rate based on all the present measurements, the following formula (Biswas and Bhattacharya, 1966) was followed.

$$\text{Absolute growth rate percent per month} = \frac{\frac{\text{Absolute growth}}{S1}}{N} \times 100$$

$$\text{Absolute growth} = S_2 - S_1$$

S_1 = mean of the maximum length of the radius within the group I

S_2 = mean of the maximum length of the radius within the group II

Thus, the absolute growth for the inter-group I and II was the subtraction of the mean growth of group I from the mean growth of group II.

Length of period (N) for the present study is two-month duration.

Accordingly, the inter-group-wise absolute growth rate was calculated for the present study as absolute growth rate percent per month.

RESULTS

Side differences

Side differences (Tables 3 and 4) were analyzed on all the group-wise radius bones of the present study on the basis of the osteometric measurements. In the males, significant left-side dominance was observed from the group II in the r-pml at 1% level and in the r-dap at 5% level. Also in the males, the r-pml showed significant left-side dominance at 5% level from the group III. In the case of females, the r-pap and the r-map showed significant left-side dominance at 5% level from the group III. Also in the females, the r-ml showed significant right-side dominance and the r-pml showed significant left side dominance and both the latter r-ml and the r-pml were at 1% level from the group II. And also in the females, the r-dml showed significant right-side dominance at 5% level from the group III and significant left-side dominance at 5% level from group IV. On the basis of the analyses, it was observed that only 8.04% showed significant side differences in the osteometric measurements (Table 5).

Sex differences

Sex differences were analyzed on all the group-wise radius bones of the present study on the basis of the osteometric measurements (Table 6). Significant sex differences were found between the males and females in the r-mml at 5% level from group I; In the r-pap, r-pml, r-dml at 5% level and in the r-map, r-mml at 1% level from group II; In the r-mml at 5% level from group III. In all these measurements, the females showed higher values. On the basis of the analyses, it was observed that only 12.5% showed significant sex differences (Table 7).

Growth rate

From the regression values (b0, b1) calculated for the osteometry, all the osteometric measurements showed an increasing trend of growth rate for every 1 mm increase in CRL and CHL. The b1 values showed (Tables 8 and 9) increase in the osteometric measurements for every one mm increase in CRL/CHL. Among all the measurements, the r-ml showed faster rate of growth both in the males and females. The fastest rate of growth was observed in female radius from the group I (11 to 16 weeks). For every 1 mm in the CRL, the r-ml was increased by .235 mm. In the group I (11 to 16 weeks), mostly the females showed slightly higher values in almost all the osteometric measurements than the males. In all the osteometric measurements, in both the males and females the group II (17 to 24 weeks) showed slightly higher rate of growth when compared to the group III (25 to 32 weeks). The growth rate of r-ml was higher in the group I compared to the group IV in both the males and females.

Table 3. Side differences based on mean and standard deviation of male radius measurements in four age groups of fetuses.

Males	**Group -I**		**Group -II**		**Group –III**		**Group –IV**	
Radius – Left	**12-16wks (18)**		**17-24wks (159)**		**25-32wks (49)**		**33-40wks (18)**	
	Mean	SD	Mean	SD	Mean	SD	Mean	SD
r-ml	9.817	3.0269	23.623	5.1219	35.180	2.8206	47.562	6.1978
r-pap	1.172	.2340	2.240	.4973	3.430	.3614	4.861	.8213
r-pml	1.261	.2709	2.384	.5181	3.662	.3876	5.181	.8645
r-dap	1.1472	.23293	2.4821	.63814	4.0449	.49542	5.8500	1.04867
r-dml	1.44	.292	3.32	.860	5.42	.634	8.10	1.396
r-map	.6778	.16469	1.3129	.28982	1.8724	.22869	2.7167	.49170
r-mml	.761	.1997	1.484	.3197	2.221	.2665	3.211	.6225
Radius – Right								
r-ml	9.833	3.0541	23.635	5.1246	35.194	2.8222	47.614	6.3000
r-pap	1.164	.2293	2.245	.4930	3.427	.3478	4.822	.8512
r-pml	1.264	.2721	2.364	.5063	3.615	.4011	5.139	.8493
r-dap	1.1556	.23129	2.4682	.62540	4.0306	.49474	5.8222	1.13036
r-dml	1.43	.296	3.31	.863	5.42	.609	8.10	1.468
r-map	.6778	.16558	1.3145	.28548	1.8735	.22915	2.7222	.51684
r-mml	.750	.1910	1.485	.3188	2.233	.2709	3.186	.6519

Number in parentheses indicates sample size

Table 4. Side differences based on mean and standard deviation of female radius measurements in four age groups of fetuses.

Females	**Group -I**		**Group -II**		**Group -III**		**Group –IV**	
Radius – Left	**12-16wks (04)**		**17-24wks (152)**		**25-32wks (42)**		**33-40wks (14)**	
	Mean	SD	Mean	SD	Mean	SD	Mean	SD
r-ml	12.563	.7487	24.636	4.9183	35.839	3.3851	46.657	4.0511
r-pap	1.325	.1190	2.371	.4815	3.480	.3580	4.664	.5119
r-pml	1.388	.0629	2.509	.4991	3.670	.3857	4.900	.4666
r-dap	1.3250	.08660	2.6079	.64096	4.0940	.46842	5.7107	.95337
r-dml	1.71	.085	3.51	.828	5.49	.698	7.63	1.055
r-map	.8375	.10308	1.4003	.27898	1.9524	.26225	2.6000	.24729
r-mml	1.013	.1250	1.602	.3355	2.339	.2801	3.096	.3456
Radius – Right								
r-ml	12.600	.5715	24.666	4.9102	35.868	3.3948	46.582	3.9280
r-pap	1.325	.0645	2.375	.4816	3.450	.3518	4.682	.5319
r-pml	1.425	.0645	2.489	.4878	3.639	.3630	4.871	.5853
r-dap	1.3250	.06455	2.6020	.63522	4.0952	.47277	5.6786	.99571
r-dml	1.73	.065	3.52	.827	5.52	.701	7.55	1.078
r-map	.8500	.10801	1.3967	.27505	1.9286	.26507	2.5571	.24951
r-mml	1.000	.1291	1.602	.3345	2.344	.2737	3.093	.3257

Number in parentheses indicates sample size

Table 5. *'t'* values for left and right side comparison for male and female radius measurements in four age groups of fetuses.

Left and Right Comparison of Radius	Group –I		Group –II		Group -III		Group –IV	
Males	**12-16wks (18)**		**17-24wks (159)**		**25-32wks (49)**		**33-40wks (18)**	
	t	Sig-P	t	Sig-P	t	Sig-P	t	Sig-P
r-ml	-1.065	.302	-1.225	.222	-.608	.546	-.806	.431
r-pap	1.144	.269	-.880	.380	.302	.764	1.353	.194
r-pml	-.437	.668	3.763	.000**	2.679	.010*	1.667	.114
r-dap	-1.144	.269	2.492	.014*	1.089	.282	.777	.448
r-dml	.589	.564	1.687	.094	.254	.801	-.059	.954
r-map	.000	1.000	-.469	.640	-.141	.888	-.383	.707
r-mml	1.719	.104	-.301	.764	-1.315	.195	1.256	.226
Females								
r-ml	-.270	.805	-2.828	.005**	-.923	.362	1.005	.333
r-pap	.000	1.000	-.777	.438	2.058	.046*	-.717	.486
r-pml	-1.567	.215	3.202	.002**	1.756	.086	.477	.641
r-dap	.000	1.000	1.016	.311	-.072	.943	1.351	.200
r-dml	-1.000	.391	-1.737	.084	-2.460	.018*	2.637	.021*
r-map	-1.000	.391	1.118	.265	2.354	.023*	1.790	.097
r-mml	1.000	.391	-.112	.911	-.488	.628	.179	.861

Number in parentheses indicates sample size.*Significance at 5% level;**Significance at 1% level; Paired t-test

Table 6. Sex differences based on mean and standard deviation of radius measurements in four age groups male and female fetuses.

Radius	Group -I		Group –II		Group -III		Group –IV	
Males	**12-16wks (18)**		**17-24wks (159)**		**25-32wks (49)**		**33-40wks (18)**	
	Mean	SD	Mean	SD	Mean	SD	Mean	SD
r-ml	9.8250	3.04035	23.6289	5.12287	35.1867	2.82021	47.5881	6.24766
r-pap	1.1681	.23117	2.2426	.49366	3.4281	.35288	4.8417	.83415
r-pml	1.2625	.27120	2.3737	.51111	3.6388	.38961	5.1597	.85531
r-dap	1.1514	.23160	2.4752	.63083	4.0378	.49295	5.8361	1.08764
r-dml	1.4347	.29245	3.3137	.86056	5.4179	.62023	8.0986	1.42925
r-map	.6778	.16492	1.3137	.28688	1.8730	.22752	2.7194	.50348
r-mml	.7556	.19489	1.4844	.31863	2.2270	.26707	3.1986	.63596
Females	**12-16wks (04)**		**17-24wks (152)**		**25-32wks (42)**		**33-40wks (14)**	
	Mean	**SD**	**Mean**	**SD**	**Mean**	**SD**	**Mean**	**SD**
r-ml	12.5813	.65140	24.6508	4.91378	35.8536	3.38845	46.6196	3.98755
r-pap	1.3250	.08660	2.3729	.48036	3.4649	.35183	4.6732	.51994
r-pml	1.4063	.05907	2.4992	.49199	3.6548	.37016	4.8857	.51727
r-dap	1.3250	.07360	2.6049	.63709	4.0946	.46753	5.6946	.97375
r-dml	1.7188	.07465	3.5164	.82656	5.5065	.69843	7.5893	1.06544
r-map	.8438	.10483	1.3985	.27630	1.9405	.26162	2.5786	.24433
r-mml	1.0063	.12645	1.6018	.33451	2.3417	.27512	3.0946	.33371

Number in parentheses indicates sample size

Absolute growth rate

The absolute growth rate percent per month for the male and female fetuses belonged to the inter-age group I, II and III were calculated (Table 10). The r-ml of males from the inter-age group I-II (11 weeks to 24 weeks) showed the highest absolute rate of fetal growth as 70.25% per month. The lowest absolute growth rate was found in the r-ml of females from the inter- age group III-IV (25 weeks to 40 weeks) as15.01% per month. Absolute growth rate for the r- ml was higher in the inter-age group I-II (11 weeks to 24 weeks) and gradually declining through the proceeding two inter-age groups II-III (17 weeks to 32 weeks) and III-IV (25 weeks to 40 weeks) (Fig. 2).

Bivariate distribution

In the case of osteometry, variations between the CRL with the r-ml were computed. Because of the smaller sample size in the groups I and

Table 7. '*t*' values for male and female comparison of radius measurements in four age groups of fetuses.

Male and Female Comparison of Radius	Group -I		Group -II		Group -III		Group –IV	
	12-16wks		17-24wks		25-32wks		33-40wks	
	t	Sig-P	t	Sig-P	t	Sig-P	t	Sig-P
r-ml	-1.772	.092	-1.794	.074	-1.025	.308	.505	.618
r-pap	-1.316	.203	-2.357	.019*	-.497	.620	.661	.514
r-pml	-1.036	.313	-2.203	.028*	-.200	.842	1.056	.300
r-dap	-1.458	.160	-1.805	.072	-.562	.576	.382	.705
r-dml	-1.895	.073	-2.118	.035*	-.642	.523	1.113	.275
r-map	-1.908	.071	-2.654	.008**	-1.317	.191	.960	.345
r-mml	-2.435	.024*	-3.169	.002**	-2.013	.047*	.554	.584

Number in parentheses indicates sample size *Significance at 5% level; **Significance at 1% level; Unpaired t- test

Table 8. Regression values (b0,b1) for growth rate in radius with CRL in four age groups in male and female fetuses. b1 shows increase in the osteometric measurements for every one mm increase in CRL.

Radius		Group –I		Group –II		Group –III		Group –IV	
Males		11-16wks (18)		17-24wks (159)		25-32wks (49)		33-40wks (18)	
Dependent Variable (Y)	Independent Variable (X)	b0	b1	b0	b1	b0	b1	b0	b1
r-ml	CRL	-6.075	.188	-5.153	.187	10.40	.110	1.614	.149
r-pap		.111	.013	-.455	.017	.403	.013	-1.197	.020
r-pml		-.033	.015	-.404	.018	.168	.015	-1.027	.020
r-dap		.081	.013	-.942	.022	.019	.018	-2.500	.027
r-dml		-.017	.017	-1.414	.031	.243	.023	-2.714	.035
r-map		-.143	.010	-.152	.010	-.006	.008	-.977	.012
r-mml		-.159	.011	-.196	.011	.044	.010	-1.410	.015
Females		11-16wks (4)		17-24wks (152)		25-32wks (42)		33-40wks (14)	
r-ml	CRL	-10.725	.235	-4.575	.183	4.481	.137	1.151	.150
r-pap		.500	.008	-.327	.017	.767	.012	-1.920	.022
r-pml		-1.275	.027	-.288	.017	.485	.014	-1.610	.021
r-dap		1.325	.000	-1.037	.023	.280	.017	-6.515	.040
r-dml		-1.375	.031	-1.200	.030	-.480	.026	-6.445	.046
r-map		-3.900	.048	-.046	.009	-.157	.009	.230	.008
r-mml		-4.150	.052	-.205	.011	.203	.009	-.697	.012

Number in parentheses indicates sample size

IV, scatter diagrams were prepared only for the groups II and III. The scatter diagrams (Figs. 3 and 4) showed that there were very close relationships found between the CRL with r-ml. The obtained scatter diagrams showed a good fit between the variables correlated.

Correlations

In the present study, there were highly significant correlations obtained between the CRL/CHL with all the osteometric measurements (Table 11). In the males, the highest value of correlation coefficient .992 at 1% level as found between the CRL and r-ml in the group I. In the females, the highest value .977 at 1% level was found in between the CHL and r-ml in the group II.

Age estimation of human fetus

As there were highly significant correlations obtained between the CRL/CHL with all the osteometric measurements, necessary regression equations were calculated to calculate the CRL and CHL from all the osteometric measurements (Tables 12 and 13). Necessary regression values (b0, b1) were calculated for the osteometric measurements for age estimation. With the help of the tables 12 and 13, the CRL and CHL can be calculated using the two values b0 and b1 and given measurements. Once the CRL/CHL was calculated, the fetal age could be estimated from the already established age estimation scale.

The formula to calculate CRL/CHL is as follows:

$$\text{CRL/CHL} = (b1 \times \text{measurement on the radius}) + b0$$

Table 9. Regression values (b0,b1) for growth rate in radius with CHL in four age groups in male and female fetuses. b1 shows increase in the osteometric measurements for every one mm increase in CHL.

Radius		**Group –I**		**Group –II**		**Group –III**		**Group –IV**	
Males		**11-16wks (18)**		**17-24wks (159)**		**25-32wks (49)**		**33-40wks (18)**	
Dependent Variable (Y)	Independent Variable (X)	b0	b1	b0	b1	b0	b1	b0	b1
r-ml	CHL	-4.480	.119	-4.753	.124	4.489	.091	-.799	.107
r-pap		.217	.008	-.410	.012	-.098	.010	-1.421	.014
r-pml		.110	.010	-.355	.012	-.367	.012	-1.163	.014
r-dap		.189	.008	-.878	.015	-.769	.014	-2.742	.019
r-dml		.118	.011	-1.330	.020	-.560	.018	-2.995	.024
r-map		-.050	.006	-.135	.006	-.352	.007	-1.089	.008
r-mml		-.065	.007	-.175	.007	-.222	.007	-1.490	.010
Females		**11-16wks (04)**		**17-24wks (152)**		**25-32wks (42)**		**33-40wks (14)**	
r-ml	CHL	-7.976	.141	-4.133	.120	.232	.104	-2.179	.108
r-pap		2.207	-.006	-.275	.011	.212	.010	-1.135	.013
r-pml		-.523	.013	-.220	.011	.022	.011	-1.067	.013
r-dap		2.648	-.009	-.951	.015	-.396	.013	-5.744	.025
r-dml		-.761	.017	-1.093	.019	-1.53	.021	-5.379	.029
r-map		-3.180	.028	-.019	.006	-.475	.007	-.073	.006
r-mml		-4.230	.036	-.164	.007	-.080	.007	-.753	.009

Number in parentheses indicates sample size

Table 10. Absolute growth rate percent per month for the inter-age groups of human fetuses.

Sex	**Intergroup I**	**Intergroup II**	**Intergroup III**
Males	70.25	24.46	17.62
Females	47.96	22.72	15.01

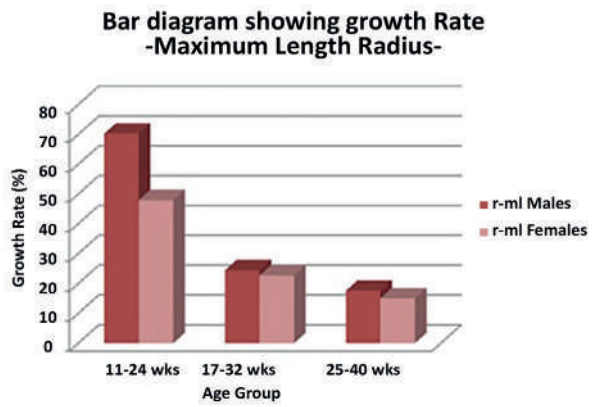

Fig. 2.- Absolute growth rate of fetus based on maximum length of radius.

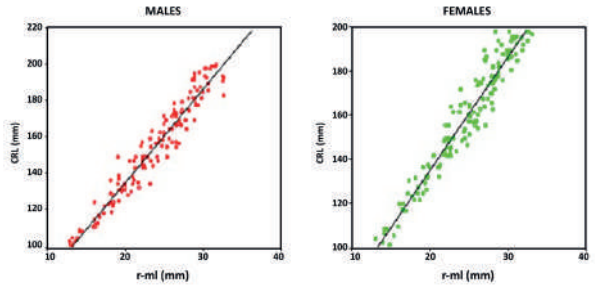

Fig. 3.- Scatter diagrams and regression fit lines for r-ml (mm) with CRL (mm) in Group II.

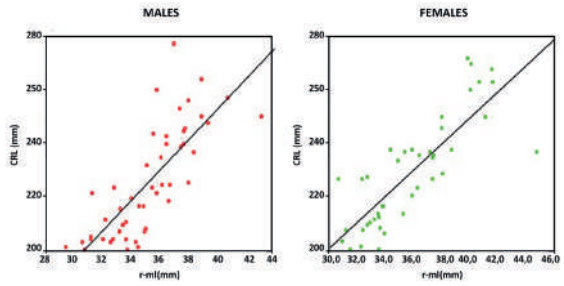

Fig. 4.- Scatter diagrams and regression fit lines for r-ml (mm) with CRL (mm) in Group III.

DISCUSSION

Side and Sex differences

The side differences in the considered measurements indicated certain specific trends that might reveal side dominance. However, there being a low percentage (8.04%) of significant side differences, in the present study all the analyses including the mean and standard deviations, correlation coefficients, regression analyses, analyses on growth and age estimation were calculated on the basis of the mean values of both

Table 11. Correlation between CRL, CHL with radius measurements in four age groups of male and female fetuses.

Correlation between CRL, CHL with Radius	**Group -I**		**Group –II**		**Group -III**		**Group –IV**	
Males	12-16wks (18)		17-24wks (159)		25-32wks (49)		33-40wks (18)	
	CRL	CHL	CRL	CHL	CRL	CHL	CRL	CHL
r-ml	.992**	.991**	.970**	.977**	.786**	.881**	.917**	.949**
r-pap	.867**	.866**	.944**	.947**	.767**	.809**	.903**	.920**
r-pml	.906**	.894**	.938**	.941**	.797**	.832**	.902**	.906**
r-dap	.876**	.875**	.935**	.937**	.729**	.789**	.956**	.966**
r-dml	.941**	.948**	.949**	.951**	.746**	.780**	.943**	.951**
r-map	.944**	.929**	.882**	.890**	.739**	.791**	.915**	.927**
r-mml	.890**	.886**	.911**	.918**	.731**	.742**	.903**	.903**
Females	**12-16wks (04)**		**17-24wks (152)**		**25-32wks (42)**		**33-40wks (14)**	
r-ml	.723	.719	.967**	.977**	.818**	.870**	.817**	.903**
r-pap	.192	-.232	.913**	.919**	.677**	.765**	.909**	.824**
r-pml	.917	.744	.921**	.922**	.756**	.812**	.900**	.849**
r-dap	.000	-.410	.929**	.931**	.720**	.794**	.899**	.867**
r-dml	.837	.757	.927**	.930**	.757**	.833**	.944**	.898**
r-map	.914	.875	.850**	.856**	.708**	.764**	.689**	.801**
r-mml	.824	.944	.878**	.880**	.686**	.728**	.814**	.851**

Number in parentheses indicates sample size *Significance at 5% level; **Significance at 1% level

the left and right sides merging together. In the case of sex differences, in spite of the very low percentage (12.5%), in the present study all the obtained results on correlation coefficients, regression constants for growth rate and also scattergrams along with regression fit lines and bar diagrams were presented sex-wise separately for evolving a broad comparative perspective on both sexes.

Table 12. Regression values (b0, b1) for estimating CRL, from radius from the total sample of 456 fetuses.

Osteometric measurements on Radius	Group –All	
	b0	b1
r-ml	16.964	5.890
r-pap	24.464	57.889
r-pml	23.237	55.199
r-dap	45.795	44.009
r-dml	46.668	32.504
r-map	19.278	104.106
r-mml	26.585	85.733

Table 13. Regression values (b0, b1) for estimating CHL, from radius from the total sample of 456 fetuses.

Osteometric measurements on Radius	Group –All	
	b0	b1
r-ml	24.491	8.807
r-pap	36.628	86.215
r-pml	35.162	82.080
r-dap	68.524	65.501
r-dml	69.933	48.350
r-map	28.526	155.294
r-mml	39.894	127.623

Growth rate

Studies on bone growth, based on quantitative analyses, enable a better understanding of the growth pattern. On the basis of the analyses on osteometry, the present study revealed that there was a positive growth trend, which was observed in all the measurements taken on the fetal radius from all the four age groups considered. Moss et al. (1955) stated that several combinations of osseous shaft lengths revealed a constant ratio between the specific growth rates of all the bones. They measured 106 fetuses, which were cleared and stained with alizarin, ranging from 30 mm to 169 mm in CRL, whereas in the present study in the same age group (I and II), 333 fetuses got measured. The present osteometric study was carried out on 912 naturally macerated, dried bones from 456 fetuses. Variations observed with the earlier results (Table 14) might be attributed to the very low sample size of the earlier studies and the mode of preparation of the bone material for the osteometric study. Moss et al. (1955) noted a characteristic interphase in the growth of the body shaft in the CRL interval of 80 - 89 mm. Before the interval, the body shafts of all the long bones grew relatively faster than the CRL, and after that the growth rate was not as fast as it was before. Fazekas and Kosa (1966a, b) determined the size of embryos from the dimensions of the radius. In the present study, measurements on fetal radius have been correlated with the CRL and CHL for fetal age estimation. Fazekas and Kosa (1966a, b) in an attempt calculated the mean lengths of all six limb bones at two weeks intervals from 12 to 40 weeks, whereas in the present study the fetuses were categorized with eight-week intervals, except for the first group which had a six-week interval. Vare and Bansal (1977) observed a linear correlation between the diaphyseal length of the upper and lower limbs and the CRL from 185 fetuses of 116 males and 69 females with CRL ranging from 185 - 415 mm. The bones were dissected from the body and got measured. Although the muscles and connective tissue were removed from the bones, the periosteum was left intact. Vare and Bansal (1977) reported about all the long bones except the clavicle. In these studies, the calculation of growth rate was found not on the basis of age groups, whereas in this study the growth rate was calculated using regression equations, in all the four age groups under the male and female categories separately for all the osteometic measurements. Thus, in this study a broad understanding was evolved on the growth rate of fetal long bones, age-wise and sex-wise. Vare and Bansal (1977) reported that for every 1 mm increase in CRL the length of radius increases by 0.15 mm, whereas the present study reported that the groups I, II, III and IV showed 0.188 mm, 0.187 mm, 0.110 mm and 0.149 mm respectively in the males and 0.235 mm, 0.183 mm, 0.137 mm and 0.150 mm respectively in the females.

Table 14. Mean of Maximum Length of Radius (r-ml): Comparison.

	Group I		Group II	
Bones	Moss et al. (1955)	Present study	Moss et al. (1955)	Present study
Radius	7.80	11.20	22.32	24.14

Absolute growth rate

As there were four age groups viz. I, II, III, IV, the absolute growth rate was calculated between these four groups. Thus, there were three inter-age groups formed from the four basic groups as I-II, II-III, and III-IV. Each inter-age group had the total number of fetuses from both the groups concerned. The absolute growth rate was calculated only for the r-ml for the present study. The bar diagram (Fig. 2) revealed the absolute growth rate for the r-ml of both the males and females between the three inter-age groups. Thus, the prepared bar diagram not only helps understand the trend of absolute growth rate but also shows sex differences.

Age estimation

As the CRL and CHL were found closely correlated with all the osteometric measurements, it showed that that a clear dynamic relationship existed between the CRL/CHL with all the osteometric measurements. Expert opinion is routinely requested from anatomists, by legal authorities, to know about the age and sex of the deceased, while dealing with suspected murder cases. While examining the adult cases, as there are already established scales available for age estimation, it becomes easy to estimate the age of deceased adult individual from the bone remains. On the contrary, when opinion about the age of a deceased fetus is asked from the available fetal bones, as there is no established scale or standards available, even anatomists are not in a comfortable position to provide precise information regarding the age of fetus from the bone remains. Mehta and Singh (1972), Vare and Bansal (1977) and Fazekas and Kósa (1978) measured fetal long bones, which include the radius, from a radiographic sample. Kosa (1997) attempted to estimate fetal age from the chemically preserved fetal long bones. Simon et al. (1992), Simon and Baig (2015a, b) and Simon et al. (2020a, b) estimated CRL/CHL from the clavicle, humerus, femur, tibia and fibula respectively, and these studies were carried out on naturally macerated fetal bones without adding any preservative. This study emphasizes that definitely there is variation between taking measurements from radiographs, ultrasonographs, photographs and bones from chemically preserved fetuses and taking measurements directly from the naturally macerated bones. In this study, once the CRL/CHL is calculated from the analyzed regression values based on the osteometry on fetal radius bones, age can be estimated from the already established age estimation scale.

Applied significance

The applied significance in the clinical aspects in this study would enable us to advance a standard, which would help comprehend the differential growth pattern between normal and abnormal fetuses. The analysis in the present study to estimate fetal age from the measurements on the human fetal radius bones would definitely help in solving problems facing the estimation of fetal age, a crucial factor in medico-legal cases. The anatomical aspects of this population-based study on growth pattern in relation to age and sex variations would open new vistas for research in the field of fetal growth.

REFERENCES

BARTOSCH C, VILAR I, RODRIGUES M, COSTA L, BOTELHO N, BRANDAO O (2019) Fetal autopsy parameters standards: biometry, organ weights, and long bone lengths. *Virchows Arch*, 475(4): 499-511.

BEUNEN G, LEFEVRE J, OSTYN M, RENSON R, SIMONS J, VAN GERVEN D (1990) Skeletal maturity in Belgian youths assessed by the Tanner-Whitehouse method (TW2). *Ann Hum Biol*, 17: 355-376.

BISWAS PC, BHATTACHARYA DK (1966) Growth trends in Northern Indian population variation of four anthropometric traits from birth to maturity. In: Malhotra MS (editor). Human adaptability to environments and physical fitness. *Defence Institute of Physiology and Allied Sciences, Madras*, pp 270-280.

BURDI AR (1969) Cephalometric growth analysis of the human upper face region during the last two trimesters of gestation. *Am J Anat*, 125: 113-122.

BUTT K, LIM K (2014) Determination of gestational age by ultrasound. *J Obstet Gynaecol Canada*, 36: 171-183.

CARDOSO HFV, ABRANTES J, HUMPHREY LT (2014) Age estimation of immature human skeletal remains from the diaphyseal length of the long bones in the postnatal period. *Int J Legal Med*, 128(5): 809-824.

CARNEIRO C, CURATE F, BORRALHO P, CUNHA E (2013) Radiographic fetal osteometry approach on age estimation for the Portuguese population. *Forensic Sci Int*, 10:231(1-3): 397.e1-5.

CARNEIRO C, CURATE F, CUNHA E (2016) A method for estimating gestational age of fetal remains based on long bone lengths. *Int J Legal Med*, 130(5): 1333-1341.

CARNEIRO C, ALEMAN I, BOTELLA M, CUNHA E (2019) Fetal age at death estimation on dry bone: testing the applicability of equations developed on a radiographic sample. *Revista Argentina de Anthropología Biológica*, 21(2).

CHITTY LS, ALTMAN DG (2002) Charts of fetal size: limb bones. *Br J Obstet Gynaecol*, 109: 19-29.

DAVIES DV, editor (1967) Gray's Anatomy. 34th edn. p 261. *Longmans*, Green, London.

DHAWAN V, KAPOOR K, SHARMA M, SINGH B, SEHGAL A (2014) Morphometry of fetal femora as an indication of gestational age. E*ur J Anat*, 18(2): 85-92.

FAZEKAS IG, KOSA F (1966a) Neuere Beitrage und vergleichende Untersuchungen von Feten zur Bestimmung der Korperlange auf Grund der Diaphysenmasse der Extremitatenknochen. *Deutsche Zeitschrift gerichtliche Medizin*, 58: 14-160.

FAZEKAS IG, KOSA F (1966b) Determination of the size of embryos from the dimensions of the radius. *Ann Med Leg Criminal Police Sci Toxicol*, 46 (Pt 4): 262-272.

FAZEKAS IG, KOSA F (1978) Forensic fetal osteology. Budapest: Akademiai Kiado.

FELTZ WJL (1954) The prenatal development of the human femur. *Am J Anat*, 94: 1-44.

FORD EHR (1956) The growth of the fetal skull. *J Anat*, 90: 63-72.

GARDNER E, GRAY DJ (1970) The prenatal development of the human femur. *Am J Anat*, 129: 121-140.

GRAY DJ, GARDNER E (1969) The prenatal development of human humerus. *Am J Anat*, 124: 431-446.

HUXLEY AK (1998) Comparability of gestational age values derived from diaphyseal length and foot length from known forensic foetal remains. *Med Sci Law*, 38(1): 42-51.

IRURITA OJ, ALEMAN AI (2017) Proposal of new regression formulae for the estimation of age in infant skeletal remains from the metric study of the pars basilaris. *Int J Legal Med*, 131(3): 781-788.

KHAN Z, FARUQUI NA (2006) Determination of gestational age of human fetuses from diaphyseal lengths of long bones - A radiological study. *J Anat Soc India*, 55: 67-71.

KOSA F (1997) Determination of body length and age of human foetuses and newborns on the basis of weights of limb bones. *Acta Biol Szeged*, 42: 225-234.

KULKARNI DS, SIMON D, BHANU BV (1981) Dermatoglyphic study on human foetus. *J Anat Sci*, 3(Pt 1): 47-52.

KULKARNI VS (1985) Profiles of growth of two Endogamous groups [doctoral thesis]. Department of Anthropology, University of Pune, Pune, India.

LOUGHNA P, CHITTY L, EVANS T, CHUDLEIGH T (2009) Fetal size and dating: Charts recommended for clinical obstetric practice. *Ultrasound*, 17: 161-167.

MAHAKKANUKRAUH P, KHANPETCH P, PRASITWATTANSEREE S, VICHAIRAT K, TROY CASE D (2011) Stature estimation from long bone lengths in a Thai population. *Forensic Sci Int*, 210(1-3): 279.

MAHON PA, COOPER C, CROZIER SR, GODFREY KM (2009) The use of 3D ultrasound to investigate fetal bone development. *Norsk Epidemiologi*,19(1): 45-52.

MEHTA L, SINGH HM (1972) Determination of Crown-Rump length from foetal long bones humerus and femur. *Am J Phys Anthrop*, 36: 165-168.

MOORE KL, PERSAUD TVN, editors (1993) The Developing Human – Clinically Oriented Embryology. 5th edn. *Saunders*, Philadelphia.

MOSS ML, NOBACK CR, ROBERTSON GG (1955) Critical development horizons in human fetal long bones. *Am J Anat*, 97: 155-175.

MUNOZ JI, LINAREZ-IGLESIAS M, SUAREZ-PENARANDA JM, MAYO M, MIGUENS X, RODRIGUEZ-CALVO MS, CONCHEIRO L (2001) Determined long bone length in a Spanish population sample. *J Forensic Sci*, 46(2): 363-366.

OKAJIMA M (1975) Development of dermal ridges in the fetus. *J Med Genet*, 12: 243-250.

O'RAHILLY R (1973) Developmental stages in human embryos. Part A. Embryos of the first three weeks (stages 1-9). pp 9-31. *Carnegie Institution of Washington*, Washington.

PADMANATHAN G, PRAKASH S, CHHIBBER SR (1990) Single occasion means of height and weight of Sri Lankan Tamil children from Jaffna. *Ann Human Biol*, 17(Pt 2): 107-113.

PIERCECCHI-MARTI MD, ADALIAN P, BOURLIERE-NAJEAN B, GOUVERNET J, MACZEL M, DUTOUR O, LEONETTI G (2002) Validation of a radiographic method to establish new fetal growth standards: radio-anatomical correlation. *J Forensic Sci*, 47: 328-331.

SCHEUER JL, MUSGRAVE JH, EVANS SP (1980) The estimation of late fetal and perinatal age from limb bone length by linear and logarithmic regression. *Ann Human Biol*, 7(Pt 3): 257-265.

SHIMURA N, KOYAMA S, ARISAKA O, IMATAKA M, SATO K, MATSUURA M (2005) Assessment of measurement of children's bone age ultrasononically with Sunlight BonAge. *Clin Pediatr Endocrinol*, 14(Suppl 24): 17-20.

SHIRLEY NR (2009) Age and sex estimation from the human clavicle: An investigation of traditional and novel methods. A Dissertation presented for Ph.D. Degree to the University of Tennessee, Knoxville.

SIMON D, KULKARNI DS, GORE AP, BHANU BV, PATWARDHAN S (1984) Somatometric study on human foetus. *J Anat Sci*, 6: 1-6.

SIMON D, DESHMUKH AN, BHANU BV (1992) Age estimation from human foetal clavicle. *Med J West India*, 20: 58-62.

SIMON D, BAIG MM (2015a) Growth analysis and age estimation of human fetus from human fetal humerus. *IJIRD*, 4(Pt 5): 142-147.

SIMON D, BAIG MM (2015b) Growth pattern and fetal age estimation from the diaphyseal length of femur. *IJIRD*, 4(Pt 5): 148-152.

SIMON D, ANNIE V, BISWAJIT B, MONIE S, DON V (2020a) Human fetal growth and age estimation based on osteometry on the diaphysis of fetal tibia. *IJIRD*, 9(5): 40-48.

SIMON D, BISWAJIT B, MONIE S, DON V, ANNIE V (2020b) Fetal growth and age estimation based on osteometry on the diaphysis of human fetal fibula. *IJIRD*, 9(5): 49-57.

SINGH IP, BHASIN MK (1989) Anthropometry. Bharti Bhavan, *Kamla-raj Enterprises*, New Delhi.

SMITH SL (2007) Stature estimation of 3-10-year-old children from long bone lengths. *J Forensic Sci*, 52(3): 538-546.

TSUZAKI S, MATSUO N, SAITO M, OSANO M (1990) The head circumference growth curve for Japanese children between 0-4 years of age: Comparison with Caucasian children and correlation with stature. *Ann Human Biol*, 17(Pt 4): 297-303.

VARE AM, BANSAL PC (1977) Estimation of Crown-Rump length from diaphyseal lengths of fetal long bones. *J Anat Soc India*, 26(Pt 2): 91-93.

WANG YZ, HUANG Y, ZHOU XR, DENG ZH (2012) Stature estimation based on the length of tibia and fibula measured by digital X-ray in Chinese Han teenagers. *Fa Yi Xue Za Zhi*, 28(6): 413-7,425.

WILLIAMS PL, WARWICK R, editors (1980) Gray's Anatomy. 36th edn. *Churchill Livingstone*, Edinburgh.

Vertical symmetry of external auditory meatus and its relationship with the occlusal plane

Reza Soleimani[1], Fahimeh Hamedirad[2]

[1] *Dental Faculty of Babol, University of Medical Sciences, Babol, Iran*

[2] *Oral Health Research Center, Health Research Institute, Babol University of Medical Sciences, Babol, I.R. Iran*

SUMMARY

This study aimed to investigate the vertical symmetry of the external acoustic meatus (EAM) and its relationship with the occlusal plane in an Iranian population. The digital facial images of 220 individuals with a face-bow device were acquired. The image size was adjusted to the actual size, using a photo editing software. Also, the desired points and reference lines were measured and recorded by using the software tools. The collected data were analyzed, using Kolmogorov-Smirnov test, independent t-test, one-way ANOVA, and post-hoc test (α=0.05).

The higher position of the right ear EAM, the higher position of the left ear EAM, and their vertical symmetry were observed in 51.5%, 44.1%, and 4.5% of the images, respectively. The mean vertical distance between the meeting points of the right and left ear EAMs on the midsagittal plane, as well as the angle between the EAMs and the midsagittal plane, varied among three modes of the vertical symmetry of EAMs. However, no significant difference was found in the mean angle of the line crossing the EAM with the midsagittal line and the occlusal plane for the three modes. The results showed that the vertical symmetry of the EAMs was not correlated with sex or age. The vertical symmetry of the EAM was only observed in 4.5% of the participants.

Key words: Symmetry – External acoustic meatus – Occlusal plane – Midsagittal

INTRODUCTION

During dental treatments, the three-dimensional position of the maxillary and mandibular arches can be replicated in an articulator (Rosati et al., 2012; Chatuverdi and Thombare, 2013), using the face-bow transfer, which relates the maxillary cast to the articulator through the hinge axis relative to the reference points in the sagittal plane (e.g., the Frankfort horizontal plane or Camper's plane) (Gandhi et al., 2017). Most patients have a degree of facial and craniofacial asymmetry, especially in the middle and lower thirds of the face (Porter and Olson, 2011). When a standard symmetric face-bow is used for a patient with an asymmetric external acoustic meatus (EAM), an error may occur in the transferred maxillary position relative to the sagittal axis. This makes the midline non-coincident with the midsagittal

Corresponding author:
Fahimeh Hamedirad. Health Research Institute, Prosthodontics Department of the Dental Faculty, Babol University of Medical Sciences, 47176-43633 Babol, Iran. Phone: 01132291408-9; Fax: 01132291093. E-mail: Fahimeh.hamedirad@gmail.com

Submitted: September 19, 2020. **Accepted:** December 17, 2020

The project has been supported by Oral Health Research Center, Health Research Institute, Babol University of Medical Sciences, Babol, I.R. Iran.

plane and raises the dental arch on one side; therefore, the occlusion may not be functional or esthetic (Shah et al., 2016; Wei et al., 2011; Gateno et al., 2003; Kim et al., 2010, 2014; Sherry and Jain, 2017; Naini, 2013).

On the other hand, standard measurements of the face are necessary to determine the occlusal plan. Variety in the position, size, and basic shape of the maxillofacial system has differences in the growth of these components in different populations, which in turn are influenced by certain genetic, climatic, and environmental factors. The results of anthropometric studies on the craniofacial characteristics of different racial groups have shown interregional diversity, and therefore the application of data from one ethnic group to another is misleading (Gandhi et al., 2017).

The present study was performed due to a lack of research on the symmetry of EAMs in an Iranian population and its importance in the success of dental treatments (Choi et al., 2015).

MATERIALS AND METHODS

This descriptive, analytical, cross-sectional study was conducted on 220 healthy adults during 2018-2019, using the available sampling method. The inclusion criteria were as follows: 1) age above 18 years; 2) willingness to participate in the study; 3) having a complete set of permanent teeth, excluding the third molars; 4) lack of dental crowns; 5) lack of orthodontic treatments; 6) no third molar extraction within the past six months; 7) no history of head and neck trauma or surgery or ear, nose, throat (ENT) surgery; 8) absence of craniofacial disorders, such as EAM abnormalities or apparent deformities in the maxilla and mandible; 9) known skin diseases with obvious effects on the appearance and soft facial tissue; and 10) lack of physical disabilities, restricting the face-bow application.

The participants entered the study after signing a written consent form. Some studies have used some techniques like MRI for determining the EAMs position (Tsutsumi et al., 2020). As these methods are unusual and expensive, we preferred to use simple clinical method that has been used in other studies (Hooda and D'Souza, 2012). To study the variables, two black bands were attached to the horizontal arm of the ear face-bow (Manico, Tehran, Iran) 10 cm apart and plotted to calibrate the size of digital images to the actual size. A black band was also attached to the ear rod arm for the ease of measurement. After the subject was seated, the ear face-bow was mounted without using a fork. A Fox plane (Manico, Tehran, Iran) was established tangentially to the maxillary occlusal plane and stabilized by occlusion with cotton rolls. It should be noted that the subject's head did not bend to the right or left; both ears were clearly visible with no earrings; the trago-orbitale-tragion line was parallel to the floor; the lips were in rest; and the subject looked directly at the camera and raised his/her head until the philtrum was visible.

A digital camera (Canon 60D EOS, Ota, Tokyo, Japan), with a macro lens (Canon EF100mm f/2.8L IS USM Macro Lens, Ota, Tokyo, Japan) and a flash (Canon COOLPIX 270EX II; Canon Speedlite, Ota, Tokyo, Japan), was used to acquire images. To adjust the frame, the upper limit was tangential to the top of the participant's head, and the lower limit was aligned in a way that the vertical and horizontal arms of the face-bow were completely inside the image; the focus point was placed directly on the eyes. The image was adjusted to the actual size in Photoshop CC 2019 (Adobe, USA), based on the ratio of actual size (a 10-cm band marked on the face-bow horizontal arm) to the digital format, as determined by the ruler tool in Photoshop. The reference points and the lines were determined by two independent observers, who were previously trained and synchronized regarding the methodology. Values were measured and recorded using the ruler tool.

Moreover, to examine the symmetry of the EAMs in Photoshop, the midpoint of the black bands on the outer edge of the right and left arms of the ear rods (the middle width of the ear rod arms) was defined as the midpoint of the EAM, from which the lines were drawn perpendicular to the midsagittal line. The alignment of these two lines indicated the vertical symmetry of the EAMs and the earholes. Next, using the Photoshop ruler tool (Fig. 1), the vertical distance between these lines

in the midsagittal line, as well as the distance between the right and left EAMs on the midsagittal line, was measured. Afterward, the angle between the line of EAMs and the midsagittal line was measured. A line was also drawn parallel to the occlusal plane (based on the Fox plane) close to the line passing through the ears, and the angle was measured using the ruler tool. Moreover, the angle between the occlusal plane and the midsagittal line was measured and recorded (Fig. 2).

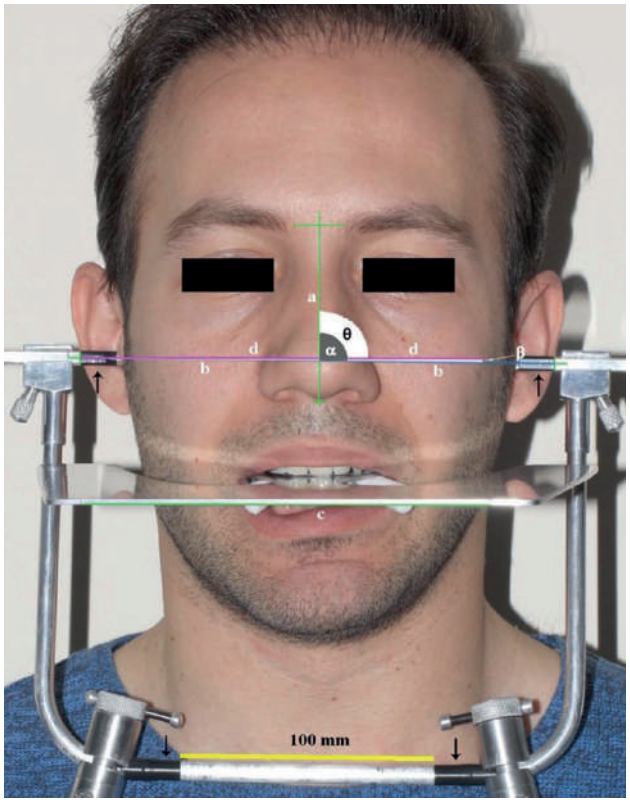

Fig. 1.- Matching of the images with software (Photoshop ruler tool).

The collected data were analyzed in SPSS Version 20.0 (IBM, New York, USA), using Kolmogorov-Smirnov test, independent t-test, one-way ANOVA, and post-hoc test (α=.05).

RESULTS

A total of 220 individuals, aged 18 to 63 years, participated in this study. The reliability test, based on Cohen's kappa coefficient, showed excellent agreement between the two examiners in evaluating different positions of vertical symmetry between the right and left EAMs (P<0.001; κ=0.898). Evaluation of the vertical symmetry of the right and left EAMs showed that 51.4% and 44.1% of the participants had the right and left EAMs in higher positions, respectively. Only in 4.5% of the participants, the two EAMs were vertically symmetric and aligned.

The mean vertical distance between the crossing lines of the right and left EAMs on the midsagittal line was 2.98±2.55 mm. The agreement between the two examiners in measuring other factors was excellent. The mean values measured by the two examiners were used to analyze facial dimensions. The mean distance between the ears and the midsagittal line is presented in Table 1. A significant difference was found in the mean vertical distance between the right and left EAM crossing points on the midsagittal line in different positions of the vertical symmetry of EAM (P=0.002).

The comparative analysis of the angles at different positions of the vertical symmetry of EAMs, based on one-way ANOVA, is shown in Table 2. A significant difference was found in the mean angle of the EAM lines with the midsagittal line in different positions of the vertical symmetry of EAM (P<0.001). The mean angles of the EAM lines with the midsagittal line and the occlusal plane were similar in different positions of the vertical symmetry of EAMs, and no significant difference was found (P=0.10 and P=0.766, respectively).

According to the present results, the mean distance of the right and left EAMs from the midsagittal line was significantly longer in males than females (P<0.001). However, no significant difference was found in terms of other factors. Also, there was no significant correlation between the vertical symmetry of EAM and sex (P=0.933; χ^2=0.044). Similarly, changes in the measured factors were independent of age variations.

DISCUSSION

We did not find any studies on the vertical symmetry of EAM in an Iranian population. Only 4.5% of the participants had vertical symmetry in the right and left EAMs, and the majority had the right EAM in a higher position. Regarding the positional symmetry of the porion and EAM on the face and its correlation with maxillary occlusal plane rotation, the results showed that in both facial symmetry and asymmetry (including

asymmetry with obvious maxillary occlusal rotation), the vertical porion tended to have a symmetric position. Since in facial asymmetry, the EAMs are positioned asymmetrically relative to the maxillary occlusal rotation, the possibility of EAM asymmetry must be considered for detecting and measuring maxillary rotation in facial asymmetry (Hooda and D'Souza, 2012). They found that in Indian population the left side is upper than the right side. The results of their study were the opposite of the results of our study.

Since the occlusal plane is adjusted in the patient's mouth, according to the anatomical and esthetic criteria, when using a standard face-bow for transferring the rims to the articulator on a face with an asymmetric EAM, an error may occur in the transferred maxillary position relative to the sagittal axis. This makes the midline non-coincident with the midsagittal plane, raises the dental arch on one side, and therefore, results in a non-functional or non-esthetic occlusion (Shah et al., 2016; Wei et al., 2011; Gateno et al., 2003; Kim et al., 2010; Sherry and Jain, 2017; Naini, 2013). Moreover, the asymmetry of the external ear holes causes the rims to tilt in the articulator and causes confusion for the technician; also, occlusal errors may occur. As the higher position of one EAM than the other one (even 1 mm) results in a tilted upper jaw in the articulator, it is recommended to use a modified position of the ear rods to compensate for this asymmetry.

According to the present results, there was no significant difference in the mean distance of the right and left EAMs from the midsagittal line in different positions of the vertical symmetry of EAMs. In a study by Min-Gun Kim et al. on the 3D symmetry and alignment of skeletal porion and soft tissue, the anterior-posterior angular deviation between these two landmarks was measured. Their results showed that, in patients with facial asymmetry, the mean porion deviation was 3 mm, which should be considered during face-bow transfer (Choi et al., 2015). Moreover, in the present study, individuals with an apparent facial asymmetry were not studied, whereas the higher position of the right ear was observed in 51.4% of the participants. The vertical difference between the ears was 2.98±2.55 mm on average. However, one participant had a vertical difference of 15.3 mm, which required modification during the face-bow transfer.

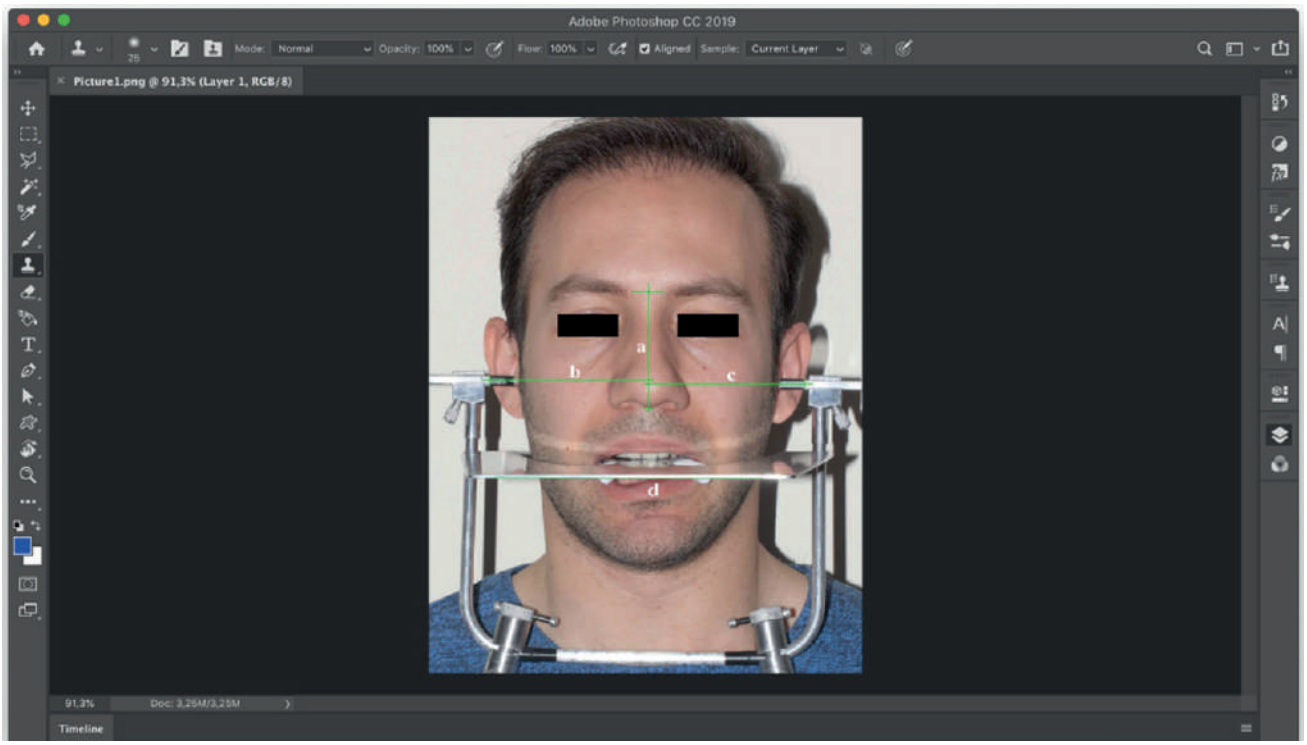

Fig. 2.- Placement of the Fox plane and the face-bow without fork on applicant's face with black bands. The graphic lines and angles on the digital image including midsagittal line (a), the line between EAMs (b), the tangential line to the Fox plane (c), the parallel line to the Fox plane (d), the angle of the line between EAMs and midsagittal line (α), the angle of the line between EAMs and parallel line to the Fox plane (β), the angle between the midsagittal line and parallel line to the Fox plane (θ).

In the present study, a significant difference was found in the mean vertical distance between the crossing points of the right and left EAMs on the midsagittal line in different positions of the EAM, and the mean distance in the symmetrical positions was less than the other two positions. This difference was attributed to the mean difference of distance in symmetric EAMs to either the higher right or left EAMs. When the EAMs are symmetric, the distance and the mean value will be zero for all individuals. Based on the statistical tests, the mean distance was 0.18 mm in the current study. The magnification error and the difference from the actual anatomic size seem to be associated with size measurements in Photoshop, depending on the software error for image analysis.

In a study by Mizgiryte et al. (2014), the mean angle between the EAM and the midsagittal plane was 90.12° (SD=1.48°) in the basal view and 90.36° (SD=2.25°) in the frontobasal view. In the current study, regardless of the mode of symmetry, the mean angle was 90.08° in the frontal view, which is consistent with the study by Mizgiryte and colleagues. Moreover, in the present study, the mean angle between the EAM lines and the occlusal plane, as well as the angle between the midsagittal line and the occlusal plane, were similar in different positions of the vertical symmetry of EAMs, and no significant difference was observed. This does not cause any problems in reconstructing the plane, except for cases where there is a significant difference. We suggest making a customized jig or using an

Table 1. Comparing the distances between the right, left EAMs and the midsagittal line, and vertical distance between the crossing points of the right and left EAMs on the midsagittal line, in different positions of vertical symmetry of the EAM.

Positions of vertical symmetry of EAMs	**symmetric**	**Right EAM at the higher position**	**Left EAM at the higher position**	**F**	**P Value***
distance(mm)	**Mean ±Std. Deviation (95% Confidence Interval)**	**Mean ±Std. Deviation (95% Confidence Interval)**	**Mean ±Std. Deviation (95% Confidence Interval)**		
Distance of the right EAM to the midsagittal line	84.79 ±5.3 (80.94 – 86.15)	87.48 ±3.7 (86.78 – 88.18)	86.78 ±4.7 (85.82 – 87.74)	2.157	0.11
Distance of the left EAM to the midsagittal line	84.52 ±2.2 (82.88 – 86.15)	84.55 ±4.7 (83.67 – 85.43)	85.38 ±4.2 (84.52 – 86.24)	0.950	0.38
Vertical distance between the crossing points of the right and left EAMs on the midsagittal line	0.18 ±0.2 (0.19 – 0.35)	3.10 ±2.8 (2.58 – 3.62)	3.14 ±2.2 (2.69 – 3.58)	6.648	0.002

*: One Way ANOVA

Table 2. Comparing the angles between the EAM lines and the midsagittal line, the EAM lines and the occlusal plane, and the angle between the midsagittal line and the occlusal plane in different positions of vertical symmetry of the EAM.

Positions of vertical symmetry of EAMs	**symmetric**	**Right EAM at the higher position**	**Left EAM at the higher position**	**F**	**P Value***
Angle	**Mean ±Std. Deviation (95% Confidence Interval)**	**Mean ±Std. Deviation (95% Confidence Interval)**	**Mean ±Std. Deviation (95% Confidence Interval)**		
Angle of the line between EAMs and midsagittal line	89.94 ±0.8 (89.88 – 89.99)	91.08 ±0.9 (90.90 – 91.25)	88.92 ±0.8 (88.76 – 89.09)	156.06	<0.001
Angle of the line between EAMs and occlusal plane	1.94 ±1.2 (1.04 – 2.83)	1.34 ±0.9 (1.16 – 1.52)	1.24 ±0.9 (1.05 – 1.44)	2.246	0.108
Angle between the midsagittal line and occlusal plane	90.13 ±1.5 (89.06 – 91.20)	89.86 ±1.5 (89.57 – 90.16)	90.02 ±1.8 (89.64 – 90.41)	2.280	0.756

*: One Way ANOVA

approximate condylar axis or the pupillary line for face-bow recording. To the best of our knowledge, no similar research has been performed in this area; therefore, a comparison is not possible.

In the present study, the frequency distribution of the vertical symmetry of EAM was similar between men and women. The mean distance between the right and left EAMs and the midsagittal line was significantly longer in males than females, which could be attributed to the larger skeletal size of men than women. However, no significant difference was found in other linear and angular parameters in the two groups.

In a study by Djordjevic et al. (2014) on healthy Serbian adolescents, the total facial symmetry was lower in men than women (53.49% vs. 58.50%), although the difference was not clinically significant. In the present study, no significant difference was observed between male and female participants in terms of the vertical asymmetry of EAMs. In this regard, Sforza et al. compared the normal dimensions of the ears, the symmetry of the ears, and developmental changes from childhood to older age between male and female participants. Considering the significant sex-age interaction, the age pattern was different between men and women (Sforza et al., 2009). In the present study, no significant relationship was found with age, sex, or other variables. Given the high percentage of asymmetry in EAMs, design of a position modifier for the ear rods of the face-bow is recommended to compensate for this asymmetry.

CONCLUSION

According to the present results, the linear value of the mean vertical distance between the crossing points of the right and left ear EAMs on the midsagittal plane, as well as the angle between the EAM lines on the midsagittal plane, differed, depending on the vertical symmetry of the EAMs. However, no significant difference was found in the angle between the EAM lines and the occlusal plane in terms of symmetry. Also, changes in the linear and angular parameters were independent of age and sex.

REFERENCES

CHATURVEDI S, THOMBARE R (2013) Cephalometrically assessing the validity of superior, middle and inferior tragus points on ala-tragus line while establishing the occlusal plane in edentulous patient. *J Adv Prosthodont*, 5: 58-66.

CHOI JW, JUNG SY, KIM HJ, LEE SH (2015) Positional symmetry of porion and external auditory meatus in facial asymmetry. *Maxillofac Plast Reconstr Surg*, 37: 33-37.

DJORDJEVIC J, TOMA AM, ZHUROV AI, RICHMOND S (2014) Three-dimensional quantification of facial symmetry in adolescents using laser surface scanning. *Eur J Orthod*, 36: 125-132.

GANDHI N, DANIEL S, KURIAN N (2017) Cephalometric study of the position of ala-tragus line in relation to Frankfort horizontal plane and occlusal plane among Ludhiana population. *Indian J Dental Sci*, 9: 165-169.

GATENO J, XIA J, TEICHGRAEBER JF, ROSEN A (2003) A new technique for the creation of a computerized composite skull model. *J Oral Maxillofac Surg*, 61: 222-227.

HOODA SH, D'SOUZA M (2012) Evaluation of facial asymmetry using digital photographs with computer aided analysis. *J Indian Prosthodont Soc*, 12: 8-15.

KIM BC, LEE CE, PARK W, KANG SH, ZHENGGUO P, YI CK, LEE SH (2010) Integration accuracy of digital dental models and 3-dimensional computerized tomography images by sequential point- and surface-based markerless registration. *Oral Surg Oral Med Oral Pathol Oral Radiol Endod*, 110: 370-378.

KIM MG, LEE JW, CHA KS, CHUNG DH, LEE SM (2014) Three-dimensional symmetry and parallelism of the skeletal and soft-tissue poria in patients with facial asymmetry. *Korean J Orthodont,* 44: 62-68.

MIZGIRYTE S, VAITELIS J, BARKUS A, ZALECKAS L, PLETKUS R, AUSKALNIS A (2014) Symmetry of external auditive meatus. A pilot study on human skulls. *Stomatologija,* 16: 102-108.

NAINI FB (2013) The Frankfort plane and head positioning in facial aesthetic analysis-the perpetuation of a myth. *JAMA Facial Plast Surg*, 15: 333-334.

PORTER JP, OLSON KL (2001) Anthropometric facial analysis of the African American woman. *Arch Facial Plast Surg*, 3: 191-197.

ROSATI R, ROSSETTI A, DE MENEZES M, FERRARIO VF, SFORZA C (2012) The occlusal plane in the facial context: inter-operator repeatability of a new three-dimensional method. *Int J Oral Sci*, 4: 34-37.

SFORZA C, GRANDI G, BINELLI M, TOMMASI DG, ROSATI R, FERRARIO VF (2009) Age-and sex-related changes in the normal human ear. *Forensic Sci Int*, 187: 1-7.

SHAH SZ, AZAD AA, HASSAN SH, ASLAM A (2016) Association of occlusal plane with the level of retromolar pad. *Pakistan Oral Dental J*, 36: 484-486.

SHERRY SA, JAIN AR (2017) Reliability of various craniofacial reference planes with occlusal plane in Dravidian population. *J Pharm Res*, 11: 1503-1505.

TSUTSUMI S, ONO H, ISHII H (2020) Positional relationship between the external acoustic meatus and sigmoid sinus: an MRI study. *Surg Radiol Anat*, 42: 791-795.

WEI R, CLAES P, WALTERS M, WHOLLEY C, CLEMENT JG (2011) Augmentation of linear facial anthropometrics through modern morphometrics: a facial convexity example. *Aust Dent J,* 56: 141-147.

Investigation of the morphometry and variations of the biceps brachii muscle ın fetal cadavers

Semra Akgün, Kenan Öztürk, Ahmet Dursun, Yadigar Kastamoni

Department of Anatomy, Faculty of Medicine, Suleyman Demirel University, 32260, Isparta, Turkey

SUMMARY

This study aimed to examine the morphometry of the biceps brachii muscle in fetal cadavers, to reveal the difference between genders and sides, and to determine the variations. Our study was conducted on 47 upper extremities of 25 human fetuses (13 females, 12 males) who were aged between 29-40 weeks of gestation and had no external pathology and anomaly. The development of the determined parameters according to gestational age (month) was evaluated. Comparisons were made between genders and sides. In our study, no statistically significant difference was found in the footprint length of the biceps brachii muscle according to gestational age. Other parameters increased statistically significantly according to gestational age. No difference was found between genders in morphometric parameters. There was no statistically significant difference between the right and left extremities in other parameters, except for motor entry point. Motor entry point was found to be statistically significantly more distal in the left extremities compared to the right extremities (p=0.012). Furthermore, all parameters were positively correlated with gestational age. We considered that they would contribute to the correct diagnosis and treatment of pathologies related to this region especially in the intrauterine period, premature birth and in the newborn, as well as to the reduction of complications that may occur after treatment.

Key words: Distal tendon – Footprint – Lacertus fibrosus – Accessory head

INTRODUCTION

The biceps brachii muscle (BBM) is a thick, fusiform muscle that is located in the anterior part of the arm and passes both in front of the shoulder and elbow joints. The BBM consists of a long head originating from the supraglenoid tubercle proximally and a short head originating from the coracoid process. The long head of the BBM provides stabilization of the shoulder joint in dynamic movements such as throwing. Furthermore, the BBM reduces stress on the lower glenohumeral ligament (Szpinda et al., 2013).

While a large part of the distal tendon of the BBM adheres to the ulnar/posterior side of the radial tuberosity, a part of it is mixed with the lacertus fibrosus (LF). The LF is the thickening

Corresponding author:
Kenan Öztürk, PhD. Department of Anatomy, Faculty of Medicine, Suleyman Demirel University, 32260, Isparta,Turkey. Phone: +90 246 211 33 01; Fax: +90 246 237 11 65. E-mail: kenanozt@hotmail.com / Orcid ID: 0000-0002-5552-8684

Submitted: October 1, 2020. **Accepted:** December 18, 2020
Not final proof's revision by the authors

of the brachial fascia that covers the proximal part of the flexor-pronator muscle groups of the forearm and joins the BBM to the ulna. In distal tendon ruptures of the BBM, the LF can also prevent the retraction of the BBM toward the proximal if it is intact (Szpinda et al., 2013; Brigido et al., 2013).

The BBM is one of the most variable muscles in the body due to its variation and morphology. The variations related to the absence of the short or long head of the BBM and insertion are rare. The absence of the long head may reduce the flexion and supination strength of the forearm. Furthermore, since the tendon of the long head is used as a landmark in shoulder arthroscopy, the absence of this head may lead to difficulties during arthroscopy (Rodríguez-Niedenführ et al., 2003). Although the most frequently reported variation is the three-headed BBM, there are cases with up to seven heads reported in the literature (Rodríguez-Niedenführ et al., 2003; Nasr and Hussein, 2013). These variations are clinically important because accessory heads may mislead surgeons during shoulder operations or may lead to the compression of neurovascular structures (Rodríguez-Niedenführ et al., 2003). The third head of the BBM generally originates from the humerus between the attachments of the coracobrachialis and the brachialis muscles. Nevertheless, the third head can start from the coracoid process, the tendon or fascia of adjacent muscles, the intermuscular septum, shoulder joint capsule, head of humerus, neck of humerus, and anteromedial aspect of the humerus (Yildiz et al., 2006; Nayak et al., 2008; Angadi et al., 2016; Saluja et al., 2017).

Due to a large number and clinical significance of variations, studies on the BBM conducted in adult cadavers are quite common (Park et al., 2007; Athwal et al., 2007). However, information on the morphometry of the BBM in fetal cadavers is limited (Szpinda et al., 2013). We aimed to determine the morphometric development of the BBM in the fetal period, its variations and differences between genders and sides to assist surgical interventions on newborn and premature babies to be performed in this region in pathologies such as humerus fracture, neurovascular lesions, and tumors.

MATERIALS AND METHODS

Our study was conducted on 47 upper extremities of 25 human fetuses (13 females, 12 males) who were aged between 29-40 weeks of gestation and had no external pathology and anomaly, in the Faculty of Medicine, Anatomy Department Laboratory, which were obtained from the Maternity and Children's Hospital between 1996-2014 by getting permissions from their families. Three extremities that were damaged during dissection and not suitable for the measurement were excluded from the study. Prior to the study, approval was obtained from the Faculty of Medicine Ethics Committee (Date: 03.05.2019, Decision No:83). The causes of death in fetal cadavers are unknown. All fetal cadavers were fixed by the arterial injection of 10% (v/v) formaldehyde solution into the water and stored in a pool of 10 L of 10% (v/v) formaldehyde solution. It is a known fact that formaldehyde has a shrinkage effect on tissues. In a study on human muscles, this effect was reported to be 2.22% on average (Cutts, 1988). The 2.22% effect should be considered in the evaluation of the data in the publication.

The gestational age of the fetuses was determined according to the Crown Rump Length (CRL), Bi-Parietal Diameter (BPD), Head Circumference (HC), and Femur Length (FU). The fetuses were evaluated by being divided into three groups. as the 8^{th} month fetuses between the weeks 29-32, 9^{th} month fetuses between the weeks 33-36, and 10^{th} month fetuses (full term) between the weeks 37-40.

The anatomical dissection method was used in all fetal cadavers to determine the parameters of the BBM. First, an incision was made from the outer end of the clavicle, ending at the lower edge of the anterior wall of the axilla. Second, an incision was made from the midpoint of first incision and ending at the interepicondylar line. The skin and subcutaneous adipose tissue were removed. The deltoid and pectoralis major muscles were released as needed by entering through the deltopectoral range in order to see the origo of the long and short heads. The skin and subcutaneous adipose tissue of the proximal forearm were removed by making another incision from the interepicondylar line

to the distal of the cubital fossa to determine the insertion of the BBM. The LF was identified and photographed with a millimeter ruler. Afterward, the LF was incised, and deep structures were uncovered. Under the "EUROMEX Edublue 1805-S binocular digital stereo microscope" (EUROMEX microscopen BV, Arnhem, Holland), the insertion of the BBM was evaluated at 10X magnification. The morphometric measurements were performed using a digital caliper with a precision of 0.01 mm. The area of the photographed LF was measured using the Image J analytical software (National Institutes of Health, Bethesda, MD) program.

For each extremity, the following parameters were examined:

- *Arm length*: distance between the acromion and olecranon while the arm in extension.
- *Long head length*: distance between the origin and common muscle belly. The joint capsule was opened and the supraglenoid tubercle was found. Long head length was measured from the beginning of the long head to the common muscle belly with an inflexible rope. Then the length of this rope was determined with a digital caliper.
- *Long head width*: the widest level of the long head.
- *Short head length*: distance between the origin and common muscle belly.
- *Short head width*: the widest level of the short head.
- *Common muscle belly length*: distance between the start of the common muscle belly and musculotendinous junction.
- *Common muscle belly width*: the widest level of the common muscle belly.
- *Motor entry point (MEP)*: distance between the acromion and point where the motor nerve enters the muscle.
- *Footprint length*: the length of the attachment of the distal tendon to the radial tuberosity.
- *Area of the lacertus fibrosus*: firstly, lacertus fibrosus was identified. Then, its perimeter was drawn with the Image J program and its area was measured.
- *Number of distal tendons* and the localization of these tendons according to the radial tuberosity.

Statistical analysis was performed using SPSS Inc. SPSS for Windows 20.0 statistical package program. Since the MEP data were not normally distributed, the Kruskal-Wallis test and Mann-Whitney U test, which are among the non-parametric tests, were used to analyze the data, and Spearman's Correlation test was used in the correlation analysis. Since other data were normally distributed, the Independent Samples T-Test and One-Way ANOVA test, which are among the parametric tests, were used to analyze the data, and Pearson's Correlation test was used in the correlation analysis. The significance level was considered to be $p<0.05$ in statistical analysis.

RESULTS

In our study, no statistically significant difference was found in the footprint length of the BBM according to gestational age (month). Other parameters increased according to gestational age, which was statistically significant. There was no statistically significant difference between the right and left extremities in other parameters, except for MEP. The MEPs were found to be statistically significantly more distal in the left extremities compared to the right extremities ($p=0.012$) (Table 1).

The averages and standard deviations of the ratios of parameters related to the BBM to arm length according to sides, gender, and gestational age are presented in Table 2. When Table 2 was analyzed, statistically significant differences ($p=0.009$ and $p=0.012$, respectively) were observed in the common muscle belly width/arm length and motor entry point/arm length ratios according to gestational age. While it was found that the difference between months in the common muscle belly width/arm length ratio resulted from the 8^{th}-10^{th} months, the difference in the motor entry point/arm length ratio resulted from the 8^{th}-9^{th} and 8^{th}-10^{th} months. The ratio of MEPs to the arm length measured between the acromion and olecranon was found to be 0.37 ± 0.04 on average in all specimens, and these points were

determined to be in the middle third of the arm. In the right-left sides comparison of the motor entry point/arm length ratio, it was observed to be statistically significantly higher in the left extremities compared to the right extremities (p=0.023). In the gender comparison of the long head width/arm length ratio, it was found to be higher in female fetal cadavers compared to male fetal cadavers (p=0.039).

All parameters were positively correlated with gestational age (week) (Table 3). The parameters with the best positive correlation according to gestational age (week) were the short head (r=0.772) and long head (r=0.762) lengths, respectively (Fig. 1). When the correlation of the parameters with respect to each other was examined, the long head and short head lengths showed the strongest correlation (r=0.908) (Table 3).

Table 1. The averages and standard deviations of the parameters related to the biceps brachii muscle according to side, gender, and gestational age (month).

Parameters		Side			Gender			Gestational Age (Month)			
		Right (n=24)	Left (n=23)	P	Female (n=25)	Male (n=22)	P	8 (n=16)	9 (n=17)	10 (n=14)	P
Long head	Length (mm)	25.24±3.17	25.46±2.88	0.758	24.77±3.17	26±2.72	0.156	22.95±1.72	25.21±2.22	28.26±2.5	**<0.001**
	Width (mm)	2.93±0.56	2.68±0.64	0.101	2.91±0.66	2.7±0.52	0.169	2.48±0.48	2.89±0.65	3.08±0.54	**0,022**
Short head	Length (mm)	23.22±2.9	22.8±2.56	0.670	22.88±3.09	23.17±2.29	0.624	20.91±1.34	22.69±1.7	25.81±2.56	**<0,001**
	Width (mm)	5.14±1.2	5.03±1.3	0.758	5.17±1.53	4.98±0.83	0.565	4.16±0.84	5.42±1.31	5.73±0.96	**0,001**
Common muscle belly	Length (mm)	35.38±4.3	36.73±3.96	0.273	35.34±4.43	36.84±3.74	0.176	33.96±3.31	34.79±3.22	39.93±3.43	**<0,001**
	Width (mm)	9.02±1.86	8.85±2.01	0.890	9.05±2.02	8.81±1.83	0.733	7.24±1.35	8.94±1.11	10.87±1.36	**<0,001**
Motor entry point (mm)		26.29±2.77	29.22±4.96	**0.012**	27.45±4.72	28.44±3.64	0.268	27.31±3.24	25.74±1.86	30.61±5.68	**0.017**
Footprint length (mm)		2.91±0.68	2.78±0.51	0.482	2.77±0.66	2.94±0.52	0.332	2.68±0.65	2.83±0.53	3.07±0.59	0.237
Area of the lacertus fibrosus (mm^2)		34.56±8.32	36.33±9.09	0.474	34.7±7.63	36.69±10.31	0.508	28.93±9.24	36.8±2.71	40.74±7.67	**0.014**

Table 2. The averages and standard deviations of the ratios of parameters related to the biceps brachii muscle to arm length according to side, gender, and gestational age (month).

Parameters		Side			Gender			Gestational Age (Month)			
		Right (n=24)	Left (n=23)	P	Female (n=25)	Male (n=22)	P	8 (n=16)	9 (n=17)	10 (n=14)	P
Long head	Length (mm)	0.34±0.03	0.34±0.02	0.655	0.33±0.02	0.34±0.02	0.337	0.33±0.02	0.35±0.02	0.33±0.02	0,094
	Width (mm)	0.03±0.008	0.03±0.007	0.085	0.039±0.007	0.036±0.008	**0.039**	0.03±0.008	0.04±0.008	0.03±0.006	0.373
Short head	Length (mm)	0.31±0.03	0.30±0.02	0.148	0.31±0.02	0.30±0.02	0.848	0.30±0.028	0.31±0.023	0.30±0.026	0.255
	Width (mm)	0.06±0.01	0.06±0.01	0.419	0.07±0.02	0.06±0.01	0.848	0.06±0.012	0.07±0.022	0.06±0.012	0.137
Common muscle belly	Length (mm)	0.48±0.04	0.49±0.03	0.469	0.48±0.03	0.48±0.03	0.831	0.49±0.041	0.48±0.042	0.47±0.026	0.446
	Width (mm)	0.12±0.01	0.11±0.02	0.655	0.12±0.02	0.11±0.02	0.418	0.10±0.024	0.12±0.019	0.13±0.014	**0.009**
Motor entry point/ arm length		0.35±0.035	0.39±0.048	**0.023**	0.37±0.05	0.37±0.03	0.915	0.39±0.034	0.35±0.029	0.36±0.061	**0.012**

The distal tendon was evaluated in 46 of 47 upper extremities in our study. In a specimen, the distal tendon could not be evaluated because it was damaged in dissection. In all specimens, it was observed that the distal tendon adhered to the ulnar/posterior side of the radial tuberosity. While two tendons were observed in 60.8% (n=28) of the specimens, three tendons and four tendons were observed in 34.7% (n=16) and 4.34% (n=2) of the specimens, respectively (Fig. 2). In our study, we found the accessory head variation of the BBM in 2 (4.2%) of 47 upper extremities. It was observed that the accessory head, which was located bilaterally in the same fetus, was located medial to the short head and anterolateral to the coracobrachialis muscle, and originated from the coracoid process with the short head (Fig. 3).

DISCUSSION

Warmbrunn et al. (2018) reported that all muscles developed similarly to adult morphology by the 8th week of the embryonic period. The age of the fetuses used in our study starts from the 29th week of gestation. Therefore, the BBM of the fetuses in our study completed its morphological development.

The BBM is an important muscle of the anterior part of the arm. Studies on the BBM are usually related to lesions, the repair of lesions, and variations of the BBM (Nasr and Hussein, 2013; Walton et al., 2015). Studies examining the morphometry of the BBM from proximal to distal in fetal cadavers are limited (Szpinda et al., 2013).

Table 3. Correlation table between parameters related to the biceps brachii muscle and gestational age in the fetal period (r).

	Arm length	Motor entry point*	Long head length	Long head width	Short head length	Short head width	Footprint length	Area of the lacertus fibrosus	Gestational Age (Month)
Arm length	1								
Motor entry point*	.580	1							
Long head length	.760	.431	1						
Long head width	.289	.101	.479	1					
Short head length	.711	.319	.908	.508	1				
Short head width	.464	.135	.568	.375	.615	1			
Footprint length	.406	.239	.192	-.080	.100	.144	1		
Area of the lacertus fibrosus	.460	.211	.474	.311	.499	.470	.079	1	
Gestational Age (Month)	.754	.301	.762	.442	.772	.707	.233	.638	1

* Spearman correlation test was used
r= correlation coefficient; Pearson correlation test result r= 1,00-0,76 very good correlation
r= 0,75-0,51 good correlation r= 0,50-0,26 average correlation r= 0,25-0,00 poor correlation

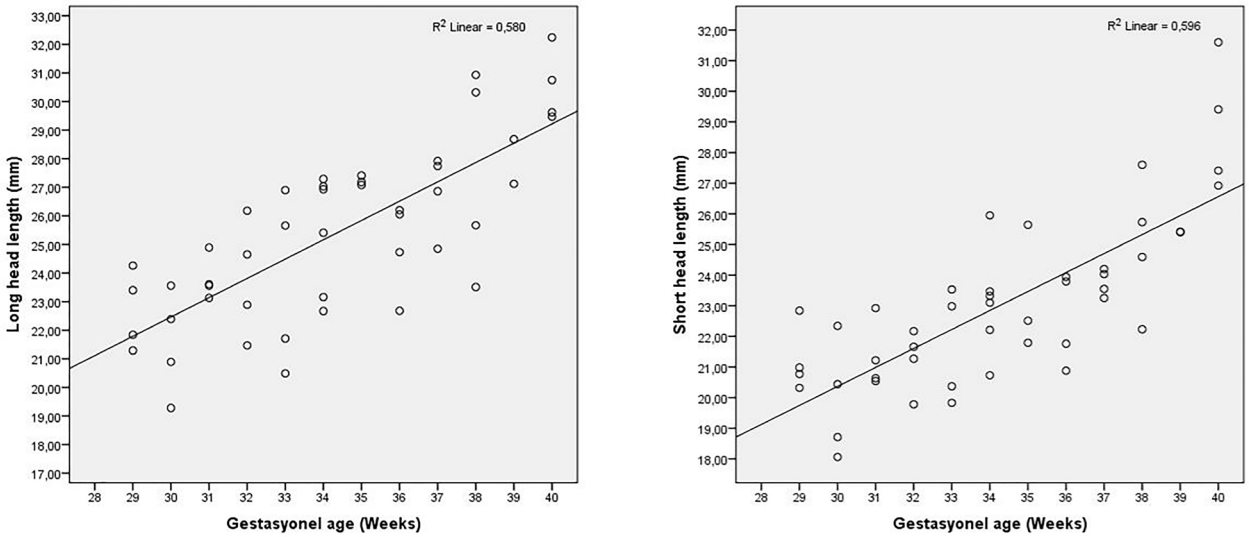

Fig. 1.- Correlation of long head and short head according to gestational age (week).

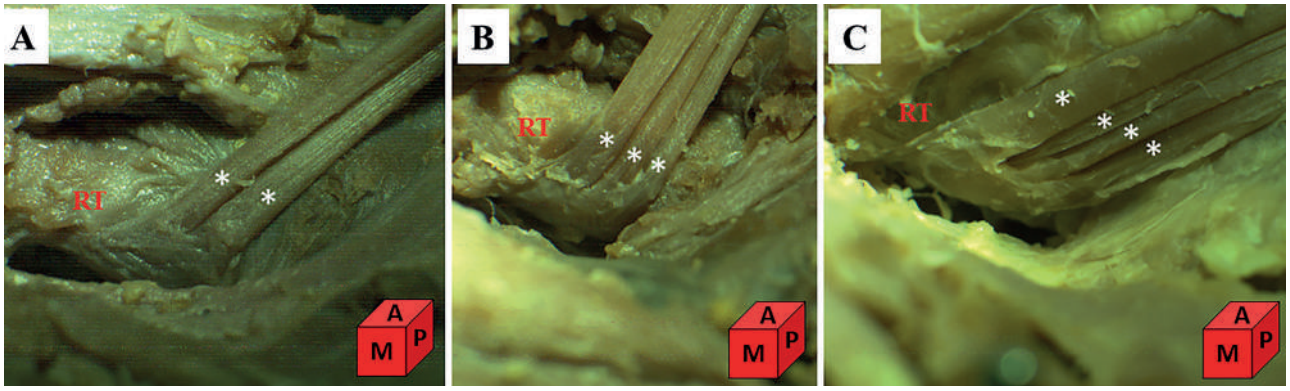

Fig. 2.- Tendon insertions of biceps brachii muscle **A.** Insertions of two tendons, **B.** Insertions of three tendons, **C.** Insertions of four tendons. **RT:** Radial tuberosity, **A:** Anterior, **M:** Medial, **P:** Proximal.

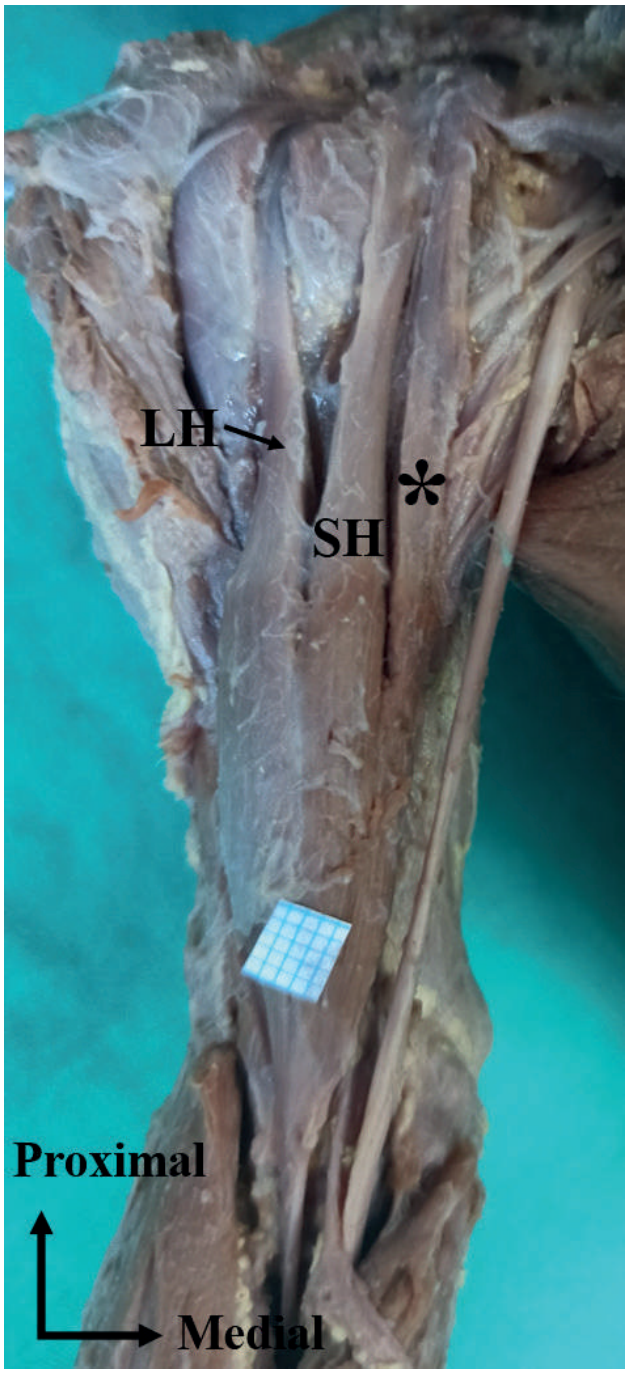

Fig. 3.- Three-head biceps brachii muscle, **LH:** Long head, **SH:** Short head, ***:** Accessory head.

In their study on the normal development of the BBM conducted in 17-30 weeks old fetal cadavers, Szpinda et al., (2013) reported that the dynamic development of the BBM was linear. They indicated that there was no significant difference between the right and left sides and genders in the parameters examined. They reported that there was a statistically significant correlation between each parameter studied and gestational age and that all parameters increased with gestational age. Likewise, in our study, it was found that the parameters were positively correlated with gestational age.

The variations observed in the origo of the BBM are quite common. The variations of its insertion are rarer (Nasr and Hussein, 2013). The third head of the BBM generally originates from the humerus between the attachments of the coracobrachialis and the brachialis muscles (Vázquez et al., 2003; Yildiz et al., 2006; Kervancioglu and Orhan, 2011; Angadi et al., 2016). Embryologically, the third head of the BBM is considered as a piece separated from the brachialis muscle and migrated to the insertion with the musculocutaneus nerve. The presence of an accessory head with or without neural variations may be caused by a change in the signal between a group of mesenchymal cells and the neuronal growth factors of the forearm muscles developing from the paraxial mesoderm or the presence of circulatory factors during the formation of the brachial plexus (Nasr and Hussein, 2013; Angadi et al., 2016).

In our study, an accessory head variation was found bilaterally in 1 (4%) of 25 fetal cadavers (Fig. 3). It was observed that the accessory

head was located medial to the short head and anterolateral to the corocobrachialis muscle, and started from the coracoid process with the short head. The incidence of the accessory head was reported between 3.3-37.5%, although it varied by races (Schwerdtfeger et al., 2018). The prevalence of the accessory head was shown to be 8% in Chinese, 10% in white Europeans, 12% in black Africans, 15% in Turkish, 18% in Japanese, and 37.5% in Colombians (Yıldız et al., 2006; Nasr and Hussein, 2013; Angadi et al., 2016; Saluja et al., 2017; Schwerdtfeger et al., 2018). The incidence of bilateral symmetrical accessory heads was reported less often (Nakatani et al., 1998; Saluja et al., 2017). In the majority of cases, accessory heads are asymptomatic and detected randomly during surgery or imaging. However, in some cases, these accessory heads may lead to clinical symptoms (Kervancioglu and Orhan, 2011). For instance, the accessory heads of the BBM may lead to high median nerve entrapment symptoms, thrombosis, and edema by compressing neurovascular structures. Functionally, they change the flexion and supination strength of the forearm. Furthermore, unilateral variations can be mistakenly interpreted as soft tissue tumors during magnetic resonance imaging (Kervancioglu and Orhan, 2011; Saluja et al., 2017).

The BBM and its accessory head are known to be usually innervated by the musculocutaneus nerve (Park et al., 2007; Schwerdtfeger et al., 2018). In our study, it was determined that all BBM and accessory heads were also innervated by the musculocutaneus nerve. Park et al. (2007) determined a reference line between the lateral epicondyle of the humerus and the coracoid process in order to identify the motor point of the musculocutaneus nerve innervating the BBM in adult cadavers. They identified that the MEP of the BBM was about half of this reference line. In their study conducted with fetuses with gestational ages ranging from 16 to 36 weeks, Kervancioğlu et al. (2011) measured the distance between the motor branches of musculocutaneus nerve and the acromion. For the BBM, they indicated that the average distance between the MEP of all motor branches and the acromion was 3.8±6.1% of the acromion-lateral epicondyle length. In our study, the average length of the BBM's MEPs to the acromion was found to be 27.73±4.22 mm. The MEPs were found to be proximal 37±4% of the arm length.

The LF is the thickening of the brachial fascia that connects the BBM to the ulna and covers the proximal part of the flexor-pronator muscle group. The LF is very important clinically. The LF located in the fossa cubitalis protects the neurovascular structures under it. Depending on the muscle activity in the forearm, it provides proprioceptive information for the BBM. It also has additional anatomical support for the BBM tendon (Caetano et al., 2017). In repairing the LF rupture, suturing the LF should be performed in pronation and extension, which could also minimize the risk of impingement of the underlying neurovascular structures (Eames et al., 2007). Besides, the LF can be used as a local graft source for chronic distal biceps tendon ruptures (Hamer and Caputo, 2008). So, it is very important to know the area of LF. In the literature review we performed to make a comparison, while it was observed that there were studies on the LF conducted in adult cadavers (Athwal et al., 2007; Caetano et al., 2017), we did not find any study on the LF in fetuses. Therefore, in our study, the area of the LF was examined and found to be 35.45±8.62 mm^2 on average. No statistically significant difference was found in the area of the LF by gender and sides.

The BBM main tendon takes an oval shape as it goes distally and turns from the frontal plane to the sagittal plane on itself and adheres to the radial tuberosity. Although it was classically defined in this way, in recent studies, it has been observed that the distal biceps tendon consists of two separate tendons, one belonging to the short head and one belonging to the long head, in most of the people (Eames et al., 2007). Nowadays, avulsion rupture of the distal biceps tendon is reported more frequently than before, and surgical methods are used for the repair of these ruptures (Safran and Graham, 2002; Hutchinson et al., 2008; Walton et al., 2015). If the biceps tendon is not fully positioned in its anatomical position and is positioned only in the center of the radial tuberosity during surgery, supination strength can

never reach its pre-injury strength (Hutchinson et al., 2008). Knowledge of the number and location of the distal tendons can assist surgeons during surgical repair of distal biceps tendon ruptures. Nevertheless, in the literature, there are few definitions of the morphometry or variations of the distal biceps tendon. However, information about the distal biceps tendon is important in deciding the most appropriate method to be applied during the surgical procedure, such as in which case a graft supplement should be used to complement the natural tendon and what the most suitable graft should be (Walton et al., 2015). Therefore, we consider that our study will provide significant data in this regard.

In their study on 15 upper extremities of adult cadavers, Athwal et al. (2007) demonstrated that the long head and short head continued completely separately without joining in the common muscle belly in two of the specimens and that distal tendons ended separately. They added that the long head ended proximally in the radial tuberosity and the short head ended distally. In eight of the specimens, they indicated that the muscle belly, the distal tendons corresponding to the long head and short head could be easily separated, and that the long head ended proximally in the radial tuberosity and the short head ended distally. In five of the specimens, they demonstrated that the long head and short head formed a common muscle belly by combining distally, and that the corresponding distal tendons were also combined. In these specimens, it was indicated that the muscle bellies could be separated by minimal dissection; however, the detection of the distal tendon footprint was difficult. Furthermore, the researchers reported that the distal biceps tendon was attached along the ulnar/posterior side of the radial tuberosity in all specimens. Likewise, in our study, the distal tendon of the BBM was attached to the ulnar/posterior side of the radial tuberosity in all specimens. While two tendons were observed in 60.8% (n=28) of the extremities, three tendons and four tendons were observed in 34.7% (n=16) and 4.34% (n=2) of the extremities, respectively. In our study, although the distal tendons of the BBM could be observed separately from each other, it was not possible to determine to which head these tendons originating from the common muscle belly belonged.

The BBM insertion is on the ulnar/posterior side of the radial tuberosity and creates a footprint on the bone (Athwal et al., 2007; Hutchinson et al., 2008). The localization of the footprint is important for the strength of supination. Several authors have reported a significant loss of supination range and strength after the distal biceps tendon repair with an anteriorly located footprint on the radial tuberosity, and have noted that a posteriorly located footprint repair is important for the restoration of supination torque (Van den Bekerom et al., 2016). Therefore, having knowledge about the dimensions and localization of footprints is important for minimizing complications during and after the surgical repair of the distal biceps tendon ruptures. The reported sizes of the distal biceps tendon insertional footprint on the radial tuberosity vary and exhibit gender differences. However, it was reported that there was no difference between the dimensions of the right and left footprints (Athwal et al., 2007; Van den Bekerom et al., 2016). In our study, the footprint length was found to be 2.85±0.6 mm on average. No statistically significant difference was determined in the footprint length between the right and left sides and genders.

The pathology of the distal biceps brachii tendon is less common than the pathology of the proximal biceps brachii tendon in the shoulder. Nowadays, the incidence of the distal biceps brachii tendon rupture is increasing due to the widespread use of ultrasound and magnetic resonance imaging for diagnosis (Brigido et al., 2013). Therefore, along with the developing technology, it has become more important to know the anatomy of the distal biceps brachii tendon (distal tendon, radial tuberosity, footprint and lacertus fibrosus) in order to understand the pathomechanism, optimize the treatment outcome, and prevent complications while repairing the distal biceps tendon.

Having a good knowledge of the anatomy of the BBM provides a better understanding of the lesions involving the shoulder and elbow and facilitates the planning of their treatment. The

data obtained in our study are considered to contribute to the studies in the fields of anatomy, obstetrics, orthopedy, surgery, radiology, and pediatrics in the determination of anomalies, pathologies, and variations related to the BBM in the fetal period.

AKNOWLEDGEMENTS

We thank Prof. Soner Albay for his contributions.

REFERENCES

ANGADI MB, TANDON A, PANDIT S, BHATNAGAR R (2016) Supernumerary head of biceps brachii and branching pattern of the musculocutaneous nerve. *Med J DY Patil Univ*, 9: 264-266.

ATHWAL GS, STEINMANN SP, RISPOLI DM (2007) The distal biceps tendon: footprint and relevant clinical anatomy. *J Hand Surg Am*, 32: 1225-1229.

BRIGIDO MK, DE MAESENEER M, MORAG Y (2013) Distal biceps brachii. Semin *Musculoskelet Radiol*, 17: 20-27.

CAETANO EB, VIEIRA LA, ALMEIDA TA, GONZALES LAM, BONA JE, SIMONATTO TM (2017) Bicipital aponeurosis. Anatomical study and clinical implications. *Rev Bras Ortop*, 53: 75-81.

CUTTS A (1988) Shrinkage of muscle fibres during the fixation of cadaveric tissue. *J Anat*, 160: 75-78.

EAMES MH, BAIN GI, FOGG QA, VAN RIET RP (2007) Distal biceps tendon anatomy: a cadaveric study. *J Bone Joint Surg Am*, 89: 1044-1049.

HAMER MJ, CAPUTO AE (2008) Operative treatment of chronic distal biceps tendon ruptures. *Sports Med Arthrosc Rev*, 16: 143-147.

HUTCHINSON HL, GLOYSTEIN D, GILLESPIE M (2008) Distal biceps tendon insertion: an anatomic study. *J Shoulder Elbow Surg*, 17: 342-346.

KERVANCIOGLU P, ORHAN M (2011) An anatomical study on the three-headed biceps brachii in human foetuses, and clinical relevance. *Folia Morphol (Warsz)*, 70: 116-120.

KERVANCIOGLU P, ORHAN M, KILINC N (2011) Patterns of motor branching of the musculocutaneous nerve in human fetuses and clinical significance. *Clin Anat*, 24: 168- 178.

NAKATANI T, TANAKA S, MIZUKAMI S (1998) Bilateral four-headed biceps brachii muscles: the median nerve and brachial artery passing through a tunnel formed by a muscle slip from the accessory head. *Clin Anat*, 11: 209-212.

NASR AY, HUSSEIN AM (2013) Morphology and clinical implication of the extra- head of biceps brachii muscle. *Folia Morphol (Warsz)*, 72: 349-356.

NAYAK SR, KRISHNAMURTHY A, KUMAR M, PRABHU LV, SARALAYA V, THOMAS MM (2008) Four-headed biceps and triceps brachii muscles, with neurovascular variation. *Anat Sci Int*, 83: 107-111.

PARK BK, SHIN YB, KO HY, PARK JH, BAEK SY (2007) Anatomic motor point localization of the biceps brachii and brachialis muscles. *J Korean Med Sci*, 22: 459-462.

RODRÍGUEZ-NIEDENFUHR M, VÁZQUEZ T, CHOI D, PARKIN I, SAÑUDO JR (2003) Supernumerary humeral heads of the biceps brachii muscle revisited. *Clin Anat*, 16: 197-203.

SAFRAN MR, GRAHAM SM (2002) Distal biceps tendon ruptures: incidence, demographics, and the effect of smoking. *Clin Orthop Relat Res*, 404: 275-283.

SALUJA S, DAS SS, KUMAR D, GOSWAMI P (2017) Bilateral three-headed biceps brachii muscle and its clinical implications. *Int J Appl Basic Med Res*, 7: 266-268.

SCHWERDTFEGER LA, PASCOE MA, CLAPP T (2018) High incidence of a third head of biceps brachii in females. *Transl Res Anat*, 12: 25-27.

SZPİNDA M, PARUSZEWSKA-ACHTEL M, DĄBROWSKA M, BADURA M, ELMINOWSKA-WENDA G, SOBOLEWSKA A, SZPINDA A (2013) The normal growth of the biceps brachii muscle in human fetuses. *Adv Clin Exp Med*, 22: 17-26.

VAN DEN BEKEROM MP, KODDE IF, ASTER A, BLEYS RL, EYGENDAAL D (2016) Clinical relevance of distal biceps insertional and footprint anatomy. *Knee Surg Sports Traumatol Arthrosc*, 24: 2300-2307.

VÁZQUEZ T, RODRÍGUEZ-NIEDENFUHR M, PARKIN I, SAÑUDO JR (2003) A rare case of a four-headed biceps brachii muscle with a double piercing by the musculocutaneous nerve. *Surg Radiol Anat*, 25: 462-464.

WALTON C, LI Z, PENNINGS A, AGUR A, ELMARAGHY A (2015) A 3-dimensional anatomic study of the distal biceps tendon: implications for surgical repair and reconstruction. *Orthop J Sports Med*, 3(6): 2325967115585113.

WARMBRUNN MV, DE BAKKER BS, HAGOORT J, ALEFS-DE BAKKER PB, OOSTRA RJ (2018) Hitherto unknown detailed muscle anatomy in an 8-week-old embryo. *J Anat*, 233: 243-254.

YILDIZ E, ALBAY S, YAZAR F, KIRICI Y, OZAN H (2006) M. Biceps brachii'nin aksesuar humeral başı: Olgu sunumu. *S.D.Ü. Tıp Fak Derg*, 13: 31-33.

Evidence of ZIO positive Langerhans cell: a dendritic cell subset in normal and polypoid nasal mucosa

J. Rachel[1], John K. Kulathu Mathew[1], Sam Marconi D[3], Zorem Sangi[2], Vedantam Rupa[2], Suganthy Rabi[1]

[1] Department of Anatomy, Christian Medical college, Vellore-632002, India

[2] Department of Otorhinolaryngology, Christian Medical college, Vellore-632002, India

[3] Department of Community Health and Development, Christian Medical college, Vellore-632002, India

SUMMARY

Nasal polyps are outgrowths of oedematous nasal mucosa of inflammatory origin. Langerhans cells (LCs) residing in the nasal mucosa are responsible for maintaining the immunological environment. This study aims to ascertain the distribution of zinc iodide osmium (ZIO) positive LCs in normal nasal mucosa, and to compare the same with that in polypoid mucosa. Normal nasal mucosa obtained from patients undergoing septoplasty (n=21) and polypoid mucosa (n=21) obtained from patients with sinonasal polyposis due to diffuse sinonasal inflammation or allergic fungal rhinosinusitis were processed for identification of LCs using the ZIO technique. The number of ZIO positive LCs were counted per unit area of lamina propria and statistically analysed. The ZIO positive LCs were seen in the epithelium, lamina propria and among the glands. Both dendritic and non-dendritic LCs were present. They were noted within the lymphatic aggregations in the lamina propria, and were also noted in and around the blood vessels. The ZIO positive LCs were present in both normal and polypoid nasal mucosa. The median number of ZIO positive LCs was 0 (range: 0-1) per mm^2 and 12 (range: 0-44) per mm^2 in the normal and polypoid groups, respectively. This difference was statistically significant (p=0.001). No significant difference was noted based on the aetiology of the polyps. This is the first report of the presence of ZIO positive LCs in the nasal mucosa. Their significantly higher number in nasal polyps suggests an immunological role in the presence of inflammation.

Key words: Dendritic Langerhans cell – Non-dendritic Langerhans cell – Allergic fungal rhinosinusitis

INTRODUCTION

The nasal cavity is lined with both the respiratory and olfactory epithelium. The respiratory epithelium is made up of pseudostratified ciliated columnar epithelium lining most surfaces of the nasal cavity. This barrier of the immune system provides mechanical protection from infectious and allergenic pathogens (Orahilly et al., 1967). A nasal polyp is a protrusion of oedematous nasal mucosa that occurs secondary to underlying

Corresponding author:
Dr. Suganthy Rabi. Department of Anatomy, Christian Medical College, Vellore, Tamil Nadu, India, 632 002. Phone No. +91 9442978775.
E-Mail: suganthyrabi@cmcvellore.ac.in / suganthyrabi@hotmail.com

Submitted: October 21, 2020. **Accepted:** December 17, 2020
Not final proof's revision by the authors

inflammation. Histologically, polyps consist of a layer of pseudostratified columnar epithelium with several mucus secreting goblet cells and an underlying oedematous stroma with sparse blood vessels, fibrous tissue and nerves. In allergic polyps a large number of eosinophils may be seen in the lamina propria. The aetiology of sinonasal polyposis is varied; allergy, infection, allergic fungal rhinosinusitis, vasomotor rhinopathy, aspirin sensitivity are some common conditions associated with polyposis (Önerci, 2010). Allergic fungal sinusitis is a type 1 hypersensitivity reaction to a fungal allergen characterised by the presence of diffuse sinonasal polyposis and allergic mucin.

Human dendritic cells are the most potent antigen presenting cells, crucially linking the innate and adaptive immune responses (Adema, 2009; Schroeder et al., 2005). Their presence at the body's portals of entry for antigens, aids in fulfilling their function of antigen processing. At the mucosal surface, a distinct subset called the Langerhans cells (LCs) plays a major role in humoral and cell-mediated immunity. Various histochemical techniques employed to demonstrate LCs include gold chloride, zinc iodide osmium (ZIO) and uranyl acetate-lead staining (Jaitley and Saraswathi, 2012). Although the role of LCs in infections like rhinosinusitis (Pezato et al., 2014) have previously been studied using various markers, the ZIO positive LCs were not demonstrated in nasal mucosa. Therefore, the present study aimed to demonstrate the morphology and distribution of ZIO positive LCs in normal as well as polypoid nasal mucosa.

MATERIALS AND METHODS

Institutional Review Board and Ethics Committee approval was obtained for conducting the study (IRB Min:10895). Two groups of patients that were seen in the department of Otorhinolaryngology were recruited to the study. The first group (Group I) consisted of 21 patients with no evidence of polyposis, and who had otherwise normal-appearing mucosa. These patients were being operated by septoplasty for a deviated nasal septum. A small piece of redundant normal septal mucosa was resected in these patients. In the second group (Group II), 21 adult patients who underwent functional endoscopic sinus surgery for sinonasal polyposis during the study period were recruited to the study. This group included patients with diffuse sinonasal polyposis of allergic or other aetiology, as well as cases of allergic fungal sinusitis. Informed consent was obtained from all the patients who participated in the study. Patients with immunocompromised status, history of chemotherapy/radiation and invasive infections or neoplasms were excluded.

The polyps and normal nasal mucosal tissue were collected in an icebox and immediately fixed in veronal-buffered zinc iodide-osmium tetroxide, pH 7.4 (Figueroa and Caorsi, 1980) for 72 hours at 4°C in the dark, washed in distilled water, dehydrated in graded ethanol, cleared in xylene and embedded in paraffin wax. Serial sections of 6 µm thickness were taken. The sections were transferred to glass slides, deparaffinized, mounted using DPX and viewed under a microscope.

The slides were studied under the Olympus BX43 microscope with an inbuilt Olympus DP21 camera, and the software used was CellSens image analysing software (version 1.4.). The number of ZIO positive LCs were counted under 40X magnification using the closed polygon-measuring option of the image-analysing software over 20 fields. Each field measured ~50,000 μm^2, thus making a total area of 1 mm^2. Data analysis was done using SPSS version 24.

RESULTS

The age distribution of patients in both groups was similar. The age of patients in group I ranged from 23 to 62 years (mean = 40.5 ± 10.79), and in group II it ranged from 18 to 65 years (mean = 40.6 ± 11.4). There were 13 male and 8 female patients in group I and 7 male and 14 female patients in group II.

LCs in nasal mucosa of group I patients

The nasal mucosa was lined by pseudostratified ciliated columnar epithelium in most of the patients, and the ZIO positive LCs were nearly absent in the surface epithelium (Fig. 1a). In

patients who had hyperplastic pseudostratified ciliated columnar epithelium, few non-dendritic ZIO positive LCs were noted (Fig. 1b). A few patients had squamous metaplasia in which no ZIO positive LCs were seen. Lamina propria had connective tissue with mucosal glands, blood vessels and nerve fibres. The ZIO positive LCs were sparsely seen within glands (Fig. 1a). The number of ZIO positive LCs ranged from 0 to 4 (mean = 0.67 ± 1.238 per mm^2) (Table 1).

Table 1. Number of ZIO positive LCs in both groups per mm^2 area of lamina propria (n=21).

	Range	Mean (SD)	Median	IQR	p-value
Group I	0-4	0.67±1.23	0	1	0.001
Group II	0-97	24.38 ± 29.54	12.0	44	

LCs in nasal mucosa of group II patients

In the nasal mucosa, ZIO positive LCs were seen in the surface epithelium, lamina propria and among the glands (Fig. 2). All the types of LCs as described by Figueroa and Caorsi (Figueroa and Caorsi, 1980), were seen in both the epithelium and lamina propria (Fig. 3). They were classified as follows: Type 1: Single process, unbranched; Type 2: One process divided into branches; Type 3: Two processes; Type 4: Three or more processes; Type 5: Three or more processes with arborization.

In addition, non-dendritic LCs were also identified in the nasal mucosa. In some cases of polyp due to allergic fungal rhinosinusitis, ZIO positive LCs were aggregated just beneath

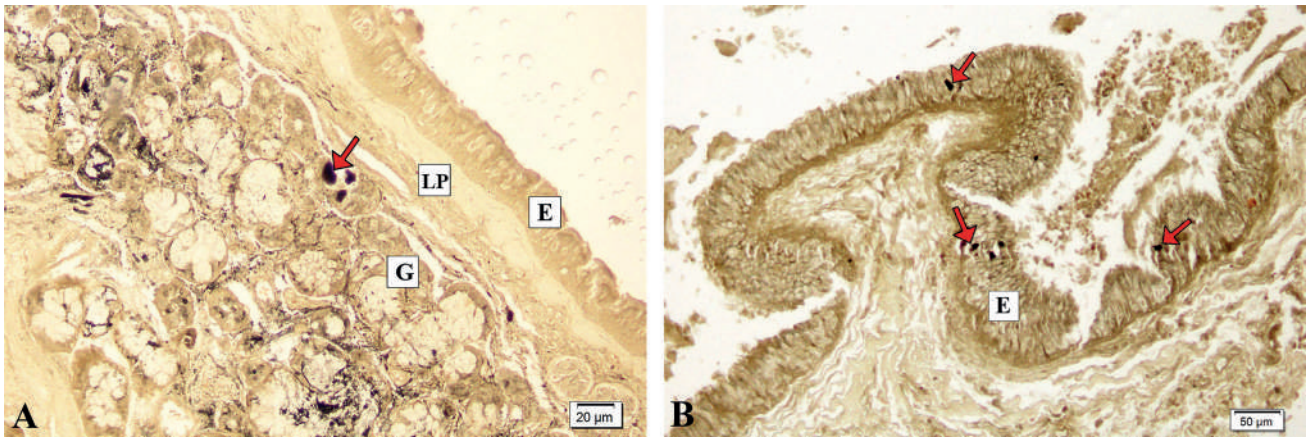

Fig. 1.- A. Arrow indicating ZIO positive LCs in the mucosal glands (G) of normal nasal mucosa. E- pseudostratified ciliated columnar epithelium; LP- lamina propria. **B.** Hyperplastic pseudostratified ciliated columnar epithelium of non-polypoid nasal mucosa. The arrows indicate ZIO positive LCs in the epithelium (E).

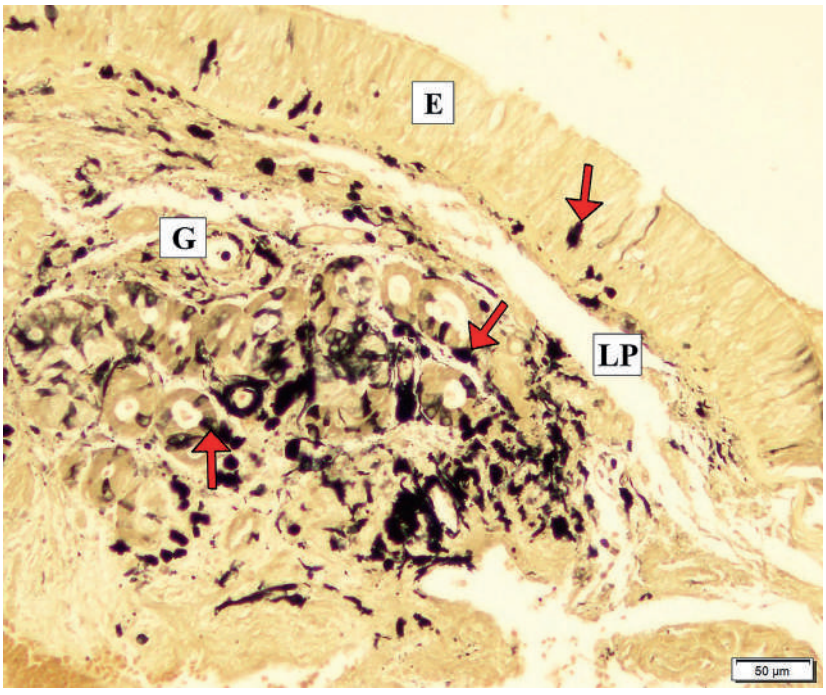

Fig. 2.- Nasal mucosa of a nasal polyp. Arrows indicating ZIO positive LCs in the surface epithelium (E), lamina propria (LP) and among glands (G).

the basement membrane (Fig. 4). A case of rhinosinusitis with polyposis showed subepithelial stroma with oedema, congestion, focal fibrosis and several thick- or thin-walled blood vessels. It also had lymphatic aggregation in the lamina propria, in which non-dendritic types of ZIO positive LCs were seen in the periphery of the follicle (Fig. 5).

7). The number of ZIO positive LCs in the polypoid group ranged from 0 to 97 with a mean of 24.38 ± 29.51 per mm^2 (Table 1). On comparing the distribution of ZIO positive LCs between the two groups, a significantly higher number of ZIO positive LCs was noted in group II patients (p=0.001). This shows that polyposis due to whatever aetiology is associated with a higher density of ZIO positive LCs (Table 1).

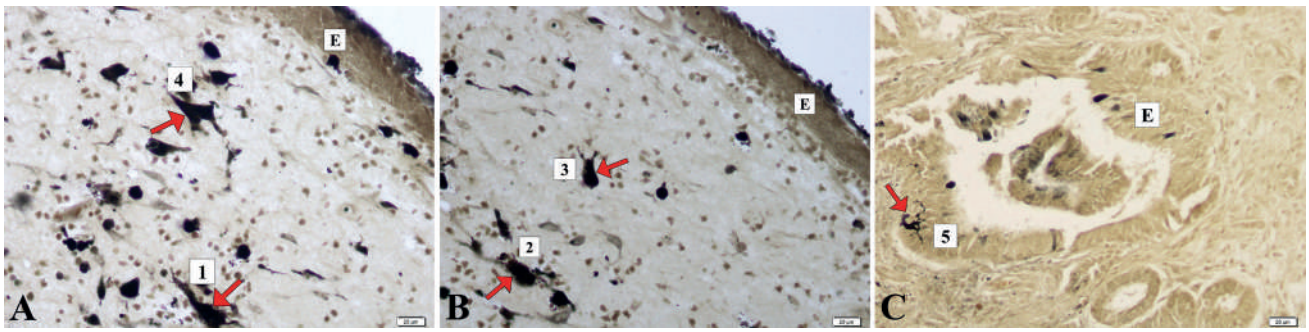

Fig. 3.- A. Type 1(single process, unbranched) and Type 4 (with three or more processes) LCs are indicated by arrows. E- Epithelium. **B.** Type 2 LC (one process which divides into branches) indicated by an arrow Type 3 LC (Two processes). E- Epithelium. **C.** Type 5 LC (with three or more processes with arborization) indicated by an arrow. E- Epithelium.

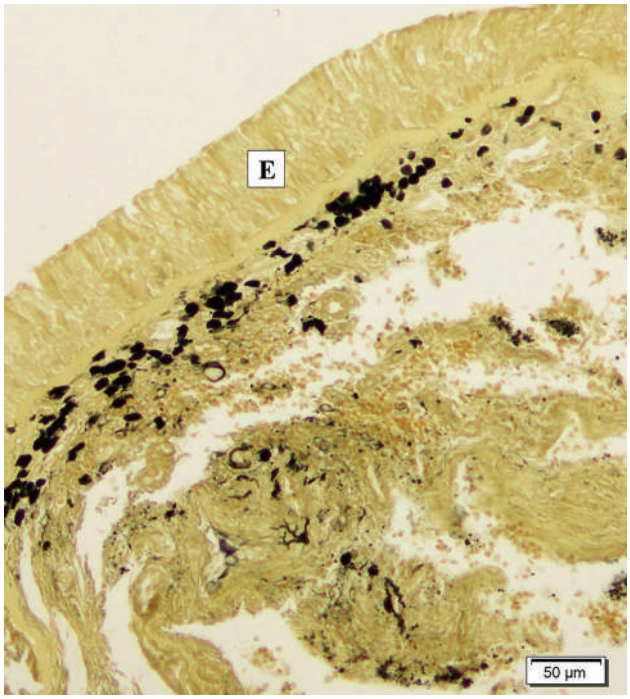

Fig. 4.- The ZIO positive LCs aggregated below the basement membrane. E-Epithelium.

The ZIO positive LCs were seen interspersed among seromucous glands in the polypoid group (Fig. 2). They were observed along the walls of the glands and also within it. In a cystically dilated gland they were embedded along its wall (Fig. 6).

The ZIO positive LCs were seen clustered in and around these blood vessels. Many of them were non-dendritic in nature, large and polygonal in shape (Fig.

DISCUSSION

The dendritic cells present in respiratory mucosa are essential for stimulating naive T cells in a primary immune response against inhaled allergens and for the development of allergic sensitization. A subset of dendritic cells called LCs, are present in different mucosal linings including the nasal mucosa (Fokkens et al., 1989a, b). Though they play a crucial role as critical regulators of many inflammatory diseases, only a limited understanding exists regarding the role of LCs in sinonasal polyposis. Of the many types of LCs, ZIO positive LCs are a distinct subtype demonstrated in other tissues like cervix, Fallopian tube and appendix and are known for their immunoregulatory role. In this study, we examined the density of ZIO positive LCs in the nasal mucosa to determine the difference between non-polypoid and polypoid groups.

LCs in the nasal mucosa

Fokkens et al. (1989a, b) had demonstrated the CD1a positive LCs in the middle and basal layers of the pseudostratified ciliated columnar epithelium of normal nasal mucosa. In the present study, the ZIO positive cells were present in the pseudostratified ciliated columnar epithelium of the polypoid group, but they were nearly absent in the non-polypoid

group. The authors have previously demonstrated that ZIO positive LCs cells are different from CD1a positive LCs in their distribution, and suggested that they are different subsets of LCs and may have different immunological roles (Rabi et al., 2014a). Additionally, all the five types of typical dendritic type of ZIO positive LCs were noted in the nasal mucosa, predominantly in the lamina propria. Godthelp et al. (1996) and Fokkens et al. (1989a, b) reported a significant increase of LCs and HLA-DR positive cells in the lamina propria of patients with allergic rhinitis.

The ZIO positive LCs have not been demonstrated in the pseudostratified ciliated columnar epithelium so far, but have been demonstrated in other epithelia such as the stratified squamous epithelium of lip, tongue, oesophagus, cervix and eyelid (Indrasingh et al., 2001; Rabi et al., 2014b, c), and the simple columnar epithelium of the small intestine and appendix (Koshy et al., 2020; Rabi et al., 2019). In this study, these cells were nearly absent in pseudostratified ciliated columnar epithelium of group I patients, but were seen in the hyperplastic pseudostratified ciliated columnar epithelium. They were also noted in the pseudostratified ciliated columnar epithelium in patients with polyps.

LCs in lymphatic aggregation of nasal polyps

Nasal/ nasopharynx associated lymphoid tissue (NALT) is a component of the immune system of the nasal mucosa and is part of the mucosa-associated lymphoid tissue (MALT) present in all mammals, which protects the body from airborne viruses and other infectious agents. It serves as a target site for local defence strategies and vaccine induction sites (Debertin et al., 2003). To begin an immune response, the maturing LCs primarily migrate to the lymphoid tissue where antigens are presented to the lymphocytes (Yao et al., 2002). The antigenic dose, the distribution of antigen that targets distinct types of dendritic cells present in the NALT, may contribute to the difference in the immunological outcome to an inhaled antigen (Iwasaki, 2007).

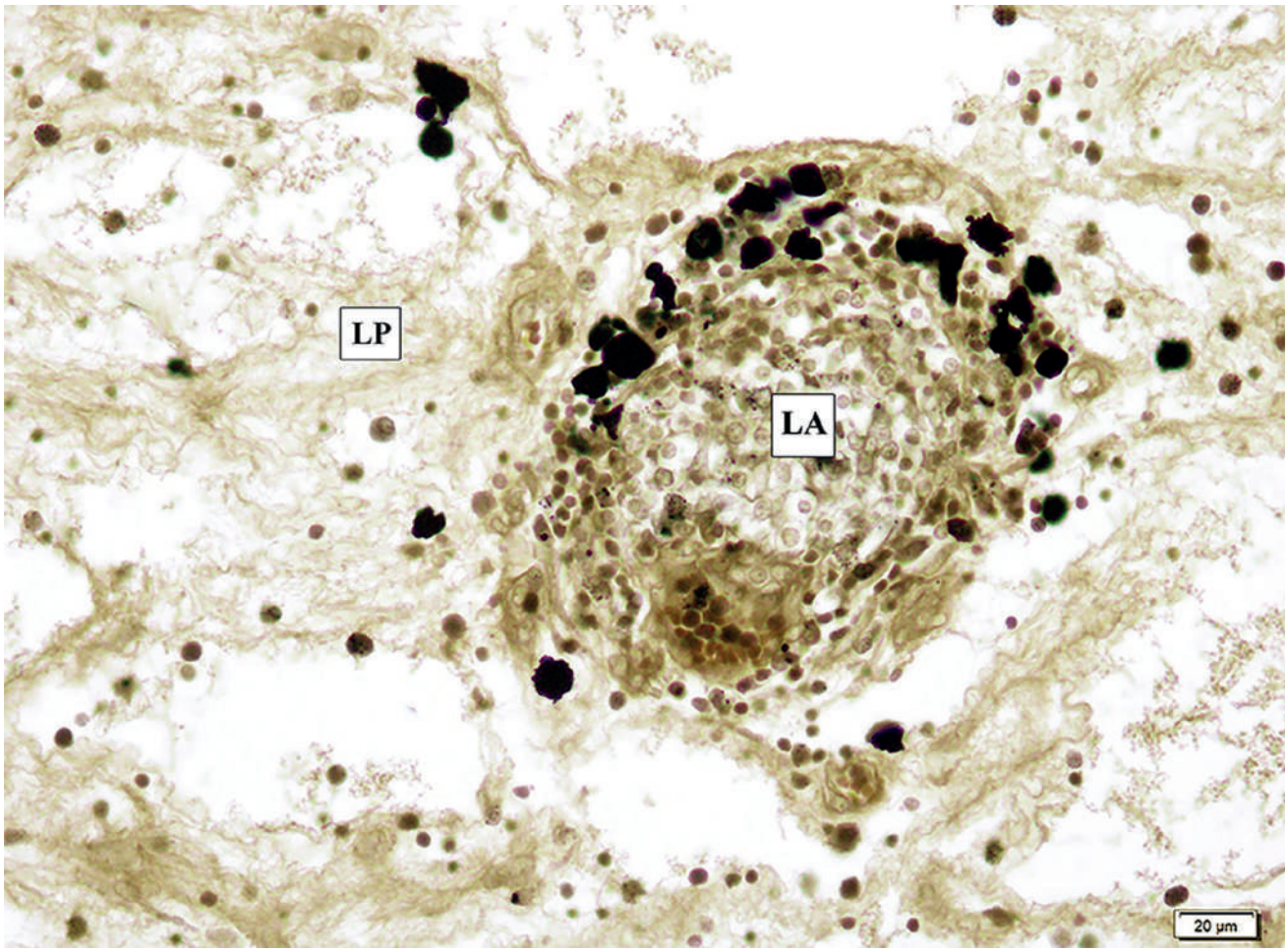

Fig. 5.- Non dendritic ZIO positive LCs among the lymphatic aggregates (LA) in the lamina propria (LP) in a case of nasal polyp.

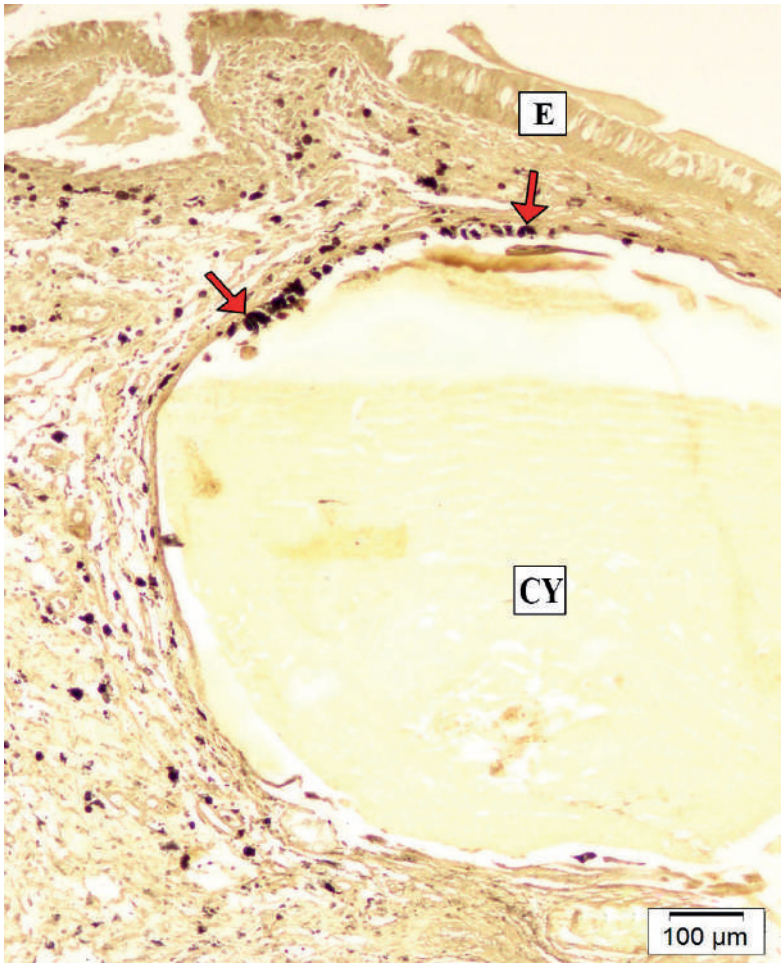

Fig. 6.- The arrows indicate ZIO positive LCs in the walls of a cystically dilated gland (CY) filled with secretory material. E- Epithelium.

This study noted that where there is an infiltration of inflammatory cells like mast cells neutrophils and lymphocytes associated with subepithelial stromal oedema and focal fibrosis, non-dendritic ZIO positive LCs were noted within the lymphatic aggregation in cases of nasal polyps. The ZIO positive non-dendritic follicular dendritic cells were observed in the germinal centre and dendritic follicular cells in the mantle zone of the normal appendix. The authors had suggested that the difference in morphology could be due to functional difference (Rabi et al., 2019). Linder et al. (1993) had also reported the presence of numerous scattered T lymphocytes and HLA-DR positive dendritic-like cells in the subepithelial areas of both nasal polyp and normal nasal mucosa. The proximity of LCs to the T lymphocytes indicates that cellular-immune responses are initiated by direct interaction of naive T cells and LCs in nasal mucosa (Iwasaki, 2007). Presence of NALT in nasal mucosa has to be extensively researched in humans.

LCs in nasal mucosal glands

The present study showed ZIO positive LCs interspersed among the seromucous glands of lamina propria, more in the polypoid group. They were noted within the glands and on their walls in both groups. The ZIO positive LCs were studded within the cystically dilated glands filled with secretory material and on their walls in the polypoid group. Similarly, Linder et al. demonstrated an aggregation of T lymphocytes and HLA-DR-positive cells adjacent to the deeper seromucous glands (Linder et al., 1993). This may suggest antigen presentation to the lymphocytes around the glands.

Vascular LCs in nasal mucosa

In the present study, ZIO positive LCs were seen surrounding some blood vessels and capillaries. Vascular dendritic cells in the arterial intima were identified with anti-CD1a and S-100 (Bobryshev and Lord, 1995a, b) way back in 1995. They were located at regular intervals along the

subendothelial layer, and were often in close contact with endothelial cells (Bobryshev and Lord, 1995b).

Rabi et al. (2014a) reported ZIO positive LCs surrounding the intraepithelial capillaries in the human cervix. These findings advocate the possibility of antigen presentation occurring even around the blood vessels.

Morphology of LCs in nasal mucosa

The ZIO positive LCs in this study were of both dendritic and non-dendritic nature in both groups. Mathew et al. had demonstrated the presence of non-dendritic and dendritic subtypes of CD1a positive LCs in the buccal mucosa (Mathew et al., 2019). The non- dendritic types of ZIO positive LCs were previously described by Rabi et al. (2014b) in the mucosa of the human exocervix. Shortman and Naik (2007) classified the dendritic cells into conventional dendritic cells and precursors of dendritic cells in his study. They described that the precursor dendritic cells, although without a dendritic form, could have an inherent capacity to develop into conventional dendritic cells at the onset of an inflammatory or microbial stimulus.

All the types of typical dendritic cells as described by Figueroa and Caorsi (1980) were identified in this study. The typical dendritic ZIO positive LCs were plenty in the nasal mucosa of the polypoid group. This is the first report of the ZIO positive LCs and their typical dendritic types in the nasal mucosa to the best of our knowledge.

In the present study, large polygonal non-dendritic types of ZIO positive LCs were noted in the epithelium, lamina propria including lymphatic aggregation and in and around blood vessels. These cells could be considered as a different subset of LCs or accessory antigen presenting cells. Extensive research in the field of non- dendritic LCs and their functions remains an unsolved question augmenting the need for further in vivo studies. A thorough understanding of specific molecular and cellular properties of NALT is essential for the development of an

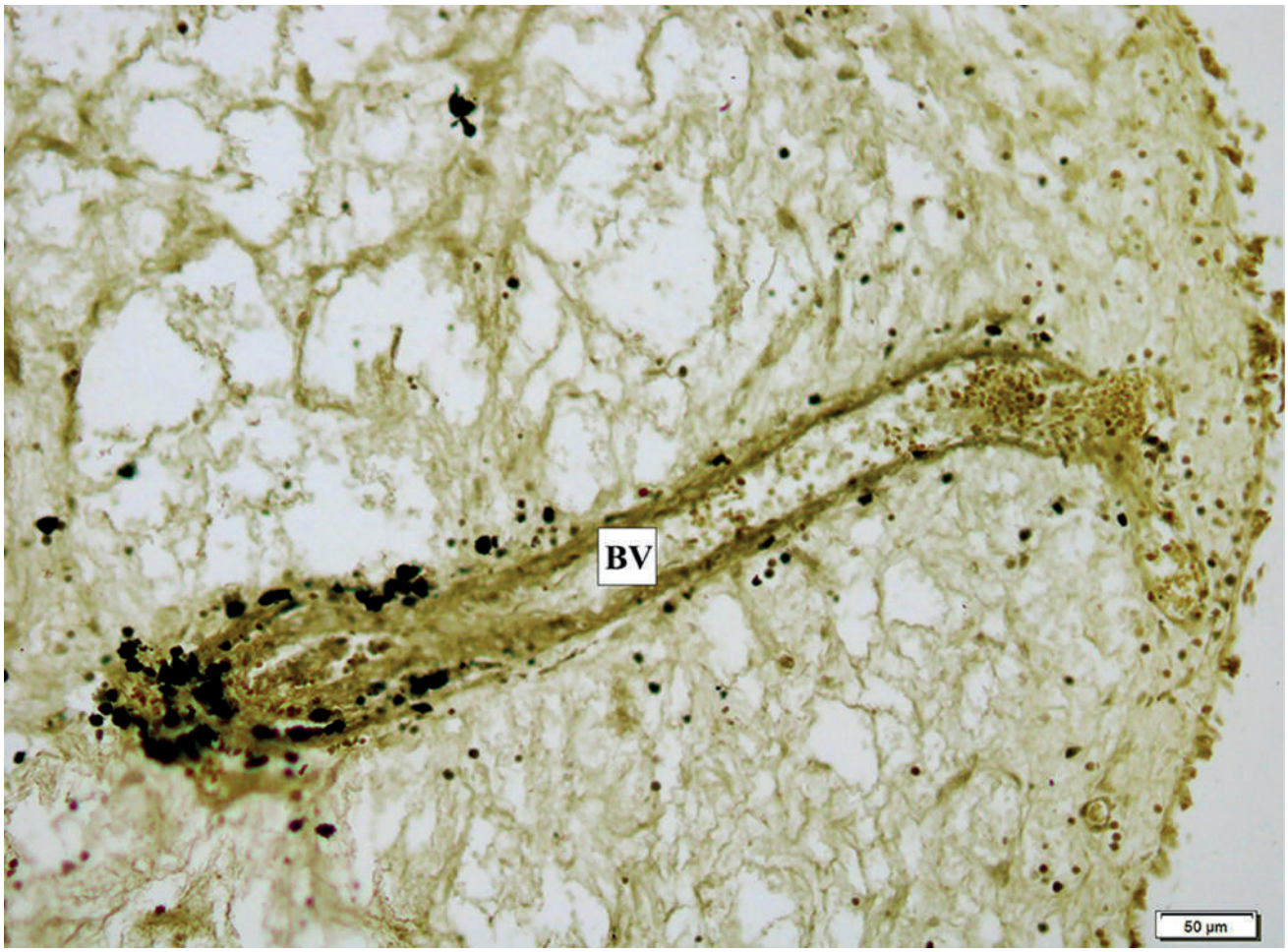

Fig. 7.- Non dendritic ZIO positive LCs in the wall of a blood vessel (BV).

effective intranasally administered vaccine. NALT-targeted immunization efficiently induces antigen-specific immune responses in both mucosal and systemic immune compartments. Presence of high density of LCs in the nasal mucosa is essential for efficient antigen uptake, which is a necessary criterion for nasal immunotherapy.

CONCLUSION

The current study shows the distribution and characteristics of ZIO positive LCs in patients with polypoid disease of the nose and sinuses, and highlights the difference in distribution of these LCs in normal mucosa and patients with sinonasal polyposis. The demonstration of ZIO positive LCs confirms the presence of immunoregulatory mechanisms that come into play in inflammatory sinus disease.

ACKNOWLEDGEMENTS

This work was supported by the Fluid Research Committee, Christian Medical College, Vellore. The authors would also like to acknowledge the contributions of Dr Meera Thomas, Professor, Department of Pathology, Christian Medical College, Vellore for providing assistance in data interpretation.

REFERENCES

ADEMA GJ (2009) Dendritic cells from bench to bedside and back. *Immunol Lett,* 122(2): 128-130.

BOBRYSHEV YV, LORD RS (1995a) S-100 positive cells in human arterial intima and in atherosclerotic lesions. *Cardiovas Res*, 29(5): 689-696.

BOBRYSHEV YV, LORD RS (1995b) Ultrastructural recognition of cells with dendritic cell morphology in human aortic intima. Contacting interactions of vascular dendritic cells in athero-resistant and athero-prone areas of normal aorta. *Arch Histol Cytol,* 58(3): 307-322.

DEBERTIN AS, TSCHERNIG T, TÖNJES H, KLEEMANN WJ, TRÖGER HD, PABST R (2003) Nasal-associated lymphoid tissue (NALT): frequency and localization in young children. *Clin Exp Immunol,* 134 (3): 503-507.

FIGUEROA CD, CAORSI I (1980) Ultrastructural and morphometric study of the Langerhans cell in the normal human exocervix. *J Anat*, 131(Pt 4): 669-682.

FOKKENS WJ, VROOM T, RIJNTJES E, MULDER P (1989a) Fluctuation of the number of CD-1(T6)-positive dendritic cells, presumably Langerhans cells, in the nasal mucosa of patients with an isolated grass-pollen allergy before, during, and after the grass-pollen season. *J Allergy Clin Immunol*, 84(1): 39-43.

FOKKENS WJ, VROOM THM, RIJNTJES E, MULDER PGH (1989b) CD-1 (T6), HLA-DR-expressing cells, presumably Langerhans cells, in nasal mucosa. *Allergy*, 44(3): 167-172.

GODTHELP T, FOKKENS WJ, KLEINJAN A, HOLM AF, MULDER PGH, PRENS EP, RIJNTES E (1996) Antigen presenting cells in the nasal mucosa of patients with allergic rhinitis during allergen provocation. *Clin Exp Allergy*, 26(6): 677-688.

INDRASINGH I, ABRAHAM S, VETTIVEL S (2001) Zinc iodide osmium positive cells and dendritic cells in stratified squamous epithelium of lip, tongue, and oesophagus of bonnet monkey (*Macaca Radiata*). *J Anat Soc India*, 50: 34-36.

IWASAKI A (2007) Mucosal dendritic cells. *Ann Rev Immunol*, 25(1): 381-418.

JAITLEY, SHWETA, SARASWATHI TR (2012) Pathophysiology of Langerhans cells. *J Oral Maxillofac Pathol*, 16(2): 239-244.

KOSHY S, INDRASINGH I, VETTIVEL S (2003) Dendritic cells in the human ileum: a light microscopic zinc iodide-osmium study. *Eur J Anat,* 7(3): 127-130.

LINDER A, KARLSSON-PARRA A, HIRVELÄ C, JONSSON L, KÖLING A, SJÖBERG O (1993) Immunocompetent cells in human nasal polyps and normal mucosa. *Rhinology,* 31(3): 125-129.

MATHEW JK, RAJADOSS MKP, PRANAY G, SUGANTHY R, TAMIL N (2019) Non-dendritic Langerhans cells: a new entity in normal and malignant buccal mucosa. *Eur J Anat*, 23(5): 383-388.

ÖNERCI, METIN (2010) *Nasal Polyposis*. Springer-Verlag, Berlin, Heidelberg.

O'RAHILLY R, MÜLLER F, CARPENTER S, SWENSON R (1967) The nose and paranasal sinuses. 2nd ed. *Basic Human Anatomy, A Regional Study of Human Structure*. WB Saunders Co., Philadelphia, pp 924-932.

PEZATO R, CLAUDINA AP, GABRIELE H, NATALIE DR, KOEN VC, GEERT DV, CLAUS B, LARA D (2014) The expression of dendritic cell subsets in severe chronic rhinosinusitis with nasal polyps is altered. *Immunobiology*, 219(9): 729-736.

RABI S, TRIPTI MJ, LIONEL J, INDRASINGH I (2014a) Different subsets of Langerhans cells in human uterine tubes and uterus. *J Obstet Gynaecol Res,* 40: 1833-1839.

RABI S, TRIPTI MJ, INDRASINGH I (2014b) Demonstration of CD 1a-positive and zinc iodide-osmium-positive Langerhans cells in the human eyelid. *Clin Exp Ophthalmol,* 42(8): 802-804.

RABI S, LIONEL J, INDRASINGH I (2014c) Morphological study of dendritic cells in human cervix by zinc iodide osmium method. *J Clin Diagn Res*, 8(6): AC01-04.

RABI S, INDRASINGH I, KOSHY S, SUGANTHY J (2019) Distribution of zinc iodide-osmium positive dendritic cells in the human appendix. *Eur J Anat,* 10(1): 15-20.

SCHROEDER JT, BIENEMAN AP, XIAO H, CHICHESTER KL, VASAGAR K, SAINI S, MARK CL (2005) TLR9- and FcRI-mediated responses oppose one another in plasmacytoid dendritic cells by down-regulating receptor expression. *J Immunol*, 175(9): 5724-5731.

SHORTMAN K, SHALIN HN (2007) Steady-state and inflammatory dendritic-cell development. *Nat Rev Immunol*, 7(1): 19-30.

YAO V, CAMERON P, JOHN CH (2002) Dendritic cells. *ANZ J Surg*, 72(7): 501-506.

The medial arm fasciocutaneous flap: a wasted alternative?

A.M. Vidal[1], José R. Sañudo[2], S. Quinones[2], Marko Konschake[3], R. García-Pumarino[1], Paloma Aragonés[2,4]

[1] Department of Obstetrics and Ginecology, Cantonal Hospital Lucerne, Switzerland

[2] Department of Human Anatomy and Embryology, Universidad Complutense, Madrid, Spain

[3] Department of Anatomy, Histology and Embriology, Medical University of Innsbruck, Innsbruck, Austria

[4] Orthopedics Department, Hospital Universitario Santa Cristina, Madrid, Spain

SUMMARY

The medial side of the upper arm is supplied by perforator arteries arising from the brachial artery, the superior ulnar collateral artery and the artery to the biceps muscle. Fasciocutaneous flaps from the medial arm region could be designed based on these perforating arteries, but the anatomical variability of this region has led to a loss of interest in it as a donor area for fasciocutaneous flaps.

The aim of this study is to identify, through cadaveric dissection, whether there are constant perforator arteries from the brachial artery that could be used to raise fasciocutaneous flaps from the inner side of the arm.

For this purpose, 15 upper extremities belonging to body-donors have been dissected. Six extremities were right-side arms and six belonged to female donors. 7 parameters and the differences between gender and side of the upper extremity were studied (distances from the acromion and the coracoid to the beginning and to the end of each perforating artery, distance from the insertion of the distal tendon of the biceps muscle to the origin of each perforator artery, length and diameter of the perforators arteries).

Perforator arteries arising from the brachial artery to the inner face of the arm were found in all the upper limbs dissected. The median number of these perforator arteries found by the upper limb was 5±1.9 (range 3-9). Anatomical variations consisted of the number of perforator arteries that were found in each limb. Only in 2 arms (13.3%), the perforator arteries arose from a superficial brachial artery or from the distal part of the brachial artery. The mean diameter of the perforating artery was 1.80±0.58 mm, and the mean length resulted in 4.67±2.07 cm.

The consistent vascular anatomy found for these perforator arteries, arising from the brachial artery, and the easy landmarks described justify the use of fasciocutaneous flaps of the medial side of the arm for reconstructive surgery.

Key words: Perforator artery – Brachial artery – Fasciocutaneous flap – Medial arm – Axillar defects – Reconstructive surgery

Corresponding author:
Paloma Aragonés, MD, PhD. Department of Orthopedics, Hospital Universitario Santa Cristina, C/Amadeo Vives, s/n. 28009 Madrid, Spain. Phone: +34625081082. E-mail: palo_82@hotmail.com / https://orcid.org/0000-0002-4067-3950

Submitted: December 1, 2020. **Accepted:** December 18, 2020

INTRODUCTION

The brachial artery (BA) is the continuation of the axillar artery, and begins at the level of the lower border of the teres major muscle. This vessel runs along the medial aspect of the arm, crosses the long and medial heads of the triceps muscle, the coracobrachialis muscle, passes on to the brachial muscle and reaches the deep face of the bicipital aponeurosis in the elbow (Cormack and Lamberty, 1994).

Cormack and Lamberty (1994) described the vascularization pattern of the medial side of the upper arm. According to these authors, this region is supplied by a row of 5 or 6 perforators arising from three sources: the BA, the superior ulnar collateral artery (SUCA) and the artery to the biceps.

The concept that the cutaneous vessels consistently perfuse their own specific areas of the skin was firstly proposed by Manchot: he attributed the vascularization of the medial aspect of the arm to the SUCA and its cutaneous branches (Manchot, 1889). Afterwards, Michel Salmon reviewed Manchot's works with the aid of X-ray (Salmon, 1930).

Later, the cutaneous vascular supply of the inner arm was studied, and it was seen that it derived from branches of the brachial artery (BA). These can either branch off the BA directly or indirectly via branches of the SUCA, inferior ulnar collateral artery (IUCA) or superficial brachial artery (SBA) (Lippert and Pabst, 1985; Taylor and Palmer, 1987).

On the medial side of the upper arm, fasciocutaneous flaps and neurovascular free flaps may be based on a single large fasciocutaneous perforator (Cormack and Lamberty, 1994). In recent years, there has been a need to increase the research in the vascular anatomy of the arm skin and the possibility of employing flaps of perforating arteries in reconstructive surgery.

With increasing clinical utilization of cutaneous flaps, there has been new anatomic knowledge of the flaps, blood supplies, and designs (Le Huec et al., 1995; Cormack and Lamberty, 1994; Hwang et al., 2005), but the data on the fasciocutaneous vascularisation of the medial aspect of the arm are incomplete in the literature. The number, situation and variable caliber of the musculocutaneous perforators do not allow for any classification (Le Huec et al., 1995).

Discrepancies between reports on vascular anatomy and a variability of terminology have also made the medial upper arm blood supply unclear (Matloub et al., 1992; Hwang et al., 2005; Karamürsel et al., 2005). Subsequently, the use of fasciocutaneous flaps from the inner face of the arm has lost interest.

Thus, the purpose of this descriptive anatomical study was to report the anatomy of the perforating arteries (PA), originating from the BA as a possible option for axillary reconstruction, and to propose the possible surgical approach based on the fasciocutaneous flap of the inner side of the arm.

MATERIAL AND METHODS

To conduct this descriptive study, the authors employed 15 upper extremities belonging to body-donors from the Department of Human Anatomy and Embryology of the Medical Faculty, Universidad Complutense of Madrid (Spain).

Of the 15 extremities, six belonged to three previously fixed cadavers preserved with 10% formaldehyde. The nine remaining extremities belonged to various unfixed fresh cadavers. Six extremities were right-side arms, and nine were left arms. Six belonged to female donors, and nine to male donors.

Anatomical dissection was performed as follows: firstly, the authors delimited the skin area of interest, continued with the dissection and traction of the skin and subcutaneous cell tissue, until the biceps brachii muscle was reached. The terminal branches of the brachial plexus—the medial antebrachial cutaneous nerve, the median nerve and ulnar nerve—and the vascular elements—the brachial veins and the brachial arteries—were identified.

The proximal part of the brachial artery was located and a thorough dissection of it was started to reach the perforating arteries, and continued until its multiple branches reached the subcutaneous cellular tissue of the inner face of the arm (Figs. 1, 2 and 3).

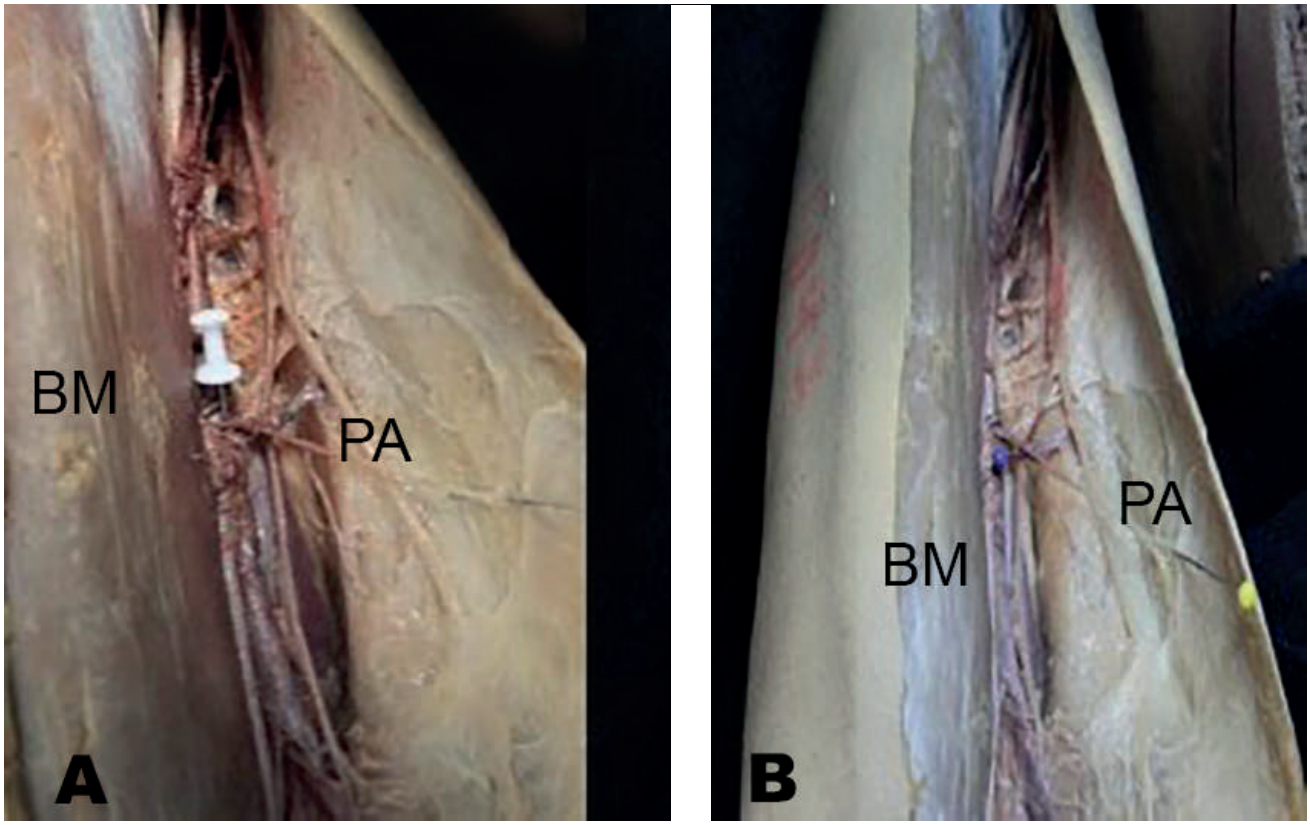

Fig. 1.- A: Right upper limb of a formolated body donor. The white pushpin points out the origin of the perforator artery (PA) from the brachial artery. **B:** Right upper limb of a formolated body donor. The blue pushpin points out the brachial artery and the origin of a PA. The yellow pushpin shows the PA. BM: biceps muscle.

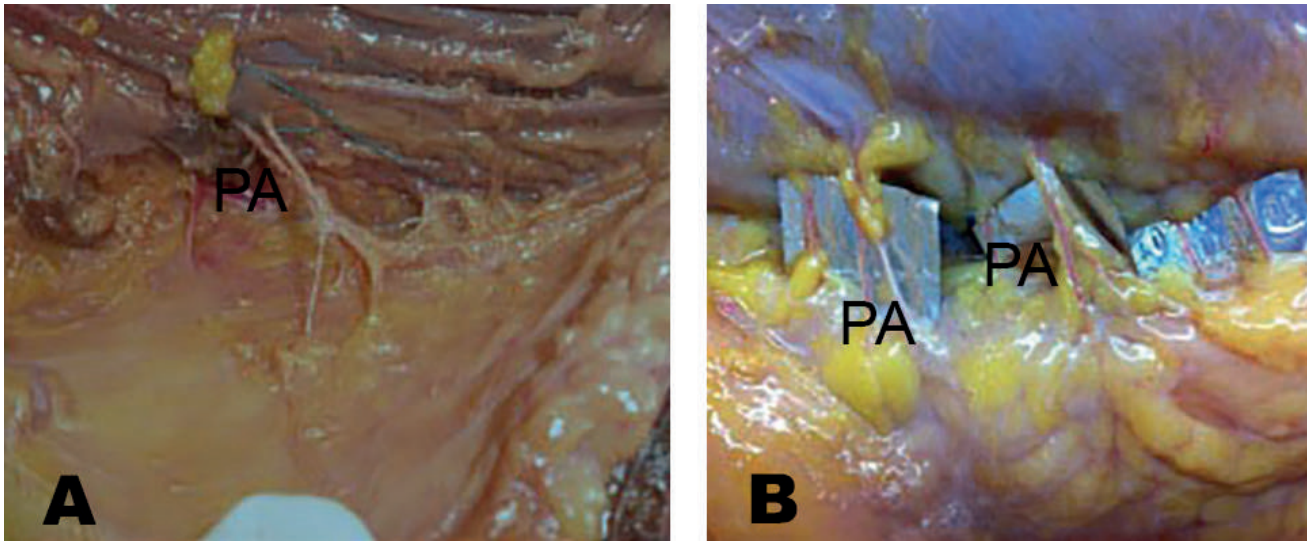

Fig. 2.- A, B: Left upper limb of a fresh cadaver. Various perforator arteries (PA) can be observed arising from the brachial artery and reaching the deep fascia.

Seven parameters and the differences between gender and side of the upper extremity were studied (Fig. 4):

- Distance from the coracoid process to the origin of the perforating artery from the brachial artery (A).
- Distance from the acromion to the origin of the perforating artery from the brachial artery (B).
- Distance from the coracoid process to the end perforating artery (C).
- Distance from the acromion to the end perforating artery (D)
- Distance from the insertion of the distal tendon of the biceps muscle to the origin of the perforating artery (E).
- Diameter of the perforating artery at the origin from the BA (F).
- Length of the perforating artery (G).

The results were treated statistically with IBM SPSS Statistics.

RESULTS

Of the 15 upper extremities, 40% belonged to female body-donors and in 40% of the cases the side was right.

Septocutaneous PA arising from the BA to the inner face of the arm were found in all the upper limbs dissected. The median number of PA arising from the BA found by upper limb was 5±1.9 (range 3-9). Anatomical variations consisted of the number of PA that were found in each limb. Only in 2 arms (13.3%), the PA arosed from a superficial brachial artery or from the distal half of the BA.

For each of the parameters A, B, C, D and E, the mean distance (MD) and the standard deviation (SD) in cm were calculated. The results have been represented in Table 1.

Table 1. Mean distance and standard deviation calculated for parameters A, B, C, D and E.

	Parameter measured				
	A	**B**	**C**	**D**	**E**
Mean distance (cm)	15.2	13.38	16.37	18.44	10.01
Standard deviation (cm)	3.07	3.39	2.77	2.77	2.73

The mean diameter and SD of the perforating artery (parameter F) was 1.80±0.58 mm, and the mean length and SD resulted in 4.67±2.07 cm (parameter G).

The ranges of the measures obtained for parameters A, B, C and D were classified by gender and represented in Table 2.

Table 2. Ranges measured for parameters A, B, C and D for males and females.

	Parameter measured							
	Males				**Females**			
	A	**B**	**C**	**D**	**A**	**B**	**C**	**D**
Range (cm)	7.5-22.50	11-24.5	13-20.5	15.5-26	7.5-18	8-19.50	10-20	12.5-21

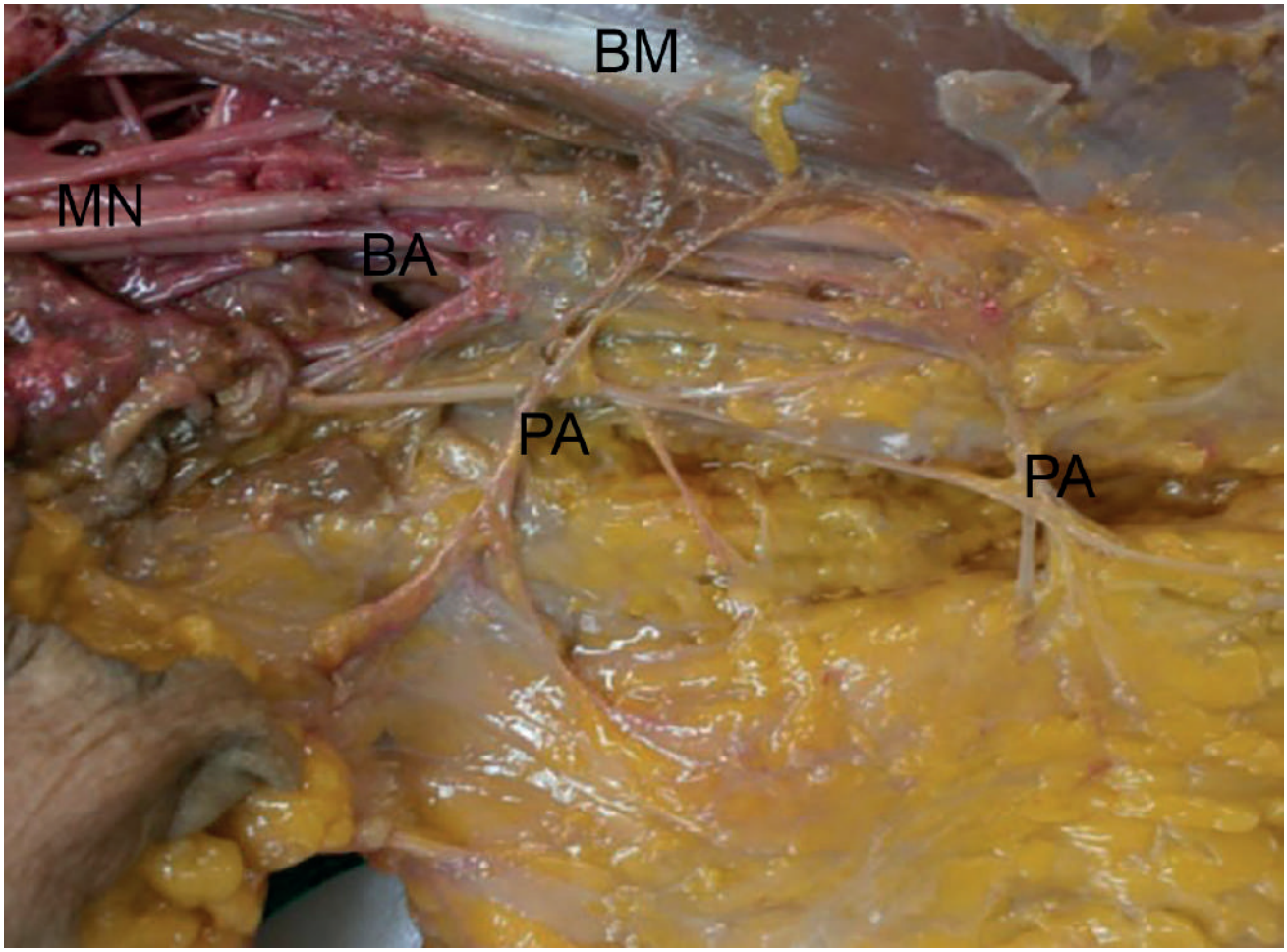

Fig. 3.- Left upper limb of a fresh cadaver. Perforator arteries (PA) arise from the brachial artery (BA) and reach the deep fascia of the inner side of the arm. BM: biceps muscle, MN: median nerve.

The minor and major diameters of the perforating artery (parameter F), as well as the maximum and minimum values of its length (parameter G) were also collected and classified by gender (Table 3).

Table 3. Ranges measured for parameters F and G for males and females.

	Parameters measured			
	Male		Female	
	F	G	F	G
Range (mm)	1-3	20-65	1-3	25-100

Among the sample, 3 different patterns of origin of the PA were found:

Pattern A. The PA branches off from the upper part of the brachial artery. This was found in 12 upper extremities (80%).

Pattern B. The PA branches off from the inferior part of the brachial artery. 2 upper extremities presented this pattern (13.3%).

Pattern C. 1 upper extremity of the sample presented 2 brachial arteries, a superficial and a deep one. The PA arose from the superficial brachial artery (6.7%).

DISCUSSION

According with the findings of Cormack and Lamberty (1994), the skin in the medial region of the arm is supplied by 5 or 6 perforating arteries that cross the deep fascia of the arm. These fasciocutaneous perforating arteries range from the brachial artery, the superior ulnar collateral artery and the artery to the biceps.

Origin and distribution of the perforator arteries of the medial arm have been investigated in several reports. Some authors (Dolmans et al., 1979; Kaplan and Pearl, 1980; Gao et al., 1985; Breidenbach et al., 1987; Bhattacharya et al., 1991; Matloub et al., 1992; Le Huec et al., 1995; Mathes and Nahai, 1996) have suggested a predominant role of the superior ulnar collateral

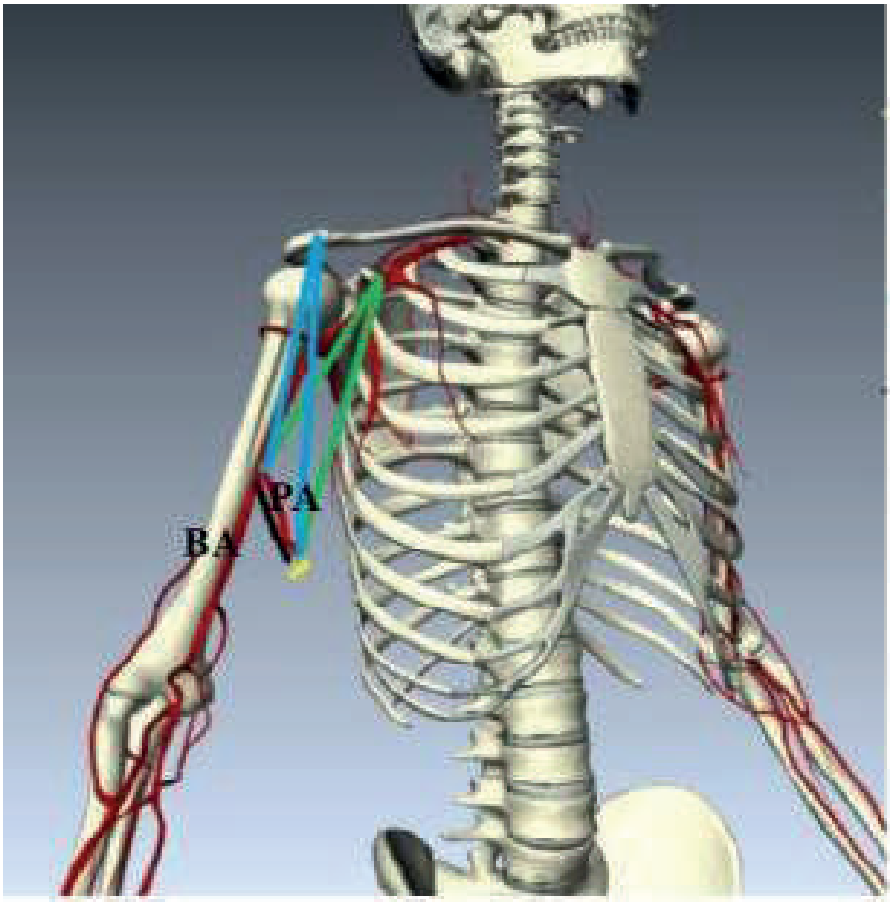

Fig. 4.- Diagram of a perforator artery arising from the brachial artery of a right upper limb. The brachial artery (BA) is shown with its perforating artery (PA) towards the inner side of the arm. Blue lines: distance from the acromion to the origin of the perforating artery from the brachial artery (parameter B) and distance from the acromion to the end of the PA (parameter D). Green lines: Distance from the acromion to the origin of the PA from the BA (parameter A) and distance from the acromion to the end of the PA (parameter C). Yellow line: Diameter of the PA (parameter F). Black line: Length of the PA (parameter G).

artery (SUCA) and its branches for the blood supply of the medial aspect of the arm, while others have defended the role of the brachial artery (Manchot, 1983; Zbrodowsky et al., 1987; Carriquiry, 1990; Karamürsel et al., 2005; Yakup et al., 2010).

Manchot (1983) described several branches arising from the BA that irrigate the anteromedial skin of the arm, and also in 1987 direct cutaneous arterial branches from the BA were reported (Zbrodowsky et al., 1987). Yakup et al. (2010), after a study of 14 body donors' upper limbs, described a constant perforator branch from the BA that supplied the distal medial skin of the arm. Carriquiry (1990) confirmed, in 14 dissected upper limbs, that direct septocutaneous branches from the BA were the main source of irrigation of the skin of the medial arm, while the branches arising from the SUCA tend to distribute in the skin more posteriorly than the BA branches do.

In a recent publication with a sample of 20 body donors' upper limbs, the authors found that the skin of the distal third and the proximal third of the medial arm was mostly supplied by perforator branches of the BA and the intermediate third by perforators of the SUCA and the BA anteriorly and by the SUCA posteriorly (Perignon et al., 2013).

Our anatomical study focused on the perforating arteries of the medial upper arm that arose from the brachial artery. The finding of a PA from the BA was constant in our entire sample, which ensures an easy and predictable dissection. The median number of PA from the BA found in each upper limb was 5±1.9 (range from 3-9). These findings coincide with those of Cormack and Carriquiry, who found several septocutaneous branches from the BA along the medial septum at different levels (Cormack and Lamberty, 1994; Carriquiry, 1990). Moreover, Tinhofer found in 20 upper limps from fresh cadavers, an average of 4.556±1.47 PA arose from the BA (Tinhofer et al., 2017).

The mean diameter of the PA from the BA in our sample was 1.80±0.58 mm (1-3 mm), while the mean length resulted in 4.67±2.07 cm (2-10 cm) (Table 3). Other authors have measured these parameters of the PA arising from the BA; the internal diameters of these PA described by Cormack and Lamberty (1994) range from 0.2 mm to 1.2 mm. Tinhofer et al. (2017) defined a mean diameter of 0.68±0.27 mm and their pedicles had an average length of 3.62±1.61 cm.

Perignon et al. (2013) reviewed the first PA of the BA and found a mean diameter of 1 ± 0.44 mm (0.5-1.8 mm), and a mean length of 3.5 ± 1.06 cm (2-6 cm). Yakup et al. (2010) and Hwang et al. (2005) described the distal brachial artery's main perforator as a constant PA of the BA with a mean diameter of 0.95 mm and 0.94 mm, and a mean length of 3.3 cm and 2.78 cm, respectively.

We measured in our cadaveric sample the distance from the coracoid to the origin of the PA from the BA (parameter A), and the values found were 15.2±3.07 cm, with a range of 7.5-22.5 cm. The distance from the acromion to the origin of the Pa from the BA (parameter B) was also measured and the values were 13.38±3.09 cm, with a range of 8-24.5 cm (Tables 1 and 2). Other authors measured, in body donors' upper limbs, the distance from the medial epicondyle to the first PA of the BA and found a distance of 19±2.69 cm (11.5-23 cm) (Perignon et al., 2013). Carriquiry (1990) described 3 to 4 septocutaneous branches arising from the BA along the medial septum, the uppermost one was close to the lower border of the pectoralis major tendon and the lowermost branch was located 2 to 4 cm above the medial epicondyle.

The medial upper arm flap was first described by Daniel et al. in 1975 for hand reconstruction in a 25-year-old man, but it was not finally attempted. This neurovascular island flap was designed based on the medial brachial cutaneous nerve and superficial branch of the SUCA, with its venae comitantes. This superficial artery is a constant artery and its diameter ranges from 0.5 to 1.4 mm. Dolmans et al. (1978) conducted a clinical trial with a neurocutaneous island flap from the medial arm on a patient, but the flap developed venous and arterial thrombosis and failed. It was not until 1979 before the first successful free transfer of the medial arm flap was carried up by Newsom (1979). This author performed a flap from medial arm skin, elevated on the superficial branch of the SUCA, to close a large oronasoantral fistula. The external diameter of the flap artery was 0.8 mm.

Yakup et al. (2010), after a study of 14 body donors' upper limbs, also advocated the use of a rotating fasciocutaneous flap in the lower part and medial region of the arm, based on a perforating artery arisen from the BA. At least one main PA and one accessory PA from the BA were found in all the extremities.

The medial arm fasciocutaneous flap has been raised in reconstructive surgery as local flap to cover elbow and axillary defects and contractures (Kaplan and Pearl, 1980; Maruyama et al., 1985; Yakup et al., 2010). Also, it has been used as fasciocutaneous free flap for reconstructions of the maxillofacial region, neck and the hand (Newsom, 1981; Song et al., 1981; Le Huec et al., 1995).

Carriquiry (1990) described axillary and elbow crease contractures released with medial arm island flaps, and thumb and hand defects covered in a cross-arm fashion.

The use of this fasciocutaneous flap of the medial arm offers many advantages: the surgical technique is simple and reproducible, the donor area is well-hidden, it can be easy closed in a linear way and it does not cause functional problems (Carriquiry, 1990).

Furthermore, the flap has thin, elastic and hairless skin, making it excellent for face, neck and hand reconstructions (Kaplan and Pearl, 1980). It also has better color match for head and neck reconstructions (Carriquiry, 1990).

As other authors have already described (Carriquiry, 1990), we propose the use of this fasciocutaneous flap based on PA from the BA as free flap to cover axillary defects. Specifically, we think that it could be a good surgical solution for the definitive treatment of hidradenitis suppurativa and for contractures after large deep burns.

Unfortunately, despite the great advantages described, the inner side of the arm appears to be frequently ignored in the choice of a potential flap due to the wider distribution of the PA from the medial intermuscular septum than the ones from the lateral intermuscular septum (Hwang et al., 2005).

We describe in our sample the PA arising from the BA, and we found them in a number of 3 to 9. The consistent vascular anatomy found for these PA and the easy landmarks described justify the use of fasciocutaneous flaps of the medial side of the arm for reconstructive surgery.

The only cases of anatomical variations in our study are due to an increase in the number of perforating arteries, and only in 2 (13.3%) of the cadavers the PA arose from the distal region of the brachial artery or from a superficial brachial artery. Instead of our findings, Yakup et al. (2010) described a distal brachial artery main perforator vessel in a sample of 14 upper limbs, and this vessel was seen in all dissected cadavers, and other authors found only one constant medial PA from the BA in the arm, located 8.9cm proximal to the medial epicondyle (Hwang et al., 2005).

Although in our study we can prove the presence of PA from the BA in a number from 3 to 9 in each limb, due to the variability described in the literature reviewed we recommend the use of a preoperative CT-angiography or Doppler ultrasound for surgical safety.

CONCLUSIONS

The fasciocutaneous flap of the medial based on PA from the BA can be raised safely and easily. Our study find that these PA appear constantly and provides anatomical references to locate these vessels in order to be applied clinically.

This flap provides advantages such as thin, elastic and hairless skin, in addition to being a well-hidden donor area without functional alterations.

ACKNOWLEDGEMENTS

To Dr. T. Vázquez (Director) and to the Technical Staff of the Center of Donors of Cadavers and dissecting Rooms of the Universidad Complutense of Madrid, Spain.

DECLARATIONS

Funding

The authors have no financial or personal relationship with any third party whose interests could be positively or negatively influenced by the

article's content. This research did not receive any specific grant from funding agencies in the public, commercial, or not-for-profit sectors.

Ethical approval

The cadavers belonged to the Donors and Dissecting Rooms Center, Universidad Complutense de Madrid, Spain. The bodies were under a strict control by the ethical committee in accordance to the ethical standards as laid down in the 1964 Declaration of Helsinki.

Consent to participate

Informed consent was obtained from all the participants included in the study.

Consent for publication

The authors affirm that human research participants provided informed consent for publication of the images in Figures 1, 2, 3 and 4.

REFERENCES

BHATTACHARYA S, BHAGIA SP, BHATNAGAR SK, PANDEY SD, CHANDRA R (1991) The medial upper arm fasciocutaneous flap. An alternative flap to cover palmar defects of hand and distal forearm. *J Hand Surg Br*, 16: 342-345.

BREIDENBACH WC, ADAMSON W, TERZIS JK (1987) Medial arm flap revisited. *Ann Plast Surg*, 18: 156-163.

CARRIQUIRY CE (1990) Versatile fasciocutaneous flaps based on the medial septocutaneous vessels of the arm. *Plast Reconstr Surg*, 86: 103-109.

CORMACK GC, LAMBERTY BGH (1994) *The arterial anatomy of skin flaps*. Ed. Churchill Livingstone, London, England, pp 80, 181-189.

DANIEL RK, TERZIS J, SCHWARZ G (1975) Neurovascular free flaps. *Plast Reconstr Surg*, 56: 13.

DOLMANS S, GUIMBERTEAU JC, BAUDET J (1979) The upper arm flap. *J Microsurg,* 1: 162.

GAO X, MAO Z, YANG Z, WANG B (1985) Medial upper arm skin flap: vascular anatomy and clinical applications. *Ann Plast Surg*, 15: 348-351.

HWANG K, LEE WJ, JUNG CY, CHUNG IH (2005) Cutaneous perforators of the upper arm and clinical applications. *J Reconstr Microsurg*, 21(7): 463-469.

KAPLAN FN, PEARL RM (1980) An arterial medial arm flap, vascular anatomy and clinical applications. *Ann Plast Surg*, 4: 205.

KARAMÜRSEL S, BAGDATH D, DEMIR Z, TÜCCAR E, CELEBIOGLU S (2005) Use of medial arm skin as a free flap. *Plast Reconstr Surg*, 115: 2025-2031.

LE HUEC JC, LIQUOIS F, LEGER O, CHAUVEAUX D, MIDY D, LE REBELLER A (1995) A study of the fasciocutaneous vascularisation of the arm: surgical applications. *Surg Radiol Anat*, 17(2): 121-128.

LIPPERT H, PABST R (1985) *Arterial variations in man: classification and frequency*. Bergmann Verlag GmbH, KG; Munich, Germany.

MANCHOT C (1883) *The cutaneous arteries of the human body*. Springer-Verlag, New York.

MARUYAMA Y, ONISHI K, YOSKIKO Y (1987) The ulnar recurrent fasciocutaneous island flap. *Plast Reconstr Surg*, 79: 381-387.

MATHES SJ, NAHAI F (1996) *Reconstructive surgery. Principles, anatomy and technique*. Elsevier, Oxford, pp 747-748.

MATLOUB HS, YE Z, YOUSIF NJ, SANGER JR (1992) The medial arm flap. *Ann Plast Surg*, 29: 517-522.

NEWSOM HT (1981) Medial arm free flap (Case report). *Plast Reconstr Surg*, 67: 63.

PERIGNON D, HAVET E, SINNA R (2013) Perforator arteries of the medial upper arm: anatomical basis of a new flap donor site. *Surg Radiol Anat,* 35: 39-48.

SALMON M (1936) Les arte ` res de la peau. Masson, Paris, pp 126-128.

SONG R, SONG Y, YU Y, SONG Y (1982) The upper arm free flap. *Clinics Plastic Surg,* 9(1): 27-35.

TAYLOR GI, PALMER JH (1987) The vascular territories (angiosomes) of the body: experimental study and clinical applications. *Brit J Plastic Surg*, 40: 113-141.

TINHOFER IE, TZOU CH, DUSCHER D, POLLHAMMER MS, WENINGER WJ, HUEMER GM, SCHMIDT M (2017) Vascular territories of the medial upper arm-an anatomic study of the vascular basis for individualized flap design. *Microsurgery*, 37: 618-623.

YAKUP C, KOCABIYIK N, OZTURK S, ISIK S, OZAN H (2010) A new perforator flap from distal medial arm: a cadaveric study. *Eplasty*, 10: 541-548.

ZBRODOWSI A, MARTI FM, GÜMEWER R, MONTANDON D (1987) Blood supply of the subcutaneous tissue of the upper limb and its importance in the subcutaneous flap. *J Hand Surg*, 12B: 189.

A different perspective on the styloid process morphometry

Ahmet Dursun[1], Kenan Öztürk[1], Fatih A. Şenel[2], Veysel A. Ayyildiz[3]

[1] *Department of Anatomy, Faculty of Medicine, Suleyman Demirel University, Isparta, Turkey*
[2] *Department of Computer Engineering, Engineering Faculty, Suleyman Demirel University, Isparta, Turkey*
[3] *Department of Radiology, Faculty of Medicine, Suleyman Demirel University, Isparta, Turkey*

SUMMARY

This study's goal was to obtain the length, medial-anterior angulation, and basis-apex coordinates of the styloid process (SP) on 3D-CT images of asymptomatic individuals. In this study, the anterior and lateral lengths, anterior and medial angulation, and coordinate values on the x, y, and z-axes of the basis-apex of the SP in 259 cases (132 males, 127 females) were investigated. The mean anterior SP lengths were detected to be 23.65 mm on the right side and 23.35 mm on the left side, and the mean lateral SP lengths were detected to be 21.77 mm and 21.64 mm on the right and left sides, respectively. The mean medial angulation of the SP was measured to be 64.37° on the right side and 64.42° on the left side, and the mean anterior angulation was measured to be 30.16° and 33.69° on the right and left sides, respectively. The SP basis coordinates (right: x= -40.70, y=0, z=0, left: x=40.39, y=0, z=0) and SP apex coordinates (right: x= -31.74, y= -18.90, z= -10.36, left: x=31.91, y= -18.01, z= -11.53) were determined in mm. The results of this study will positively affect the quality of the report of radiologists who report CT images of the SP in daily routine practice. Furthermore, it is important for the prevention of complications, which may be encountered during the pre-postoperative period by otorhinolaryngologists dealing with the surgery of this region.

Key words: Styloid process – MATLAB – Coordinate – Computed tomography – Angulation

INTRODUCTION

The styloid process (SP) is a thin needle-like protrusion located in the anterior part of the stylomastoid foramen, emerging from the lower surface of the petrous part of the temporal bone, extending downward and anteriorly, and extending between the external and internal carotid arteries toward the tonsillar fossa (Kosar et al., 2011).

The SP continues to elongate as a result of ossification until the age of 8, and its elongation slows down at the age of about 30 (Baylan, 2017). The SP length may vary according to individual factors in different populations (Şener et al., 2018). However, in the literature, the normal length of this structure was reported to be between 20-30 mm. In cases with the SP length of more than 30 mm, it was called the elongated SP, and it was reported that it might cause Eagle syndrome (Şener et al., 2018). In many studies conducted to evaluate the SP, the elongated

Corresponding author:
Kenan Öztürk, PhD. Department of Anatomy, Faculty of Medicine, Suleyman Demirel University, 32260, Isparta, Turkey. Phone: +90 246 2113301; Fax: +90 246 237 1165. E-mail: kenanozt@hotmail.com. Orcid ID: 0000-0002-5552-8684.

Submitted: March 10, 2020. **Accepted:** December 25, 2020
Not final proof's revision by the authors

SP was reported in 4% of patients (Shayganfar et al., 2018). Of these patients, 4-10.3% were reported to be symptomatic (Shayganfar et al., 2018). In the case of elongated SP, it can cause symptoms, such as foreign body sensation in the throat, pain when moving the head, vertigo, dysphagia, otalgia, facial pain, headache, tinnitus, and trismus by creating pressure on the adjacent neurovascular structures (Hettiarachchi et al., 2019)prevalence and type of elongation, and angulation of the styloid process in relation to sex and side on digital panoramic radiographs in a Sri Lankan population. Methods: A total of 100 digital panoramic images selected from the database at the Division of Oral Medicine and Radiology, Faculty of Dental Sciences, University of Peradeniya, Sri Lanka were evaluated for the radiological features of the styloid process. Lengths greater than 30 mm were consider as elongated. Elongated styloid processes were also classified into three types based on Langlais classification (elongated, pseudo articulated; and segmented. It is possible to confuse the elongated SP with other diseases causing the same symptoms in the head and neck region. Therefore, the elongated SP is difficult to diagnose only with clinical findings and should be radiologically examined for a definitive diagnosis (Piagkou et al., 2009). It has been reported that the SP length can be evaluated in the best way upon 3D-computed tomography (CT), multi-slice CT, multi-plane reconstruction, and maximum intensity projection (Okur et al., 2014).

Cranial nerves IX, X, XI, and XII, the sympathetic trunk, the internal jugular vein, and the internal carotid artery are localized in the medial of the SP (Hettiarachchi et al., 2019)prevalence and type of elongation, and angulation of the styloid process in relation to sex and side on digital panoramic radiographs in a Sri Lankan population. Methods: A total of 100 digital panoramic images selected from the database at the Division of Oral Medicine and Radiology, Faculty of Dental Sciences, University of Peradeniya, Sri Lanka were evaluated for the radiological features of the styloid process. Lengths greater than 30 mm were consider as elongated. Elongated styloid processes were also classified into three types based on Langlais classification (elongated, pseudo articulated; and segmented. The deviation of the apex of the SP to the anterior and medial is clinically significant because it affects the adjacent neurovascular structures. Therefore, this study aimed to obtain the lengths, medial and anterior angulations, and especially the basis and apex coordinates of the SP, which had not been examined in the literature yet, in asymptomatic individuals (individuals who were thought not to have Eagle syndrome).

MATERIALS AND METHODS

This study was performed retrospectively on 3D-CT images of asymptomatic individuals (by obtaining 3D images from CT images using a RadiAnt DICOM viewer) acquired from the hospital's "Picture Archiving and Communicating System" (PACS) in the Radiology Department. Approval was obtained from Suleyman Demirel University Faculty of Medicine Clinical Research Ethics Committee. In this study, the morphometric properties of the SP were investigated in 259 individuals (132 males, 127 females) aged between 5 and 98 years (mean age 46.25 ± 24.58).

Morphometric measurements

SP length: The anterior (Fig. 1) and lateral (Fig. 2) SP lengths were obtained by measuring the right and left-side SP lengths separately from the anterior and lateral sides.

Origin point: The point at which the vertical axis passing through the pharyngeal tubercle intersects the axis, which joins the SP bases, was considered to be the origin point (Fig. 1).

Apex coordinates: The coordinates of the SP apexes were determined on the coordinate plane (x, y, z).

x: On the coronal plane, it was accepted as the transverse axis, which joins the bases of the SP (Fig. 1).

y: On the coronal plane, it was accepted as the vertical axis, which passes through the pharyngeal tubercle (Fig. 1).

z: It was taken as the sagittal axis, which passes through the junction of the x and y-axes (Fig. 2).

Basis coordinates: The distances of the bases of the SP from the origin point were measured.

Medial angulation of the SP (MA): The angle between the long axis of the SP on the coronal plane and the axis joining the SP bases was measured.

Anterior angulation of the SP (AA): The angle between the axis passing through the back edge of the SP in the sagittal plane and the vertical axis passing through the base of the SP was measured (AA measurement was made in this way, as it will provide more practical use when performing radiological evaluation).

In 3D-CT images, the length measurements of the SP from the anterior and lateral parts are different from each other, because the angulations of the SP toward the anterior and medial parts are different. For both measurements to be equal to each other, the angulations of the SP toward the anterior and medial parts should be corrected to be zero. If measurements are performed by correcting these angulations, the length measurements of the SP, made from both the anterior and lateral parts,

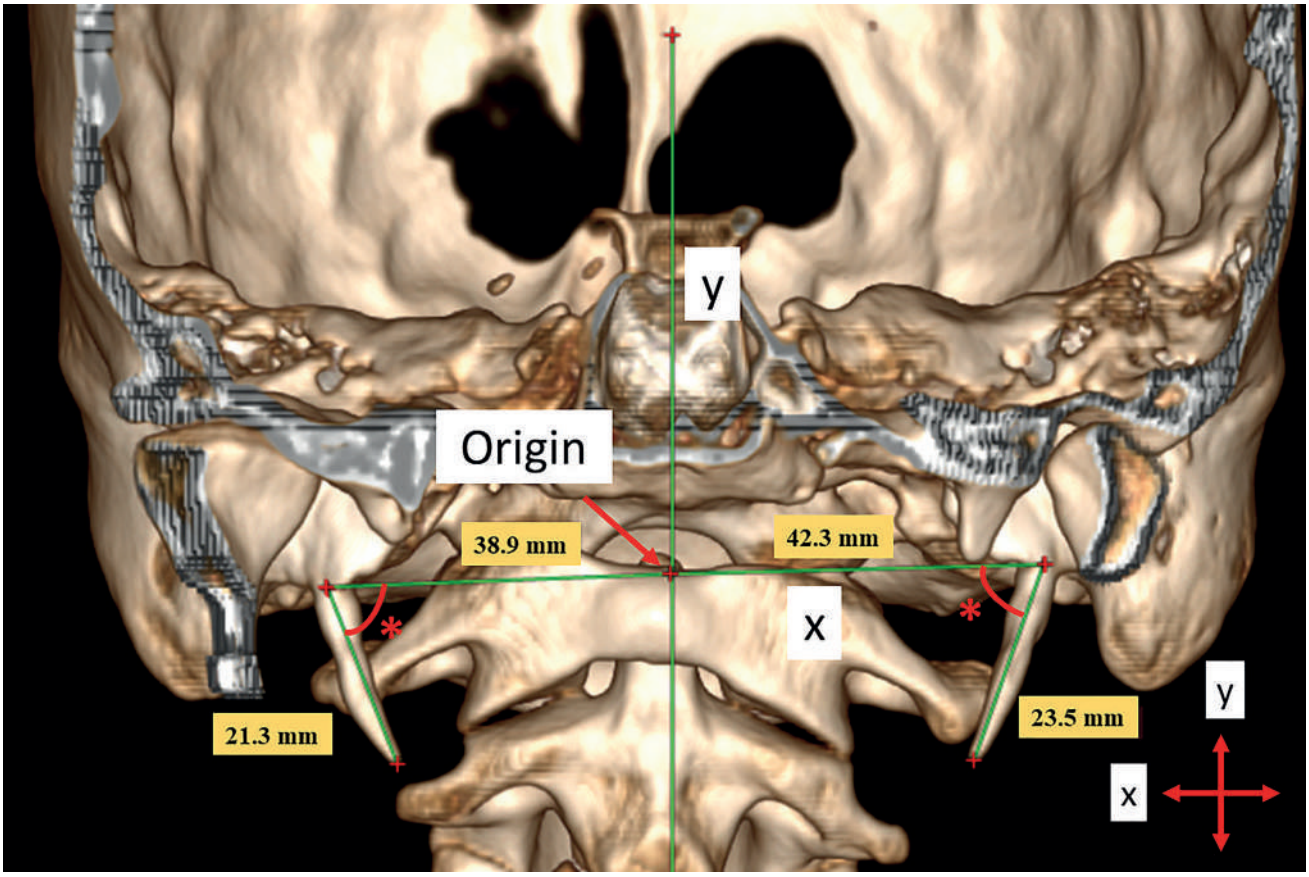

Fig. 1.- A 19-year-old male patient. The SP lengths measured from the anterior view and the x- and y-coordinate planes. (*) Medial angulation.

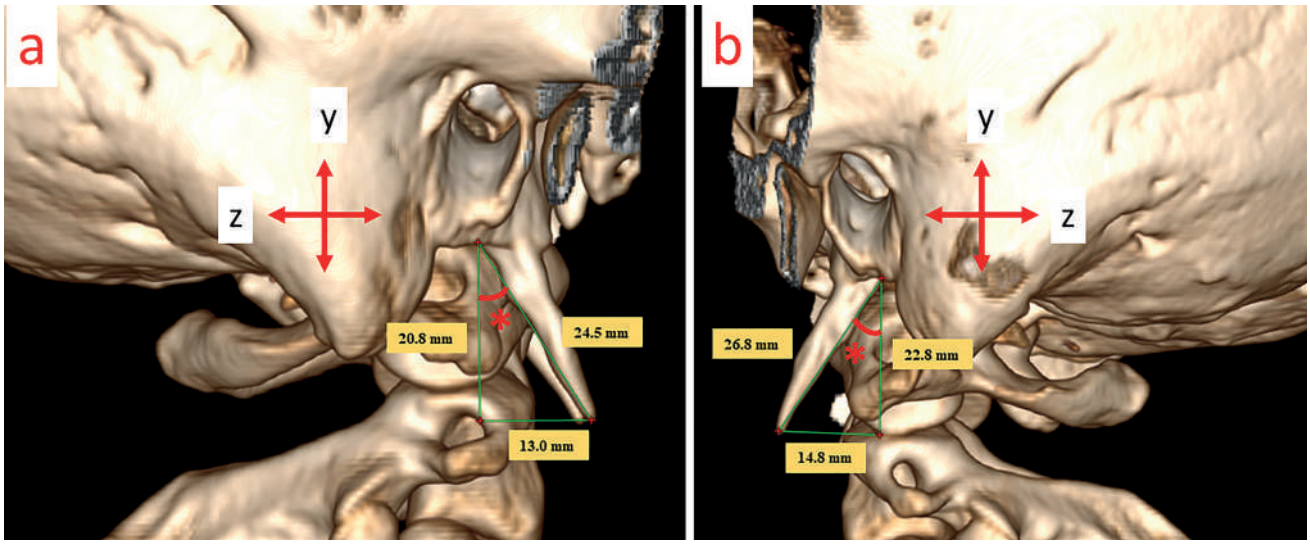

Fig. 2.- A 19-year-old male patient (The same patient as in Fig. 1). The SP lengths measured from the lateral (**a.** right, **b.** left) view and the y- and z-coordinate planes; (*) Anterior angulation.

will be equal to each other. In practical use, these angulation corrections are very difficult to apply. Therefore, the SP lengths were measured from the anterior and lateral parts separately, which can be used in a radiological evaluation.

By converting the CT images of the patients into a 3D format using a "RadiAnt DICOM viewer 4.6.9", the places to be measured were marked, and the screen image was taken and transferred to the MATLAB program. Afterward, using the ginput tool of the MATLAB program, the SP lengths, angulations, and positions on the coordinate plane were determined according to a specified reference measure. Drawings showing the position of the SP on the coordinate plane were also obtained using the MATLAB program (Figs. 3, 4, 5).

Statistical analysis

Statistical analysis was performed using SPSS Inc. for Windows 20.0 program. The arithmetic means and standard deviations of the parameters were determined according to age, side, and gender. The Kruskal-Wallis test was used to compare parameters between the age groups (decades). The Independent Samples T-Test was used to perform pairwise comparison between the genders, sides and decades. Pearson's correlation analysis was used for the correlation analysis.

RESULTS

The SP length was measured from the anterior and lateral sides (Table 1). The SP lengths (anterior, lateral) were compared on the right and

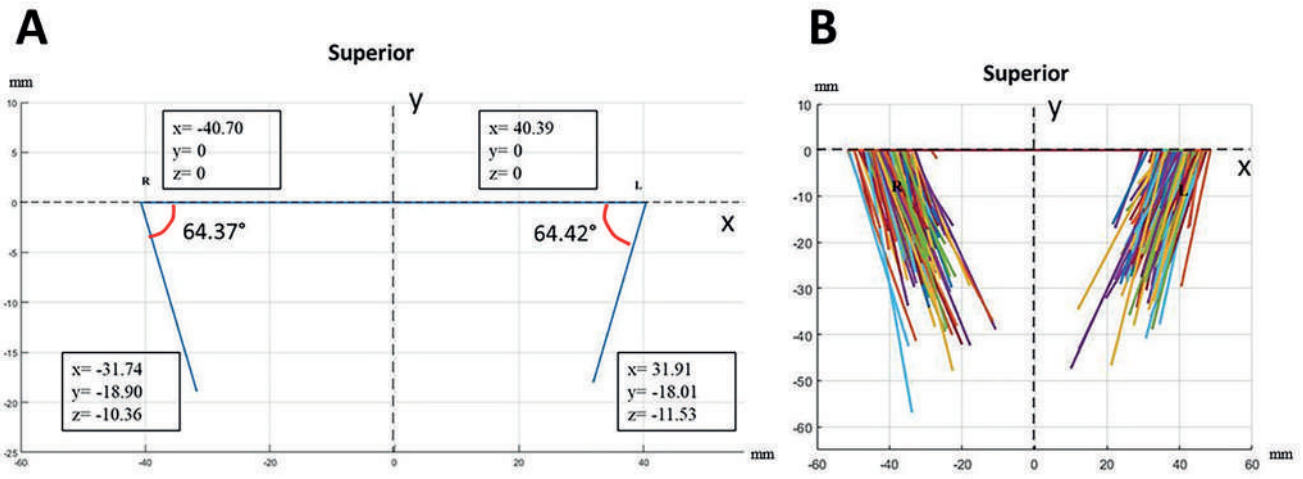

Fig. 3.- a. The mean medial angulations and the mean coordinate values of the base and apex of the SP when viewed from the anterior part; **b.** The anterior views of all SPs.

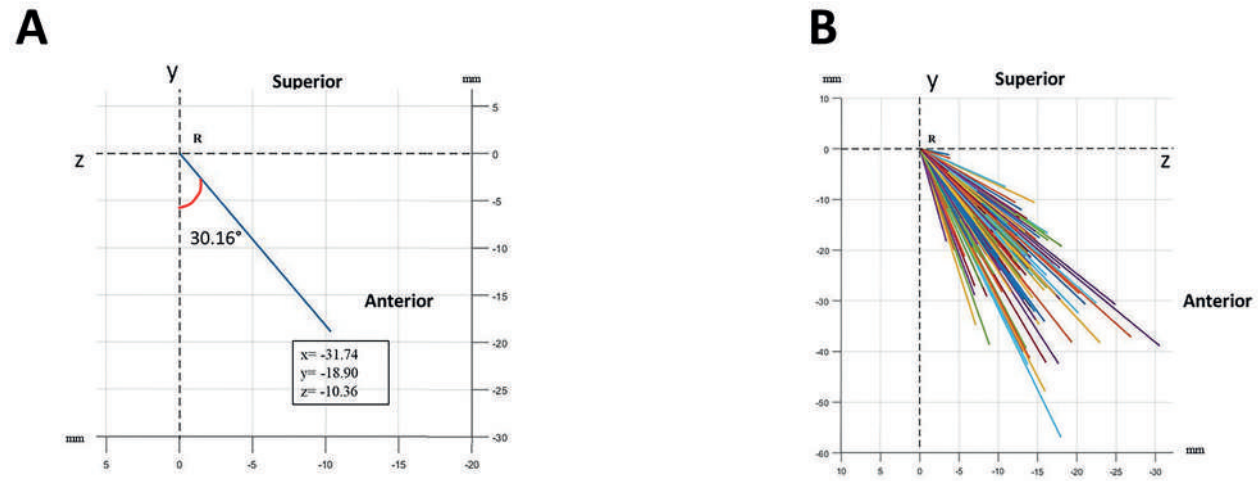

Fig. 4.- a. The mean anterior angulation and the mean coordinate values of the apex of the SP when viewed at the right SP from the lateral part; **b.** The lateral views of all the right SPs.

left sides according to gender, and the SP lengths on both sides were found to be more significant in male patients. However, only the right lateral SP length was statistically significantly longer in male patients (p=0.032) (Table 1). There was no statistically significant difference between the anterior and lateral SP lengths on the right and left sides (Table 1). The mean medial angulation (MA) and anterior angulation (AA) on the right and left sides were determined (Table 1, Figs. 3a, 4a, 5a). The MA and AA were compared on the right and left sides according to gender. The MA was found to be statistically significantly higher in male patients on both sides (p=0.029 on the right side and p<0.001 on the left side). The AA was also higher in male patients on both sides. However, it was not statistically significant (Table 1). The MA and AA on the right and left sides were compared regardless of gender. Only the AA was found to be statistically significantly higher on the left side (p<0.001) (Table 1).

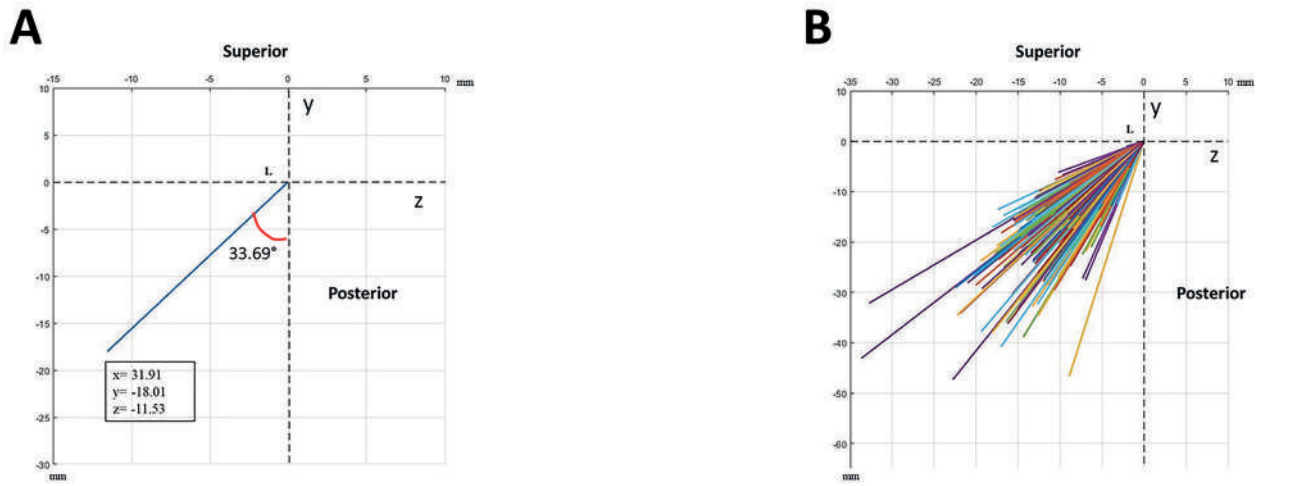

Fig. 5.- a. The mean anterior angulation and the mean coordinate values of the apex of the SP when viewed at the left SP from the lateral part; **b.** The lateral views of all the left SPs.

Table 1. The results of our study (5 to 98 years old) regarding the SP length, angulation, and coordinate values.

		Male (n=132)	Female (n=127)	Total (n=259)	P	Coordinate values (n=259)				
		Mean±SD	Mean±SD	Mean±SD				x (mm)	y (mm)	z (mm)
SP lengths anterior (mm)	Right	24.68±10.03	22.58±8.85	23.65±9.51	0.076	SP basis	Right	-40.70	0	0
	Left	24.07±9.03	22.60±8.30	23.35±8.70	0.174		Left	40.39	0	0
	P			0.437						
SP lengths lateral (mm)	Right	22.93±9.40	20.58±8.03	21.77±8.82	0.032*	SP apex	Right	-31.74	-18.90	-10.36
	Left	22.55±8.55	20.68±7.54	21.64±8.11	0.063		Left	31.91	-18.01	-11.53
	P			0.696						
Medial angulation	Right	65.33°±6.85°	63.38°±7.46°	64.37°±7.21°	0.029*					
	Left	66.16°±8.25°	62.60°±6.82°	64.42°±7.78°	<0.001*					
	P			0.923						
Anterior angulation	Right	30.63°±9.16°	29.68°±9.09°	30.16°±9.12°	0.403					
	Left	34.40°±9.27°	32.96°±8.87°	33.69°±9.09°	0.205					
	P			<0.001*						

SP: Styloid Process, * p<0.05, SD: Standard deviation

The mean coordinate values of the bases and apexes of the SPs were determined (Table 1). All SPs were displayed from the anterior (Fig. 3b) and lateral (Figs. 4b, 5b). The mean coordinate values of the bases and apexes in the anterior and lateral views of the SPs and the MA and AA values were displayed on the coordinate plane (Figs. 3a, 4a, 5a).

The mean values of the anterior and lateral SP lengths, MA and AA according to decades were obtained, and it was determined whether there was a statistically significant difference between the decades (Table 2). The MA did not differ statistically significantly between the decades on both sides (Table 2). While the AA on the right side did not differ statistically significantly between the decades, it differed statistically significantly between the decades on the left side AA. When a pairwise comparison was made between the decades, it was observed that this difference originated from the 3rd and 8th decades. A statistically significant difference was observed between the decades in all parameters related to the SP length ($p<0.05$). This difference originated from the 1st decade in all parameters (Table 2).

DISCUSSION

Eagle (1937) reported the normal length of the SP to be between 25-30 mm and accepted the SP longer than 30 mm as elongated. Eagle (1937) also stated that the elongated SP might cause Eagle syndrome. Jung et al. (2004)based on early reports, do not respect the natural variation of the SP. The aim of this study is to investigate the natural variation of the length of the SP. Knowing this variation is a prerequisite for consistent terminology in anatomy and anthropology; it is essential for the classification of the SP as elongated on panoramic radiographs (PRs accepted the SP to be elongated if it was longer than 45 mm. The most prominent symptom of Eagle syndrome is chronic pain in the head and neck region, which is caused by the elongated SP creating pressure on the adjacent structures. However, despite the elongated SP in many patients, its symptoms were not encountered (Burulday et al., 2017; Hettiarachchi et al., 2019; Kosar et al., 2011; Okur et al., 2014)which is an affective modality in the identification of ES, and a comparison with related studies. Three-dimensional (3D.

Knowing the SP length is important for the diagnosis of Eagle syndrome. However, it is not sufficient to know only the SP length, because the deviations of the SP also lead to Eagle syndrome by affecting the adjacent structures. It has been reported that although the SP has normal dimensions, it can be palpated in the tonsillar fossa as a result of its medial deviation (Frommer, 1974). Furthermore, lateral deviation causes compression in the external carotid artery, and posterior deviation causes compression in cranial nerves IX, X, XI, and XII. Anterior deviation irritates the mucosa and creates pressure on vital structures in the tonsillar region (Mazzetto et al., 2013; Piagkou et al., 2009). Therefore, studies investigating the medial and anterior angulation of the SP in addition to its length have been conducted in asymptomatic individuals (Burulday et al., 2017; Kosar et al., 2011). In the present study, the coordinates of the basis and apex of the SP were determined, in addition to examining the above-mentioned parameters. These coordinates will demonstrate with which structures the apex of the SP is closely related, and will provide more detailed information about the probability of its influencing the adjacent structures.

Multi-slice CT and 3D-CT are among the best imaging modalities to evaluate the SP length (Okur et al., 2014). 3D-CT was reported to be the most reliable imaging method to determine the SP length and MA, and to investigate the relationship between the SP and adjacent structures (Pokharel et al., 2013). Considering that there are clinicians using imaging methods other than 3D-CT, it is thought to be more useful to measure the SP length separately from the anterior and lateral sides.

Ekici et al. (2013) and the distribution of the SP lengths in different age and sex groups using MDCT. MDCT scans were performed in 805 patients (401 males, 404 females found a higher mean SP length in males than in females ($p<0.001$) (Table 3). They determined the mean SP length to be 30.7 mm in the 4th decade, 32.9 mm in the 5th decade, 32.1 mm in the 6th decade, and 32.6 mm in the 7th decade. Cullu et al. (2013) found the SP length in multidetector computed tomography

(MDCT) images to be 28.5 mm in the 4th decade and 28.2 mm in the 5th decade. The results of the present study are smaller than the results obtained by Ekici et al. (2013)and the distribution of the SP lengths in different age and sex groups using MDCT. MDCT scans were performed in 805 patients (401 males, 404 females and Cullu et al. (2013). This situation may be due to different imaging methods and measurement locations.

The results obtained by Custodio et al. (2016) regarding the lateral SP length in the skull are presented in Table 3. The results of the current study regarding the lateral SP length are consistent with the above-mentioned lateral measurement results. This may be since 3D-CT imaging is the imaging method closest to reality. Shayganfar et al. (2018) reported in their study that the SP length varied between 4.1-57 mm on the right

Table 2. The mean values of the SP length and angulation according to age groups (decade) and genders.

Decade	Gender	N	SP lengths anterior (mm)		SP lengths lateral (mm)		Medial angulation (°)		Anterior angulation (°)	
			Right	Left	Right	Left	Right	Left	Right	Left
	Male	11	13.33±6.94	14.54±9.25	12.03±6.34	13.24±8.52	62.60±10.59	64.92±13.29	32.05±14.30	35.54±15.14
5-10	Female	7	13.20±7.73	16.58±4.46	11.47±6.66	14.42±4.32	53.75±8.41	57.15±6.06	41.07±17.49	25.34±7.11
	Mean	18	13.28±7.03	15.33±7.64	11.81±6.27	13.70±7.04	59.16±10.52	61.90±11.49	35.55±15.77	31.57±13.37
	Male	23	24.96±10.73	24.43±8.74	23.16±10.07	22.80±8.35	65.28±5.82	65.99±9.25	28.16±8.59	31.78±9.76
11-20	Female	23	20.95±10.03	21.56±9.50	18.92±9.02	19.54±8.61	64.03±9.26	61.92±6.54	30.31±10.69	31.56±8.50
	Mean	46	22.96±10.47	22.99±9.14	21.04±9.69	21.17±8.55	64.65±7.67	63.96±8.18	29.24±9.65	31.67±9.05
5-20 Total		64	20.23±10.53	20.84±9.35	18.45±9.76	19.07±8.78	63.11±8.84	63.38±9.18	31.02±11.91	31.64±10.33
	Male	5	25.09±11.02	22.94±11.61	23.31±10.72	21.69±11.23	64.27±7.48	68.19±8.04	28.23±6.68	32.48±9.67
21-30	Female	6	25.69±9.60	24.81±7.98	23.22±8.45	22.86±7.09	64.53±6.68	66.78±5.03	21.90±7.84	23.02±6.16
	Mean	11	25.41±9.73	23.96±9.31	23.26±9.04	22.33±8.72	64.41±6.69	67.42±6.25	24.78±7.71	27.32±8.99
	Male	14	25.40±7.56	25.90±9.96	23.61±6.63	24.19±8.65	66.91±4.85	67.21±6.17	27.40±7.65	30.56±8.17
31-40	Female	19	21.41±5.03	19.85±4.40	19.90±4.71	18.28±3.97	66.02±6.68	64.00±8.43	28.62±6.81	32.54±8.90
	Mean	33	23.10±6.44	22.42±7.77	21.47±5.81	20.78±6.93	66.40±5.91	65.36±7.62	28.10±7.09	31.70±8.52
	Male	18	25.71±6.78	22.73±6.76	23.91±6.24	21.60±6.37	65.22±6.82	68.12±5.14	32.89±7.41	36.34±6.80
41-50	Female	20	25.23±11.14	26.33±12.76	23.04±10.03	24.16±11.26	63.65±4.61	64.21±6.55	27.14±6.71	32.53±5.49
	Mean	38	25.45±9.22	24.62±10.39	23.45±8.35	22.95±9.24	64.39±5.74	66.06±6.17	29.86±7.53	34.34±6.36
	Male	23	24.11±8.41	24.48±9.74	22.58±7.83	22.92±9.63	66.09±5.90	64.12±9.60	33.43±9.45	36.50±10.14
51-60	Female	11	23.78±9.98	23.92±5.43	21.60±8.56	21.79±4.62	62.77±6.42	61.93±5.71	31.74±5.18	34.38±5.99
	Mean	34	24.00±8.79	24.30±8.50	22.26±7.96	22.56±8.28	65.02±6.18	63.41±8.51	32.88±8.26	35.81±8.97
	Male	16	28.47±11.20	27.22±8.31	26.62±10.40	25.72±7.90	67.44±4.67	67.95±5.99	27.49±5.64	33.14±7.50
61-70	Female	13	24.36±5.41	24.46±6.25	22.31±5.24	22.34±5.97	63.44±6.11	61.18±7.12	28.67±7.53	33.36±9.83
	Mean	29	26.63±9.17	25.98±7.46	24.69±8.63	24.20±7.18	65.65±5.64	64.92±7.25	28.02±6.46	33.24±8.46
	Male	13	27.45±12.09	24.79±5.14	25.78±11.98	23.26±4.77	65.22±7.16	65.98±7.45	32.48±12.07	37.04±7.35
71-80	Female	10	25.35±9.76	23.44±8.19	22.82±9.08	21.65±7.48	61.12±7.92	61.37±6.86	30.94±7.99	40.33±7.07
	Mean	23	26.54±10.95	24.20±6.50	24.49±10.69	22.56±5.99	63.43±7.61	63.98±7.41	31.81±10.31	38.47±7.26
	Male	4	27.84±4.48	30.15±5.98	24.79±3.45	28.27±5.27	60.64±14.93	67.99±10.19	33.83±7.92	34.94±7.33
81-90	Female	15	22.06±7.33	21.88±6.52	20.27±6.78	20.35±6.22	64.47±7.78	63.31±6.75	30.72±7.90	37.24±10.63
	Mean	19	23.28±7.14	23.62±7.14	21.22±6.43	22.01±6.76	63.66±9.32	64.30±7.52	31.38±7.79	36.75±9.89
	Male	5	23.11±16.38	25.59±11.97	20.82±14.41	23.33±11.07	62.31±7.75	60.42±4.70	31.93±7.41	36.57±7.39
91-98	Female	3	21.78±3.87	20.69±4.70	19.90±4.19	18.99±4.17	64.03±7.79	61.87±2.69	24.73±6.07	34.13±13.93
	Mean	8	22.61±12.57	23.76±9.73	20.48±11.13	21.70±8.95	62.96±7.24	60.96±3.90	29.23±7.47	35.66±9.39
21-98 Total		195	24.78±8.90	24.18±8.33	22.87±8.22	22.48±7.71	64.79±6.56	64.76±7.25	29.88±8.02	34.37±8.56
5- 98 Total		259	23.65±9.51	23.35±8.70	21.77±8.82	21.64±8.11	64.37±7.21	64.42±7.78	30.16±9.12	33.69±9.09
P a			<0.001 b	0.004 b	<0.001 b	0.001 b	0.377	0.474	0.107	0.005 c

[a] Comparison of all decades, [b] The difference between decades arises from the 1st decade, [c] The difference between decades arises from decades 3 and 8.

side and 7-62 mm on the left side (age range 12-75). In our study, the SP length was determined to be between 2.12-61.02 mm on the right side and 2.35-60.65 mm on the left side (age range 5-98). The reason for this small difference between the study carried out by Shayganfar et al. (2018) and our results may be that the samples in our study started from a younger age.

In Table 3, differences between the results of the studies conducted on the SP length in the Turkish population suggest that the effect of ethnicity on the SP length is weak, although measurement and imaging methods are different. Steinmann (1968) suggested three different theories that attempted to explain the cause of the elongated SP. The first one is the "Reactive Hyperplasia Theory", in which the post-traumatic stylohyoid ligament continues to ossify from the end of the SP. The second theory is the "Reactive Metaplasia Theory", in which the stylohyoid ligament ossifies with a traumatic stimulus. The second theory is explained by the presence of ossification centers in the stylohyoid ligament. These two theories assert the ossification of the stylohyoid ligament after a traumatic event in any age group. The third theory was suggested as a simple anatomical variation with normal ossification without any trauma. This anatomic variation explains the ossification observed in children and young people who have not experienced any trauma.

Table 3. Comparison of the results of this study with the results of other studies.

Authors	Study group	Population	Method		N	SP length (mm)		Medial angulation (°)		Anterior angulation (°)	
		Age				Right	Left	Right	Left	Right	Left
Balcioğlu et al. (2009)	AS	Turkish	Panoramik radyografi	M	103	25.78±5.68	25.80±5.75	-	-	-	-
		18-70		F	124	22.69±3.68	22.75±3.65				
Shayganfar et al. (2018)	AS	Iranian	MDCT	M	226	26.2±7.4	25.8±7.9	-	-	-	-
		12-75		F	177	24.5±7.2	24.6±7.8				
Hettiarachi et al. (2019)	AS	Sri Lanka	Panoramik radyografi	M	43	28.4±6.2	26.4±5.4	-	-	-	-
		20-30		F	57	25.8±4.4	24.8±5.5				
Ekici et al. (2013)	AS	Turkish	MDCT	M	404	33.2±13.2		70.5±4.2		-	-
		18-97		F	401	29.6±10.5					
Cullu et al. (2013)		Turkish	MDCT	M	98	29.2±5.6		-	-	-	-
		31-50		F	62	27.2±5.2					
Custodio et al. (2016)	-	Brazilian	Skull	LM	15	18.90±13.14	19.25±14.54	-	-	-	
		-		PM		26.04±12.65	24.98±12.94				
Vadgaonkar et al. (2015)	-	Indian	Skull	-	110	17.8±9.3	-	-	-	-	-
		-									
Yavuz et al. (2008)	-	Turkish	Towne's X- ray	-	31	28±13	26±12	-	-	21.4±7.7	18.5±8.1
		23-80									
Burulday et al. (2017)	AS	Turkish	3D-CT	-	25	16.6±9.5	17.1±8.4	65.6±5.3	67.5±4.7	-	-
		19-60									
Büyük et al. (2018)	AS	Turkish	CBCT	M	424	36.37±10.2		72.23±6.43		-	
		>18		F	576	32.75±8.82		70.34±6.61		-	
Kent et al. (2015)	AS	American	3D-CT	M	16	-		70±6		24±8	
		>18		F	14	-					
Ayyıldız et al. (2019)	ES	Turkish	3D-CT	M	14	44.45±10.08	38.09±10.94	65.13±4.13	65.18±7.14	25.24±8.30	27.79±9.72
		21-92		F	10	37.25±6.12	33.25±10.78	59.82±1.88	60.97±3.69	31.87±6.89	34.12±6.49
Our study	AS	Turkish	3D-CT	M	98	25.89±9.42	25.06±8.52	65.64±6.57	66.34±7.36	31.05±8.59	34.88±8.29
		21-98		F	97	23.65±8.24	23.28±8.08	63.92±6.47	63.16±6.81	28.70±7.25	33.85±8.84

AS: Asymptomatic, ES: Eagle syndrome, M: Male, F: Female, LM: Lateral measurement, PM: Posterior measurement

Camarda et al. (1989) explained the ossification observed in adults due to aging without trauma by the "Theory of Aging Developmental Anomaly".

In previous studies (Balcioglu et al., 2009; Buyuk et al., 2018; Shayganfar et al., 2018), similarly to our study, the anterior SP length was found to be longer in male patients than in female patients (Table 3). While no statistically significant difference was observed between genders in the present study, a significant difference was reported in the studies conducted by Büyük et al. (2018), Balcıoğlu et al. (2009), and Shayganfar et al. (2018). In our study, no statistically significant difference was observed between the anterior and lateral SP lengths on the right and left sides. Balcıoğlu et al. (2009) and Burulday et al. (2017) indicated that there was no statistically significant difference between the SP lengths on both sides, similarly to our study. The anterior and lateral SP lengths differed statistically significantly on both sides between decades (Table 2). When a pairwise comparison was made between decades, it was determined that this difference originated from the 1st decade. Although the mean in the 3rd decade was higher than that in the 2nd decade, there was no statistically significant difference between them. This situation suggests that the SP development was very fast in the 1st decade, slowed down in the 2nd decade and completed in the 3rd decade.

According to Table 3, the MA results of this study are consistent only with the results obtained by Burulday et al. (2017). Although the method employed was the same, the results obtained by Kent et al. (2015) were different from the MA results of the present study. The reason for this difference may be that the population studied was different. Although Büyük et al. (2018) and Ekici et al. (2013) conducted research with the same population as in our study, they employed different imaging methods such as cone beam computed tomography (CBCT) and MDCT, respectively. This may be the reason why the MA results of the present study differ from the results obtained by Büyük et al. (2018) and Ekici et al. (2013).

The AA acquired by Kent et al. (2015) was smaller than that in our study (Table 3). This situation may be due to a different ethnic origin. The reason for the fact that the AA found in our study was different from the AA obtained by Yavuz et al. (2008) in Table 3 may be the use of a different imaging method (Towne's X-ray) and the use of different reference lines when measuring the angulation.

It is thought that the difference between the 3rd and 8th decades in the left AA is due to the randomly collected samples evaluated in these decades. The fact that the difference in the left AA did not originate from the 1st decade (the difference in lengths originated from the 1st decade) indicates that the anterior and medial angulations did not change statistically significantly from the 1st decade.

In the study performed by Ayyıldız et al. (2019) on Eagle syndrome patients, the imaging method and measurement methods used were the same as in our study. Upon comparing the above-mentioned results with the results of our study in asymptomatic individuals, the results of the SP anterior and medial angulation were similar. However, the results of the SP anterior and lateral lengths were different (Table 3). Therefore, it is thought that the anterior and medial angulation alone cannot be sufficient for the diagnosis of Eagle syndrome, and it may be more useful to know the SP length and coordinates.

In conclusion, the fact that the present study was conducted using the 3D-CT imaging method will provide detailed and reliable information about the SP length, angulation, and coordinates. The results of this study on the SP will help clinicians dealing with the SP in determining the variational status of the SP more easily. Knowing the length, angulation, and coordinates of the SP in asymptomatic individuals will positively affect the quality of the report of radiologists who report CT images of this region in daily routine practice. Furthermore, it is important for the prevention of complications, which may be encountered during the pre-postoperative period by otorhinolaryngologists dealing with the surgery of this region, and for the guidance of the surgery.

REFERENCES

AYYILDIZ VA, SENEL FA, DURSUN A, OZTURK K (2019) Morphometric examination of the styloid process by 3D-CT in patients with Eagle syndrome. *Eur Arch Oto-Rhino-Laryngology*, 276: 3453-3459.

BALCIOGLU HA, KILIC C, AKYOL M, OZAN H, KOKTEN G (2009) Length of the styloid process and anatomical implications for Eagle's syndrome. *Folia Morphol (Warsz)*, 68: 265-270.

BAYLAN H (2017) The anatomical basis of the symptoms of an elongated styloid process. *J Hum Rhythm*, 3: 32-35.

BURULDAY V, AKGUL MH, BAYAR MULUK N, YAGDIRAN B, INAL M (2017) The importance of medial-lateral styloid process angulation/coronal plane angle in symptomatic Eagle syndrome. *Clin Anat*, 30: 487-491.

BUYUK C, GUNDUZ K, AVSEVER H (2018) Morphological assessment of the stylohyoid complex variations with cone beam computed tomography in a Turkish population. *Folia Morphol (Warsz)*, 77: 79-89.

CAMARDA AJ, DESCHAMPS C, FOREST DI (1989) Stylohyoid chain ossification: A discussion of etiology. *Oral Surg Oral Med Oral Pathol*, 67: 508-514.

CULLU N, DEVEER M, SAHAN M, TETIKER H, YILMAZ M (2013) Radiological evaluation of the styloid process length in the normal population. *Folia Morphol*, 72: 318-321.

CUSTODIO ALN, SILVA MRA, ABREU MH, ARAÚJO LRA, DE OLIVEIRA LJ (2016) Styloid process of the temporal bone: morphometric analysis and clinical ımplications. *Biomed Res Int*, 2016: 1-5.

EAGLE W (1937) Elongated styloid process. Report of two cases. *Arch Otolaryngol*, 25: 584-587.

EKICI F, TEKBAS G, HAMIDI C, ONDER H, GOYA C, CETINCAKMAK MG, GUMUS H, UYAR A, BILICI A (2013) The distribution of stylohyoid chain anatomic variations by age groups and gender: An analysis using MDCT. *Eur Arch Oto-Rhino-Laryngology*, 270: 1715-1720.

FROMMER J (1974) Anatomic variations in the stylohyoid chain and their possible clinical significance. *Oral Surg Oral Med Oral Pathol*, 38: 659-667.

HETTIARACHCHI PVKS, JAYASINGHE RM, FONSEKA MC, JAYASINGHE RD, NANAYAKKARA CD (2019) Evaluation of the styloid process in a Sri Lankan population using digital panoramic radiographs. *J Oral Biol Craniofacial Res*, 9: 73-76.

JUNG T, TSCHERNITSCHEK H, HIPPEN H, SCHNEIDER B, BORCHERS L (2004) Elongated styloid process: When is it really elongated? *Dentomaxillofacial Radiol*, 33: 119-124.

KENT DT, RATH TJ, SNYDERMAN C (2015) Conventional and 3-dimensional computerized tomography in Eagle's syndrome, glossopharyngeal neuralgia, and asymptomatic controls. *Otolaryngol - Head Neck Surg*, 153: 41-47.

KOSAR MI, ATALAR MH, SABANCIOGULLARI V, TETIKER H, ERDIL FH, CIMEN M, OTAG I (2011) Evaluation of the length and angulation of the styloid process in the patient with pre-diagnosis of Eagle syndrome. *Folia Morphol (Warsz)*, 70: 295-299.

MAZZETTO MO, ANDRADE KMD, MAGRI LV, RODRIGUES CA, WATANABE PCA (2013) Anterior and medial angulations of the styloid process in subjects with TMD: Clinical and radiographic findings. *Braz Dent J*, 24: 80-84.

OKUR A, OZKIRIS M, SERIN HI, GENCER ZK, KARACAVUS S, KARACA L, KANTARCI M, SAYDAM L (2014) Is there a relationship between symptoms of patients and tomographic characteristics of styloid process? *Surg Radiol Anat*, 36: 627-632.

PIAGKOU MN, ANAGNOSTOPOULOU S, KOULADOUROS K, PIAGKOS G (2009) Eagle's syndrome: A review of the literature. *Clin Anat*, 22: 545-558.

POKHAREL M, KARKI S, SHRESTHA I, SHRESTHA BL, KHANAL K, AMATYA RCM (2013) Clinicoradiologic evaluation of Eagle's syndrome and its management. *Kathmandu Univ Med J*, 11: 305-309.

SENER E, GURHAN C, CEYLAN N, GUNERI P (2018) Elongation or angulation of styloid process: discussion with a case report and review of the literature. *Cumhur Dent J*, 21: 396-403.

SHAYGANFAR A, GOLBIDI D, YAHAY M, NOURI S, SIRUS S (2018) Radiological evaluation of the styloid process length using 64-row multidetector computed tomography scan. *Adv Biomed Res*, 7: 85.

STEINMANN EP (1968) Styloid syndrome in absence of an elongated process. *Acta Otolaryngol*, 66: 347-356.

VADGAONKAR R, MURLIMANJU BV, PRABHU LV, RAI R, PAI MM, TONSE M, JIJI PJ (2015) Morphological study of styloid process of the temporal bone and its clinical implications. *Anat Cell Biol*, 48: 195-200.

YAVUZ H, CAYLAKLI F, YILDIRIM T, OZLUOGLU LN (2008) Angulation of the styloid process in Eagle's syndrome. *Eur Arch Oto-Rhino-Laryngology*, 265: 1393-1396.

Morphology and morphometry of the deltoid region applied to intramuscular injections

Bruna Garbin de Souza[1], Lázaro A. dos Santos[2], Lorena T. de Menezes[2], Roberto Bernardino Júnior[2], Daniela C. de Oliveira Silva[2]

[1] Course of Nursing, Faculty of Medicine, Federal University of Uberlândia, Uberlandia, MG, Brazil

[2] Department of Human Anatomy, Institute of Biomedical Sciences, Federal University of Uberlândia, Uberlandia, MG, Brazil

SUMMARY

Intramuscular injections administered in the deltoid region must be performed in the denser part of the muscle in an area below the acromion to the deltoid tuberosity. Despite being the most used region, it is the one that presents the greatest risk to the patient's integrity. Thus, the aim of this work was to analyze the morphology and morphometry of the deltoid region and to establish correlations with neurovascular structures. Thirty upper limbs of adult human cadavers were fixed in formalin solution and subsequently dissected. Parameters as length, width, thickness and distance between the neurovascular bundle and intramuscular injection point were verified using a digital caliper. It was observed that in 100% of the limbs the deltoid muscle presented three multipennate bellies. Lateral margin length (16.71 ± 1.21 cm) was significantly lower compared to that of the anterior (18.69 ± 1.84 cm) and posterior (20.14 ± 2.08 cm) margins. Anterior belly thickness (1.62 ± 0.59 cm) was lower than that of the posterior (2.03 ± 0.53 cm) and similar to that of the lateral belly (1.75 ± 0.41 cm). The total width of the muscle was 12.87 ± 1.97 cm, while the distance from the neurovascular bundle to the intramuscular injection point was 2.85 ± 1.16 cm. There was no morphometric difference between the antimeres, except for the anterior belly thickness, with higher value in the right antimere. It can be concluded that the neurovascular bundle is located in the posterior and posterolateral parts of the muscle and, therefore, within the intramuscular injection area. Thus, the most anterior part of the lateral belly and the whole anterior belly seem to be more favorable sites for administering intramuscular injections.

Key words: Anatomy – Deltoid muscle – Intramuscular injections – Nurse – Neurovascular structures

INTRODUCTION

Since the 1970s, research in nursing regarding the various forms of injections has been developed to investigate various factors, such as complications, better administration sites, procedures to reduce pain and techniques for applying intramuscular injections (Keen, 1986; Beecroft and Redick, 1989; Losek and Gyuro, 1992; Nicoll and Hesby, 2002; Coskun et al., 2016). At this time, intramuscular injections are used frequently and its safe implementation is the nurse's responsibility (Small, 2004; Coskun

Corresponding author:
Dr. Daniela Cristina de Oliveira Silva. Federal University of Uberlandia, Pará Avenue 1720, Campus Umuarama, 38400-902, Uberlandia, MG, Brazil. Phone: +55 34 3225 8475; +55 34 99171-0898. E-mail: dcosilva@ufu.br

Submitted: August 6, 2020. **Accepted:** December 16, 2020

et al., 2016). For this purpose, the anatomical knowledge, which constitutes an area of morpho-functional study, provides theoretical support for the various structures of the organism as well as its function, contributing to the success of the technique performed by health professionals (Da Silva and Vaz Vidal, 2013).

The intramuscular route is the best one of administration for antibiotics, corticosteroids and similar drugs in hospital environments, as well for vaccines in primary care centers. Intramuscular injection is chosen for situations in which the absorption rate of a drug is very slow by the subcutaneous route or very fast by the intravenous route (Hopkins and Arias, 2013; Coskun et al., 2016). When performing an injectable administration in the muscle belly, the nurse must be aware of the general factors of anatomical variation including biotype, age, sex, race and local conditions, which follow the characteristics of individual variations in the regions of clinical and therapeutic implications, such as: shape, length, width, thickness and disposition of muscle fibers (Da Silva and Vaz Vidal, 2013). Several studies indicate that intramuscular injections have disadvantages that must be considered, such as abscess formation, erythema, infiltrations in the subcutaneous tissue, embolisms and nerve injuries (Greenblatt and Allen, 1978; Valderrama and Miguel, 1981; Thomaz and Baltar, 1988; Mcivor et al., 1991; Cassiani et al., 1998). Other complications that have been reported include violent pain, radiated or not, during or immediately after the application of the medication, flushing, hematomas, nodules, paresis, paralysis or necrosis (Cassiani et al., 1998).

The main regions selected for intramuscular drug application in the patient and with the greatest clinical implication in the cranio-podalic sense are the deltoid, dorsogluteal and ventrogluteal regions, and the lateral aspect of the thigh (Da Silva and Vaz Vidal, 2013). Among these, the deltoid region is used for the administration of small volume non-irritating drugs, such as vaccines (hepatitis A and B), analgesics, antiemetics, antibiotics and antipsychotics (Mcgarvey and Hooper, 2005; Cocoman and Murray, 2008). Some authors state that administration in this region has been avoided by health professionals due to the higher percentage of complications resulting from muscle punctures when compared to other regions, in addition to its great anatomical disadvantage (Godoy et al., 2004; Meireles and Motta-Filho, 2004; Da Silva and Vaz Vidal, 2013). Other disadvantages that this region can offer to the patient include the small tissue reservoir to absorb the medication, which makes it impossible to introduce large volumes in the muscle belly; the intolerance to irritable substances; and the possibility of injuries to vascular and nervous branches that can seriously compromise their irrigation and drainage as well as the motor function of the arm (Giovani, 2006; Da Silva and Vaz Vidal, 2013).

The "deltoid" injection site is so called because it has the shape of the Greek letter "delta", which means "V-shaped triangle" (Cocoman and Murray, 2008). The main structure forming this site is a muscle of the same name, the deltoid, a thick and strong muscle, with rough texture, which covers the shoulder and forms its rounded profile. The deltoid muscle is divided in anterior and posterior semipennate parts and a middle multipennate part. The muscle parts can act separately or together. Its proximal fixation is on the lateral third of the clavicle, the acromion and the scapula spine; its distal fixation is on the deltoid tuberosity of the humerus (Moore et al., 2019).

The deltoid muscle is irrigated by the deltoid branch of the thoracoacromial artery, a wide and short trunk that bifurcates from the 2nd part of the axillary artery; and the posterior circumflex humeral artery, which originates from 3rd part of the axillary artery and crosses medially the posterior wall of the axilla through the quadrangular space. Together with the arteries, the posterior circumflex humeral and cephalic veins drain the deltoid muscle; the latter follows over the deltoid muscle along the delto-pectoral groove, between the deltoid and the pectoralis major muscles. The innervation of the deltoid muscle is done by branches of the axillary nerve, which is the terminal branch of the posterior fascicle of the brachial plexus, receiving fibers from C5 and C6; these branches are the upper

lateral cutaneous nerve of the arm, which spirals around the surgical neck of the humerus deep into the deltoid muscle, innervating the skin over the lower region of the muscle; and the anterior and posterior branches of the axillary nerve (Moore et al., 2019).

Similar to all intramuscular injections, those injected into the deltoid muscle must be performed in the densest part of the muscle. This part is located by drawing an imaginary horizontal line of two to three finger widths, 2 to 5 cm below the lower margin of the acromial process (Craven and Hirnle, 2008; Rodger and King, 2000). The injection must be applied into an imaginary triangle, whose base is the central half of this horizontal line, and the inverted apex is formed at the midpoint of the lateral aspect of the arm in line with the axilla (Kozier et al., 1993; Rodger and King, 2000).

Considering the possibility of individual anatomical variations that can result in lesions of some structures of the neurovascular bundle when intramuscular injections are administered in the deltoid region (Castellanos, 1977), morphological and morphometric investigations of this region are necessary. In that sense, morphology studies the organic forms, emphasizing the arrangement of anatomical structures belonging to each system and region of the body, while the morphometry investigates the shape variation of the organisms, through correlations between measures of distance and size of body structures (Mandarim-Lacerda, 1995).

Within this context, this research aimed to describe the morphology of the deltoid muscle in human cadavers, evidencing the shape, proximal and distal fixations (origin and insertion) and muscle fibers disposition, as well as the path and distribution of their neurovascular structures. In addition, measurements of the upper limb length, as well as the length, width and thickness of the deltoid muscle and the distance from the neurovascular bundle to the intramuscular injection point were quantified in order to establish comparisons and correlations between the different parameters analyzed, and between right and left antimeres.

MATERIALS AND METHODS

Study design and sample

The research on the morphology and morphometry of the deltoid region applied to intramuscular injections is an experimental, descriptive, quantitative and analytical study, and was performed from January to December 2019.

Thirty upper limbs of adult human cadavers of unknown sex, coming from the laboratory of human anatomy, were used and fixed in 10% formalin solution through subcutaneous, intravenous, intramuscular and intracavitary injections, and kept immersed in containers containing the same solution.

As inclusion criteria in the study, the upper limbs should be healthy, with all segments (shoulder, arm, forearm and hand) present, and the deltoid region intact, especially the deltoid muscle. Exclusion criteria involved upper limbs with missing clavicles, damaged deltoid muscles or neurovascular bundle, or any other injury to the deltoid region.

Data collection instruments

In order to proceed with morphological description and morphometric analysis, all the cadaveric pieces were dissected using a scalpel handle number 4, blades number 23 and 24, straight rat tooth tweezer (16 cm), straight serrated tweezer (16 cm), straight Metzembaum scissors (14 cm), straight Mayo Stille scissors (15 cm) and straight fine/blunt surgical scissor (15 cm).

The parameters of upper limb length as well as length, width and thickness of the deltoid muscle and the distance from the neurovascular bundle to the intramuscular injection point were measured using cotton string (number 6, thickness 4/8, raw), stainless steel pins with round plastic head (5 cm length) and a universal digital caliper, 12", 300mm, 0.01mm resolution, Zaas Precision (Tecnoferramentas Comercial, Importação e Exportação Ltda, São Paulo, Brazil). The neurovascular bundle was located using a disposable hypodermic needle (model 25x0.8mm, Labor Import) and a syringe (10 ml, Descarpack Luer Slip).

Procedures

The preparation of the anatomical pieces followed the usual dissection techniques and procedures (Rodrigues, 2010). First, the cadaver was placed in a prone position, with the arm adducted at 45º, using a wooden block. The skin and adipose tissue of the back, thoracic region and upper limb were removed; for this, a transverse incision was made on the middle third of the neck, connecting the posterior to the anterior median line. Then, two sagittal sections were performed on the posterior and anterior median lines, extending from the initial incision to the level of the xiphoid process. A fourth incision was made transversally from the posterior to anterior median line at the level of the xiphoid process. After removing the skin, the fasciae were removed and it was possible to visualize and identify the shoulder muscles.

The deltoid muscle margins were defined, with regards to the origin in the lateral third of the clavicle, acromion and scapula spine. The muscle was sectioned from the scapula spine and the acromion by using a scalpel, leaving it attached only in the clavicle. Then, the deltoid muscle was removed towards the anterior plane; the margins of the quadrangular and triangular spaces were defined and the neurovascular structures were exposed and dissected. All structures were prepared with no magnifying glasses and, when necessary, a 10-times magnifying glass was used. Once dissected, the pieces were washed in water for 24 hours in order to remove excess formaldehyde and facilitate the appreciation of the material, which was stored in water containers.

Morphological characteristics of the proximal and distal fixations, shape and topographic relationships of the deltoid muscle were described, as well as origin, path and distribution of neurovascular structures within the muscle.

Morphometric analysis was quantified according to the parameters described in Table 1. The reference points for the parameter measurements of the upper limb length (ULL - sum of arm length-AL and forearm length-FL), muscle length (ML), belly width (BW) and the distance between the neurovascular bundle and the intramuscular injection point (NBII) were marked with the aid of string and pins (Fig. 1A-F, H). Belly thickness (BT) was measured by using the pin, which was inserted deeply until reaching the humerus bone (Fig. 1G), and then, using a pen, a mark was made on it. After each measurement carried out with the string, it was placed on a flat surface, together with the pins, and thus the distance between the points was calculated using the caliper (Fig. 1I). For the BT parameter, the pin was positioned on a flat surface and the measurement was obtained with the caliper (Fig. 1J).

Table 1. Morphometric parameters obtained from the upper limb and deltoid muscle with description of the reference points for measurements.

Parameters	Reference points for measurements
ULL – upper limb length (AL + FL)	AL – arm length: distance between the acromion and the olecranon (Fig. 1A) FL – forearm length: distance between the olecranon and the styloid process of the ulna (Fig. 1B)
ML – muscle length	AML – anterior margin length: distance between the clavicle and the deltoid tuberosity (Fig. 1C) LML – lateral margin length: distance between the acromion angle and the deltoid tuberosity (Fig. 1D) PML – posterior margin length: distance between the scapular spine and the deltoid tuberosity (Fig. 1E)
BW – belly width	Distance between the anterior and posterior margins, at the midpoint of the LML measurement (Fig. 1F)
BT – belly thickness	ABT- anterior belly thickness: distance between the surface and the bone, at the midpoint between the AML and LML measurements (Fig. 1G) LBT- lateral belly thickness: distance between the surface and the bone, at the midpoint of the LML measurement (Fig. 1G) PBT- posterior belly thickness: distance between the surface and the bone, at the midpoint between the PML and LML measurements (Fig. 1G)
NBII – neurovascular bundle and intramuscular injection	Distance between the neurovascular bundle and the intramuscular injection point (Fig. 1H)

In order to locate the neurovascular bundle (NB), the deltoid posterior belly was removed and the axillary nerve, together with the posterior circumflex humeral artery and vein, were dissected (Fig. 2A). The NB reference point was obtained by crossing the needle with the aid of a syringe from the surface of the deltoid posterior belly to the point of contact with the NB (Fig. 2B).

The reference point of the intramuscular injection was located using the string, which was placed at a distance of three fingers below the lower margin of the acromion angle, forming the base of a triangle, whose apex was located at a distance of one finger above the deltoid tuberosity; the needle with the syringe was inserted in the center of this triangle. Thereafter, the distance between the NBII was measured (Fig. 1H).

Data analysis

All data were analyzed by means of descriptive and analytical statistics, using the Graph Pad Prism 6 program (San Diego, USA). In the descriptive phase, the mean, standard deviation, median and amplitude (minimum and maximum) of each parameter were analyzed; simple percentages were calculated and compared between the

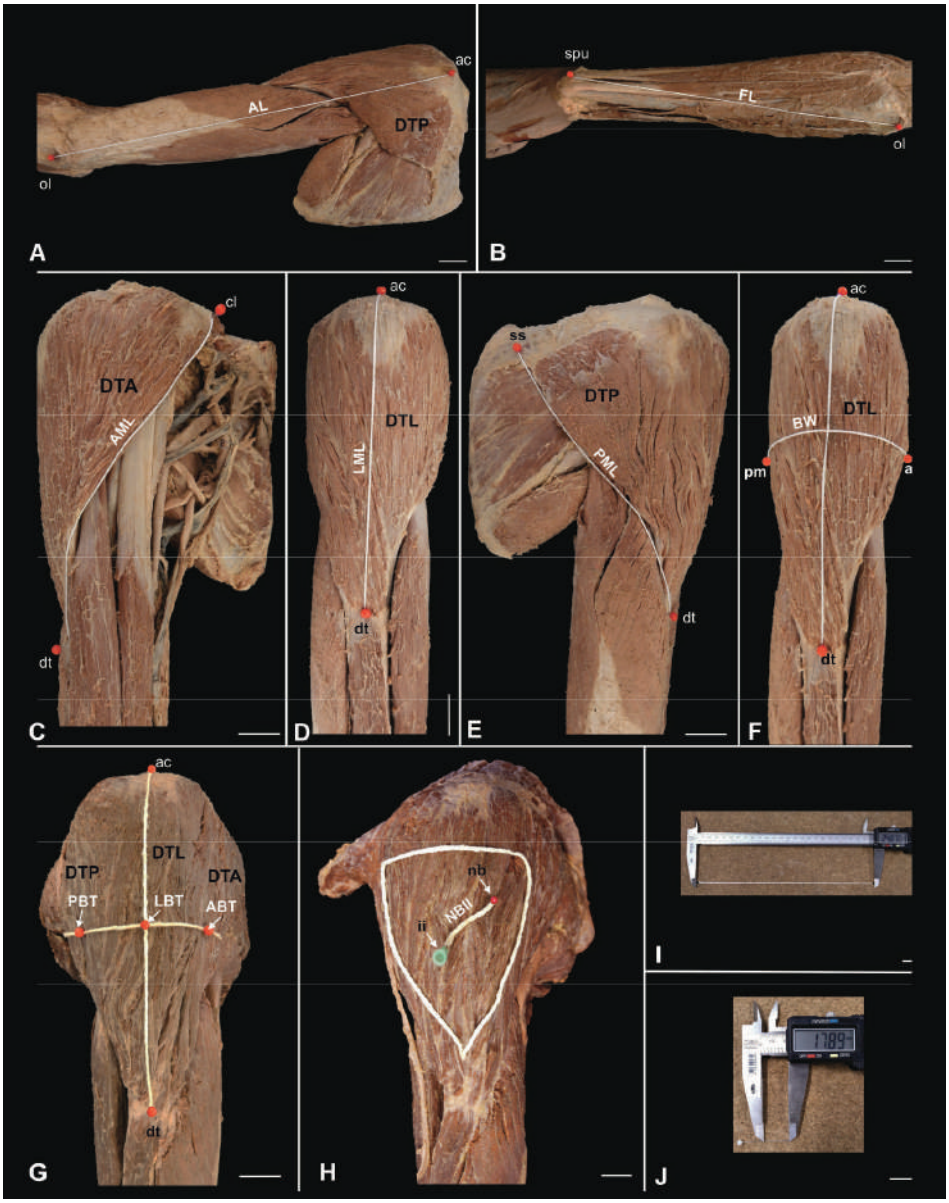

Fig. 1.- Upper limb and shoulder region showing the deltoid muscle parts (anterior part – DTA, lateral part – DTL, posterior part - DTP) and the reference points for the measurements of the analyzed parameters. A. arm length (AL), B. forearm length (FL), C. anterior margin length (AML), D. lateral margin length (LML), E. posterior margin length (PML), F. belly width (BW), G. anterior belly thickness (ABT), lateral belly thickness (LBT), posterior belly thickness (PBT), H. application area of the intramuscular injection and distance between the neurovascular bundle and the intramuscular injection point (NBII), I Caliper and string, J. Caliper and pins. ac: acromion, cl: clavicle, ss: scapula spine, nb: neurovascular bundle, ii: intramuscular injection, am: anterior margin, pm: posterior margin, ol: olecranon, spu: styloid process of the ulna, dt: deltoid tuberosity. Scale bar: A-H: 3 cm. I-J: 1 cm.

means. In the analytical phase, the mean values of muscle length and belly thickness were compared between the anterior, lateral and posterior parts using paired non-parametric tests as the Friedman test and Dunn's multiple comparison post-test. The mean values of all parameters were compared between antimeres (right and left) using Student *t* or Mann-Whitney test, when appropriate. Correlations were performed between the parameters of length, thickness and width of muscle bellies or margins, using the Pearson or Spearman correlation coefficient test, when appropriated. Differences were considered statistically significant when $p < 0.05$.

RESULTS

Regarding the morphological characteristics, in 100% of the dissected upper limbs the deltoid muscle showed bulky with coarse texture and surrounded glenohumeral articulation on all sides except inferomedially, lending the shoulder its rounded profile (Fig. 3A-C). The muscle presented three distinct parts (bellies) with a multipennate aspect, named according to the place of origin of the muscle fibers: (1) anterior or clavicular: anterior border and superior surface of the lateral third of the clavicle (Fig. 3A); (2) lateral or acromial: lateral margin and superior surface of the acromion (Fig. 3B); (3) posterior or scapular: lower edge of the crest of the scapular spine (Fig. 3C). All three parts converged inferiorly to a short tendon, which was attached to the deltoid tuberosity on the lateral aspect of the humerus. The clavicular and scapular parts showed two intramuscular septa, while the acromial part, larger than the first, showed four intramuscular septa that descended from the acromion to interdigitate with three septa ascending from the deltoid tuberosity (Fig. 3A-C). In all the pieces analyzed, the deltoid muscle was supplied by acromial and deltoid branches of the thoracoacromial artery, the anterior and posterior circumflex humeral arteries, subscapular artery and the deltoid branch of the profunda brachii artery; its innervation occurred through the axillary nerve (Fig. 3D).

Table 2 shows the morphometric analysis with descriptive statistics showing the values of mean, standard deviation, median and amplitude of the analyzed parameters obtained from the upper limb and the deltoid muscle. Regarding the length of the anterior, lateral and posterior margins, it was observed that the mean values of PML (20.14 ± 2.08 cm), AML (18.69 ± 1.84 cm) and LML (16.71 ± 1.21 cm) corresponded to 34.38%, 31.91%

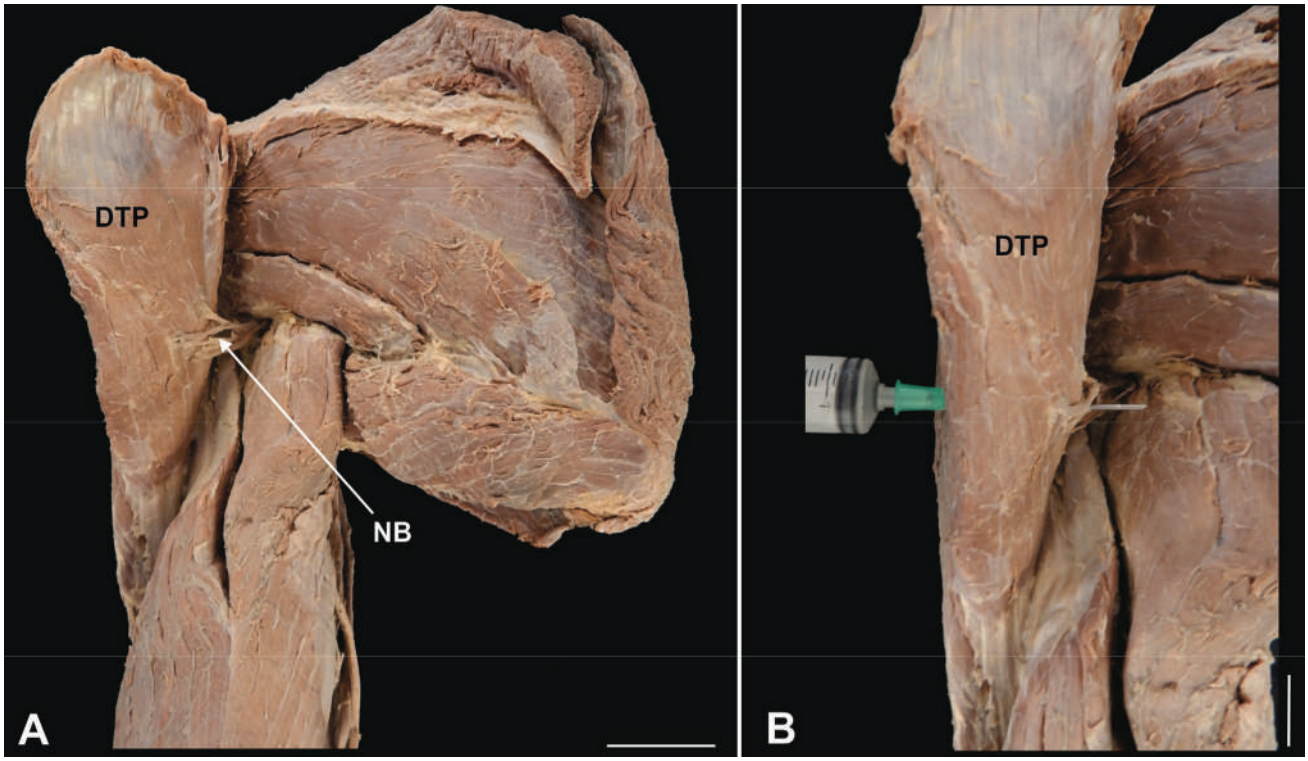

Fig. 2.- Posterior view of the upper limb and shoulder region. A. Posterior belly of the folded deltoid muscle (DTP) showing the neurovascular bundle (NB), B. Needle through the posterior belly of the deltoid muscle. Scale bar: 3 cm.

and 28.52% of the ULL value (58.57 ± 2.32 cm), respectively. Considering the thickness of the anterior, lateral and posterior bellies, the mean values of PBT (2.03 ± 0.53 cm), LBT (1.75 ± 0.41 cm) and ABT (1.62 ± 0.59 cm) represented 15.77%, 13.59% and 12.58% of the BW (12.87 ± 1.97 cm), respectively. The distance from the neurovascular bundle to the intramuscular injection point (NBII) showed a mean value of 2.85 ± 1.16 cm, ranging between 0.63 and 5.11 cm (Table 2).

Figure 4 shows the analytical statistics with comparison of the mean values of the length and thickness morphometric parameters of the deltoid muscle. The mean value of LML (16.71 cm ± 1.21 cm) was significantly lower compared to that of AML (18.69 cm ± 1.84 cm, $p < 0.01$) and PML (20.14 cm ± 2.08 cm, $p < 0.001$), with no significant difference between the AML and PML values (Fig. 4A). On the other hand, the mean value of ABT (1.62 cm ± 0.59 cm) was statistically lower than PBT (2.03 cm ± 0.53 cm, $p < 0.001$) and similar to LBT (1.75 cm ± 0.41 cm) values, with no significant differences between LBT and PBT values (Fig. 4B).

Comparison of the mean values of all morphometric parameters obtained from the upper limb and the deltoid muscle between the right and left antimeres is shown in Fig. 5. Statistically significant difference was observed only between the mean value of the right and left ABT ($p = 0.0433$) (Fig. 5C). For the other parameters, there were no significant differences ($p > 0.05$).

Correlations between the selected parameters are shown in Table 3. A positive correlation was found only between the parameters ULL and LML (r: 0.4661, $p = 0.0288$), BW and ABT (r: 0.3973,

Table 2. Descriptive statistics showing the mean, standard deviation (SD), median and amplitude (minimum and maximum) of the morphometric parameters obtained from the upper limb and the deltoid muscle.

Parameters	Mean ± SD	Median	Minimum	Maximum
ULL	58.57 ± 2.32	58.74	53.82	64.14
AML	18.69 ± 1.84	18.58	14.69	22.05
LML	16.71 ± 1.21	16.64	13.45	19.23
PML	20.14 ± 2.08	19.89	16.91	24.38
BW	12.87 ± 1.97	12.79	8.29	18.39
ABT	1.62 ± 0.59	1.89	1.05	3.34
LBT	1.75 ± 0.41	1.79	0.84	2.91
PBT	2.03 ± 0.53	1.47	0.79	3.22
NBII	2.85 ± 1.16	2.67	0.63	5.11

ULL: upper limb length, AML: anterior margin length, LML: lateral margin length, PML: posterior margin length, BW: belly width, ABT: anterior belly thickness, LBT: lateral belly thickness, PBT: posterior belly thickness, NBII: distance from the neurovascular bundle to the intramuscular injection point. Values expressed in centimeters (cm).

Table 3. Correlation between the morphometric parameters obtained from the upper limb and the deltoid muscle.

Parameters	r value	p value		Parameters	r value	p value
ULL x AML	0.3192	0.1476		LML x LBT	0.0711	0.7088
ULL x LML	0.4661	0.0288*		NBII x ULL	0.1383	0.5194
ULL x PML	-0.0045	0.9841		NBII x AML	0.0594	0.8206
BW x AML	-0.1430	0.5109		NBII x ABT	0.5275	0.0081*
BW x LML	0.1565	0.5879		NBII x LML	-0.1849	0.3871
BW x PML	-0.4867	0.8667		NBII x LBT	-0.0451	0.8339
BW x ABT	0.3973	0.0328*		NBII x PML	0.2479	0.2429
BW x LBT	0.2656	0.1637		NBII x PBT	0.1338	0.5330
BW x PBT	0.2073	0.2805		NBII x BW	0.3713	0.0741

ULL: upper limb length, AML: anterior margin length, LML: lateral margin length, PML: posterior margin length, BW: belly width, ABT: anterior belly thickness, LBT: lateral belly thickness, PBT: posterior belly thickness, NBII: distance from the neurovascular bundle to the intramuscular injection point. r: Pearson or Spearman correlation test. * $p < 0.05$.

p = 0.0328) and NBII and ABT (r: 0.5275, p = 0.0081) (Fig. 6). All other parameters showed no significant correlation (p > 0.05).

DISCUSSION

In this study, the morphology and morphometry of the deltoid region of human cadavers, as well as the path and distribution of its neurovascular structures were described and analyzed. In addition, this is a pioneer study for measuring the distance from the neurovascular bundle to the intramuscular injection point. Therefore, this research demonstrates relevant information regarding the anatomical and morphometric dimensions of the deltoid muscle in order to facilitate the revision of the intramuscular injection technique, resulting in greater success and less adversity.

The present work showed a bulky deltoid muscle, with a coarse texture, covering the dorsal, ventral and lateral parts of the shoulder joint and presenting three distinct bellies (anterior, lateral and posterior) with multipennate aspect. Moore et al. (2019) support these results, but describe the anterior and posterior parts as semipennate, and the lateral part as multipennate. The distal fixation of the deltoid muscle at deltoid tuberosity as observed in the present study is in agreement with that found by Moore et al. (2019) and Standring (2015).

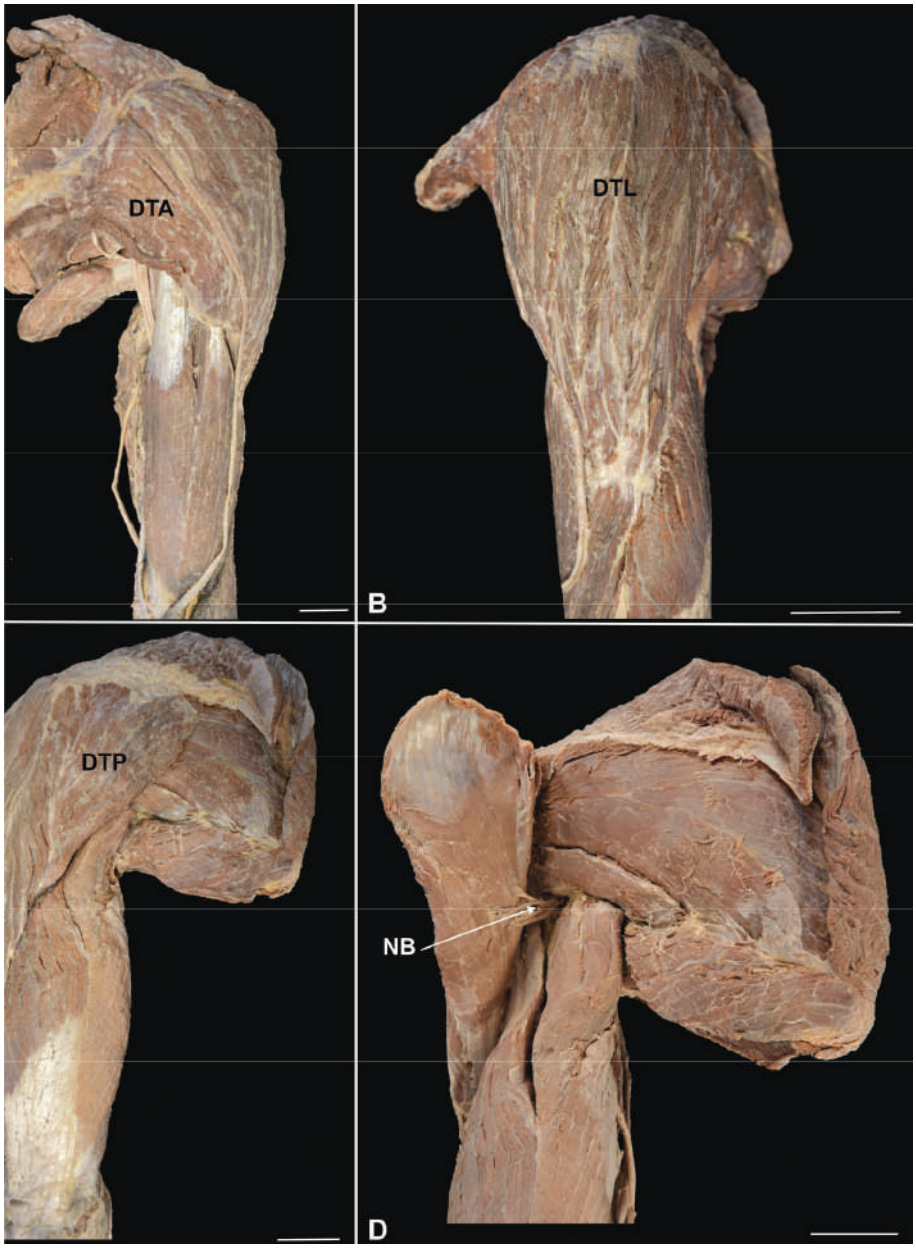

Fig. 3.- Left upper limb showing the deltoid muscle. A. Anterior view, B. Lateral view, C. Posterior view, D. Posterior view - folded deltoid muscle. DTA: Anterior or clavicular part, DTL: Lateral or acromial part, DTP: Posterior or spinal part, NB: Neurovascular bundle. Scale bar: 3 cm.

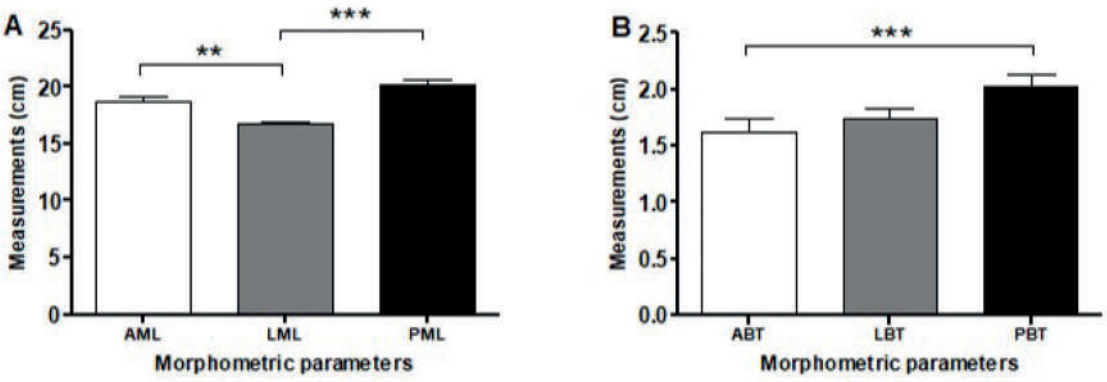

Fig. 4.- Comparison of the mean values (cm) of the length (A) and thickness (B) morphometric parameters of the deltoid muscle. AML: anterior margin length, LML: lateral margin length, PML: posterior margin length, ABT: anterior belly thickness, LBT: lateral belly thickness, PBT: posterior belly thickness. ** $p < 0.01$; *** $p < 0.001$. (Friedman test and Dunn's multiple comparison post-test).

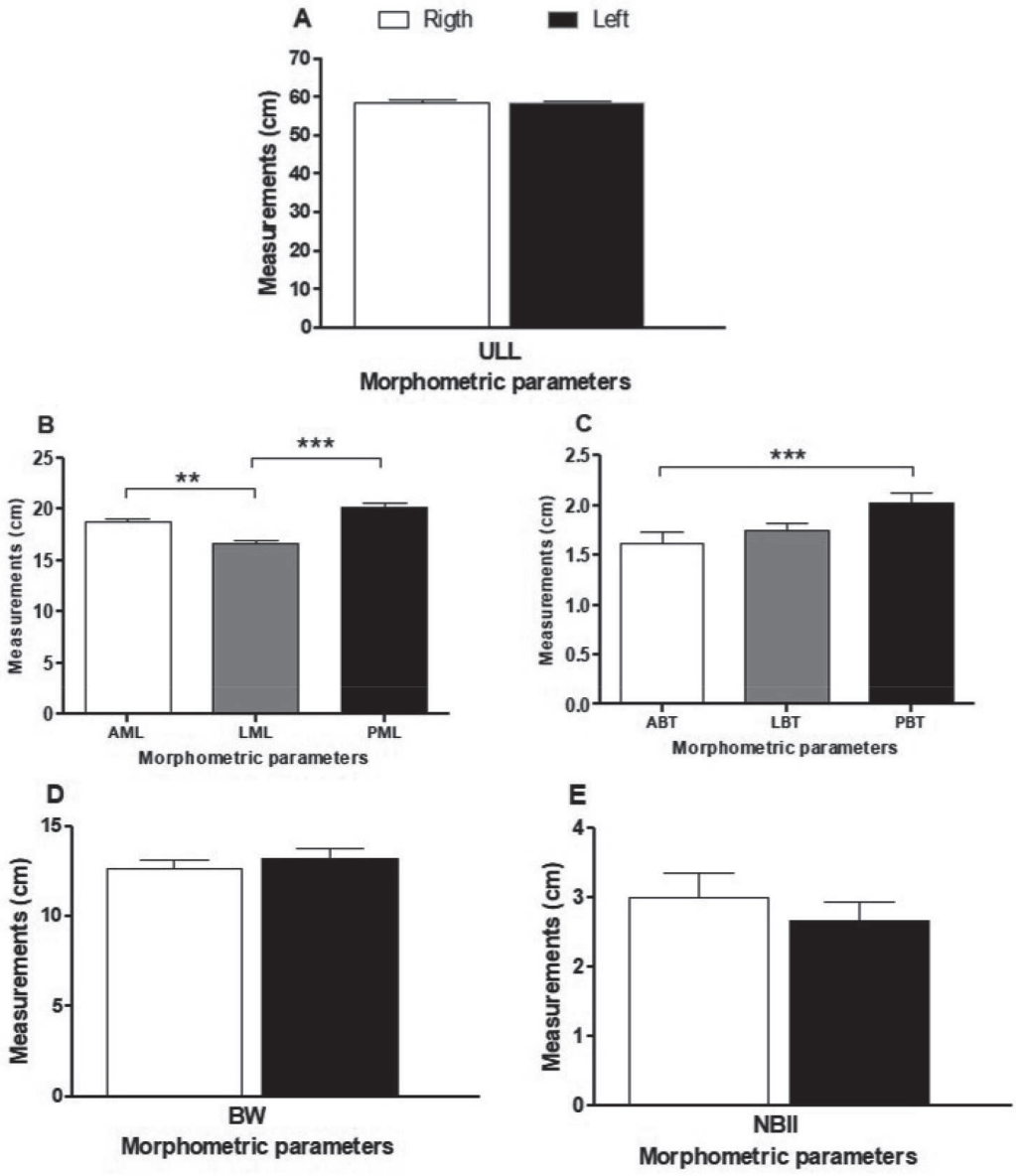

Fig. 5.- Comparison of the mean values (cm) of the morphometric parameters obtained from the upper limb and the deltoid muscle between the right and left antimeres. A. ULL: upper limb length, B. AML: anterior margin length, LML: lateral margin length, PML: posterior margin length, C. ABT: anterior belly thickness, LBT: lateral belly thickness, PBT: posterior belly thickness, D. BW: belly width, E. NBII: distance from the neurovascular bundle to the intramuscular injection point. * $p = 0.0433$ (Student t test).

Regarding the irrigation and innervation of the deltoid muscle, the same pattern as described by Standring (2015) was found, with participation of the acromial and deltoid branches of the thoracoacromial artery, the anterior and posterior circumflex humeral arteries, the subscapular artery and the deltoid branch of the profunda brachii artery, and the axillary nerve. However, other authors have proposed the irrigation only through the deltoid branch of the thoracoacromial artery and the posterior circumflex humeral artery (Moore et al., 2019).

Although variations and anomalies of the deltoid muscle are not common, Kayikcioglu et al. (1993) reported a bilateral separation of posterior fibers by a fascia that has not been previously described. The continuation of the deltoid muscle fibers in the trapezius muscle, the fusion with the pectoralis major muscle and the presence of additional slips in the vertebral margin of the scapula, infraspinatus fascia and the axillary margin of the scapula are the commonly reported variations of the deltoid muscle (Standring, 2015). In the present study, there was no variation in the deltoid muscle in relation to its morphology.

The morphometric description of the deltoid region has seldom been investigated. In this research, the descriptive analysis showed that the posterior margin length of the deltoid muscle represented the majority of the upper limb length and the smallest portion was attributed to the lateral margin length, while the anterior one showed an intermediate value. These dimensions can be explained anatomically by the points of proximal fixation of the deltoid muscle, that is, in the anterior margin and superior surface of the lateral third of the clavicle (AML), lateral margin and adjacent superior surface of the acromion (LML) and lower edge of the scapular spine crest (PML), as described elsewhere (Moore et al., 2019; Standring, 2015; Gardner et al., 1988).

Considering the mean values of deltoid belly thickness, it was found that the posterior one represented the most part of the belly width, suggesting that this analysis is related to the action of the deltoid muscle and the specific functions of the clavicular (anterior), acromial (lateral) and scapular (posterior) fibers. According to Standring (2015), the posterior fibers act with the latissimus dorsi and teres major muscles when pulling the arm back and turning it laterally, which seem to be intense and more frequent movements, in comparison to the anterior fibers that assist the pectoralis major muscle to pull the arm forward and rotate it medially, while the acromial fibers, aided by the supraspinatus muscle, abduct the arm until the joint capsule is tensioned.

The mean value (2.85 cm) of the distance from the neurovascular bundle to the intramuscular injection point (NBII) towards the posterior part, and often in the posterolateral part of the deltoid muscle, indicates that the neurovascular bundle is located within the region of application of the intramuscular injection. According to Kozier et al. (1993) and Rodger and King (2000), this region represents an imaginary triangle, whose base is an imaginary horizontal line of two to three finger widths, 2 to 5 cm below the lower margin of the acromial process, and the apex is formed inverted at the midpoint of the arm lateral face in line with the axilla.

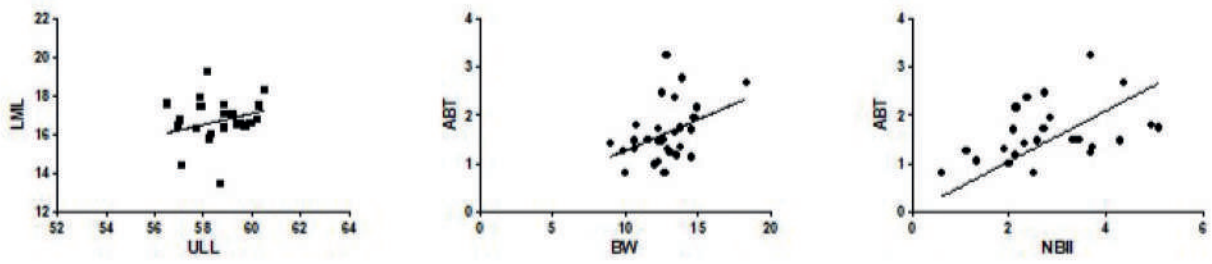

Fig. 6.- Dispersion curve and correlation between the morphometric parameters obtained from the upper limb and the deltoid muscle. ULL: upper limb length, LML: lateral margin length, BW: belly width, ABT: anterior belly thickness, NBII: distance from the neurovascular bundle to the intramuscular injection point. (Pearson or Spearman correlation test).

Next, the morphometric parameters of the muscle length and belly thickness regarding the anterior, lateral and posterior parts of the muscle deltoid were compared. The significantly lower mean value of the lateral margin length compared to anterior and posterior ones can be explained by anatomical muscle format, which is a curved triangle in shape of the Greek letter delta (Testut and Latarjet, 1979; Standring, 2015) with the shortest length between the proximal and distal fixation located laterally, and the longest lengths in the anterior and posterior parts of the muscle. On the other hand, the mean value found for the anterior belly thickness, which was significantly lower than posterior one, suggests that the anterior part of the deltoid muscle is less functionally required compared to the posterior one, while the lateral part acts equal to the anterior and posterior ones. This analysis implies that the ideal place for the application of intramuscular injection should be the posterior part, as it presents greater thickness; however, the neurovascular bundle was found in this region. Therefore, it is not recommended to consider only the muscle thickness parameter to choose the best site for the intramuscular injection.

When comparing the mean values of all analyzed parameters between the right and left antimeres, the significant difference found only for the anterior belly thickness, with a higher value on the right antimere, can be explained by the fact that a large part of the world population is right-handed and, therefore, making more use of the right upper limb for routine tasks. Thus, it can be inferred that when intramuscular injections are administered in the anterior belly of the deltoid muscle, the most appropriate side would be on the right antimere, as it is thicker, while for injection in the other muscle bellies, there is no preference on the side.

In this research, possible correlations between some parameters were also examined. The positive correlation found between upper limb length and deltoid lateral margin length can be due to the fact that these measures are on the same axis, namely, longitudinal axis. Other positive correlations verified between the anterior belly thickness *vs* the belly width or the distance from neurovascular bundle and intramuscular injection point indicate that the anterior part of the deltoid muscle could be chosen as a possible site for injection administration, despite its smaller thickness.

Taken together, the results of the present study provide an anatomical basis to confirm that, in 100% of the analyzed pieces, the neurovascular bundle is included in the recommended area for intramuscular injection in the deltoid region as previously reported (Kozier et al., 1993; Rodger and King, 2000). McGarvey and Hooper (2005) proposed that the injection site be into the center of this area; however, this region would not be the most suitable for such procedure, as it presents an imminent risk of injury to neurovascular structures.

Other studies have also shown that the deltoid region may not be ideal for administering intramuscular injection. During the practice of professionals from the nursing team of a Teaching Hospital at surgical and gynecological units, where the deltoid region is one of the most chosen regions, it was observed that 78.12% of professionals delimited it incorrectly (Godoy et al., 2003). The authors state that the possibility of improper puncture of a vessel is great in this region, due to the presence of circumflex vessels that can be reached in the case of the incorrect location of the application site. Also, another study identified a variation in the anatomical location of the axillary nerve in the deltoid region (Meirelles and Filho, 2004). Considering the potential of the sequel caused by the neural injury, the authors indicate that the intramuscular injection in the deltoid muscle should not be the site of first choice. In addition, the risk of complications with the use of this route is much greater when compared to others, such as the superolateral quadrant of the gluteal region or the lateral face of the quadriceps muscle (Meirelles and Filho, 2004).

Finally, even though the action of drugs on the deltoid muscle was not herein verified, studies have shown that during intramuscular injection procedures, inflammatory lesions of the local soft tissues derive from the caustic action of the product, its concentration, volume and, more rarely, from the mechanical action of the needle, although

the aggression to nerve endings has a similar origin. The oily drug, when penetrating the artery, generates emboli and occludes the lumen; thus, the medication in an aqueous vehicle, when gaining the lumen from the arterial and/or venous vessel, injures the endothelium and causes secondary thrombosis. Lesions of somatic and/or peri-vessels nerve endings trigger vasomotor sympathetic reflexes with vascular constriction and worsening of ischemia and/or infarction of tissues irrigated by these vessels (Duque and Chagas, 2009).

Limitations

This study was performed on formalin-fixed cadaveric upper limbs and, therefore, the effect of formalin on skin cannot be ruled out; thus, thickness of the subcutaneous tissue could not be measured and this may have influenced the morphometric parameters.

Furthermore, the body weights and sexes of most cadavers were unknown, making it impossible to estimate the fat layer in them, leading to generalized results.

CONCLUSIONS

The deltoid muscle consists of three parts (anterior, lateral and posterior); the anterior part has the smallest thickness and the lateral part, the smallest length. There is no morphometric difference between the antimeres, except for the thickness of the anterior belly with the highest value on the right side. The neurovascular bundle is located in the posterior and posterolateral part of the muscle and, therefore, within the area of intramuscular injection. Thus, considering the morphology and morphometric measurements of the deltoid muscle, the most anterior part of the lateral belly and the whole anterior belly seem to be more favorable sites for administering intramuscular injections.

ACKNOWLEDGEMENTS

We would like to thank the National Council for Scientific and Technological Development (Conselho Nacional de Desenvolvimento Científico e Tecnológico – CNPq, Brazil) for support this research.

REFERENCES

BEECROFT PC, REDICK S (1989) Possible complications of intramuscular injections on the pediatric unit. *Pediatr Nurs*, 15: 333-336.

CASSIANI SHB, RANGEL SM, TIAGO F (1998) Complicações após aplicações, por via intramuscular, do diclofenaco de sódio: estudo de um caso. *Medicina (Ribeirão Preto)*, 31: 99-105. https://doi.org/10.11606/issn.2176-7262.v31i1p99-105

CASTELLANOS BEP (1977) Estudo sobre as regiões para aplicação de injeção por via intramuscular. *Rev Esc Enferm USP*, 11: 261-324. https://doi.org/10.1590/0080-6234197701100300261.

COCOMAN A, MURRAY J (2008) Intramuscular injections: a review of best practice for mental health nurses. *J Psychiatr Ment Health Nurs*, 15: 424-434.

COSKUN H, KILIC C, SENTURE C (2016) The evaluation of dorsogluteal and ventrogluteal injection sites: a cadaver study. *J Clin Nurs*, 25: 1112-1119.

CRAVEN RF, HIRNLE CJ (2008) *Fundamentals of nursing: human health and function*, 6th ed. Lippincott Williams and Wilkins, Philadelphia.

DA SILVA PS, VAZ VIDAL S (2013) Las relaciones anatómicas involucradas en la administración de medicamentos por vía intramuscular: un campo de estudio de la enfermera. *Enferm Glob,* 12: 170-182. https://doi.org/10.6018/eglobal.12.2.143231

DUQUE FLV, CHAGAS CAA (2009) Acidente por injeção medicamentosa no músculo deltoide: lesões locais e à distância, revisão de 32 casos. *J Vas Bras*, 8: 238-246. https://doi.org/10.1590/S1677-54492009000300009

GARDNER E, GRAY DJ, O'RAHILLY R (1988) *Anatomia: estudo regional do corpo humano*. 4th ed. Guanabara Koogan, Rio de Janeiro.

GIOVANI AMM (2006) *Calculation and administration of drugs*. 10th ed. Scrinium, São Paulo.

GODOY S, NOGUEIRA MS, MENDES IAC (2004) Intramuscular medication application: knowledge analysis among nursing professionals. *Rev Esc Enferm USP*, 38: 135-142. https://doi.org/10.1590/s0080-62342004000200003

GREENBLATT DJ, ALLEN MD (1978) Intramuscular Injection - site complications. *JAMA*, 240: 542-544.

HOPKINS U, ARIAS CY (2013) Large-volume IM injections: a review of best practices. *Oncol Nurse Advisor*, 4: 32-37.

KAYIKÇIOGLU A, CELIK HH, YILMAZ E (1993) An anatomic variation of the deltoid muscle (case report). *Bull Assoc Anat (Nancy)*, 77: 15-16.

KEEN MF (1986) Comparison of intramuscular injection techniques to reduce site discomfort and lesions. *Nurs Res*, 35: 207-210.

KOZIER B, ERB G, BLAIS K (1993) *Techniques in clinical nursing*. 4th ed. Prentice Hall, London.

LOSEK JD, GYURO J (1992) Pediatric intramuscular injections: do you know the procedure and complications? *Pediatr Emerg Care*, 8: 79-81.

MANDARIM-LACERDA CA (1995) *Métodos quantitativos em morfologia*. UERJ, Rio de Janeiro.

MCGARVEY MA, HOOPER ACB (2005) The deltoid intramuscular site in the adult. Current practice among general practitioners and practice nurses. *Ir Med J*, 98: 105-107.

MCIVOR A, PALUZZIM M, MEGUID MM (1991) Intramuscular injection abscess: past lessons relearned. *N Engl J Med*, 324: 1897-1898.

MEIRELES H, MOTTA-FILHO GR (2004) Lesão do nervo axilar causada pela injeção intramuscular no deltóide: relato de caso. *Rev Bras Ortop*, 39: 615-619.

MOORE KL, DALLEY AF, AGUR AMR (2019) Anatomia orientada para a clínica. 8th ed. Guanabara Koogan, Rio de Janeiro.

NICOLL LH, HESBY A (2002) Intramuscular injection: an integrative research review and guideline for evidence-based practice. *Appl Nurs Res*, 15: 149-162.

RODGER MA, KING L (2000) Drawing up and administering intramuscular injections: a review of the literature. *J Adv Nurs*, 31: 574-582.

RODRIGUES H (2010) *Técnicas anatômicas*. 4th ed. Edson Maltez Heringer, Vitória.

SMALL SP (2004) Preventing sciatic nerve injury from intramuscular injections: literature review. *J Adv Nurs*, 47: 287-296.

STANDRING S, editor (2015) *Gray's Anatomy: the anatomical basis of clinical practice*. 41th ed. Elsevier, Amsterdam.

TESTUT L, LATARJET A (1979) Tratado de anatomia humana. 9th ed. Publishing Company Salvat, Barcelona.

THOMAZ JB, BALTAR CAF (1988) Acidente isquêmico no membro superior produzido por injeção intramuscular de penicilina benzatina. *Arq Bras Med*, 62: 175-178.

VALDERRAMA JAF, MIGUEL RE (1981) Fibrosis of the gluteus maximus: a cause of limited and adduction of the hep in children. *Clin Orthop Relat Res*, 156: 67-78.

Histological and biochemical alterations in the livers of rats treated with MSCs and placental extract against Doxorubicin as chemotherapy

Alsayed A. Abdelhady[1], Mahmoud. Diab[2], Ahmed Nabeeh[3]

[1] Anatomy and Embryology Department, Faculty of Medicine, Helwan University Cairo, Egypt
[2] Anatomy and Embryology Department, Faculty of Medicine. Al-Azhar University Cairo, Egypt
[3] Zoology Department, Faculty of Science, Al-Azhar University Cairo, Egypt

SUMMARY

The objective of this study was to analyze the potential hepatotoxicity of the doxorubicin (DOX). 50 male albino rats were treated with doxorubicin daily for 30 days. Hepatotoxicity was monitored by quantitative analysis of the serum alanine aminotransferase (ALT), Gamma-glutamyl transferase (γ-GT) activities, total protein, and albumin. The second aim of this study to investigate affected chlorpyrifose or glyphosate alone or together on lipid profile levels of cholesterol, triglyceride, low-density lipoprotein-cholesterol (LDL-C) and high-density lipoprotein-cholesterol (HDL-C) respectively, Triiodothyronine (T3), thyroxin (T4) and thyroid-stimulating hormone (TSH) were measured, and livers were collected for histopathological study for light and electron microscope. The results testify to significant elevation liver functions (ALT and GGT), as well as significant decrease in total protein and albumin level. The hormones registered a significant decrease in T3 and T4 while there is an increase in TSH. Histopathology revealed vacuolar of hepatocytes with random hepatocyte necrosis and mononuclear cell infiltration. The administration of the MSCs and placenta extract have beneficial and decrease side-effects against the deleterious changes of Doxorubicin. Histopathology revealed degeneration vacuolar of hepatocytes with random hepatocyte necrosis and mononuclear cell infiltration. The administration of the MSCs and HPL had beneficial and decrease side effects against the deleterious changes of DOX. In conclusion, results suggest a potential contribution of DOX to the etiology of some diseases, while MSCs and PE have beneficial effects, as they tends to dampen DOX toxicity in rats.

Key words: Doxorubicin – Mesenchymal Stem Cells (MSCs) – Placenta extract (PE) – Liver functions – Hormones

INTRODUCTION

Chemotherapy employs chemical agents to discontinue the growth and annihilate cancer cells even at remote sites from the source of the primary tumor. However, it does not

Corresponding author:
Ahmed Nabeeh. Zoology Department, Faculty of Science, Al-Azhar University Cairo, Egypt. E-mail: Anabeeh33@yahoo.com

Submitted: May 6, 2020. **Accepted:** January 1, 2021
Not final proof's revision by the authors

discriminate between cancer and normal cells, and eradicates not only fast-growing cancer cells but also other rapidly growing cells in the body. Chemotherapeutic drugs used to treat cancer are given to most of the people which help to sustain the completion of cancer treatment (El-Sayyad et al., 2009). In addition to devastating production of reactive oxygen species (ROS) the destructive side effects of chemotherapeutic agents have to be considered. Therefore, an escalating amount of facts suggests that the simultaneous treatment of chemotherapy and chemo-preventive agents with antioxidant action may augment the efficacy of chemotherapeutics (Aydin et al., 2011). It is very active against a wide spectrum of cancers, and is mainly used in the treatment of lymphomas, leukemia and other solid tumors like carcinoma of ovaries, breast, lung, thyroid, etc. (Gianni et al., 2007). Doxorubicin (DOX) is an anthracycline glycoside antibiotic that acquires an effective and broad-spectrum antitumor activity against a variety of human solid tumors like ovarian, breast, lung, uterine and cervical cancers, Hodgkin's disease, soft tissue, and primary bone sarcomas, as well against several other cancer types and hematological malignancies (Chang et al., 2011; Thippeswamy et al., 2011). However, its use in chemotherapy has been restricted mostly due to its varied toxicities including cardiac, pulmonary, hepatic, renal, hematological and testicular toxicity (Mohan et al., 2010). Doxorubicin as an anticancer agent can cause dose-dependent cardiotoxicity and heart failure in the long term. Rutin is a polyphenolic flavonoid that has been proved to protect hearts from diverse cardiovascular diseases (Ma et al., 2017). Doxorubicin (DOX), a prominent anticancer agent, has enjoyed considerable popularity in the last few decades because of its usefulness in the management of various forms of cancers, but its organotoxic potential (cardiotoxicity, hepatotoxicity, and nephrotoxicity) has constrained its clinical use (Lahoti et al., 2012). Hepatotoxicity is one of the main side effects associated with Doxorubicin (DOX) treatment (Mohan et al., 2011). Multipotent MSCs (mesenchymal stem cells) have shown potential in tissue regeneration in human diseases (Salem and Thiemermann, 2010). MSCs represent a rare heterogeneous subset of pluripotent stromal cells that can be isolated from a number of different adult tissues as well as BM (bone marrow), and have the potential to give rise to cells of diverse lineages. Thus, MSCs are an attractive cell source for regenerative medicine. Numerous studies have reported the beneficial effects of MSCs in tissue repair and regeneration (Quertainmont et al., 2012; Kon et al., 2012; Joyce et al., 2012). After culture expansion and in vivo administration, MSCs home and engraft in injured tissue and modulate the inflammatory response through synergistic downregulation of pro-inflammatory cytokines and up-regulation of pro-survival and anti-inflammatory factors (Cho et al., 2012). Besides their differentiating potentials, autologous bone-marrow-derived mesenchymal stem cells (BMSCs) can be isolated from the bone marrow and expanded, which makes BMSCs a conceivable source of stem cells for repairing damaged tissues. So far, BMSCs have been tested in several animal brain and heart ischemia models and have shown beneficial effects by promoting tissue repair and functional recovery (Hu et al., 2008). Placenta embedding therapy began in the 1930s. The extraction of active ingredients from the human placenta was established in the 1960s, and human placental extract (HPE) was later approved by the Food and Drug Administration for use in humans (Kwon et al., 2015). The human placenta is an organ for fetus development and an abundant reservoir of various bioactive molecules. Interest in human placenta extract (HPE) is growing, and application with a trial of HPE is widening in oriental medicine, including liver diseases (Jung et al., 2011). Human placental extract (HPE) is a source of numerous biologically active molecules and has been used clinically to treat chronic hepatitis, liver cirrhosis and other chronic diseases (Yamauchi et al., 2019). Studies using animal models have provided evidence that placenta extract improves liver function (Jung et al., 2011), and wound healing (Hong et al., 2010). In clinical situations, HPE has been prescribed to treat chronic hepatitis, liver cirrhosis, viral hepatitis, and other hepatic diseases. HPE is also used in the treatment of menopausal symptoms (Kong et al., 2008; Wu et al., 2008). Analysis of human placenta extracts (HPEs) has revealed that such extracts appear to possess antioxidant

activity. Thus, HPEs have been shown to scavenge hydroxyl radical, nitric oxide and superoxide radical; to reduce ferric iron; to chelate transition metal ions; and to prevent lipid peroxidation (Rozanova et al., 2010).

MATERIALS AND METHODS

Animals

All animals in this study were conducted under the criteria of the investigations and Ethics Committee of the Community Laws governing the use of experimental animals.

Mature male Sprague Dawley albino rats of average weights (200-220 g) (obtained from laboratory of Schistosoma Biological Supply Program -SBSP- Theodor Bilharz Research Institute) were housed in stainless steel cages with water and food ad libitum, temperature of 22±2ºC, humidity around 56% and 12 h light-dark cycle. The rats were transferred to the animal house in Zoology Department, Faculty of Science, Al-Azhar University, Cairo.

Chemicals and reagents

Doxorubicin (DOX) dose used in this study to induce hepatotoxicity was 5 mg/kg/week for 4 weeks (Oliveira et al., 2013). Mesenchymal Stem Cells Dose (5 × 106) in 200 µl platelets rich plasma (PRP) according to methods of Zahkouk et al. (2015). Placental extract (Laennec) used by liver cirrhosis patients for liver regeneration (2 ml/70 kg). This dose was converted to rat dose using conversion factors by Paget and Barnes (1964) to suit (0.4 ml/200 g) rats.

Mesenchymal Stem Cells (MSCs) preparation

MSCs were isolated according to a protocol modified from Snykers et al. (2006).

Placental extract dose

Placental extract (Laennec) used by liver cirrhosis patients for liver regeneration (2 ml/70 kg). This dose was converted to rat dose using conversion factors by Paget and Barnes (1964) to suit (0.4 ml/200 g) rats.

Rat BMSC cultures

Bone marrow-derived mesenchymal stem cells (BMSCs) were isolated from Wistar rats as previously described. In brief, BMSCs were obtained from the femoral and tibial bones of rats. Cells were flushed from the femurs and tibias of rats using a 25-gauge needle. Mononuclear cells were suspended in Dulbecco's modified Eagle's medium supplemented with 10% fetal bovine serum and plated in flasks. Cultures were maintained at 37°C in a humidified atmosphere containing 5% carbon dioxide. After 24 h, non-adherent cells were discarded, and adherent cells were washed three times with phosphate-buffered saline solution (PBS). Fresh complete medium was added and replaced every 4 days. Each primary culture was sub-cultured 1:2 when BMSCs grew to 80% confluency (Zeng et al., 2012).

Platelet-Rich Plasma (PRP) preparation

PRP preparation was carried out by adapting the protocol proposed by Sonnleitner et al. (2000).

Experimental design

50 male albino rats were randomly divided into 10 equal groups and labeled as groups 1, 2, 3, 4 and 5, each group contain 10 rats. Rats received all treatments daily via oral gavage tube along the period of the experiment. **Group 1:** Control rats; **Group 2:** 10 rats that received 4 injections of 5 mg/kg body weight (B.W) (i.p) of doxorubicin (DOX) every week. **Group 3:** 10 rats received DOX as the above regimen of group 2 and then left for one week without medication before being injected with MSCs therapy in a single dose of 5 x 106 in 200 ml (PRP)/ week MSCs per rat for 4 weeks via the caudal vein. **Group 4:** 10 rats received DOX as the above regimen of group 2 and then left for one week without medication before being injected with placental extract in a single dose of (40 µl Placental Extract) / week for 4 weeks via the caudal vein. **Group 5:** 10 rats received DOX as the above regimen of group 2 and then left for one week without medication before being injected with placental extract and MSCs therapy. The animals will observe daily for a sign of toxicity during the period of the experiment. The ten rats from each group scarified after the 30 days.

Sample collection

The rats were anesthetized through i.p injection of Thiopental Sodium (6 mg/kg) (Harms and Ojeda, 1974) on day 30 and blood samples were collected from all animals through retro-orbital venous plexus. Put into chilled non heparinized tubes, serum was obtained by centrifugation at 3000 r.p.m for 10 minutes; sera were frozen at -20°C for estimation of liver functions, and hormonal profile. Animals were sacrificed after 24 hours of the last treatment, the abdominal cavities were opened, livers were rapidly and carefully excised and all attached vessels and ligaments were trimmed off to work light microscope and transmission electron microscopy (TEM).

Histopathological examination

The liver tissues were excised and immediately fixed in 10% buffered formalin at the end of the experiment. The tissue specimen was embedded in paraffin after being dehydrated in alcohol and subsequently cleared with xylene. Five-micrometer thick serial histological sections were obtained from the paraffin blocks and stained with hematoxylin and eosin (Suvarna et al., 2013). The sections were examined under light microscope to evaluate pathological changes and photomicrographs were taken.

For transmission electron microscope (TEM) examination, small liver specimens (1 mm^3) were fixed in 2.5% glutaraldehyde solution. They were then post-fixed in 1% osmium tetroxide, dehydrated and embedded in Epon. Ultrathin sections were cut, stained with uranyl acetate and lead citrate (Johannessen, 1978) and then examined using TEM1010- EXII (Joel, Tokyo, Japan) at the electron microscopic unit at the Regional Center for Mycology and Biotechnology (RCMB), Al-Azhar University.

Biochemical parameters

Serum alanine aminotransferase (ALT) was determined according to the method of Bergmeyer et al. (1986). Gamma-glutamyl transferase (γ-GT) was determined according to the method of Rosalki et al. (1971). Total protein (TP) was determined according to the method described by Gornal et al. (1949). Albumin (ALB) was determined according to the method of Doumas et al. (1971). Serum triglycerides were determined according to the method described by Fossati and Prencipe (1982). Cholesterol level was determined according to the method described by Allain et al. (1974). The LDL-C calculations were conducted according to the formula of Wieland and Seidel (1982). Serum HDL-C level was determined according to the method described by Burstein et al. (1970) using the kit from Elitech diagnostic Co. France.

Hormonal profile

Serum T3 and T4 were determined according to the method described by Wheeler and Lazarus (1994). TSH was determined according to the method described by Beck (1986) and Caldwell et al. (1985). Using the electro-chemiluminescence immunoassay "ECLIA" is intended for use on Elecsys and Cobas e immunoassay analyzers.

Statistical analysis

The statistical package for social sciences SPSS/PC computer program (version 19) was used for statistical analysis of the results. Data were analyzed using one-way analysis of variance (ANOVA). The data were expressed as mean ± S.E. Differences were considered statistically significant at ($P < 0.05$).

RESULTS

Histopathological findings

Light microscopic findings

Group 1 - Control rats: Examined serial sections from the liver of this group revealed normal histo-morphological structures of the examined organs. Liver sections showed preserved lobular arrangement, hepatic cords orientations, portal triads structural components, sinusoids, on Kupffer cells and stroma (Fig. 1A, B).

Group 2 - Doxorubicin (anthracycline) treated rats: Liver sections revealed dramatic histopathological changes represented by moderate to massive portal and interstitial aggregations of round cells, mostly lymphocytes and plasma cells, sometime eosinophils were

included. The bile ducts appeared moderately hyperplastic and suffered chronic obstructive cholangitis. Mild portal vascular congestion and perivascular edema were seen. Multifocal hepatocellular necrosis with partial replacement by inflammatory cells and erythrocytes were seen. A moderate number of hepatocytes at the vicinity of the aforementioned lesions were atrophied, apoptotic or degenerated (Fig. 1C, D).

Group 3 - Doxorubicin (anthracycline) treated rats co-administered with MSCs. Liver sections of this group revealed mild to moderate portal and interstitial aggregations of lymphocytes. Moderate numbers of hepatocytes were degenerated (hydropic degeneration) (Fig. 1E, F).

Group 4 - Doxorubicin (anthracycline) treated rats co-administered with placental extracts: Changes in this group were little pet worth. **Liver s**ections denoted degenerative, apoptotic and necrotic changes in a moderate number of hepatocytes. Most of the degenerative changes were the hydropic type. The portal triads showed moderate aggregation of lymphocytes, plasma cells, and eosinophils. The bile ducts were mildly hyperplastic (Fig. 1G, H).

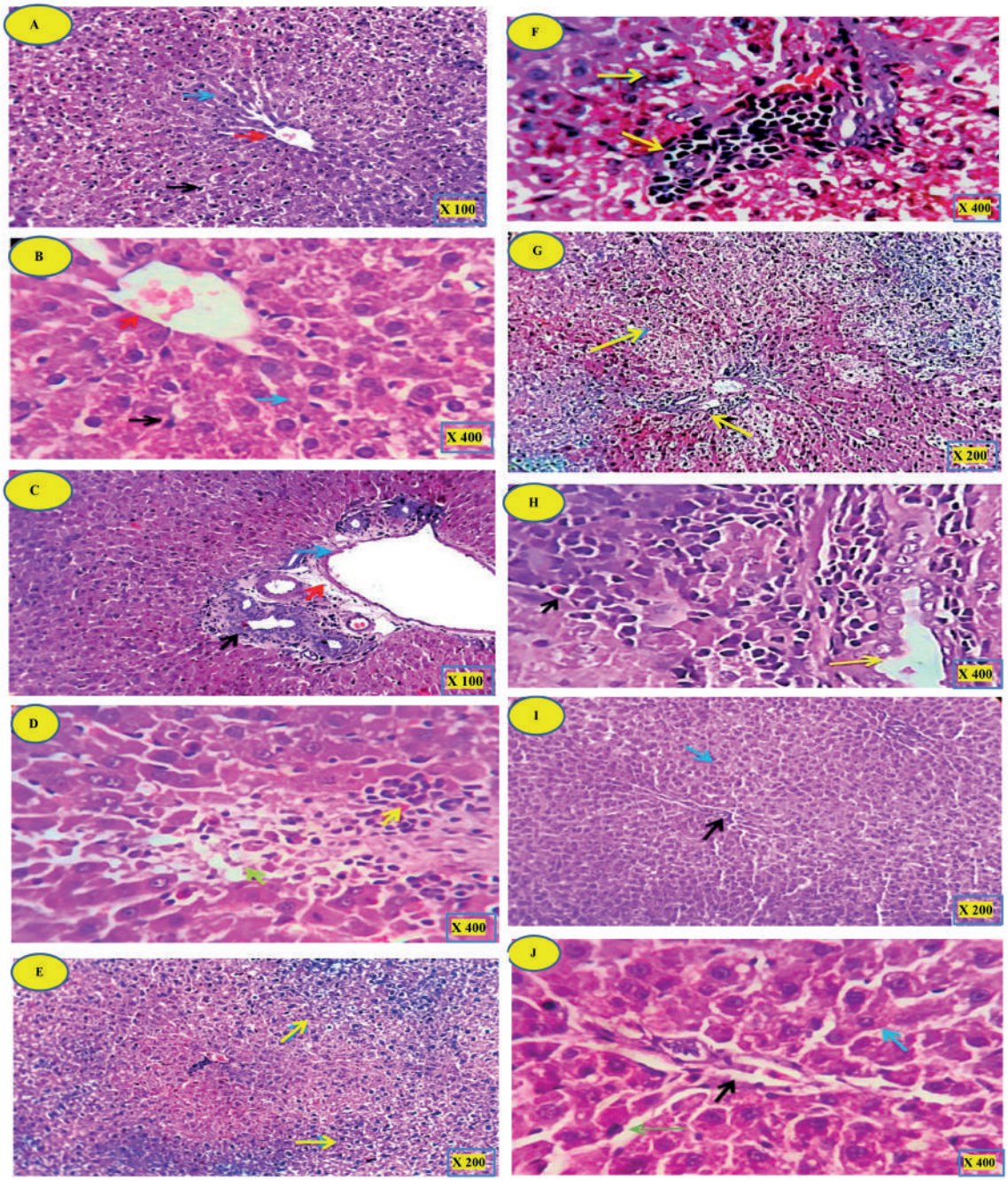

Fig. 1.- (**A, B**): Liver control rat demonstrating normal hepatocyte structure. (**C, D**): DOX group. (**E, F**): DOX + MSCs group. (**G, H**): DOX + PE group. (**I, J**): DOX + MSCs + PE. H&E staining. Magnifications: A, C = x 100; B, D, F, H, J = x 400; E, G, I = x 200. For explanation see results section.

Group 5 - Doxorubicin (anthracycline) treated rats co-administered with both MSCs and PE: Changes in this group were promising as hepatic was apparently normal with preserved histomorphological of liver lobules, hepatic cord arrangement, portal triads structures, sinusoids, and Von-Kupffer cells (Fig. 1I, J).

Electron microscopic findings

Group 1: Liver of control rats showed normal nuclear structures with preserved nuclear membrane and nucleolus. The mitochondrial contents and the rough endoplasmic reticulum beside the Golgi complex appeared normal with activated functional morphology. There were no abnormal depositions, vacuoles, electron-dense bodies or phagolysosomes (Fig. 2A, B).

Group 2. Doxorubicin treated rats: All the cellular structural contents revealed different degenerative and necrotic changes. The nucleus and nuclear membrane showed pyknosis and degenerative reactions. The mitochondria revealed dilated cisterns and membranous swelling (degenerated mitochondria). A large number of rough endoplasmic reticulum appeared lost, damaged and distorted. Intracytoplasmic phagolysosomes, endosomes and vacuoles were prominent. Electron dense bodies of different shape and size (damaged ribosomes) were encountered. The glycogen storage contents of most cells were depleted (Figs. 2C, D).

Group 3. Doxorubicin-treated rats co-administrated with MSCs: electron-micrographs from this group revealed a highly activated nucleus with normal nuclear chromatin and intact nuclear membranes. The cytoplasmic organelles represented highly active and prominent mitochondria, rough endoplasmic reticulum and Golgi apparatus. Some of the mitochondria appeared elongated. The intercellular cytoplasmic membrane, intercellular bridges, and desmosomes appeared healthy (Fig. 2E, F).

Group 4. Doxorubicin-treated rats co-administrated with placental extracts: this group showed normal nucleus, nuclear chromatin and intact nuclear membranes. The cytoplasmic organelles were run in parallel with highly active and prominent mitochondria, rough and smooth endoplasmic reticulum and dispersed electron-dense ribosomes. The intercellular cytoplasmic membrane was apparently healthy. The portal triads, hepatic sinusoids, Von-Kupffer cells, and bile canaliculi were all well preserved (Fig. 2G, H).

Group 5. Doxorubicin-treated rats co-administrated with MSCs and placental extracts: A prominent regenerative activity in hepatocytes was a characteristic feature. The nuclei, nucleoli, nuclear membranes, mitochondria, rough endoplasmic reticulum, and Golgi apparatus, all, were highly activated. The cytoplasm of most cells showed moderate amounts of stored glycogen and electron-dense dispersed ribosomes. The portal area showed dilated blood spaces and the intercellular plasma membrane was prominent (Fig. 2I, J).

Biochemical results

Doxorubicin induced hepatic damage as reflected by significantly ($p < 0.05$) elevated serum ALT and γ-GT enzymes activities when compared to control group after 30 days. Rats treated with DOX + MSCs, DOX + placental extract (PE) and DOX + MSCs + placental extract (PE) revealed a significant decrease ($p < 0.05$) when compared with intoxicated groups after 30 days (Table 2).

Data presented in Table 2 recorded that a significant decrease ($p < 0.05$) in serum total protein (TP) and albumin (ALB) level in rats intoxicated with doxorubicin when compared with control group after 30 days. Rats treated with DOX + MSCs, DOX +PE and DOX + MSCs + PE observed a significant increase ($p < 0.05$) when compared with intoxicated groups after 30 days.

Doxorubicin induced hepatic damage as reflected by significantly ($p < 0.05$) elevated serum TC, TG and LDL-L when compared to control group after 30 days. Rats treated with DOX + MSCs, DOX + PE and DOX + MSCs + PE revealed a significant decrease ($p < 0.05$) when compared with intoxicated groups after 30 days (Table 2).

Data presented in Table 2 recorded a significant decrease ($p < 0.05$) in serum HDL-C level in rats intoxicated with doxorubicin when compared with control groups after 30 days. Rats treated with DOX + MSCs, DOX + PE and DOX + MSCs +

PE observed a significant increase ($p < 0.05$) when compared with intoxicated groups after 30 days.

Doxorubicin induced significantly ($p < 0.05$) decrease serum T3 and T4 when compared to control group after 30 days. Rats treated with DOX + MSCs, DOX + PE and DOX + MSCs + PE observed a significant increase ($p < 0.05$) in serum T3 and T4 when compared with intoxicated groups after 30 days (Table 3).

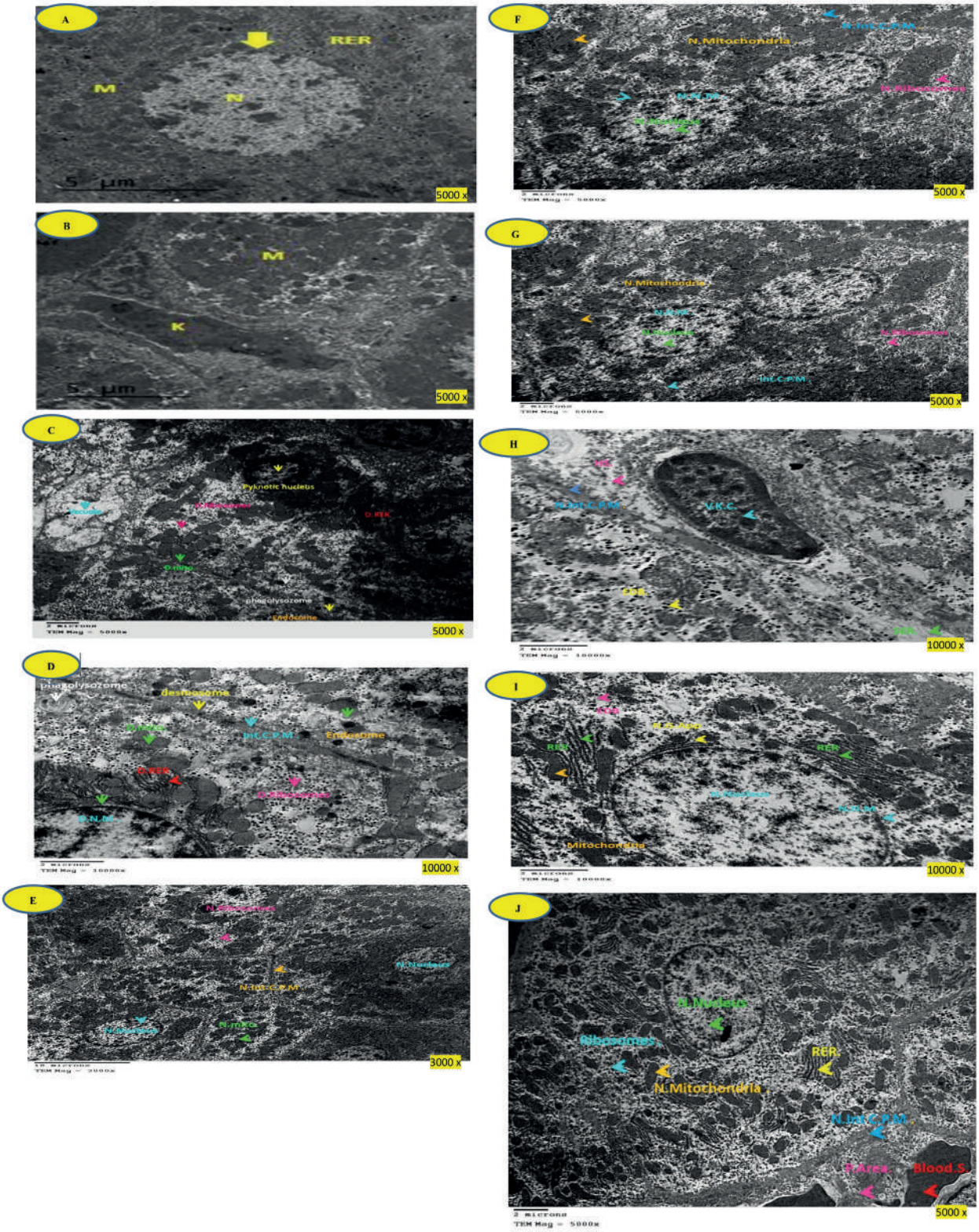

Fig. 2.- (**A, B**): Electron micrograph of liver control rat demonstrating normal hepatocyte structure. Scale bar = 5 microns, TEM magnification: x 5000. (**C, D**): DOX group. Scale bars = 2 microns. C = TEM magnification 5000x, D =TEM magnification 10000x. (**E, F**): DOX + MSCs group. Scale bars = 10 microns. E = TEM magnification 3000x, F = TEM magnification 5000x. (**G, H**): DOX + PE group. Scale bars = 2 microns. G = TEM magnification 5000x, H = TEM magnification 10000x. (**I, J**): DOX + MSCs + PE group. Scale bars = 2 microns. I = TEM magnification 10000x, J = TEM magnification 5000x. For explanation see results section.

Table 1. Serum ALT and γ-GT activity (U/L), TP and ALB level in adult male albino rats subjected to different treatment conditions for 30 days.

	days		Groups				
			Control	DOX.	DOX+ MSCs	DOX + PE	Dox + MSCs + PE
ALT (U/L)	30	Mean± S.E	27.2±1.2a	86.8±2.7b	65.6±1.9c	54.6±1.9d	46.8±3.9e
γ-GT (U/L)	30	Mean± S.E	2.08±0.06a	5.54±0.15b	3.64±0.09c	3.66±0.14c	3.04±0.08d
TP (g/dl)	30	Mean± S.E	7.09±0.12a	4.010.07b	4.76±0.12c	5.08±0.08d	6.06±0.09e
ALB (g/dl)	30	Mean± S.E	4.56±0.09a	2.08±0.02b	3.05±0.09c	2.93±0.05c	3.45±0.09d

Each value represented means of 5 records ± S.E.
a,b,c,d.e means comparison between all groups which the groups have the same letter mean there is no significance difference and which have different letter mean there is a significance change.
Dox: doxorubicin. ALT: alanine aminotransferase. γ-GT : γ-Gamma-Glutamyl Transferase. TP: total protein. ALB: albumin.

Table 2. Serum TC and TG, LDL-C and HDL-L (mg/dl) level in adult male albino rats subjected to different treatment conditions for 30 days.

	days		Groups				
			Control	DOX.	DOX+ MSCs	DOX + PE	Dox + MSCs + PE
TC. (mg/dl)	30	Mean± S.E	69.0±1.3a	99.2±1.6b	86.0±1.04c	77.4±0.92d	73.4±1.2e
TG (mg/dl)	30	Mean± S.E	44.8±1.3a	83.4±1.7b	70.0±0.84c	70.0±1.0c	63.2±1.2d
LDL-C (mg/dl)	30	Mean± S.E	15.5±1.5a	57.5±1.4b	38.1±1.5c	32.8±1.4d	22.6±1.5e
HDL-C (mg/dl)	30	Mean± S.E	44.6±0.23a	25.0±0.55b	33.9±0.48c	30.6±0.68d	38.2±1.07e

Each value represented means of 5 records ± S.E.
a,b,c,d,e means comparison between all groups which the groups have the same letter mean there is no significance difference and which have different letter mean there is a significance change.
Dox: doxorubicin. TC: total cholesterol TG: triglyceride LDL-C: low-density lipoprotein- cholesterol, HDL-C: high-density lipoprotein- cholesterol.

Table 3. Serum triiodothyronine (T3), thyroxin (T4) and thyroid-stimulating hormone (TSH) level (µg/ml) in adult male albino rats subjected to different treatment conditions for 60 days.

	days		Groups				
			Control	DOX.	DOX+ MSCs	DOX + PE	Dox + MSCs + PE
T3 (µg/ml)	30	Mean± S.E	1.39±0.01a	1.06±0.03b	1.18±0.06c	1.11±0.07d	1.27±0.10e
T4 (µg/ml)	30	Mean± S.E	5.13±0.03a	4.30±0.02b	4.60±0.03c	4.28±0.02b	4.78±0.01d
TSH (µg/ml)	30	Mean± S.E	10.11±0.02a	13.32±0.03b	12.24±0.02c	12.57±0.01d	12.02±0.02e

Each value represented means of 5 records ± S.E.
a,b,c,d,e means comparison between all groups which the groups have the same letter mean there is no significance difference and which have different letter mean there is a significance change.
Dox: doxorubicin. T3: triiodothyronine, T4: thyroxin. TSH: thyroid stimulating hormone.

Table 3 recorded a significant increase ($p < 0.05$) in serum TSH level in rats intoxicated with doxorubicin when compared with control groups after 30 days. Rats treated with DOX + MSCs, DOX + PE and DOX + MSCs + PE observed a significant decrease ($p < 0.05$) when compared with intoxicated groups after 30 days.

DISCUSSION

Histological examination

Doxorubicin (DOX) is one of the most effective anticancer drugs, but its clinical use is limited by life-threatening cardiotoxicity. Apart from its therapeutic cytotoxic effect on cancer cells through interacting DNA, Dox-induced ROS formation and oxidative damage. Both effects are particularly important in the pathogenesis of cardiac and hepatic injury (Stěrba et al., 2013; Yang et al., 2014).

DOX showed cardiotoxic and hepatotoxic effects in animals. It is known that antibiotics such as DOX (Kalender et al., 2002). For this reason, their prolonged use and excessive dosage cause death. These drugs disrupt basal metabolism by showing toxic effects, especially in liver and heart tissues (Kalender et al., 2005). Our biochemical, light and electron microscopic findings showed that Dox caused a hepatotoxic effect.

The present investigation showed many histopathological and ultrastructural abnormalities in the liver including inflammatory infiltration, hyperplasia, periportal fibrosis, marked disruption of hepatic cords and dilated blood sinusoids. A lot of hepatocytes showed karyomegaly and pyknotic nuclei indicating apoptosis.

The enzyme activation of doxorubicin begins with the drug conversion to a semiquinone free radical via one-electron reduction as reported previous studies, and such a reaction is catalyzed by several enzymes, including P-450 reductase (Bartoszek, 2002). In the present study, inflammatory cells forming granulomatous lesions and periportal fibrosis were detected after doxorubicin administration. Doxorubicin has been shown to induce accumulation of inflammatory cells (Saad et al., 2001), associated with increased activities of serum aminotransferases indicating hepatic damage (Deepa and Varalakshmi, 2003). Two different ways of free radical formation by DOX have been described. The first way implicates the formation of a semiquinone free radical by the action of several NADPH-dependent reductases that produce a one-electron reduction of the DOX to the corresponding DOX semiquinone. In the presence of oxygen, redox cycling of DOX-derived quinone–semiquinone yields superoxide radicals. In a second way, DOX free radicals come from a non-enzymatic mechanism that involves reactions with iron. For example, Fe^{3+} reacts with DOX in a redox reaction after which the iron atom accepts an electron and a Fe^{2+} DOX free radical complex is produced. This iron-DOX complex can reduce oxygen to hydrogen peroxide and other active oxygen species (Quiles et al., 2002). DOX generate superoxide anion radicals, H_2O_2 and hydroxyl radicals as a result of oxidative metabolism in rats (Doroshow, 1983). Damage at the cell level by oxidants is attenuated by antioxidant enzymes such as Superoxide dismutase (SOD), Glutathione peroxidase (GPx) and Catalase (CAT).

It has been investigated that the use of DOX results in an increased production of free radicals such as superoxide, hydroxyl radicals, and hydrogen peroxide, which have a great potential to react rapidly with lipids, which causes lipid peroxidation (Oz et al. 2005).

It is clear from the present work that the drug Doxorubicin has a toxic impact on organs especially the liver.

Doxorubicin is a very potent antitumor antibiotic. The reported acute and chronic side effects associated with doxorubicin use in clinics are the onsets of cardiotoxicity and hepatotoxicity (Kolarovic et al., 2010). In agreement with application trials on doxorubicin-induced hepatotoxicity, the present data showed that the significant increase in the activities of Aspartate Aminotransferase (AST), alkaline phosphatase (ALP) and ALT and histopathological changes in the liver were due to doxorubicin therapy. Doxorubicin toxicity is attributed to its pro-oxidant action. Many studies have described that lipid peroxidation of heart and liver cells membrane, caused by reactive oxygen species

(ROS), is the main reason for tissue damage induced by doxorubicin (Dodda et al., 2014). DOX not only increases free radical production in the tissue but also decreases its ability to detoxify reactive oxygen species.

This study has shown that the abnormal histopathological changes in the liver can be attributed to increased apoptotic widely and inflammatory response.

Results of the present study indicate that the MSCs and placental extract significantly protected DOX-induced hepatotoxicity. The dose of DOX used in this study corresponds to the dose that is currently being used in the clinical practice (Chabner et al., 2001). Electron microscopy studies showed that DOX cause pathological changes in hepatocytes. This effect was seen in mitochondria, Dox-induced toxic manifestations.

Light and electron microscopic examination of DOX/MSCs group revealed an improvement of the liver structure. Most of the hepatocytes appeared nearly like those of the control group and regained their function. The damaged hepatocytes were repaired and fibrosis was resolved, resulting in an overall improvement in liver function (Oyagi et al., 2006). The liver fibrosis was also resolved after MSCs and HPE administration. The area percentage of the collagen fibers was significantly decreased as compared to DOX-alone group. MSCs ameliorated liver fibrosis by down-regulating the profibrotic genes and up-regulating anti-fibrotic hepatic genes (Ali and Masoud, 2012). Moreover, MSCs might play an inhibition role in process of Hematopoietic stem cells (HSCs) transition from the inactive state to activated state, and induce HSCs apoptosis through the release of interleukin-10 (Dai et al., 2009). Recently, it was found that BM-MSCs reduced the expression of collagen type I (Shao et al., 2014).

Upon liver injury, the body attempts to repair the damage through increasing the expression of hepatocyte growth factor (HGF), transforming growth factor-beta (TGF-β) and other cytokines to enhance hepatocyte proliferation and initiate tissue-repairing process (Paradis et al., 2001). It was found that MSCs secrete a variety of these cytokines and growth factors, which suppress the local immune system, inhibit fibrosis and apoptosis, enhance angiogenesis and stimulate mitosis and differentiation of tissue-intrinsic stem cells (Caplan et al., 2006).

Human placental extract (HPE), which is sometimes used to promote certain functions of liver or cure certain diseases such as hepatitis and liver cirrhosis through stimulating cell proliferation, has been known to promote Interleukin 8 (IL-8) expression through in vitro and liver regeneration in the CCl_4-injured liver rat model (Jung et al., 2011).

Several bioactive molecules in HPE have been spotlighted in Western medicine as well as in Oriental medicine (Kang et al., 2007). Because the placenta supports fetal development through the synthesis of various molecules during pregnancy (Parolini et al., 2008), there are abundant biologically important factors, and some of these cytokines and growth factors are known to be essential for liver regeneration (Pal et al., 2002). Also, it has been reported that placenta extract stimulates tissue-repair process (Seo et al., 2006). These results are in agreement with Yamauchi et al. (2017), who showed that HPE ameliorates the pathology of MCD-induced NASH in mice by suppressing inflammation, oxidative stress, and fibrosis. Furthermore, we found that HPE directly suppresses endothelial cell damage. HPE could thus be an effective therapeutic agent with which to suppress progression from simple fatty liver to NASH.

Liver functions

One of the essential organs in the animal body is the liver, because it is primarily the site of elimination and deactivation of certain toxic xenobiotics. Transaminases (AST and ALT) play an important role in amino acids catabolism and biosynthesis. They are responsible for detoxification processes, metabolism and biosynthesis of energetic macromolecules for different essential functions (Seven et al., 2004).

The treatment of DOX led to an increase in ALT and γ-GT activity and a decrease in TP and ALB, which are marker enzymes in serum used in hepatic damage. Therefore, GPT elevated in

serum. These enzymes leaked to the blood stream due to peroxidative damage of DOX to the cell membrane of the liver (Burton, 1989).

On the other hand, groups treated with MSCs and placenta extract recorded decrease in ALT and γ-GT and increase in TP and ALB: this result is in agreement with Mehrabani et al. (2019), which recorded that thioacetamide (TA) leads to increase of liver functions and MSCs ameliorate effect of TA-induced model of rat fibrosis, and the treatment of liver fibrosis with BMSCs leads to a significant reduction in the number of inflammatory cells and collagen deposition in the hepatic parenchyma. Liver function tests denoted a decrease in serum: this indicated the healing effect of MSCs, as the secretion of many bioactive factors by MSCs can provide a microenvironment for the rearrangement of liver injuries (Togel et al., 2007). These factors can inhibit scarring (i.e., fibrosis) and apoptosis, promote angiogenesis and stimulate host progenitor cells for division and differentiation into functional regenerative units (Mehrabani et al., 2013). Furthermore, the trophic effects of MSCs can have prominent clinical use (Mehrabani et al., 2016).

In transplanted encapsulated human MSCs and in the mouse model of liver fibrosis, it was observed that MSC-derived soluble molecules were responsible for antifibrotic effects (Meier et al., 2015). The effect of BMSCs on hepatic fibrosis was evaluated in a TA-induced cirrhotic rat model, and the results showed that the treatment with BMSCs could attenuate hepatic fibrosis (Jang et al., 2014).

Several bioactive molecules in placenta extract have been spotlighted in Western medicine as well as in Oriental medicine (Yeom et al., 2003; Kang et al., 2007). Because the placenta supports fetal development through the synthesis of various molecules during pregnancy (Parolini et al., 2008), there are abundant biologically important factors, and some of these cytokines and growth factors are known to be essential for liver regeneration (Pal et al., 2002). Also, it has been reported that placenta extract stimulates tissue repair process (Seo et al., 2006), has therapeutic effects in chronic non-healing wounds (Shukla et al., 2004; Tiwary et al., 2006), and has anti-inflammatory effects (Sur et al., 2003). However, despite the identification of biologically active molecules and trials for several diseases, precise underlying mechanisms remain largely unknown and warrant further investigation (Uehara et al., 1995).

In agreement with Jung et al. (2011), placental extract administration could improve liver function after treated rat with CCl_4 and led to an increase in liver enzymes, since the liver is the main organ responsible for the biotransformation and subsequent detoxification of xenobiotics, the enzymes for biotransformation are critical. Therefore, we investigated the alteration of enzymes after transplantation of MSCs into the mouse liver injured by CCl_4 administration, and found a reduction in AST after injection with CCl_4, which causes increase it because of the role of MSCs (Cho et al., 2012) and placenta extract which lows from free radicals.

The present study did record a significant increase in cholesterol, triglyceride and LDL-C concentration and decrease in HDL-C concentration in rats exposed to DOX when compared to control groups, due to the fact that cholesterol is crucial for maintaining cellular homeostasis. It is a precursor for steroid hormones and a component of membrane bilayers that is essential for their integrity and to enable cell proliferation **(Simons and Ikonen, 1997).** In addition, cholesterol depletion from the cell membrane results in lipid raft internalization from the cell membrane, causing the deregulation of cellular signaling that leads to cell death **(Li et al., 2006; Yun et al., 2019).** Some cholesterol is provided by the diet, but it is primarily synthesized in the liver and distributed to cells via the bloodstream **(Kuzu et al., 2016).** On the other hands, stem cell and placenta extract induce ameliorate effect on lipid profile.

The groups treated with DOX recorded a decrease in T3, T4 and increase in TSH: these results in agreement with Olson et al., (2005), due to the fact that T3 and T4 are important regulators of metabolism and physiology of most normal tissues. Cytochrome P450 family 3A members are drug-metabolizing enzymes involved in the activation and detoxification of several drugs

(Flaqué et al., 2019), which happen in the liver, as the liver is responsible for conversion about 80 percent of T4 to T3 inside it.

Placenta extract and MSCs recorded ameliorative effect against DOX.

CONCLUSION

It could be concluded that, as indicated by biochemical and histological Changes, DOX has deleterious effects on the liver. By increasing liver functions and Apoptosis, MSC and Placental extract have protective effects against DOX-induced hepatotoxicity. Accordingly, prohibiting the use of DOX and using MSCs and Placental extract as hepatoprotective agents are highly recommended.

ACKNOWLEDGEMENTS

We deeply acknowledge Dr. Ahmed Belal Mehany, lecturer of genetic engineering, for her assistance in performing the biochemical investigations. This work was not supported by any funds from any organization.

REFERENCES

ALI G, MASOUD MS (2012) Bone marrow cells ameliorate liver fibrosis and express albumin after transplantation in CCl4-induced fibrotic liver. *Saudi J Gastroenterol*, 18(4): 263-267.

ALLAIN C, POON L, CHAN C, RICHMOND W, FU P (1974) Enzymatic determination of total serum cholesterol. *Clin Chem*, 20(4): 470-475.

AYDIN B, UNSAL M, SEKEROGLU ZA, GÜLBAHAR Y (2011) The antioxidant and antigenotoxic effects of pycnogenol® on rats treated with cisplatin. *Biol Trace Elem Res*, 142(3): 638-650.

BARTOSZEK A (2002) Metabolic activation of adriamycin by NADPH-cytochrome P450 reductase; overview of its biological and biochemical effects. *Acta Biochim Pol*, 49(2): 323-31.

BECK JR (1986) Laboratory decision science applied to chemometrics: strategic testing of thyroid function. *Clin Chem*, 32(9): 1707-1713.

BERGMEYER HU, HORDER M, REY J (1986) Approved recommendation on IFCC methods for the measurement of catalytic enzymes. Part 2: IFCC method for aspartate aminotransferase. *J Clin Chem Clin Biochem*, 24: 497-510.

BURSTEIN M, SCHOLNICK HR, MORFIN R (1970) Rapid method for the isolation of lipoproteins from human serum by precipitation with polyanions. *J Lipid Res*, 11(6): 583-595.

BURTON GW (1989) Antioxidant action of carotenoids. *J Nutr*, 119: 109-111.

CALDWELL G, GOW SM, SWEETING VW, KELLETT HA, BECKETT GJ, SETH J, TOFT AD (1985) New strategy for thyroid function testing. *Lancet*, 325(8438): 1117-1119.

CAPLAN AI, DENNIS JE (2006) Mesenchymal stem cells as trophic mediators. *J Cell Biochem*, 98(5): 1076-1084.

CHABNER BA, RYAN DP, PAZ-ARES L, GARCIACARBONEVO R, CALABRESI P (2001) Antineoplastic agents. In: Hardman JG, Limbird LE, Gilman AG (eds.) *Goodman and Gilman's the Parmacological Basis of Therapeutics*. McGraw Hill Companies Inc., USA, pp 1389-1459.

CHANG YL, LEE HJ, LIU ST, LIN YS, CHEN TC, HSIEH TY, HUANG HS, HUANG SM (2011) Different roles of p53 in the regulation of DNA damage caused by 1,2 heteroannelatedanthraquinones and doxorubicin. *Int J Biochem Cell Biol*, 43(12): 1720-1728.

CHO KA, WOO SY, SEOH JY, HAN HS, RYU KH (2012) Mesenchymal stem cells restore CCl4-induced liver injury by an antioxidative process. *Cell Biol Int*, 36(12): 1267-1274.

DAI LJ, LI HY, GUAN LX, RITCHIE G, ZHOU JX (2009) The therapeutic potential of bone marrow-derived mesenchymal stem cells on hepatic cirrhosis. *Stem Cell Res*, 2(1): 16-25.

DEEPA PR, VARALAKSHMI P (2003) Protective effect of low molecular weight heparin on oxidative injury and cellular abnormalities in adriamycin-induced cardiac and hepatic toxicity. *Chemico-Biological Interactions*, 146(2): 201-210.

DODDA D, CHHAJED R, MISHRA J (2014) Protective effect of quercetin against acetic acid induced inflammatory bowel disease (IBD) like symptoms in rats: Possible morphological and biochemical alterations. *Pharmacol Reports*, 66(1): 169-173.

DOUMAS BT, WATSON WA, BIGGS HG (1971) Albumin standards and the measurement of serum albmin with bromocresol green. *Clin Chem Acta*, 31(1): 87-96.

EL-SAYYAD HI, ISMAIL MF, SHALABY FM, ABOU-EL-MAGD RF, GAUR RL, FERNANDO A, OUHTIT A (2009) Histopathological effects of cisplatin, doxorubicin and 5-flurouracil (5-FU) on the liver of male albino rats. *Int J Biol Sci*, 5(5): 466.

EL-SHEIKH AA, MORSY MA, MAHMOUD MM, RIFAAI RA, ABDELRAHMAN AM (2010) Effect of coenzyme-q10 on Doxorubicin-induced nephrotoxicity in rats. *Adv Pharmacol Sci*, 2012.

FLAQUÉ MCD, CAYROL MF, STERLE HA, DEL ROSARIO ASCHERO M, ALBUJA JAD, ISSE B, FARÍAS RN, CERCHIETTI L, ROSEMBLIT C, CREMASCHI GA (2019) Thyroid hormones induce doxorubicin chemosensitivity through enzymes involved in chemotherapy metabolism in lymphoma T cells. *Oncotarget*, 10(32): 3051-3065.

FOSSATI P, PRENCIPE L (1982) Serum triglycerides determined colorimetrically with an enzyme that produces hydrogen peroxide. *Clin Chem Acta*, 28(10): 2077-2080.

GIANNI L, SALVATORELLI E, MINOTTI G (2007) Anthracycline cardiotoxicity in breast cancer patients: Synergism with trastuzumab and taxanes. *Cardiovasc Toxicol*, 7(2): 67-71.

GORNAL AC, BARDWILL CJ, DAVID MM (1949) Determination of serum proteins by means of the biuret reaction. *J Biol Chem*, 177(2): 751-766.

HARMS PG, OJEDA SR (1974) A rapid and simple procedure for chronic cannulation of the rat jugular vein. *J Appl Physiol*, 36(3): 391-392.

HONG JW, LEE WJ, HAHN SB, KIM BJ, LEW DH (2010) The effect of human placenta extract in a wound healing model. *Ann Plastic Surg*, 65(1): 96-100.

HU X, YU SP, FRASER JL, LU Z, OGLE ME, WANG JA, WEI L (2008) Transplantation of hypoxia-preconditioned mesenchymal stem cells improves infarcted heart function via enhanced survival of implanted cells and angiogenesis. *J Thorac Cardiovasc Surg*, 135(4): 799-808.

JOHANNESSEN JV (1978) Electron microscopy in human medicine. McGraw-Hill International Book Co., New York.

JOYCE NC, HARRIS DL, MARKOV V, ZHANG Z, SAITTA B (2012) Potential of human umbilical cord blood mesenchymal stem cells to heal damaged corneal endothelium. *Mol Vis*, 18: 547-564.

JUNG J, LEE HJ, LEE JM, NA KH, HWANG SG, KIM GJ (2011) Placenta extract promote liver regeneration in CCl_4-injured liver rat model. *Int Immunopharmacol*, 11(8): 976-984.

KALENDER S, KALENDER Y, ATES A, YEL M, OLCAY E, CANDAN S (2002) Protective role of antioxidant Vitamin E and catechin on idarubicin-induced cardiotoxicity in rats. *Braz J Med Biol Res*, 35(11): 1379-1387.

KALENDER Y, YEL M, KALENDER S (2005) Doxorubicin hepatotoxicity and hepatic free radical metabolism in rats. The effects of vitamin E and catechin. *Toxicology*, 209(1): 39-45.

KANG SS, WOO SS, IM J, YANG JS, YUN CH, JU HR (2007) Human placenta promotes IL-8 expression through activation of JNK/SAPK and transcription factors NF-kappaB and AP-1 in PMA-differentiated THP-1 cells. *Int Immunopharmacol*, 7(11): 1488-1495.

KOLAROVIC J, POPOVIC M, ZLINSKÁ J, TRIVIC S, VOJNOVIC M (2010) Antioxidant activities of celery and parsley juices in rats treated with doxorubicin. *Molecules*, 15(9): 6193-6204.

KON E, FILARDO G, ROFFI A, DI MARTINO A, HAMDAN M, DE PASQUAL L (2010) Bone regeneration with mesenchymal stem cells. *Clin Cases Miner Bone Metab*, 9(1): 24-27.

KONG MH, LEE EJ, LEE SY, CHO SJ, HONG YS, PARK SB (2008) Effect of human placental extract on menopausal symptoms, fatigue, and risk factors for cardiovascular disease in middle-aged Korean women. *Menopause*, 15(2): 296-303.

KUZU OF, NOORY MA, ROBERTSON GP (2016) The role of cholesterol in cancer. *Cancer Res*, 76(8): 2063-2070.

KWON TR, OH CT, PARK HM, HAN HJ, JI HJ, KIM BJ (2015) Potential synergistic effects of human placental extract and minoxidil on hair growth-promoting activity in C 57 BL/6 J mice. *Clin Exp Dermatol*, 40(6): 672-681.

LAHOTI TS, PATEL D, THEKKEMADOM V, BECKETT R, RAY SD (2012) Doxorubicin-induced in vivo nephrotoxicity involves oxidative stress-mediated multiple pro-and anti-apoptotic signaling pathways. *Curr Neurovasc Res*, 9(4): 282-295.

LI YC, PARK MJ, YE SK, KIM CW, KIM YN (2006) Elevated levels of cholesterol-rich lipid rafts in cancer cells are correlated with apoptosis sensitivity induced by cholesterol-depleting agents. *Am J Pathol*, 168(4): 1107-1118.

MA Y, YANG L, MA J, LU L, WANG X., REN J, YANG J (2017) Rutin attenuates doxorubicin-induced cardiotoxicity via regulating autophagy and apoptosis. *Biochim Biophys Acta (BBA)-Molecular Basis of Disease*, 1863(8): 1904-1911.

MEHRABANI D, MEHRABANI G, ZARE S, MANAFI A (2013) Adipose-derived stem cells (ADSC) and aesthetic surgery: a mini review. *World J Plast Surg*, 2(2): 65-70.

MEHRABANI D, MOJTAHEDJABERI F, ZAKERINIA M, HADIANFARD MJ, JALLI R, TANIDEH N, ZARE S (2016) The healing effect of bone marrow-derived stem cells in knee osteoarthritis: a case report. *World J Plast Surg*, 5(2): 168-174.

MEHRABANI D, KHAJEHAHMADI Z, TAJIK P, TAMADON A, RAHMANIFAR F, ASHRAF M, TANIDEH N, ZARE S (2019) Regenerative effect of bone marrow-derived mesenchymal stem cells in thioacetamide-induced liver fibrosis of rats. *Arch Razi Inst*, 74(3): 279-286.

MOHAN M, KAMBLE S, SATYANARAYANA J, NAGESHWAR M, REDDY N (2011) Protective effect of solanum torvum on doxorubicin-induced hepatotoxicity in rats. *Int J Drug Dev Res*, 3(3): 131-138.

OLSON RD, GAMBLIEL HA, VESTAL RE, SHADLE SE, CHARLIER HA, CUSACK BJ (2005) Doxorubicin cardiac dysfunction. *Cardiovasc Toxicol*, 5(3): 269-283.

OYAGI S, HIROSE M, KOJIMA M, OKUYAMA M, KAWASE M, NAKAMURA T, OHGUSHI H, YAGI K (2006) Therapeutic effect of transplanting HGF-treated bone marrow mesenchymal cells into CCl4-injured rats. *J Hepatol*, 44(4): 742-748.

ÖZ E, ILHANMN (2006) Effects of melatonin in reducing the toxic effects of doxorubicin. *Mol Cell Biochem*, 286(1-2): 11-15.

PAGET GE, BARNES JM (1964) Toxicity tests in evaluation of drug activities pharmacometries (Laurence DR, Bacharach AL, eds.). *Academic Press*, London, New York.

PAL P, MALLICK S, MANDAL SK, DAS M, DUTTA AK, DATTA PK (2002) A human placental extract: in vivo and in vitro assessments of its melanocyte growth and pigment inducing activities. *Int J Dermatol*, 41(11): 760-767.

PARADIS V, YOUSSEF N, DARGÈRE D, BÂ N, BONVOUST F, DESCHATRETTE J, BEDOSSA P (2001) Replicative senescence in normal liver, chronic hepatitis C, and hepatocellular carcinomas. *Hum Pathol*, 32(3): 327-332.

PAROLINI O, ALVIANO F, BAGNARA GP, BILIC G, BUHRING HJ, EVANGELISTA M (2008) Concise review: isolation and characterization of cells from human term placenta: outcome of the first international Workshop on Placenta Derived Stem Cells. *Stem Cells*, 26(2): 300-311.

QUERTAINMONT R, CANTINIEAUX D, BOTMAN O, SID S, SCHOENEN J, FRANZEN R (2012) Mesenchymal stem cell graft improves recovery after spinal cord injury in adult rats through neurotrophic and pro-angiogenic actions. *PLoS One*, 7(6): e39500.

RASH AR, ABDELLA EM (2010) Modulatory effects of Rosemary leaves Aqueous on doxorubicin-induced histological lesions, apoptosis and oxidative stress in mice. *Iranian J Cancer Prev*, 3: 1-22.

ROSALKI SB, TARLOW D, RAU D (1971) Plasma gamma-glutamyl transpeptidase elevation in patients receiving' enzyme-inducing drugs. *Lancet*, 298(7720): 376-377.

ROZANOVA SL, NAUMENKO EI, ROZANOVA ED, NARDID OA (2010) Change of anioxidative properties of human placental extracts after freezing. *Problems Cryobiol*, 20(3): 288-297.

SAAD SY, NAJJA TA, AL-RIKABI AC (2001) The preventive role of deferoxamine against acute doxorubicin-induced cardiac, renal and hepatic toxicity in rats. *Pharmacol Res*, 43(3): 211-218.

SALEM HK, THIEMERMANN C (2010) Mesenchymal stromal cells: current understanding and clinical status. *Stem Cells*, 28(3): 585-596.

SEO TB, HAN IS, YOON JH, SEOL IC, KIM YS, JO HK (2006) Growth-promoting activity of Hominis Placenta extract on regenerating sciatic nerve. *Acta Pharmacol Sin*, 27(1): 50-58.

SEVEN A, GUZEL S, SEYMEN O, CIVELEK S, BOLAYIRLI M, UNCU M, BURCAK G (2004) Effects of vitamin E supplementation on oxidative stress in streptozotocin induced diabetic rats: investigation of liver and plasma. *Yonsei Med J*, 45(4): 703-710.

SHAO CH, CHEN SL, DONG TF, CHAI H, YU Y, DENG L, WANG Y, CHENG F (2014) Transplantation of bone marrow-derived mesenchymal stem cells after regional hepatic irradiation ameliorates thioacetamide-induced liver fibrosis in rats. *J Surg Res*, 186(1): 408-416.

SHUKLA VK, RASHEED MA, KUMAR M, GUPTA SK, PANDEY SS (2004) A trial to determine the role of placental extract in the treatment of chronic non-healing wounds. *J Wound Care*, 13(5): 177-179.

SIMONS K, IKONEN E (1997) Functional rafts in cell membranes. *Nature*, 387(6633): 569-572.

SNYKERS S, VANHAECKE T, PAPELEU P, LUTTUN A, JIANG Y, VAN DER HEYDEN Y, VERFAILLIE C, ROGIERS V (2006) Sequential exposure to cytokines reflecting embryogenesis: the key for in vitro differentiation of adult bone marrow stem cells into functional hepatocyte-like cells. *Toxicol Sci*, 94(2): 330-341.

SONNLEITNER D, HUEMER P, SULLIVAN DY (2000) A simplified technique for producing platelet-rich plasma and platelet concentrate for intraoral bone grafting techniques: a technical note. *Int J Oral Maxillofac Implants*, 15(6): 879-882.

STĚRBA M, POPELOVÁ O, VÁVROVÁ A, JIRKOVSKÝ E, KOVAŘÍKOVÁ P, GERŠL V (2013) Oxidative stress, redox signaling, and metal chelation in anthracycline cardiotoxicity and pharmacological cardioprotection. *Antioxid Redox Signal*, 18(8): 899-929.

SUR TK, BISWAS TK, ALI L, MUKHERJEE B (2003) Anti-inflammatory and anti-platelet aggregation activity of human placental extract. *Acta Pharmacol Sin*, 24(2): 187-192.

SUVARNA KS, LAYTON C, BANCROFT JD (2013) Bancroft's Theory and Practice of Histological Techniques, E-Book. Elsevier Health Sciences, 7th edition.

THIPPESWAMY AH, SHIRODKAR A, KOTI BC, SADIQ AJ, PRAVEEN DM, SWAMY AH, PATIL M (2011) Protective role of *Phyllantusniruri* extract in doxorubicin-induced myocardial toxicity in rats. *Indian J Pharmacol*, 43(1): 31-35.

TIWARY SK, SHUKLA D, TRIPATHI AK, AGRAWAL S, SINGH MK, SHUKLA VK (2006) Effect of placental-extract gel and cream on non-healing wounds. *J Wound Care*, 15(7): 325-328.

TOGEL F, WEISS K, YANG Y, HU Z, ZHANG P, WESTENFELDER C (2007) Vasculotropic, paracrine actions of infused mesenchymal stem cells are important to the recovery from acute kidney injury. *Am J Physiol Renal Physiol*, 292(5): F1626-F1635.

UEHARA Y, MINOWA O, MORI C, SHIOTA K, KUNO J, NODA T, KITAMURA N (1995) Placental defect and embryonic lethality in mice lacking hepatocyte growth factor/scatter factor. *Nature*, 373(6516): 702-705.

WHEELER MH, LAZARUS JH (1994) Diseases of the Thyroid. Chapman and Hall Medical, London, Glasgow, Weinheim, New York, Tokyo, Melbourne, Madras, pp 107-115.

WIELAND H, SEIDEL D (1982) Improved assessment of plasma lipoprotein patterns. IV. Simple preparation of a lyophilized control serum containing intact human plasma lipoproteins. *Clin Chem*, 28(6): 1335-1337.

WU J, WANG C, LIU Q, YANG T, ZHANG Q, PENG J, LIU K (2008) Protective effect of JBP485 on concanavalin A-induced hepatocyte toxicity in primary cultured rat hepatocytes. *Eur J Pharmacol*, 589(1-3): 299-305.

YAMAUCHI A, KAMIYOSHI A, KOYAMA T, IINUMA N, YAMAGUCHI S, MIYAZAKI H, HIRANO E, KAKU T, SHINDO T (2017) Placental extract ameliorates non-alcoholic steatohepatitis (NASH) by exerting protective effects on endothelial cells. *Heliyon*, 3(9): e00416.

YAMAUCHI A, KAMIYOSHI A, SAKURAI T, MIYAZAKI H, HIRANO E, LIM HS, KAKU T, SHINDO T (2019) Placental extract suppresses cardiac hypertrophy and fibrosis in an angiotensin II-induced cachexia model in mice. *Heliyon*, 5(10): e02655.

YANG F, TEVES SS, KEMP CJ, HENIKOFF S (2014) Doxorubicin, DNA torsion, and chromatin dynamics. *Biochim Biophys Acta*, 1845(1): 84-89.

YEOM MJ, LEE HC, KIM GH, SHIM I, LEE HJ, HAHM DH (2003) Therapeutic effects of Hominis placenta injection into an acupuncture point on the inflammatory responses in subchondral bone region of adjuvant-induced polyarthritic rat. *Biol Pharm Bull*, 26(10): 1472-1477.

YUN UJ, LEE JH, SHIM J, YOON K, GOH SH, YI EH, YE AK, LEE JS, LEE H, PARK J, LEE IH (2019) Anti-cancer effect of doxorubicin is mediated by downregulation of HMG-Co A reductase via inhibition of EGFR/Src pathway. *Lab Invest*, 99(8): 1157-1172.

ZAAHKOUK SMA, BAKRY S, MANSOUR A, IBRAHIM RH (2015) Therapeutic role of mesenchymal stem cells in cisplatin induced renal failure in adult male rats. *Adv Biol Res*, 9(3): 201-209.

ZENG X, YU SP, TAYLOR T, OGLE M WEI L (2012) Protective effect of apelin on cultured rat bone marrow mesenchymal stem cells against apoptosis. *Stem Cell Res*, 8(3): 357-367.

Metabolic activities and cytokeratin-7 (CK7) expression in gossypol induced hepatotoxicity treated with aqueous extract of *Phoenix dactylifera* in rat model

Dare J. Babatunde[1], Doshiya Joseph[2], Lawal I. Adetayo[3], Ibiyemi T. Victoria[4], Abayomi Taiwo[5]

[1] *Department of Anatomy, Osun State University, Osogbo, Nigeria*
[2] *Department of Anatomy, Bingham University Karu, Nasarawa State, Nigeria*
[3] *Department of Anatomy, Alhikmah University, Ilorin, Nigeria*
[4] *Department of Anatomy, Olabisi Onabanjo University, Sagamu, Nigeria*
[5] *Department of Anatomy, Osun State University, Osogbo, Nigeria*

SUMMARY

Cotton seed extract contains gossypol, actives component. The gossypol toxicity has been documented to possess most importantly anti-infertility properties. This study investigates the effects of cotton seed extracts on liver tissues and the protective effects of date palm (*Phoenix dactylifera*) extract on gossypol toxicity.

A total of thirty-five (35) adult female rats were used for this study and were grouped into seven (7) groups (n = 5). Group A - 0.1ml of phosphate buffer solution; Group B - 40mg/kg of *Phoenix dactylifera* only; Group C - 15 mg/kg gossypol; Group D - 30mg/kg of gossypol; Group E - 15 mg/kg gossypol + 40 mg/kg *Phoenix dactylifera*; Group F - 15 mg/kg Vitamin E; Group G - 15 mg/kg gossypol + 15 mg/kg vitamin E. After final administration of experimental gossypol, and *Phoenix dactylifera extract,* the animals were euthanized by cervical dislocation and the liver tissue was excised. The left lobe of the liver from each rat was fixed in Bouin's fluid for routine histological haematoxylin & eosin (H/E) and immunohistochemical (CK7) stains, while the right liver lobe was homogenized in 5% sucrose solution for enzyme assay using antioxidant and enzymes of carbohydrates metabolism.

Histological observations showed loss of hepatic sinusoids following derangement of horizontally placed hepatic plates; degeneration of hepatocytes and the reduced expression of cell proliferation as indicated by CK-7 demonstration in cotton-seed-extract-treated animals when reference to the *Phoenix dactylifera* treated groups and the control animals with the characteristic features of hepatic architecture. Evidence obtained in the enzymes of antioxidant using SOD and GH showed significant reduction in the enzymes' activities, with associated increase in lipid peroxidation among the cotton-seed-extract-treated animals. *Phoenix dactylifera* extract and the treatment with vitamin E preserved the antioxidant enzyme integrity

Corresponding author:
Dr. Dare, Babatunde Joseph. Department of Anatomy, Osun State University, Osogbo, Nigeria. Phone: +2348077805474. E-mail: babatund.dare@uniosun.edu.ng

Submitted: September 16, 2020. **Accepted:** January 2, 2021
Not final proof's revision by the authors

and maintained the carbohydrates metabolism measured by the D-6-PD and the LH level.

Date palm (*Phoenix dactylifera)* extracts and treatment with vitamin E maintained hepatic integrity and preserved the histological appearances and the enzymes of carbohydrates metabolism and antioxidant properties against cotton seed (gossypol) toxicity.

Key words: Cotton seed extract – Liver – Phoenix dactylifera – Antioxidant enzymes – Histology – Carbohydrate metabolism – Immunohistochemistry

INTRODUCTION

Phoenix dactylifera L. (date palm) fruit, due to its rich components, has been implicated to have a wide range of beneficial medicinal properties such as immunostimulant, hepatoprotective, nephroprotective, free radical scavenging, antimutagenic, antimicrobial, anticancer and antioxidant properties (Al-Farsi and Lee, 2008; Ishurd et al., 2004; Vayalil, 2002). *Phoenix dactylifera L.* is highly rich in dietary fiber, fat, carbohydrate, vitamins and amino acids (Zhang et al., 2013; Ali and Abdu, 2011). The antioxidant efficacies of *Phoenix dactylifera L.* are attributed to a wide range of flavonoids, phenolic compounds, sterols and volatile oil (Baliga et al., 2011; Al-Farsi and Lee, 2008; Hong et al., 2006).

The usage and cultivation of *Phoenix dactylifera L.* plant dates back to about 5000 years. The plant belongs to the family of Arecaceae; it is a diploid, perennial, monocotyledonous and dioecious plant (Ragab et al., 2013). In 2018, Mobasher and other scientists reported that both the aqueous and methanolic extract of *Phoenix dactylifera L.* significantly ameliorate Azithromycin-induced hepatic and renal toxicities; the aqueous extract of the plant is more potent and active than the methanolic extract of *Phoenix dactylifera L.*, according to the data from this research work (Mobasher et al., 2018).

Gossypol is a lipid-soluble polyphenolic compound extracted from the cotton plant (genus Gossypium) and the tropical tree *Thespesia populnea* (L.) Sol. ex Correa (Hoda and Bahram, 2014). Gossypol, due to it phenolic component, may possess beneficial effects to the organism, but when abused it may result in debilitating effects. The gossypol LD_{50} has been determined for several mammalian species, including rats (925-1,350 mg/kg), mice (500-950 mg/kg), rabbits (350-600 mg/kg), guinea pigs (280-300 mg/kg) (Eagle et al., 1948), and pigs (550 mg/kg) (Lyman et al., 1963).

Gossypol have been reported to possess varying beneficial properties in humans and animals due to its chemical composition such as anti-oxidative (Wang et al., 2008), anti-tumor (Zhai at el., 2006), anti-viral (Vander Jagt et al., 2000; Lin et al., 1993), anti-malaria (Razakantoanina et al., 2000; Royer et al., 1986), antimicrobial (Vadehra et al., 1985) and reduced cholesterol production (Shandilya et al., 1982) properties.

In contrast to all the aforementioned beneficial properties, Gossypol toxicities have been also explored and documented. Gossypol has been found out to have antifertility properties, without altering hormonal production (i.e., non-steroidal) and expression in male. Instead, it acts as a contraceptive by subduing enzyme production responsible for energy metabolism in sperm and spermatogenic cells in humans and animals alike (Coutinho, 2002; Wang et al., 2009). Amy and others reported that gossypol, administered in increasing dosage to Northern bobwhites, resulted in structural alterations in certain tissues such as hepatocellular pigmentation, pancreatic necrosis and intestinal toxicity (Amy et al., 2019). Gossypol may also possess immunosuppressive properties, as reports have shown that gossypol cause a reduced number of leukocytes and primary lymphocytes, which affects the animals' immunocompetence (Braga et al., 2012). In vivo and in vitro mouse experiments also depicted gossypol's immunosuppressive tendencies by inhibiting lymphocyte proliferation and inducing apoptosis (Xu et al., 2009).

This research work aimed to elucidate the toxic effects, if any, of gossypol on liver tissue in murines, as well as the possible protective actions of *Phoenix dactylifera L.*

MATERIALS AND METHODS

Animal source and handling

A total of thirty (35) adult Wistar rats weighing between 150-200g were procured from the Animal Holding Facility in Jos, for this experiment. Animals were maintained in a controlled environment (22 ± 2C; 14 h of light from 06:00 h to 20:00 h) and had free access to pellet laboratory chow rat-mouse diet and acclimatized for four weeks before the experiment commenced. The rats were fed with standard diet (growers mash); water was given *ad libitium* and maintained under standard conditions. The animal room was kept at 25-27 degrees Celsius under day and night. The rats were distributed into seven (7) groups of five (5) rats each.

Ethical clearance

Animals were treated humanely and with regard to alleviation of suffering for the care and use of laboratory animals. The experimental protocol was approved by the Ethical Review Committee (ERC) of Bingham University, Karu, Nigeria. The study was carried out in the animal house of the College of Health Sciences, Bingham University, Karu, Nigeria.

Extract preparation

Cotton seed was obtained from Dengi market, Plateau state, Nigeria. The seeds were pounded to powder using a mortar and pestle and the cotton seed oil was extracted using the solvent extraction method described by Orheva and Efomah (2012). The experimental process involved the following; collection of seeds, cleaning of seeds, drying, cooling, size reduction, weighing of the crushed seeds, solvent extraction, weighing of the cottonseed cake, recovery of solvent and recovery of crude cottonseed oil. The samples collected were properly cleaned in order to remove any foreign materials. They were oven-dried in the laboratory at a temperature of 130°C, to a moisture content of 12%. This was done because the lesser the moisture content, the more the oil yields (Taiwo et al., 2008). The seeds were then crushed into powder using Thomas Willey mill (Model ED-5). Twelve (12) grammes (g) of the crushed sample was weighed and mixed with 5 ml of N-hexane. The mixed sample was placed on a filter paper and the filter paper was then properly folded and inserted into the assembled soxhlet apparatus. The weight of the filter paper and sample was recorded. One hundred and fifty milliliters (150 ml) of the solvent (N- hexane) was measured using a measuring cylinder, and then poured into a five-hundred-milliliter (500 ml) round-bottom flask, which is the lower part of the Soxhlet apparatus. This was now heated with a heating mantle at 60°C for 6 hours. As the solvent boiled, it evaporated into the reflux condenser, and this hot solvent vapour was cooled by the surrounding water that flowed continuously through the soxhlet arrangement. The cooled solvent then condensed back into the portion of the soxhlet containing the folded sample and this facilitated the extraction of the oil from the sample. The extracted solution in the round-bottom flask was a combination of oil and solvent. The sample left, after the oil had been removed, was subjected to hot pressing using hydraulic press to remove the bulk of the oil remaining in the press cake (Orhevba and Efomah, 2012)

Gossypol was extracted from the cottonseed oil using 70% cold acetone. This is because the decomposition rate of gossypol is lower in acetone than in other organic solvents such as methanol, chloroform, ethanol, and acetonitrile (Nomeir and Abou-Dounia, 1982).

Date palm fruits were obtained from Masaka market in Nassarawa state. The seeds were removed from the fruit and the pulp was pounded to powder using mortar and pestle. 435 g of the powder was soaked in 4350 ml of distilled water for 24 hours. The solution was then filtered using fine sieve and the residue was discarded. The filtrate was evaporated at 60°C using water bath till a thick semisolid paste with a fruity smell was obtained. This was dissolved in phosphate buffer solution before being administered to the rats. An aqueous extract was selected because most of the antioxidant components in dates are extracted in water (Vayalil, 2002; Al-Farsi *et al.,* 2005b).

Preparation of *Phoenix dactylifera* extract

The extraction procedure was adapted from the reports in Emilia et. al. (2018); date fruit pod

was obtained and authenticated in the Biology Department, Bingham University, Nigeria. The date fruit pod was broken in order to remove the seeds and pounded. The powder was extracted twice with distilled water (1:10 w/d). 125g of powdered date fruit pod was weighed into 2x500 ml conical flask; 70 % ethanol was introduced and allowed over-night; the content was the shaken for an hour and filtered through a Whatman #43 filter paper; several paths of rinsing were done. The filtered solution was then concentrated by rotary evaporation. The extract was stored at 6°C overnight. The extract obtained from this procedure was subjected to further extraction by adding acetone water to remove the oil. The acetone water filtrate was again extracted by using chloroform; the aqueous layer was the concentrated to dryness to obtain the needed extract, which is the normal acetone water extract.

Animal grouping

The rats were distributed into seven (7) groups (n = 5). Group A received- 0.1ml of phosphate buffer solution; Group B received – 40 mg/kg of *Phoenix dactylifera* only; Group C received - 15 mg/kg gossypol; Group D received – 30 mg/kg of gossypol; Group E received - 15 mg/kg gossypol + 40 mg/kg *Phoenix dactylifera*; Group F received - 15 mg/kg Vitamin E; Group G - 15 mg/kg gossypol + 15 mg/kg vitamin E. The administration of experimental substances was done via oral gavage using oropharyngeal cannula for a period of 56 days.

Sample collection and processing

The animals were euthanized by cervical dislocation twenty-four hours after last administration and the liver tissue was excised. The left lobe of the liver from each rat was fixed in Bouin's fluid for routine histological haematoxylin & eosin (H/E), and immunohistochemical (CK7) stains while the other was homogenized in 5% sucrose solution for enzyme assay.

Histological preparation

The histology of the liver was done by modification of the method described by Akpantah et al. (2003). The organs were cut in slabs of about 0.5cm thick transversely and fixed in 10% buffered formalin for a day, after which it was transferred to 70% alcohol for dehydration. The tissues were passed through 90% and absolute alcohol and xylene for different durations before they were transferred into two (2) changes of molten paraffin wax for 1hr each in an oven at 65°C for infiltration. They were subsequently embedded and serial sections were cut using rotary microtome at six microns. The tissues were transferred onto albuminised slides allowed to dry on a hot plate for 2 minutes. The slides were then dewaxed with xylene and passed through absolute alcohol 2 changes); 70% alcohol, 50% alcohol and then to water for 5 minutes. The slides were then stained with haematoxylin and eosin. The slides were mounted in Canada balsam. Photomicrographs were taken using.

Biochemical assay

Enzyme biochemistry

The homogenized liver tissue was utilized for malondaldehyde (MDA), glutathione (GSH), superoxide dismutase (SOD), glucose phosphate dehydrogenase (G6PDH) and lactate dehydrogenase (LDH) assay. The oxidative stress and bioenergetics markers were assessed by an enzyme-linked immunosorbent assay kit (IBL-America, Minneapolis, Minnesota, USA).

Excised liver tissues were put in a Lao style mortar containing 1ml of 0.25 Mn (5%) sucrose solutions and were homogenized thoroughly. Tissue homogenate was collected in 5 ml plain serum bottles for enzyme assay; Glucose-6-phosphate dehydrogenase (G6PD), superoxide dismutase (SOD), Malondialdehyde (MDA), Glutathione peroxidase (GSH-Px) and Lactate Dehydrogenase (LDH)

Determination of Malondialdehyde (MDA) level in tissue homogenates

Malondialdehyde level in tissues were measured according to the protocol outlined by Stocks and Domandy (1971), 0.1 ml of homogenate was pipette into a plastic test tube. 1 ml of 20% Trichloroacetate was added to it. The mixture was processed and centrifuged at 2000 g for 5 minutes. 0.5 ml of the supernatant was pipetted into a pyrex test tube 0.05 ml of 10.0 µmol/L of

1,1,3,3-Tetramethoxypropane was pipetted into another pyrex test tube (std). 0.5 ml of Trichroacetic acid solution and 1.0 ml of Thibarbituric acid was pipetted into a 3rd pyrex test tube (blank). All tubes were stoppered tightly. The test tubes were heated in a water bath at 100ºC for 20 minutes. All tubes were cooled in water. The spectrophotometer was blanked using the reagent blank at 532 nm. Absorbance of test and standards were read.

Determination of Glucose 6 phosphate Dehydrogenase (G-6-PDH) Activity in tissue homogenate

Activity of G-6-PDH in homogenate was measured using the method of Lohr and Walker (1974). A reaction mix of 1350 µl TRAP buffer (triethanolamine 50 mM, ethylenediaminetetraacetic acid 5 mM pH 7.5), 50 µl of magnesium chloride 1M, 25 µl of haemolysate (0.9% w/v sodium chloride saline washed erythrocytes disrupted with a saturated solution of digitonine), 25 µl of NADP (nicotinamide-adenine-dinucleotide phosphate 30mM) were started by finally adding 25 µl of G6P (glucose 6 phosphate, 50mM). Photometric extinction rate compared to a blank without haemolysate was recorded at 37°C. Results of the G6PD testing values were calculated in units per µMol metabolic rate/10^{11} erythrocytes/min (normal value: 30.5 ± 4.5). Activity was then converted into Units per g Haemoglobin (U/g Hb, Trinity Biotech for 37°C at 366nn, normal range 4.6-13.5 U/g Hb) by the following formula: (activity in µmol metabolic rate/10^{11} erythrocytes/min * RBC M/µL * 0.66)/Hb g/dL.

Determination of Lactase Dehydrogenase (LDH) Activity in tissue homogenate

Activity of LDH in the homogenate was measured according to the method in Jeyaraman et al. (2009). The homogenate was centrifuged at 10,000×g for 10 minutes at 4ºC. The clear supernatant obtained was used for the measurement of LDH activity.

Reagents

- 0.2 M Tris·HCl, pH 7.3
- 6.6 mM NADH in above 0.2 M Tris·HCl buffer, pH 7.3
- 30 mM Sodium pyruvate in above 0.2 Tris·HCl buffer, pH 7.3

Enzyme

Dissolve at 1 mg/ml in 0.2 M Tris·HCl buffer. Dilute enzyme prior to use to obtain a rate of 0.02-0.04 ΔA/min. in Tris buffer and keep cold.

Procedure

Spectrophotometer was set at 340 nm and 25°C.

Pipette into cuvette as follows:

Tris·HCl, 0.2 M pH 7.3	2.8 ml
6.6 mM NADH	0.1 ml
30 mM Sodium pyruvate	0.1 ml

Incubate was done spectrophotometer 4-5 minutes to achieve temperature equilibration and establish a blank rate.

Add 0.1 ml of appropriately diluted enzyme and record ΔA_{340}/min from initial linear portion.

Calculation

$$\text{Unit/ml} = \frac{\Delta A_{340}/\text{min}}{6.22 \times \text{mg enzyme/ml reaction mixture}}$$

Determination of Superoxide dismutase (SOD)

Superoxide dismutase activity in homogenates was determined using the method of Misra and Fridovich, (1972). 200 µl R1 reagent (WTS solution diluted 20-fold with buffer) was pipetted into a plastic cuvette and incubated at 37°C for 108 sec. Subsequently, 20 µl of sample was added and in 378 sec. The reaction was started by adding 20 µl R2 reagent (enzyme solution diluted 167-fold with buffer). The reaction was incubated for 72 sec and then absorbance was measured at λ=450 nm. The kinetic reaction was measured for 108 sec and the absorbance was recorded every 9 sec.

Determination of Malondialdehyde (MDA)

Malondialdehyde (MDA) activity in homogenates was determined using the method by Reilly and Aust (1999) as shown below;

Reagents

- 30% Tricarboxylic Acid (TCA): 3g of TCA was added to 10ml of distilled water.

- 0.75% Thiobarbituric Acid (TBA): 0.225g of Thiobarbituric Acid (TBA) was added to 30ml of 0.1M of HCl.
- 0.15M Tris KCl buffer solution (pH 7.4)
- 1.12g of KCl was added to 2.36g of Tris base.
- 200ml of distilled water was added
- pH was adjusted to 7.4

Procedure

- 0.4ml of sample was added to (1.6ml of Tris-KCL buffer and 0.5ml of 30% TCA).
- 0.5ml of TBA was added.
- The solution was incubated for 45minutes at 80˚C (produced a pink colour).
- Then cooled in ice and centrifuged at 14000g for 15minutes.
- The absorbance was read at 532nm.

Calculation

$$\text{MDA (Unit/mg protein)} = \frac{\text{Absorbance x Volume of Mixture}}{E_{532} \text{ x Volume of Sample X mg protein}}$$

Where E_{532} = Molar absorptivity at 532nm = 1.56×10^5

Data analysis

Data collected were analysed using one-way analysis of variance (ANOVA) followed by Tukey's (HSD) multiple comparison test with the aid of GraphPad Prism v.6 (GraphPad Software, Inc., La Jolla, CA, USA). Data were presented as means ± SEM (standard error of mean). P value less than 0.05 ($P < 0.05$) was considered statistically significant.

RESULTS

Histological observations

Administration of *Phoenix dactylifera L.* and Vitamin E preserved the hepatic histo-architecture that characterized the histological features of the liver in the control animals that received only phosphate buffered saline (PBS). The integrity of the hepatic sinusoids and the arrangement of the horizontal placed hepatic plate with the intact nuclei were maintained. Continuous cell division as indicated in ure 1 among the positive and the negative control animals was significant by the karyolysis of the nucleus. However, administration of the gossypol present in cottonseed extracts causes derangement in the horizontal hepatic plates. Degeneration in the hepatic nuclei was a result of chromatolysis and pkynosis. Increase in vacuolation and loss of hepatic sinusoidal spaces was evident in the gossypol-treated animals as shown in Fig. 1 Engorged blood sinusoid, rupture, granular degeneration of hepatocytes, oedema, focal necrosis, and proliferation of fibroblasts were the alterations. Co-administration of gossypol with *Phoenix dactylifera L.* and Vitamin E shows hepatopretective impacts of *Phoenix dactylifera L.* and Vitamin E. The testicular histology was preserved similar to the control animals and the arrangement in the hepatic sinusoid with the intact nuclei demonstrate the protective effects of both the Vitamin E and the *Phoenix dactylifera L.* ethanolic extracts.

Cytokeratin 7 (CK7) demonstration has been shown to be generally negative in hepatocellular tumour and in colorectal carcinoma, Merkel cell carcinoma, prostatic adenocarcinoma, adrenocortical tumours and squamous cell carcinoma. The hepatic demonstration of Cytokeratin 7 (CK7) in the gossypol treated groups showed less affinity for the Cytokeratin 7 (CK7) protein demonstrations (negative) particularly in the group that was given 30 mg/g body weight of cotton seed extracts. Cytokeratin 7 (CK7) is the marker expression in membranous and cytoplasmic normal epithelia; the control animal significantly expressed this protein in line with the animals that were given *Phoenix dactylifera L.* and Vitamin E when compared with the level of expression in gossypol treated animals as shown in Fig. 2. The expression of Cytokeratin 7 (CK7) in the negative control posed with less variation with the positive control group, with moderate expression of Cytokeratin 7 (CK7) among the groups co-treated with the gossypol and *Phoenix dactylifera L* as well as those given Vitamin E.

It is worth note that macrosteatosis and microsteatosis were most prominent histopathologic features among the gossypol treated group particularly the group with 30 mg/g body weight

of cotton seed extracts. The lobular fat deposition demonstrating the macrosteatosis was more defined in the periportal, midzonal, or centrilobular regions of the hepatic lobule. Vitamin E treated group display a unique pattern of macrosteatosis and microsteatosis across the periportal, midzonal, or centrilobular regions of the hepatic lobule, however in a consistent and moderate patterns.

Oxidative stress & Cellular bioenergetics markers assay

The levels of glutathione metabolizing enzymes, G6PD and LDH was measured as well, and decrease in the level of G6PD and LDH activities was noted as shown in figure 3 among the animals treated with cotton seed extract, gossypol. This decrease could normally result from the deficient flow of G-6-P through the hexose monophosphate shunt and decreased supply of reduced NADPH for the conversion of GSSG to GSH, thereby causing a switch in the $NADP^+$/NADPH ratio in favour of NADP. However, across the positive and the negative control groups the enzymes' integrity was preserved and the activities of these enzymes were maintained. The intervention groups, gossypol damage liver treated with *Phoenix dactylifera L.* and Vitamin E significantly maintained the carbohydrate enzymes' activities similar to the control animals as revealed in Fig. 3.

DISCUSSION

Oxidative stress has been considered as a conjoint pathological mechanism with the attendant liver (hepatic) injury. Reactive oxidative substances such as; alcohol, drugs, environmental pollutants and irradiation, induce oxidative stress in liver tissue. This study, therefore investigated structural alterations, and the changes in the level of activities of the antioxidant enzymes and the enzymes of carbohydrates metabolism in animals exposed to varying dosage of cotton seed extract (Gossypol) and the hepato-protective effects of *Phoenix dactylifera* and vitamin E was examined as well. Saber and Shalaby (2012) noted impaired hepatic lobules and derangement of the hepatic sinusoid as well as enlargement and congestion of blood vessel and marked cytoplasmic vacuolization among the pregnant

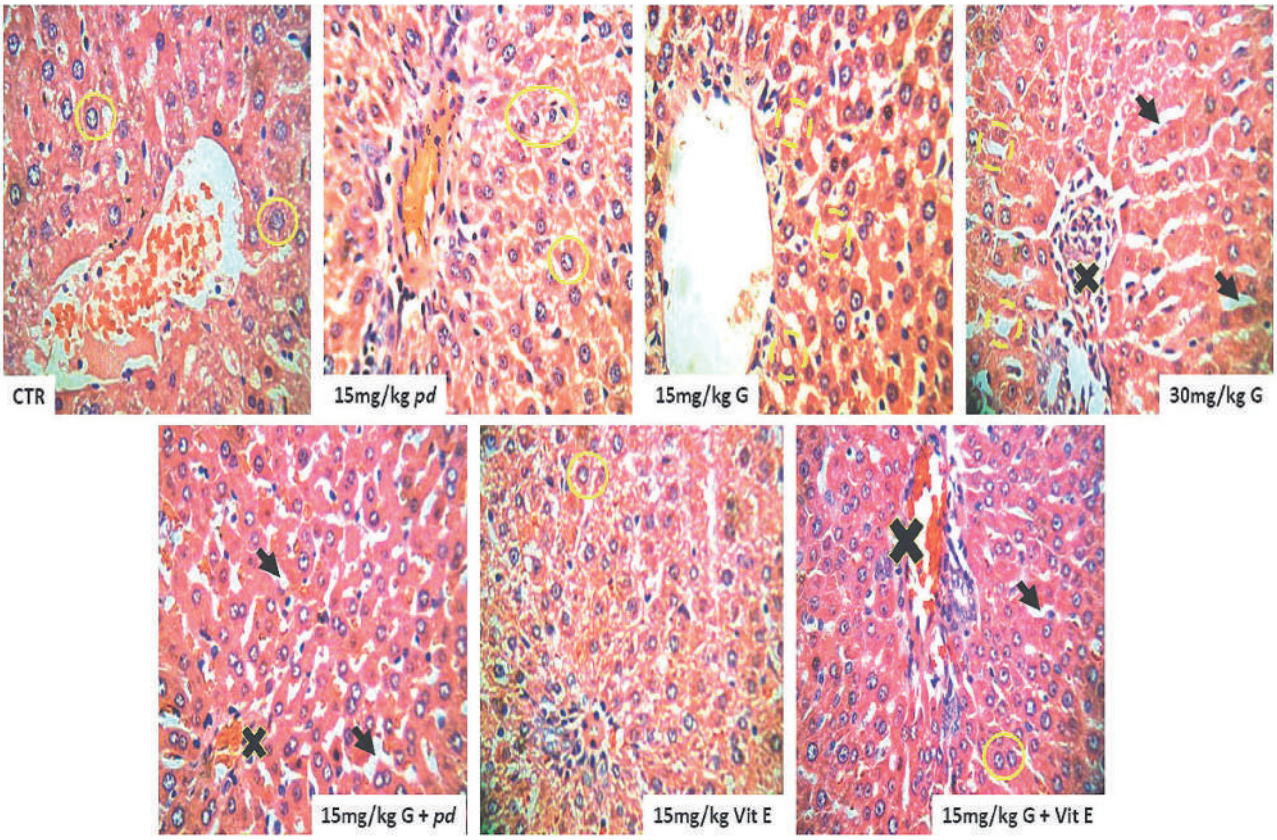

Fig. 1.- Effects of aqueous extract *Phoenix dactylifera* on histopathological changes induced by Gossypol exposure in Wistar rats. Stain – Hematoxylin & Eosin, magnification - x400. Yellow circle - showed numerous healthy hepatocytes; X shape - portal vessels; Fenestrated circles - showed degeneration of hepatocyte; Black arrow head – sinusoids.

mice treated with oral metiram, acting fungicide of dithiocarbamate group. These findings agreed with our histological observations using H/E stains as specified in Fig. 1 above; the gossypol treatment significantly disrupt the horizontal plate arrangement of hepatocytes, increased cytoplasmic vacuolation as a result of hepatocytes loss and glandular tissue damage. Our study revealed that most cells of the gossypol treated animals showed nuclei with signs of karyolysis and pyknosis as well as obvious fatty degeneration indicated by large number of fatty droplets with different size was observed in accordance with the study conducted by Brante et al. (2010).

He observed macrosteatosis and microsteatosis characterised the histopathologic of animals treated with alcohol intoxication, with most animals displaying panlobular or defined foci of microsteatosis in periportal, midzonal, or centrilobular regions of the hepatic lobule. Therefore, gossypol in this study had profound histological alteration in the hepatic tissue similar to the damage caused by known free-radical-generating substances such as the alcohol administration. Gossypol hepatotoxic, ascites and hepatocyte degeneration (strong cytoplasmic eosinophilia and nuclear pyknosis) had been observed in rats that received a single intraperitoneal gossypol dose of 25 mg/kg BW or 30 mg/kg BW, with characteristic mitochondrial vacuolation, an enlarged endoplasmatic reticulum, an expanded perinuclear space, and collagen fiber proliferation in the perisinusoidal space that is according to Lordelo (2005).

Administration of *Phoenix dactylifera* extracts as a natural ascorbic acid substance, with well documented antioxidant capability according to Brady (2011), provides protective mechanism for the gossypol hepatic damage. *Phoenix dactylifera* extracts has been proven to have antioxidants that prevent oxidative stress related to diseases such as cancer, aging, inflammation and cardiovascular diseases by eliminate free radicals which contribute to theses chronic diseases (Blomhoff et al., 2010). Histological appearances of the liver treated with *Phoenix dactylifera* extracts and vitamin E was maintained as observed in this study. This finding could be explained along Al-Qarawi et al. (2003) work that showed that date palm fruit had both protection and restoration effects of liver damage in the rats.

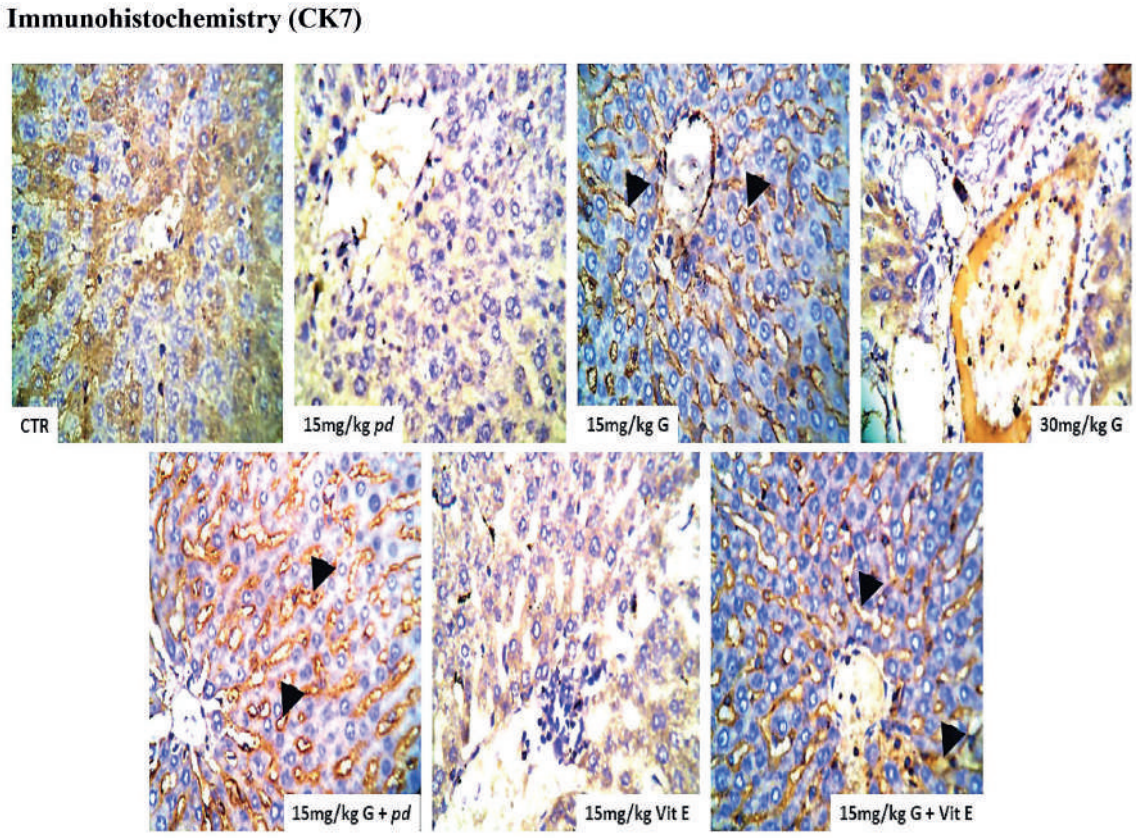

Fig. 2.- Effects of aqueous extract *Phoenix dactylifera* on histopathological changes induced by Gossypol exposure in Wistar rats. Stain – CK7; magnification - x400. Arrow head – CK7 expression.

Cytokeratin 7 (CK7) has been proven a membranous and/or cytoplasmic marker with expression in normal epithelia and even in epithelial tumours. Despite wide distribution, it is useful as part of a panel in determining primary site of metastatic carcinoma in tissue and generally expressed with little variation in adenocarcinoma of lung, breast, thyroid, endometrium, cervix, ovary, salivary gland and upper GI tract, urothelial carcinoma, papillary renal cell carcinoma and Paget disease, but usually negative in colorectal carcinoma, Merkel cell carcinoma, hepatocellular carcinoma, prostatic adenocarcinoma, adrenocortical tumours and squamous cell carcinoma according Kruti and Brandon (2020). This study observed the expression of protein CK7 in the control and those that were treated with Vitamin E and *Phoenix dactylifera* extracts, which is evidence of continuous cell proliferation and differentiation, whereas the gossypol-treated group showed reduced evidence of tissue regeneration an indication of hepatic injury according to Adrian and Stefan (2010) and Goldstein et al. (2001).

The molecular and cellular mechanisms that involve process of lipid peroxidation initiate or propagate liver injury and fibrosis. At the molecular level, the production of reactive oxygen species such as superoxide anion radical ($O_2^{\cdot-}$) is an essential event in the formation of hydroxyl radical ($OH^{\cdot}$), which can then abstract a hydrogen atom from cellular membrane lipids, resulting in the autocatalytic production of lipid radicals and the peroxidative degradation of membrane lipid this is according to Brante et. al. (2010), this also flow with this study, we observed increased in MDA activities and lowering of SOD activities and the expression of receptor of GSH in gossypol treated animals. This is otherwise not achieved in the animals treated with the antioxidant-like substances, as noted in the Vitamin E and *Phoenix dactylifera* extracts treated animals. GSH has been noted as a natural compound in the body: made from the amino acids glutamic acid, cysteine, and glycine, it plays a detoxification role in the body and usually occurs inside cells of the liver, kidney, intestines, and lungs. GSH has been associated with lipid peroxidation, because of its ability

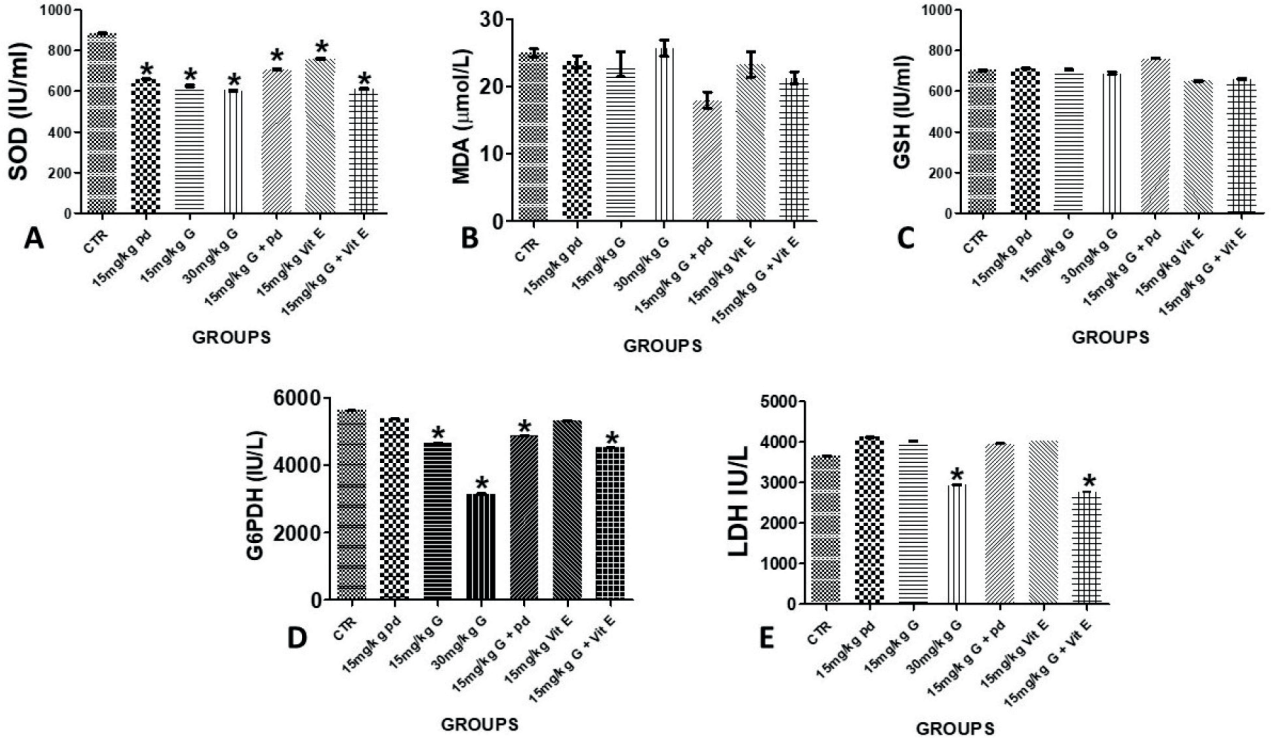

Fig. 3.- Effects of aqueous extract Phoenix dactylifera on Gossypol induced hepatotoxicity in Wistar rats. (**A**) malondialdehyde (MDA) concentration, (**B**) superoxide dismutase (SOD) concentration, (**C**) glutathione (GSH) concentration, (**D**) showing the glucose phosphate dehydrogenase (G6PDH) and (**E**) lactate dehydrogenase (LDH) concentration in the liver cells of experimental animals.

to combine with free radicals that may initiate lipid peroxidation, as well as reduced hydrogen peroxide formed in cells according to Singh et al. (2013). Hepatic GSH has been observed to decrease according to gossypol concentration and the consequent depletion in the antioxidant enzymes as noted in this study. However, increase in the antioxidant enzymes was observed in the Vitamin E and *Phoenix dactylifera* extracts suggesting the antioxidant promoting capacities of the *Phoenix dactylifera* extracts in gossypol damage wistar rats.

The study of cytokeratin (CK) expression in liver tissues has offered valuable findings on hepatic ultrastructure in healthy and disease states. Normal functioning liver cells, hepatocytes express different forms of cytokeratin in healthy and diseased states. In healthy liver tissue, hepatocytes expressed CK8 and CK18 but in diseased condition, liver tissue have been reported to express CK7 and CK19 (Adrian and Stefan, 2010; Goldstein et al., 2001). CK7 immunohistochemistry conducted on liver tissue showed numerous CK7 hepatocytes especially on gossypol treated groups. This implies that gossypol may cause serious damage to liver tissue when abused and/taken over a long period of time.

Gossypol has been documented to cause oxidative stress in exposed subjects: i.e., irregularity in the production and clearance of free radicals that can be detrimental to hepatocytes health and functionality. Findings from this study showed a slight increment in an oxidative stress marker, MDA in the liver of gossypol treated animals and a likewise insignificant reduction of MDA levels in *Phoenix dactylifera* and vitamin-E-treated animals compared to gossypol group. Excess of oxidative stress markers in cells tend to affect the production and function of natural cellular oxidants such as SOD, GSH, etc. While the concentration of GSH seems unaffected across all experimental groups, SOD concentration was reduced significantly. This implies that the possible mechanism gossypol exerted its debilitation actions on the liver was via oxidative stress induction. Our finding is contrary to Wang et al. (2008) who reported that gossypol has anti-oxidative properties. Also, Mobasher et al. (2018) reported that *Phoenix dactylifera L.*, via its antioxidative and antihyperlipidemic activities, reverted the azithromycin toxicity exerted on the hepatic and renal cyto-architecture and functions. *Phoenix dactylifera* and vitamin E were unable to significantly upregulate cellular oxidant (SOD & GSH) production in gossypol-treated animals.

Glucose-6-phosphate dehydrogenase (G6PDH) is an enzyme that maintains supply of reducing energy to body cells to aid cell growth and proliferation. It also protects RBC against oxidative damage (Tian et al., 1998; Thomas et al., 1991). Lactate dehydrogenase (LDH) is well expressed in body tissues. It is not released except in response to assault or tissue damage, and hence it is a common marker for injuries and diseases. Our findings revealed that gossypol altered G6PDH concentration in all gossypol-exposed groups, lowest in 30mg/kg gossypol group, which may impact hepatocellular health and functions.

CONCLUSION

Gossypol at dosages and duration tested in sexually active female rats showed debilitating effects on liver health and functions, and *Phoenix dactylifera* could not completely revert the toxic actions of gossypol on liver tissue.

REFERENCES

AL-FARSI MA, LEE CY (2008) Nutritional and functional properties of dates: A review. *Crit Rev Food Sci Nutr*, 48: 877-887.

ADRIAN CB, STEFAN GH (2010) Cytokeratin expression as an aid to diagnosis in medical liver biopsies. *Histopathology,* 56: 415-425.

ALI A, ABDU S (2011) Antioxidant protection against pathological mycotoxins alterations on proximal tubules in rat kidney. *Funct Foods Health Dis,* 1: 118-134.

AMY LF, THOMAS WS, DAVID JG, HEATHER AM, KIMBERLY AG (2019) Acute toxicity of gossypol in northern bobwhites. *J Appl Animal Res,* 47(1): 326-332.

BALIGA MS, BALIGA BRV, KANDATHILC SM, BHATD HP, VAYALIL PK (2011) A review of the chemistry and pharmacology of the date fruits (*Phoenix dactylifera L.*). *Food Res Int,* 44: 1812-1822.

BRAGA AP, MACIEL MV, GUERRA DGF, MAIA IS, OLORIS SCS, SOTO-BLANCO B (2012) Extruded-expelled cottonseed meal decreases lymphocyte counts in male sheep. *Revue de Medecine Veterinaire,* 163(3): 147-152.

COUTINHO EM (2002) Gossypol: A contraceptive for men. *Contraception,* 65: 259-263.

EAGLE E, CASTILLON LE, HALL CM, BOATNER CH (1948) Acute oral toxicity of gossypol and cottonseed pigment glands for rats, mice, rabbits and Guinea pigs. *Arch Biochem,* 18: 271-277.

GOLDSTEIN NS, SOMAN A, GORDON SC (2001) Portal tract eosinophils and hepatocyte cytokeratin 7 immunoreactivity helps distinguish early-stage, mildly active primary biliary cirrhosis and autoimmune hepatitis. *Am J Clin Pathol,* 116: 846-853.

HODA K-N, BAHRAM G (2014) Therapeutic potential of gossypol: An overview. *Pharmaceutical Biol,* 52(1): 124-128.

HONG YJ, TOMAS-BARBERAN FA, KADER AA, MITCHELL AE (2006) The flavonoid glycosides and procyanidin composition of Deglet Noor dates (*Phoenix dactylifera*). *J Agric Food Chem,* 54: 2405-2411.

ISHURD O, ZGHEEL F, KERMAGI A, FLEFLA M, ELMABRUK M (2004) Antitumor activity of beta-D-glucan from Libyan dates. *J Med Food,* 7: 252-255.

LIN TS, SCHINAZI RF, ZHU J (1993) Anti-HIV-1 activity and cellular pharmacology of various analogs of gossypol. *Biochem Pharmacol,* 46: 251-255.

LYMAN CM, EL-NOCKRASHY AS, DOLLAHITE JW (1963) Gossyverdurin: A newly isolated pigment from cottonseed pigment glands. *J Am Oil Chem Soc*, 40: 571-575.

MOBASHER A, IQRA M, HAFEEZ I, RUKHSANA A, AFROZE M, SAIRAH HK, USMAN A (2018) Pharmacological investigation of *Phoenix dactylifera* L. in azithromycin induced toxicity. *Int J Pharmacol,* 14(1): 61-67.

RAGAB AR, ELKABLAWY MA, SHEIK BY, BARAKA HN (2013) Antioxidant and tissue-protective studies on Ajwa extract: dates from Al Madinah Al-Monwarah, Saudia Arabia. *J Environ Anal Toxicol,* Vol. 3. 10.4172/2161-0525.1000163.

RAZAKANTOANINA V, NGUYEN KIM PP, JAUREGUIBERRY G (2000) Antimalarial activity of new gossypol derivatives. *Parasitol Res*, 86: 665-668.

ROYER RE, DECK LM, CAMPOS NM (1986) Biologically active derivatives of gossypol: Synthesis and antimalarial activities of periacylated gossylic nitriles. *J Med Chem*, 29: 1799-1801.

SHANDILYA LN, CLARKSON TB, ADAMS MR, LEWIS JC (1982) Effects of gossypol on reproductive and endocrine functions of male cynomolgus monkeys (*Macaca fascicularis*). *Biol Reprod*, 27: 241-252.

THOMAS D, CHEREST H, SURDIN-KEJAN Y (1991) Identification of the structural gene for glucose-6-phosphate dehydrogenase in yeast. Inactivation leads to a nutritional requirement for organic sulfur. *EMBO J*, 10(3): 547-553.

TIAN WN, BRAUNSTEIN LD, PANG J, STUHLMEIER KM, XI QC, TIAN X, STANTON RC (1998) Importance of glucose-6-phosphate dehydrogenase activity for cell growth. *J Biol Chem*, 273(17): 10609-10617.

VADEHRA DV, KALLA NR, SAXENA M (1985) Antimicrobial activity of gossypol acetic acid. *IRCS Med Sci*, 13: 10-11.

VANDER JAGT DL, DECK LM, ROYER RE (2000) Gossypol: Prototype of inhibitors targeted to dinucleotide folds. *Curr Med Chem*, 7: 479-498.

VAYALIL PK (2002) Antioxidant and antimutagenic properties of aqueous extract of date fruit (*Phoenix dactylifera L. Arecaceae*). *J Agric Food Chem*, 50: 610-617.

WANG X, HOWELL CP, CHEN F, YIN J, JIANG Y (2009) Gossypol a polyphenolic compound from cotton plants. *Adv Food Nutr Res,* 58: 215-263.

WANG X, BECKHAM T, MORRIS J (2008) Bioactivities of gossypol, 6-methoxy gossypol and 6,60-dimethoxy gossypol. *J Agric Food Chem*, 56: 4393-4398.

XU WB, XU LH, LU HS (2009) The immunosuppressive effect of gossypol in mice is mediated by inhibition of lymphocyte proliferation and by induction of cell apoptosis. *Acta Pharmacol Sinica*, 30(5): 597-604.

ZHAI D, JIN C, SATTERTHWAIT AC, REED JC (2006) Comparison of chemical inhibitors of antiapoptotic Bcl2 family proteins. *Cell Death Differ*, 13: 1419-1421.

ZHANG CR, ALDOSARI SA, VIDYASAGAR PS, NAIR KM, NAIR MG (2013) Antioxidant and anti-inflammatory assays confirm bioactive compounds in Ajwa date fruit. *J Agric Food Chem,* 61: 5834-5840.

Patent processus vaginalis in Vietnamese adults who underwent laparoscopic transperitoneal surgery

Tri Huu Nguyen[1A], Tung Sanh Nguyen[1A], Vung Phuoc Doan[2A], Hoang Nguyen[1A], Bao Hoai Vo[1A], Phuc Thanh Nguyen[1A], Luu Ba Nguyen[1A], Thao Minh Nguyen[1A], Ernest F. Talarico, Jr.[3B]

[1] *Department of Anatomy and Surgical Training*

[2] *Department of Digestive Surgery*

[3] *Department of Anatomy*

[A] *Hue University of Medicine and Pharmacy, Hue University, Hue city, Việt Nam*

[B] *Tan Tao University School of Medicine, Long An Province, Việt Nam*

SUMMARY

The processus vaginalis (PV) is an embryonic diverticulum of the parietal peritoneum at the deep inguinal ring. The patent processus vaginalis (PPV) is the etiology for the development of an indirect inguinal hernia, and is associated with undescended testis, scrotal hydrocele. The aim of this study was to examine the characteristics of PPV in Vietnamese patients: a total of 309 adult patients who underwent transperitoneal laparoscopic surgery (TPLS) from March 2019 to March 2020 at Hue University of Medicine and Pharmacy Hospital. When a PPV was identified, the side and the size of PPV was recorded. Statistical analysis was done using the p-Value test for strength of evidence. The incidence of PPV of 309 subjects was 22 cases (7.1%). The rate of PPV in males was 12.1% and 3.0% in females (p = 0.002). The rate on the right side was 4.5%, 1.9% on the left and 0.7% on both sides. The mean PPV size was 6.1 mm ± 4.1 mm and 3.0 mm ± 0.7 mm in males and females, respectively (p = 0.004). Of all patients (both male and female) that had PPV, 3 patients (4.7%) had a BMI ≥ 23 and 19 patients (7.3%) had a BMI <23. Knowledge of the anatomy and embryology of PV and the mechanisms of obliteration and PPV can assist clinicians and ultrasonographers in the evaluation and treatment of patients who present with asymptomatic PPV.

Key words: Inguinal Hernia – Laparoscopic surgery – Patent processus vaginalis – Processus vaginalis

ABBREVIATIONS

Body Mass Index (BMI)

Computed Tomography (CT)

Laparoscopic Transperitoneal Surgery (LTPS)

Patent Processus Vaginalis (PPV)

Perforated Duodenal Ulcer (PDU)

Processus Vaginalis (PV)

Tunica Vaginalis (TV)

Corresponding author:
Ernest F. Talarico, Jr., Ph.D., Professor of Anatomy & Radiology. Department of Anatomy, Tan Tao University School of Medicine, Tân Đức, Đức Hòa, E.City Đức Hòa Long An, Việt Nam. E-mail: talaricojrernest@gmail.com

Submitted: November 5, 2020. **Accepted:** January 8, 2021
Not final proof's revision by the authors

INTRODUCTION

The processus vaginalis (PV) is an embryonic diverticulum (i.e., blind ended-pouch) of the parietal peritoneum at the deep inguinal ring, growing into the mesenchyme of the gubernaculum, inguinal canal and the scrotum. The PV begins forming in the 8th week of embryogenesis in both males and females (Godbole et al., 2010). In males it is linked to testicular descent down within the gubernaculum (Bouzada et al., 2017), and is found in all species where the male gonad descends through the inguinal canal (Godbole et al., 2010; Brainwood et al., 2020). Although the mechanism of its role in testicular descent remains unclear, it has been suggested that the PV dilates the pathway for testicular descent through the inguinal canal and into the scrotum (Burgu et al., 2010). PV closure (i.e., fusion) occurs at any point from a few weeks before birth (i.e., prenatally), to a few weeks after birth (i.e., postnatally) (Clarnette and Hutson, 1999; Brainwood, et al., 2020). The remaining portion around the testes becomes the tunica vaginalis (Clarnette and Hutson, 1999). In females, if the PV does not close, it forms the Canal of Nuck, an open pouch of peritoneum extending into the labia majora. It is more rudimentary than in males (Sameshima et al., 2017; Laing et al., 2007). The Canal of Nuck accompanies the gubernaculum, which differentiates to become the round ligament of the uterus (Clarnette and Hutson, 1999; Sameshima et al., 2017; Laing et al., 2007). It has been suggested that it assists the gubernaculum in the normal anteverted, anteflexed positioning of the uterus, and in preventing ovarian descent into the inguinal canal (Rees et al., 2017; Holley, 2018).

There are many theories regarding the timing of PV closure. In normal development, the PV with the exception of the TV (in males) is obliterated prenatally or early in life (Clarnette and Hutson, 1999; Mitchell, 1939; Hata et al., 2004; Van Veen et al., 2007, Moore et al., 2011). Prior studies show that prenatal obliteration occurs in 80% of males and 60% of females (Favorito et al, 2005; Rahman et al., 2009). At 8 weeks of age, 63% of male neonates may have a patent processus vaginalis (PPV) with closure or obliteration occurring up until the age of 2 years (Van Veen et al., 2007). While the incidence of PPV has been suggested to decrease after one year of age and to plateau by 3-5 years of age (Clarnette and Hutson, 1999), more recent studies have documented that 40% of males continue to have PPV and half are asymptomatic throughout life (Van Veen et al., 2007; Favorito et al., 2009). PPV in children has been studied by many authors. Weaver et al. (Weaver et al., 2016) indicated that the prevalence of the asymptomatic PPV in children who underwent laparoscopic surgery was approximately 20%.

When obliteration fails, a wide variety of conditions associated with PPV may occur (Wessem et al., 2003; Van Veen et al., 2007; Abrahamson, 1998). These conditions include indirect inguinal hernias in children and in adults, as well as hydroceles and undescended testes (Van Wessem et al., 2003; Van Veen et al., 2007; Abrahamson, 1998; Rafailidis et al., 2016; Dagur et al., 2017; Rees et al., 2017; Godbole et al., 2010, Han et al., 2002). Because cryptorchidism (i.e., undescended testes) is a risk factor in testicular cancers, PPV may also have a role in the genesis of male gonadal cancers (Talarico, Jr., et al., 2018).

A survey of the literature shows that the incidence of PPV and resulting medical conditions have not been documented in Vietnam. Although a potential association between testicular cancer in dogs and their service in Vietnam following exposure to Agent Orange has been shown (Hayes et al, 1990; Hayes et al., 1991; Hayes et al. 1995; NASEM, 2018), it is not clear that this is related to PPV or data of testicular cancers in humans. Currently, laparoscopic transperitoneal surgery (LTPS) done for different medical conditions allows surgeons to efficiently investigate the deep inguinal ring, and results in identification of PPV in patients who underwent the LTPS. In the present study, LTPS is used for examining the characteristics of PPV in the adult Vietnamese population.

MATERIALS AND METHODS

Subject Cohort

Prior to the beginning of this study and subject recruitment, approval was obtained from the

Internal Review Board of Hue University of Medicine and Pharmacy Hospital, a single tertiary care hospital. Patient consent was obtained. The benefit(s) to patients for participation in this study were none, and patient care/treatment was not affected by enrolment in, or exclusion from, this research investigation.

A total of 309 adult patients (141 males and 168 females), who underwent LTPS from March 2019 to March 2020, were enrolled in this study. All subjects in this study were given thorough physical examinations, and each had ultrasound examination to rule out the presence of asymptomatic inguinal hernia. Only in the case of patients with colon cancer, preoperative abdominal computed tomography (CT) was done. Subjects were excluded from this cohort if they (1) had multiple adhesions at the deep inguinal ring that prevented the surgeon from observation, (2) had symptoms of inguinal hernia, or (3) had prior hernia repair. The age range of subjects was 17 to 90 years with a mean age of 43.2 years. Body Mass Index (BMI) ranged from 13 to 32 kg/m^2, with a mean BMI of 21.0 kg/m^2. The reasons for LTPS were appendectomy, cholecystectomy, colectomy or perforated duodenal ulcer (PDU). The majority of patients (91.9%) underwent laparoscopic appendectomy. These demographics are summarized in Table 1.

Table 1. Patient Demographics.

VARIABLES	VALUE (n=309)
Age (years) (min - max)	43.2 ± 17.0[a] (17-90)
Sex, no. (%) Male Female	 141 male (45.6) 168 female (54.3)
BMI (kg/m^2) (min - max)	21.0 ± 2.7[a] (13-32)
Reasons for LTPS Appendectomy, no. (%) Cholecystectomy, no. (%) Colectomy, no. (%) Others (PDU,..), no. (%)	 284 (91.9) 13 (4.2) 9 (2,9) 3 (1.0)

[a] Value is mean ± standard deviation.
Laparoscopic Transperitoneal Surgery (LTPS)
Perforated Duodenal Ulcer (PDU)

LTPS Procedure and Measurements

Patients were placed in the Trendelenburg position at a 30º angle for inspection of both sides of the deep inguinal ring. A 30º telescope was used to visualize the deep inguinal ring region. The deep inguinal ring is the site where the vas deferens and the testicular vessels join to pass through the abdominal wall in males. In female, the round ligament was used for identifying the deep inguinal ring. A PPV was identified as a peritoneal protrusion at the deep inguinal ring site. When a PPV was found, the side and the size of PPV were recorded. The size of PPV was measured in comparison with the 5 mm tip of the suction-irrigation tube. All metric data were tabulated in Microsoft Excel 2016 (Microsoft®, Redmond, Washington, USA), and statistical analysis was done using the p-Value test for strength of evidence.

RESULTS

PPV Characteristics

The incidence of PPV of 309 subjects was 22 cases (7.1%). Of these cases, 17 were males (12.1%; Table 2 and Fig. 1) and 5 females (3.0%; Table 2 and Fig. 2). Overall, 14 (4.5%) were right-sided and 6 (1.9%) were left-sided (p = 0.002). In only 2 cases (0.7%), bilateral PPV was discovered. For all subjects, the mean size of the PPV was 5.6 mm; with a range of 2 mm - 15 mm. The mean PPV size was 6.1 mm ± 4.1 mm and 3.0 mm ± 0.7 mm in males and females, respectively (p = 0.004). The PPV characteristics of this cohort are summarized in the Table 2.

Table 2. Characteristics of Patent Processus Vaginalis discovered during laparoscopic procedures.

PPV CHARACTERISTICS	VALUE	P VALUE
PPV no. (%)	**22 (7.1)**	
Sex, no. (%) Male, no. (%) Female, no. (%)	 17 (12.1) 5 (3.0)	0.002
Location (side) Right side, no. (%) Left side, no. (%) Bilateral, no. (%)	14 (4.5) 6 (1.9) 2 (0.7)	0.002
Size of PPV (mm) (min - max) Male (mm) Female (mm)	**5.6 ± 3.9[a] (2 - 15)** 6.1 ± 4.1[a] 3.0 ± 0.7[a]	0.004

[a] Value is mean ± standard deviation
Patent Processus Vaginalis (PPV)

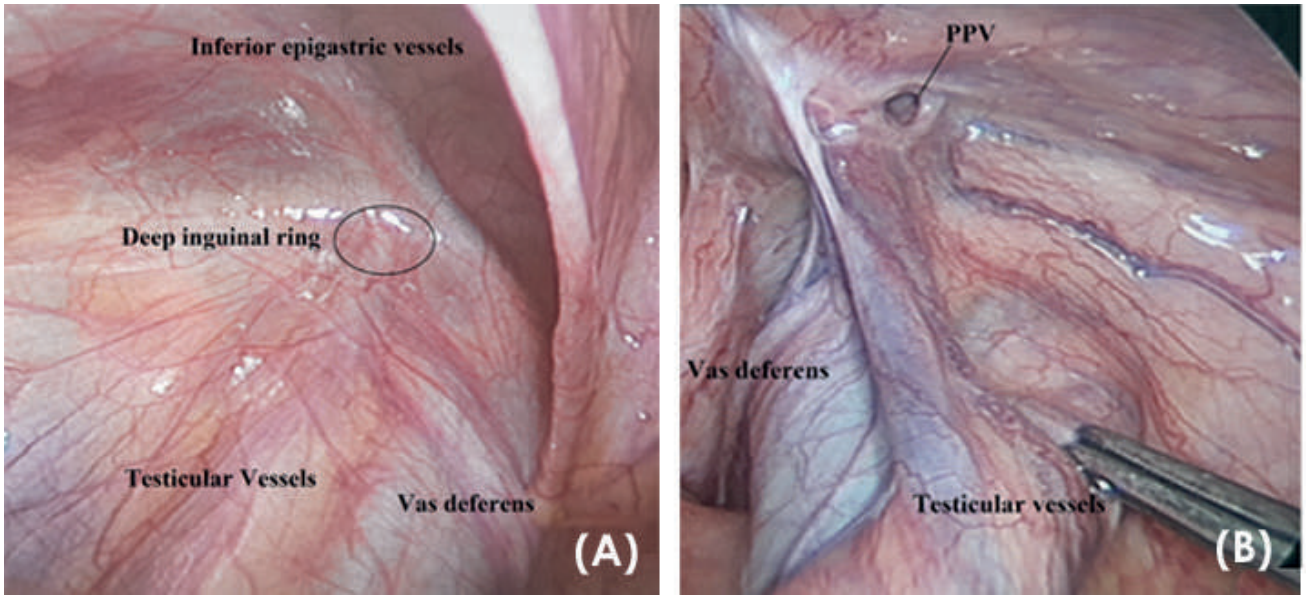

Fig. 1.- Patent Processus Vaginalis (PPV) on the left and the deep inguinal ring in Vietnamese male patients. These views are samples from an unaffected patient and an affected subject in the study cohort. (A) TPLS view of a normal deep inguinal ring (oval). (B) PPV in the area of the deep inguinal ring.

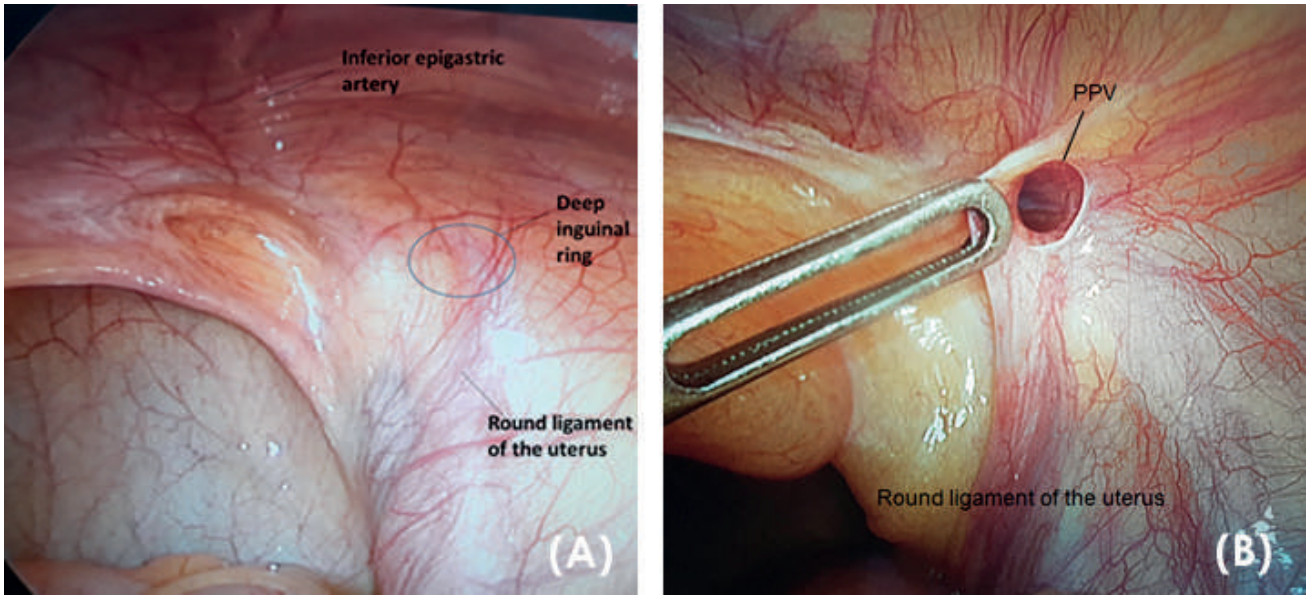

Fig. 2.- Patent Processus Vaginalis (PPV) on the left and the deep inguinal ring in Vietnamese female patients. These sample views are from an unaffected patient, and a sample subject in the study cohort. (A) TPLS view of a normal deep inguinal ring (oval). The region/course of the round ligament of the uterus is observed. (B) PPV in the area of the deep inguinal ring. Passing through the PPV at its proximal location results in entering the Canal of Nuck.

BMI and PPV

In Việt Nam, high BMI is defined as ≥ 23 (Thandassery et al., 2013; WHO, 2004). Generally, male subjects had higher BMIs than females. Of the subjects evaluated in this study, 102 (72.3%) of males and 143 (85.1%0 of females had a normal BMI, whereas 39 (27.7%) of males and 25 (14.9%) of females had an elevated BMI. Of all patients (both male and female) that had PPV, 3 patients (4.7%) had a BMI ≥ 23 and 19 patients (7.3%) had a BMI <23 ($p = 0.395$). These results are summarized in Table 3.

DISCUSSION

The PV is an embryonic protrusion of the parietal peritoneum at the deep inguinal ring. Normally, the PV is obliterated, except for the distal part covering for the testes persisting as the tunica vaginalis (Clarnette and Hutson, 1999). PPV is associated with various pathological conditions, including congenital indirect inguinal hernias and hernias in adults (Clarnette and Hutson, 1999; Van Wessman et al., 2003; Van Veen et al., 2007; Brainwood et al., 2020), and scrotal hydroceles and encrusted hydroceles of the cord (Brainwood

et al., 2020). Many investigations suggest a strong relationship between PPV and cryptorchidism (Favorito et al., 2005; Cives et al., 1996; Lee et al., 2015). Secondarily, due to the association between cryptorchidism and testicular cancers, PPV may also be related to seminomas and non-seminoma cancers (Talarico et al., 2018).

The mechanism(s) of PV closure are not understood, but seem to involve apoptosis of smooth muscle cells within the PV (Mouravas et al., 2010; Hosgor et al., 2004). Currently, it is thought that obliteration occurs in three stages (I, II and III) in males in contrast to two stages in females (Rafailidis et al., 2016; Rees et al., 2017; Brainwood et al., 2020). Stage I is proximal closure of the deep inguinal ring sealing off the PV from the peritoneum (Rafailidis et al., 2016). Stage I occurs in both males and females. Stage II in males is the distal closure of the PV superior to the testis. Stage III is atresia of the funicular process (i.e., the remaining tube-like structure between these two proximal and distal points of closure) (Brainwood et al., 2020; Singh et al., 2010). However, the distalmost portion of the PV remains forming the TV. In contrast, Stage II (the final stage) in females is the atresia of the Canal of Nuck (Rees et al., 2017). Failure of closure can occur at any stage. However, when closure fails across all three stages, the PPV extends from the deep inguinal ring to the scrotum (or labia majora in females), and is thought to result in indirect inguinal hernias and hydroceles (Rafailidis et al., 2016). This communication may also allow the movement of pus or an infectious process into the scrotum or labia majora, as well as the implantation of endometriosis or zygotes at any location within the Canal of Nuck (Rahman et al., 2008; Okoshi et al., 2017; Shehzad and Riaz, 2011; Gaeta et al., 2010; Noguchi et al., 2014).

A survey of the published literature shows that most studies on PPV were conducted on children, and that PPV studies are quite rare in adults. Still further, no studies were found where the subject cohort was a Vietnamese population. In the present work, of 309 subjects examined only 22 (7.1%) had asymptomatic PPV (Table 2). The mean size of PPV was 5.6 ± 3.9 mm, and the mean size of PPV in males was higher than in females: 6.1 mm vs 3.0 mm (p = 0.004) (Table 2). These results are similar to those of Watson et al. (Watson et al, 1994) and Van Veen et al. (Van Veen et al., 2007), who reported rates of asymptomatic PPV in adults of 9.0% and 15.4%, respectively. Further, the presence of asymptomatic PPV in Vietnamese subjects did not correlate to age. This supports a study done by Van Veen et al. (Van Veen et al., 2007) that showed no significant correlation between age and the prevalence of PPV. In contrast, Weaver et al. (Weaver et al., 2016) examined 1548 infants and children who underwent a non-hernia-related TPLS and found the rate of asymptomatic PPV was 20%.

In this Vietnamese cohort, there was a significant difference between the rate of PPV (in adults) on the right and left sides: 4.5% vs 1.9% for the right side and left side, respectively (p = 0.002) (Table 2). Comparing these results to published studies, many authors reported a difference of PPV between prevalence on the right side and the left side. In one study, the rate of PPV in children was much higher on the right side (46%) in contrast to the left side (14%) (Weaver et

Table 3. Body Mass Index relationship to Sex and PPV.

	Male **No. (%)**	**Females** **No. (%)**	**Total Subjects** **No. (%)**	**Obliterated PV** **No. (%)**	**PPV** **No. (%)**
BMI (kg/m^2) **<23**	102 (72.3%)	143 (85.1%)	245 (79.3%)	226 (78.7%)	19 (7.3%)
≥23 (high)	39 (27.7%)	25 (14.9%)	64 (20.7%)	61 (21.3%)	3 (4.7%)
Total =	141	168	309	287	22
					High BMI in males vs. females, p = 0.006 PPV in normal vs. High BMI, p = 0.395

Body Mass Index (BMI)
Persistent Processus Vaginalis (PPV)
Processus Vaginalis (PV)

al., 2016). It is suggested that one reason for this is that the left PV is obliterated earlier; therefore, the PPV prevalence is higher than on the left side (Clarnette and Hutson, 1999; Brainwood et al., 2020). From a clinical viewpoint, it is interesting to note that the incidence of a contralateral PPV in children who also had a unilateral inguinal hernia was very high. Rowe et al. (Rowe et al., 1969) studied 2764 patients ranging from 1 day to 16-years-old who underwent surgery for inguinal hernia, and showed that the rate of PPV on the side opposite the hernia was 63% in the first 2 months of life, and 41% in patients from the age of 2 to 16 years. George et al. (George et al., 1996) reported a similar rate of PPV on the side opposite of 41% in patients under 10 years of age.

There was a significant difference in the comparison between the rate of PPV in Vietnamese males and females, or 12.1% and 3.0%, respectively ($p = 0.002$). Prior studies done in different populations also show similar results. Watson et al. (Watson et al., 1994) reported the rate of PPV of 19% and 8% in American males and females, respectively. Of children born and living near Aberdeen, Scotland, the rate of PPV was 84.2% in males and 70% in females. (Mitchell, 1939). Van Veen et al. (Van Veen et al., 2007) demonstrated the incidence of PPV was 3.44 times higher in men born and living in the Netherlands (30.9% in men vs 9.5% in women).

PPV is the aetiology for the development of indirect inguinal hernia in children and in adult (Van Veen et al., 2007; Weaver et al., 2016). The higher incidence of PPV in men and on the right side might explain the reason why the indirect hernias in men and on the right side higher than in women and on the left side (Zhao et al., 2017). Rowe et al. (Rowe et al., 1969) reported that the prevalence of the inguinal hernia on the right, on the left and bilateral were 60%, 30%, 10% respectively. According to Van Veen et al. (Van Veen et al., 2007), the incidence of indirect inguinal hernias was five times higher in men.

BMI is a person's weight in kilograms divided by the square of height in meters (kg/m^2). A high BMI can be an indicator of high body fatness. BMI can be used to screen for weight categories that may lead to health problems, but it is not diagnostic of the body fatness or health of an individual. The results of the present research showed that in all subjects who had PPV, 3 patients (4.7%) had a BMI ≥ 23 and 19 patients (7.3%) hnd a BMI <23. Prior studies suggest that the incidence of primary inguinal hernia decreases as BMI increases (Zendejas et al., 2014; Anders et al., 2008). However, there seems to be an association between high BMI and recurrent inguinal hernia (Anuk, 2018). Based on the present study and a review of the literature, it is not clear whether there is an association between PPV and low BMI respective to the development of inguinal hernias. The relationship between recurrent inguinal hernia, high BMI and prior PPV was not examined in this study.

Limitations

Regarding the present work, some investigators may raise concern that clinical examination (i.e., physical examination) and ultrasound study, rather than CT, were used to rule out the presence of asymptomatic inguinal hernia. The availability of CT and nuclear imaging modalities throughout Vietnam is relatively limited. However, studies do confirm that ultrasound can accurately diagnose and rule out occult inguinal hernia in patients (Bradley et al., 2003; Dreuning et al. 2019). Further, it is difficult to measure the intraoperative size of the PPV when performing a laparoscopic surgery. Therefore, in this study the size of PPV was measured in comparison with the tip of suction-irrigation tube of 5 mm. Lastly, some investigators may suggest that the use of pneumoperitoneum could have some influence in increasing the size of PPV. Two studies suggest that pneumoperitoneum may assist in the detection of contralateral PPV (Palmer and Rastinehad, 2007; Onal and Kogan, 2008), but a survey of the literature does not document a study that suggest that pneumoperitoneum will have an effect of increasing the size of a PPV.

CONCLUSION

Asymptomatic PPV has a suggested prevalence of 7.1% in Vietnamese adults, and is more common in males than female and on the right side. PPV can result in a spectrum of pathologies

beyond foetal life. Knowledge of the anatomy and embryology (i.e., development and mechanisms of obliteration) of PV and PPV can assist clinicians and ultrasonographers in the evaluation and treatment of patients who present with asymptomatic PPV.

ACKNOWLEDGEMENTS

The authors wish to express their sincere gratitude to the patients who agreed to participate in this investigation. We also wish to thank the surgical technicians of Hue University of Medicine and Pharmacy Hospital (Việt Nam). The authors are appreciative for the editorial assistance and manuscript review of Michael J. Gnezda, B.S., graduate of the Indiana University - Northwest Campus (Gary, IN USA), human cadaver prosector and assistant instructor for human gross anatomy.

REFERENCES

ABRAHAMSON J (1998) Etiology and pathophysiology of primary and recurrent groin hernia formation. *Surg Clin North Am*, 76(6): 953-972.

ANUK T (2018) Factors influencing recurrence in inguinal herniorrhaphy. *Ann Med Res*, 25(4): 619-622.

BRADLEY M, MORGAN D, PENTLOW B, ROE A (2003) The groin hernia - an ultrasound diagnosis?. *Ann R Coll Surg Engl*, 85(3): 178-180.

BOUZADA J, VAZQUEZ T, DURAN M, DELMAS V, LARKIN T, CUESTA MA, SANUDO J (2017) New insights into the morphogenesis of the gubernaculum testis and the inguinal canal. *Clin Anat*, 30(5): 599-607.

BRAINWOOD M., BEIRNE G, FENECH M (2020), Persistence of the processus vaginalis and its related disorders. *AJUM*, 23(1): 22-29.

BURGU B, BAKER LA, DOCIMO SG (2010) Chapter 43 - cryptorchidism A2 - Gearhart, John P. *In:* Rink RC, Mouriquand PDE (editors). *Pediatric Urology,* 2nd ed. W.B. Saunders Philadelphia, pp 563-576.

CIVES RV, CASASNOVAS AB, MARTIN AA, ARIAS MP, SIERRA RT (1996) The influence of patency of the vaginal process on the efficacy of hormonal treatment of cryptorchidism. *Eur J Pediatr*, 155(11): 932-936.

CLARNETTE TD, HUTSON J (1999) The development and closure of the processus vaginalis. *Hernia*, 3: 97-102.

DREUNING KMA, TEN BROEKE CEM, TWISK JWR, ROBBEN SGF, RIJN RRV, VERBEKE JIML, VAN HUREN LWE, DERIKX JPM (2019) Diagnostic accuracy of preoperative ultrasonography in predicting contralateral inguinal hernia in children: a systematic review and meta-analysis. *Eur Radiol*, 29(2): 866-876.

FAVORITO LA, COSTA WS, SAMPAIO FJ (2005) Relationship between the persistence of the processus vaginalis and age in patients with cryptorchidism. *Int Braz J Urol*, 31(1): 57-61.

GAETA M, MINUTOLI F, MILETO A, RACCHIUSA S, DONATO R, BOTTARI A, BLANDINO A (2010) Nuck canal endometriosis: MR imaging findings and clinical features. *Abdom Imaging*, 35(6): 737-741.

GEORGE B, HOLCOMB W, MORGAN WM, BROCK JW (1996) Laparoscopic evaluation for contralateral patent processus vaginalis: Part II. *J Pediatr Surg*, 31(8): 1170-1173.

GODBOLE PP, STRINGER MD (2010) Chapter 44 - patent processus vaginalis A2 - Gearhart, John P. In: Rink RC, Mouriquand PDE (editors). *Pediatric Urology*, 2nd ed. W.B. Saunders Philadelphia, pp 577-584.

HAN CH, KANG SH (2002) Epididymal anomalies associated with patent processus vaginalis in hydrocele and cryptorchidism. *J Korean Med Sci,* 17*:* 660-662.

HATA S, TAKAHASHI Y, NAKAMURA T, SUZUKI R, KITADA M, SHIMANO T (2004) Preoperative sonographic evaluation is a useful method of detecting contralateral patent processus vaginalis in pediatric patients with unilateral inguinal hernia. *J Pediatr Surg*, 39(9): 1396-1399.

HAYES HM, TARONE RE, CANTOR KP (1995) On the association between canine malignant lymphoma and opportunity for exposure to 2,4-dichlorophenoxyacetic acid. *Environ Res*, 70(2): 119-125.

HAYES HM, TARONE RE, CANTOR KP, JESSEN CR, MCCURNIN DM, RICHARDSON RC (1991). Case-control study of canine malignant lymphoma: positive association with dog owner's use of 2,4-dichlorophenoxyacetic acid herbicides. *J Natl Cancer Inst*, 83(17): 1226-1231.

HAYES HM, TARONE RE, CASEY HW, HUXSOLL DL (1990) Excess of seminomas observed in Vietnam service U.S. military working dogs. *J Natl Cancer Inst*, 82(12): 1042-1046.

HOLLEY A (2018) Pathologies of the canal of Nuck. *Sonography,* 5(1)*:* 29-35.

HOSGOR M, KARACA I, OZER E, ERDAG G, ULUKUS C, FESCEKOGLU O, AIKAWA M (2004) The role of smooth muscle cell differentiation in the mechanism of obliteration of processus vaginalis. *J Pediatr Surg*, 39(7): 1018-1023.

LAING FC, TOWNSEND BA, RODRIGUEZ JR (2007) Ovary-containing hernia in a premature infant: sonographic diagnosis. *J Ultrasound Med*, 26(7): 985-987.

LEE DGI, LEE YSUK, PARK KH, BAEK M (2015) Risk factors for contralateral patent processus vaginalis determined by transinguinal laparoscopic examination. *Exp Ther Med*, 9(2): 421-424.

MITCHELL GAG (1939) The condition of the peritoneal vaginal processes at birth. *J Anat*, 73(Pt 4): 658-661.

MOORE KL, PERSAUD TVN, TORCHIA MG (2011) Before we are born: Essentials of Embryology and Birth Defects. *Elsevier Health Sciences / Mosby*, Maryland Heights, Missouri.

MOURAVAS VK, KOLETSA T, SFOUGARIS DK, PHILIPPOPOULOS A, PETROPOULOS AS, ZAVITSANAKIS A, KOSTOPOULOS I (2010) Smooth muscle cell differentiation in the processus vaginalis of children with hernia or hydrocele. *Hernia*, 14(2): 187-191.

NATIONAL ACADEMIES OF SCIENCES, ENGINEERING, AND MEDICINE (2018) Veterans and Agent Orange: Update 11 (2018). Washington, DC, *NAP*, https://doi.org/10.17226/25137.

NOGUCHI D, MATSUMOTO N, KAMATA S, KANEKO K (2014) Ectopic pregnancy developing in a cyst of the canal of Nuck. *Obstet Gynecol*, 123(2 Pt 2 Suppl 2): 472-476.

OKOSHI K, MIZUMOTO M, KINOSHITA K (2017) Endometriosis-associated hydrocele of the canal of Nuck with immunohistochemical confirmation: a case report. *J Med Case Rep*, 11(1): 354.

ONAL B, KOGAN BA (2008) Additional benefit of laparoscopy for nonpalpable testes: finding a contralateral patent processus. *Ped Uro*, 71(6): 1059-1063.

PALMER LS, RASTINEHAD A (2008) Incidence and concurrent laparoscopic repair of intra-abdominal testis and contralateral patent processus vaginalis. *Urology*, 72(2): 297-299.

RAFAILIDIS V, VARELAS S, APOSTOLOPOULOU F, RAFAILIDIS D (2016) Nonobliteration of the processus vaginalis. Sonography of related abnormalities in children. *J Ultrasound Med,* 35(4): 805-818.

RAHMAN N, LAKHOO K (2009) Patent processus vaginalis: a window to the abdomen. *Afr J Paediatr Surg*, 6(2): 116-117.

REES MA, SQUIRES JE, TADROS S, SQUIRES JH (2017) Canal of Nuck hernia: a multimodality imaging review. *Pediatr Radiol*, 47(8): 893-898.

ROSEMAR A, ANGERÅS U, ROSENGREN A (2008) Body mass index and groin hernia: a 34-year follow-up study in Swedish men. *Ann Surg*, 247(6): 1064-1068.

ROWE MI, COPELSON LW, CLATWORTHY HW (1969) The patent processus vaginalis and the inguinal hernia. *J Pediatr Surg*, 4(1): 102-107.

SALEEM MM (2008) Scrotal abscess as a complication of perforated appendicitis: a case report and review of the literature. *Cases J*, 1(1): 165:1-4.

SAMESHIMA YT, YAMANARI MG, SILVA MA, NETO MJ, FUNARI MB (2017) The challenging sonographic inguinal canal evaluation in neonates and children: an update of differential diagnoses. *Pediatr Radiol*, 47(4): 461-472.

SHEHZAD KN, RIAZ AA (2011) Unusual cause of a painful right testicle in a 16-year-old man: a case report. *J Med Case Rep*, 5(1): 27:1-3.

SINGH AK, KAO S, D'ALESSANDRO M, SATO Y (2010) Case 164: funicular type of spermatic cord hydrocele. *Radiology*, 257*(3):* 890-*89*2.

TALARICO, JR. EF, MAS JL, JONES JA (2018) A comprehensive anatomical characterization and radiographic study of stage III testicular cancer in a 31-year-old male patient. *Eur J Anat*, 22(3): 241-256.

THANDASSERY RB, APPASANI S, YADAV TD, DUTTA U, INDRAJIT A, SINGH K, KOCHHAR R (2014) Implementation of the Asia-Pacific guidelines of obesity classification on the APACHE-O scoring system and its role in the prediction of outcomes of acute pancreatitis: a study from India. *Dig Dis Sci*, 59(6): 1316-1321.

VAN VEEN RN, VAN WESSEM KJP, HALM JA, SIMONS MP, PLAISIER PW, JEEKEL J, LANGE JF (2007) Patent processus vaginalis in the adult as a risk factor for the occurrence of indirect inguinal hernia. *Surg Endosc*, 21: 202-205.

VAN WESSEM KJP, SIMONS MP, PLAISIER MP, LANGE JF (2003) The etiology of indirect inguinal hernias; congenital and/or acquired? *Hernia*, 7(2): 76-79.

WATSON RW, SHARP KW, VASQUEZ JM (1994) Incidence of inguinal hernias diagnosed during laparoscopy. *South Med J*, 87(1): 23-25.

WEAVER KS, POOLA AS, GOULD JL, SHARP SW, HOLCOMB GW, ST. PETER SD (2016) The risk of developing a symptomatic inguinal hernia in children with an asymptomatic patent processus vaginalis. *J Pediatr Surg*, 22(1): 60-64.

WHO (2004) Appropriate body-mass index for Asian populations and its implications for policy and intervention strategies. *Lancet*, 363(9403): 157-163.

ZHAO J, CHEN Y, LIN J, JIN Y, YANG H, WANG F, ZHONG H, ZHU J (2017) Potential value of routine contralateral patent processus vaginalis repair in children with unilateral inguinal hernia. *Br J Surg*, 104(1): 148-151.

Toxic effects of aluminium on testis in presence of ethanol coexposure

Buddhadeb Ghosh[1], Ravi Kant Sharma[1], Suman Yadav[2]

[1] Department of Anatomy, Government Medical College, Amritsar, Punjab, India

[2] Department of Anatomy, Dr RP Government Medical College, Kangra, Himachal Pradesh, India

SUMMARY

Both aluminium and ethanol are pro-oxidants and toxic. Uncontrolled use of aluminium and increasing trends of ethanol consumption in India increased the chance of co-exposure to aluminium and ethanol. There are possibilities, that both of them follow common mechanisms to produce reproductive toxicity. The present study was planned to identify the effects of aluminium administration on the microscopic structure of testis in presence of ethanol.

Sixteen male rats were divided into one vehicle control and three experimental groups and exposed to aluminium (4.2 mg/kg body weight) and ethanol (1 g/kg body weight) for 3 months. After the exposure period, testes were processed for light microscopic examination. Aluminium-treated and ethanol-treated rats showed loss of normal distribution of spermatogenic cells in the seminiferous tubules and few fragmented sperms in the lumen. Combined treatment of aluminium and ethanol showed acute degeneration of the spermatogenic epithelium. Vacuolar degenerative changes appeared in the cytoplasm of the spermatogenic epithelium and Sertoli cells. Abnormal distribution of spermatozoa was seen in the lumen. Most of the tubules showed that the germ layers were detached from the basal lamina. It has been suggested that the ethanol induced augmentation of impacts of aluminium on the testis.

Key words: Aluminium – Ethanol – Testis – Seminiferous tubule – Histopathology

INTRODUCTION

Aluminium (Al) is the 3rd most common element found in nature after silicon and oxygen, comprising approximately 8% of the earth crust (Elif et al., 2018). Al is a ubiquitous element with known toxicity in the human body, mainly in the central nervous system, and may act as foetal teratogen (Dominigo, 1995; Nayak, 2010). In the 70s of the last century, the medical fraternity considered the toxicity of the so-called 'biologically inert' metal, aluminium. A large volume of research, since then, has been conducted to get insight of and combat Al toxicity. While the awareness about the toxic effects is bringing down the daily and avoidable uses of the Al in developed countries, Al wares are the commonly used cooking utensils and containers in India, as they are the cheapest. In 1989, a joint FAO/WHO Expert committee on food additives (JECFA) recommended a provisional tolerable weekly intake (PTWI) of 7.0 mg / kg body weight aluminium. This was changed in 2007 to 1.0mg /

Corresponding author:
Dr. Buddhadeb Ghosh. Department of Anatomy, Government Medical College, Amritsar, Punjab, India. Mob +918894114210. E-mail: debanatomy@gmail.com / dr.ghosh86@gmail.com

Submitted: May 12, 2020. **Accepted:** January 12, 2021

kg body weight because of potential effects on the reproductive system and the developing nervous system (Kawahara et al., 2011). Al toxicity causes Alzheimer disease (AD), dialysis dementia, parkinsonism, and amyotrophic lateral sclerosis. It also affects skeletal system brain tissue, bone, blood cells, liver and kidney (Berihu, 2015). It has been shown that Al has severe toxic effects on the mouse embryo/foetus, which leads to significant increase in resorption rate, decreased body weight and major anomalies, foetal death, and skeletal anomalies (Karimpour, 2005). Transplacental passage of Al from pregnant mice to the foetus's organs is noted after maternal transcutaneous exposure (Anane et al., 1997). It has been reported that oral Al exposure increases the incidence of foetal abnormalities in rats and mice (Agrawal, 1996). Exposure to Al is inevitable because of its abundance in the earth's crust, use in cookware, foods and drinks, medications, etc. (Nayak, 2010). The nervous system is the most sensitive to Al toxicity, as it induces cognitive deficiency and dementia in brain. Accumulation of excessive amounts of Al leads to testicular dysfunction in both humans and animals. High Al contents in human testes, spermatozoa, seminal plasma, Leydig cells, blood and urine, were associated with impaired sperm quality and viability (Hovatta et al., 1998; Reusche et al., 1994). Alteration in the microscopy of testis (Kutlubay et al., 2007), deterioration in spermatogenesis and sperm quality and alterations in antioxidant enzymes (Yousef et al., 2005, 2007), interruption in sex hormone secretion (Guo et al., 2005) are several of the aspects suggested that Al exposure causes adverse impact on male reproduction. Addiction to alcohol abuse led to increased risk of major depression (Fergusson et al., 2009). Alcohol has impacts on the central nervous system. It increases oxidative stress, and impairs cerebral vasoreactivity, and thus may result in an increase in ischemic stroke and induce brain damage (Sun et al., 2008). Alcohol consumption can harm the foetus during pregnancy. It also may have toxic effects in the reproductive process through miscarriage, aneuploidy, anomaly, disordered foetal growth, developmental delay and perinatal death (Fraser, 2006). The effects of alcohol on the reproductive system become very interesting for the researcher. The most important endocrine consequences of long-term alcohol use are its effects on the gonads. Chronic alcohol consumption leads to disorder of spermatogenesis in human (Pajarinen, 1996). Alcohol toxicity in male induces erectile dysfunction and infertility, and it is explained by alcohol induced reduction in testosterone (Bannister et al., 1987). Chronic ethanol ingestion confirms gonadal dysfunction and it is suggested that alcohol is a testicular toxin (Van Thiel et al., 1975). Testicular atrophy and impaired testosterone production are due to alcohol consumption in men, and result in impotence, infertility, and reduced male secondary sexual characteristics (Adler, 1992). Ethanol-treated animals enhanced testicular DNA fragmentation, and increased the number of apoptotic spermatogonia as well as spermatocytes (Zhu et al., 2000; Bamac et al., 2005). Alcohol also causes an adverse effect on the secretory function of Sertoli cells. It is also noted that moderate alcohol consumption increases the HDL level and reduces the cholesterol level in the blood; it also reduces the risk of stroke and stress, anxiety and tension and AD (Elizabeth et al., 2000). Moderate alcohol consumption and risk of coronary heart disease among women with type 2 diabetes mellitus (Regan, 2000). It is also noted that moderate alcohol consumption lowers the risk of type 2 diabetes (Koppes, 2005). Consumption of large amounts of alcohol can result in acute and delayed impairments in cognitive and executive functions, spatial learning and memory impairment. These impairments lead to medical and social problems including dementia, violence and decreased work productivity (Kuzmin, 2013). However, the Al load caused by Al exposure may be influenced by ethanol co-exposure (Nayak, 2006; Nayak et al., 2013). Consumption of alcohol is suggested to increase susceptibility of rats to certain effects of Al, but it is also noted that consumption of beer may supply a protective for the toxic effect of Al (Flora, 1991; Pena, 2007; Gonzalez-Munoz, 2008).

The brain is the primary organ affected by Al toxicity. Only a few studies have described its effect on the structure of the testis. Furthermore, the use of ethanol against Al toxicity needs to be

investigated. Many studies on the effects of alcohol on male reproductive system but combined effects of Al and ethanol has not been documented yet. The aim of the study was to identify the effects of Al administration on the microscopic structure of testis in the presence of ethanol.

MATERIALS AND METHODS

Sixteen Wistar male rats of an average weight of 200 g and an average age of 120 days were used in this study. Animals were kept individually in plastic cages in noise-free, air-conditioned animal house with temperature maintained at 75°F and on a light dark cycle of 12:12 hours. Humidity was maintained with a minimum of 50%. Rats were fed on diet pellets, tap water ad libitum and treated with utmost humane care. The experimental protocol was approved by the Institute of Animal Ethics Committee and the procedures were performed according to the guidelines of the Committee for the Purpose of Control and Supervision of Experiments on Animals (CPCSEA, India). After one week of acclimatization, rats were randomly divided (with the help of Random Allocation Software Version 1.0, May 2004) into 4 groups, namely:

Group I (Vehicle Control group, 4 animals) received the normal saline water.

Group II (Experimental group, 4 animals) received aluminium chloride (4.2 mg/kg body weight) dissolved in drinking water containing sodium chloride (0.9%).

Group III (Experimental group, 4 animals) received ethanol (1g/kg body weight) dissolved in drinking water containing sodium chloride (0.9%).

Group IV (Experimental group, 4 animals) received aluminium chloride (4.2 mg/kg body weight) and also ethanol (1 g/ kg body weight).

The treatments were carried out through oral feeding gavage once daily for periods of 90 days. Their weights were recorded daily. After 3 months, the animals were anaesthetized with pentobarbitone (i.p) and an intracardiac perfusion of normal saline followed by 10% formaldehyde saline was performed. The testis of both groups of animals were dissected out and blotted. The testes were separated from the epididymis. After transverse sectioning, the testes of all animals were processed for routine paraffin embedding.

Histological study

The testes were fixed in 10% formaldehyde solution, passed through ascending series of ethanol baths, cleared in xylene and embedded in paraffin. Tissues were sectioned at 5 µm and stained with Haematoxylin and Eosin (H&E) staining according to John D Bancroft Theory and Practice of Histological Techniques. Haematoxylin and eosin staining slides were deparaffinized through xylene (2-3 min) and absolute alcohols (1-2 min), then dipped in 95 % alcohol, followed by 70% alcohol, 50% alcohol and 30% alcohol; then washed thoroughly with distilled water and placed in haematoxylin for 3-5 minutes, and then the section examined after rinse with distilled water under low magnification of microscope to confirm its over-staining; then rinsed in distilled water and the slide placed in another jar of 30% alcohol for 3 minutes, then placed in 50% alcohol, followed by 70% alcohol and 95% alcohol. Then the slides were counter-stained in 0.5-1 % eosin in 90% alcohol for 30 seconds to 1 minute until the cytoplasm took a deep pink stain, and then dipped in 95% alcohol for a few second and placed into absolute alcohol for 3 minutes. To ensure full dehydration, it was next kept in absolute alcohol for 3 minutes. Then the slides were transferred in xylene for 2 minutes and followed by next xylene for 2 minutes until the section appeared absolutely clear or transparent. The stained slides were labelled properly and placed under light microscope, obtained with a digital camera attached to the microscope for observation.

RESULTS

The general health status of all the rat groups was good and water and fodder intakes were adequate during the experimental time. No significant behavioural alteration or illnesses were found.

Seminiferous tubules from the vehicle control group rats showed circular or oval outlines with normal stratified germinal epithelium, containing spermatogenic cells resting on the basal lamina.

Spermatogonia, primary spermatocyte, secondary spermatocyte, spermatids were identified, and the lumen of the tubules contained spermatozoa. Leydig cells were present in between seminiferous tubules. (Figs. 1a, 1b).

Aluminium-treated rats showed loss of normal distribution of spermatogenic cells in the seminiferous tubules and few fragmented sperms in the lumen (Figs. 2a, 2b). Ethanol-treated rats also showed degeneration of spermatogenic epithelium and fragmented sperm in the lumen. Few seminiferous tubules showed a single layer of basal spermatogonia (Figs. 3a, 3b). A significantly acute degeneration of the spermatogenic epithelium was observed in the combined treatment group compared to the other groups. Vacuolar degenerative changes appeared in the cytoplasm of the spermatogenic epithelium and Sertoli cells. Abnormal distribution of spermatozoa were seen in the lumen. Most of the tubules showed that the germ layers were detached from the basal lamina (Figs. 4a, 4b).

DISCUSSION

The testes are male gonads which are responsible for testosterone hormone and for generating sperm. Seminiferous tubules are present within the testis and are responsible for spermatogenesis (Elaine, 2004; Scott, 2000). Microscopic examination of rats orally treated with Al induced

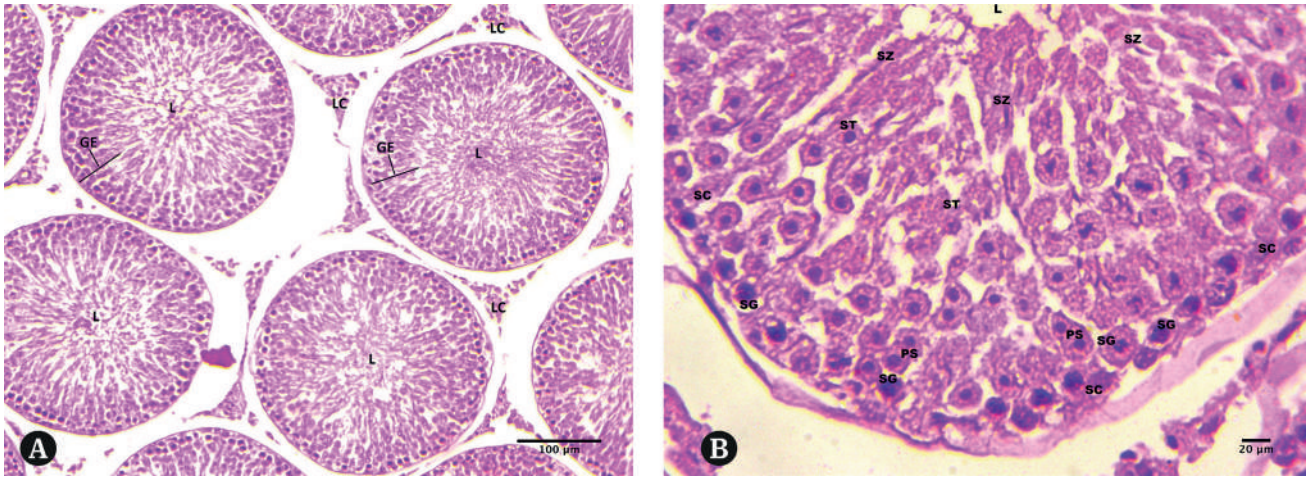

Fig. 1.- Testis of the control group I (Haematoxylin & Eosin staining). **1a:** cross section of the seminiferous tubules showing germinal epithelium (GE) containing cells of the spermatogenic cells with spermatozoa in the lumen (L). Interstitial Leydig cell (LC) seen between the seminiferous tubules. (x100, scale bar = 100 µm). **1b:** cross section of the seminiferous tubules showing spermatogenic cells, Spermatogonia (SG), Primary spermatocyte (PS), Spermatids (ST), and the lumen (L) containing spermatozoa (SZ). Sertoli cell (SC). (x400, scale bar = 20 µm).

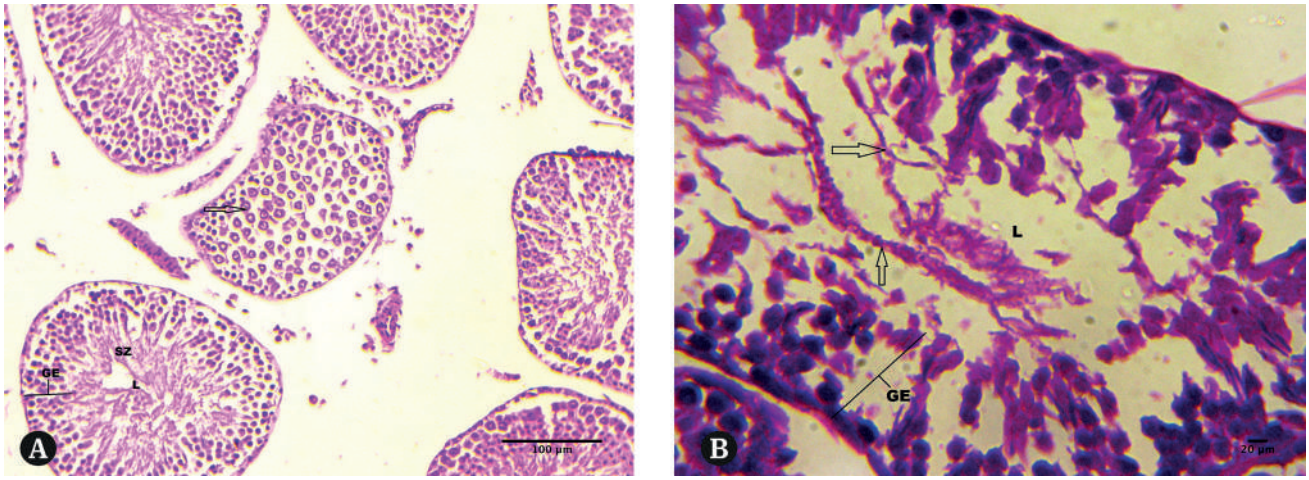

Fig. 2.- Testis of the aluminium treated group II (Haematoxylin & Eosin staining). **2a:** cross section of the seminiferous tubules showing loss of normal distribution of germinal epithelium (GE). Spermatozoa (SZ) in the lumen (L). Vacuolar cytoplasm (arrow) with loss of normal distribution of the spermatogenic cells seen. (x100, scale bar = 100 µm). **2b:** cross section of the seminiferous tubules showing loss of normal distribution of germinal epithelium (GE). Fragmented sperms (arrow) in the lumen (L). (x400, scale bar = 20 µm).

marked degeneration and necrosis of germ cells lining seminiferous tubules, as well as interstitial edema with complete absence of germ cells (Khattab, 2007). Deleterious effects of Al treatment for 2 to 5 weeks and its histopathological changes in testicular tissues showed spermatogenetic loss as necrosis in the spermatids and spermatozoa (Guo et al., 2005). Al exposures of experimental animals induce coiling tail in rats' sperm, cytoplasmic droplet in rats, interstitial edema, Leydig cell proliferation and sperm hyperemic blood vessel (Aitken et al., 2008). The present study showed morphological changes in the seminiferous tubule with vacuolar cytoplasm, with loss of normal distribution of the epithelial lining with few fragmented sperms in the lumen.

It is also reported that aluminium chloride (AlCl3) induced histological and ultrastructural changes in the testis with severe damage of germ cells, and the electron microscopy observations include atrophy of the tubular membrane, mitochondria, endoplasmic reticulum, golgi apparatus and nucleus (Khattab, 2007). Histological and ultrastructural studies on the testis of rats after treatment with aluminium chloride showed that administration of sodium fluoride together with AlCl3 to mice for 30 days caused inhibition of spermatogenesis and formation of giant cells (Chinoy et al., 2005). Apoptosis has been detected in spermatogonia and primary spermatocytes after AlCl3 administration (Abdel Moneim, 2013) and primarily results from microtubule targeting

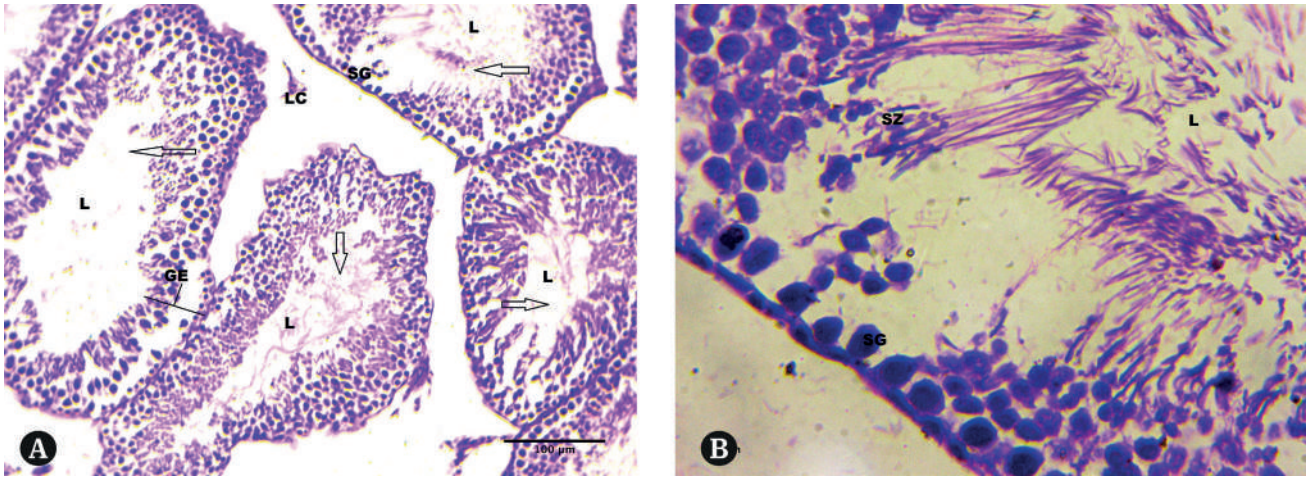

Fig. 3.- Testis of the ethanol treated group III (Haematoxylin & Eosin staining). **3a:** cross section of the seminiferous tubules which attained different shapes and hypocellularity reduction in cells of the spermatogenic series of germinal epithelium (GE) and widened empty (arrow) lumen (L). Few interstitial Leydig cell (LC) seen between the seminiferous tubules. (x100, scale bar = 100 µm). **3b:** cross section of the seminiferous tubules. Most of the spermatocyte appeared with dark stained pyknotic nuclei. Spermatogonia (SG), Spermatozoa (SZ) in the lumen (L). (x400, scale bar = 20 µm).

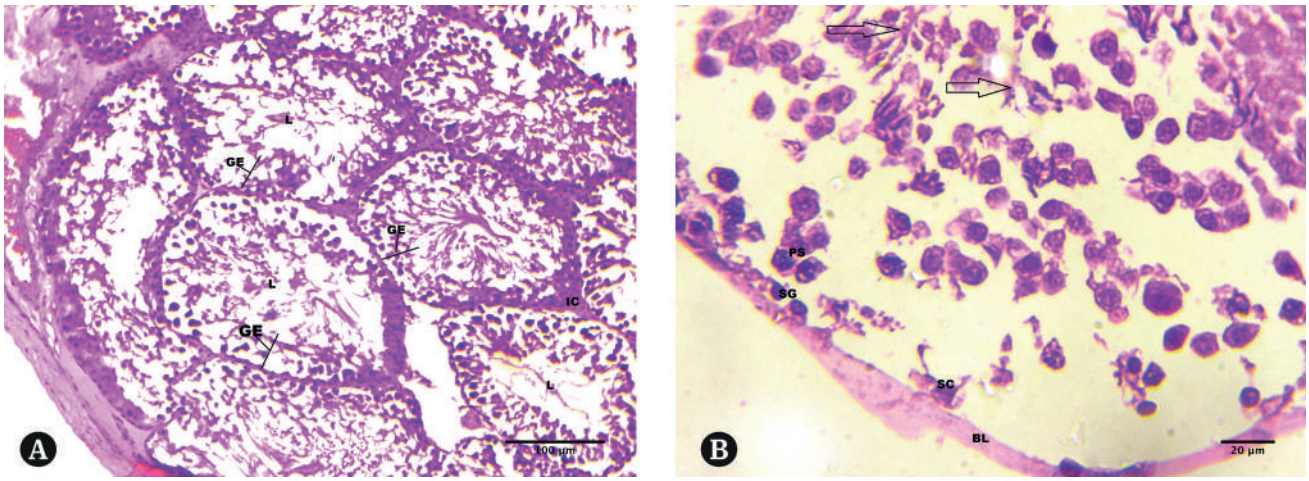

Fig. 4.- Testis of the aluminium and ethanol treated group IV (Haematoxylin & Eosin staining). **4a:** many distorted seminiferous tubules. Most of the tubules show marked reduction in the thickness of the germinal epithelium (GE). Fragmented sperms in the lumen (L). Few interstitial Leydig cell (LC) seen between the seminiferous tubules. (x100, scale bar = 100 µm). **4b:** acute degeneration of the spermatogenic cells. Spermatogonia (SG), Primary spermatocyte (PS), most of the tubules showed that the germ layers were detached from the basal lamina (BL), disintegrated Sertoli cell (SC) and abnormal distribution of spermatozoa (arrow) seen. (x400, scale bar = 20 µm).

and mitotic arrest. Saberzadeh et al. (2016) reported that Al-maltolate induced apoptosis in PC12 cells. It was reported that oxidative stress can induce male infertility and cause an increase in germ cell apoptosis and subsequent hypo spermatogenesis. Al is considered to be a non-redox active metal; it promotes biological oxidation both in vitro and in vivo because of its pro-oxidant activity (Turner and Lysiak, 2008). It is also reported that AlCl3 caused reproductive toxicity in male rats and induced oxidative stress results from the production of excess oxygen radicals (Yousef et al., 2009). Thus, the effects of AlCl3 on reproduction of male rats may be due to its generated oxidative stress. Histological study on testes of male albino rats intoxicated with Al for 90 days alone showed more exaggerated features of focal areas of spermatogenesis, arrest at the spermatid level in the form of degenerative changes in the germinal cells, together with few fragmented sperms in the lumen and acquired a thick, irregular basement membrane damage of testicular tubules and spermatogenesis, which showed histological changes in the seminiferous tubule of that testes (Thirunavukkarasu et al., 2010; Buraimoh et al., 2012). Similar results are also reported—that the effects of Al nitrite show necrosis on spermatocytes and spermatids (Libet et al., 1995).

Alcohol is well known as teratogenic and fetotoxic in humans. It has effects on sperm production and sperm quality. Many studies explain alcohol-altered testosterone production and testicular atrophy due to decrease the diameter of the seminiferous tubules (Fraser, 1992). The present study showed destruction of the seminiferous tubules and different shapes and hypocellularity reduction in cells of the spermatogenic series and widened empty lumen. Few seminiferous tubules show a single layer of basal spermatogonia. This is consistent with previous studies that showed degenerative changes of the epithelial component of the seminiferous tubules in mice and testicular lesions including a significant decrease in the diameter of the seminiferous tubules, decrease of Leydig cell's number and the presence of degenerative germ cells in rats (Hu et al., 2003; El Sokkary, 2001). There is histological evidence of testicular lesions and incomplete progression of spermatogenesis in pigs treated with ethanol also with many basal vacuoles and great reduction in sperm density (Wallock Montelius et al., 2007). Ethanol has been shown to induce nervous system damage, including long-term reduced neurogenesis in the hippocampus and induced inflammation in the brain and widespread brain atrophy (Blanco et al., 2005). Ethanol can interfere with the function of the hypothalamic pituitary gonadal axis, thereby causing impotence, infertility, and reduced male secondary sexual characteristics (Emanuele and Emanuele, 1998). Oxidative stress in the testes due to ethanol administration along with increased extent of lipid peroxidation or due to decreased antioxidant defences, and thereby induces germ cell apoptosis leading to testicular atrophy (Ganaraja et al., 2008). Ethanol consumption disturbs epididymal spermatozoa motility, nuclear maturity and DNA integrity of spermatozoa in rats; and this may be one possible cause of infertility following ethanol consumption (Talebi et al., 2011). The less sperm count of ethanol-treated mice in this study may be attributed to the effect of alcohol on the gonadotrophic cells of the pituitary gland and/or directly on the seminiferous tubules and Leydig cells, in addition to the neurotoxin activity of ethanol. Alteration of sperm count and semen morphology was observed in rats exposed to aluminium chloride with dose 64 mg/kg body weight (ZHU et al., 2014). It is also reported that, due to chronic alcohol consumption in the liver, it showed elongated and distorted mitochondria without normal organization (Kiessling et al., 1964). Decrease in spermatozoa viability as observed in the large number of nonmotile/dead spermatozoa in the ethanol-treated groups is one of the indicators that chronic ethanol consumption may compromise the structural integrity of the spermatozoa via the mitochondrial pathway. Hence, ethanol-induced elevation of germ cell apoptosis, together with necrosis and suppression of cell proliferation, may contribute to testicular atrophy (Zhu et al., 2000). These effects were observed in the reduced tubular diameter and cross-sectional areas of the treated animals.

Most previous studies focused on the individual toxic effects of a single chemical; however, there is a possibility that humans and animals can be exposed to a mixture of toxic agents (Ghorbel et al., 2016). However, when the animals were co-exposed to both ethanol and aluminium, the vacuolar degenerative changes appeared in the cytoplasm of the spermatogenic epithelium and in the Sertoli cells, and abnormal distribution of spermatozoa in the lumina. Clusters of degenerating spermatozoa and desquamated spermatogenic cells were frequently observed deep within the lumina of the seminiferous tubules. Most of the tubules showed that the germ layers were detached from the basal lamina. An important aspect of spermatogenesis is the detachment of germ cells from the basement membrane and their subsequent migration towards the tubule lumen. Procollagen I, a precursor of type I collagen, is a trimer consisting of two α1 chains and one α2 chain whose sequences are encoded by two different genes; COL1A1 and COL1A2, respectively (Chamberlain et al., 2004). The distribution of procollagen I within the seminiferous tubules of immature and adult mice correlates with the process of germ cell attachment and detachment from the basement membrane. The unique distribution pattern of procollagen I in adult mouse testes implies a possible role for COL1A1, COL1A2, and procollagen I in regulating the adhesion of spermatogonia and preleptotene spermatocytes to the basement membrane and the detachment and migration of spermatocytes and spermatids towards the lumen during spermatogenesis (He et al., 2005). From a histologic point of view, we agree with authors who reported that Al can produce a marked degeneration and necrosis of the germ cells lining, interstitial edema and testicular degeneration with complete absence of germ cells in male rats treated with aluminium chloride at higher dose. The present study also found acute degeneration of seminiferous tubules epithelium in presence ethanol co-exposure in given doses. The present study explored the histopathological changes in testis by Al itself and in presence of pro-oxidants ethanol.

CONCLUSION

The result of the present study provides the evidence of adverse effects of Al on testis histology by degenerative changes in spermatogenic cells in given moderate dose. We further concluded that ethanol acts as a pro-oxidant and augments the toxic effects of Al in the testis by acute degeneration of the seminiferous tubules and spermatogenic cells.

ACKNOWLEDGEMENTS

The authors would like to thank Dr Y V Bhardwaj, Asst Director, I/C Central Lab Animal House and Mr Chaman Sen, Sr. Lab Technician, Department of Anatomy, Dr R P Govt. Medical College, Kangra India to carry out this project in the Institute. Authors wish to thankfully acknowledge the support received from Department of Pharmacology and Department of Pathology, Government Medical College, Amritsar, India to carry out the work.

REFERENCES

ABDEL MONEIM AM (2013) Effects of taurine against histomorphological and ultrastructural changes in the testes of mice exposed to aluminium chloride. *Arh Hig Rada Toksikol*, 64: 405-414.

ADLER RA (1992) Clinically important effects of alcohol on endocrine function. *J Clin Endocrinol Metabol*, 74: 957-960.

AGRAWAL SK (1996) Evaluation of the developmental neuroendocrine and reproductive toxicology of aluminium. *Food Chem Toxicol*, 34: 49-53.

AITKEN RJ, ROMAN SD (2008) Antioxidant systems and oxidative stress in the testes. *Oxidative Med Cellular Longevity*, 1: 15-24.

ANANE R, BONINI M (1997) Transplacental passage of aluminium from pregnant mice to fetus organs after maternal transcutaneous exposure. *Hum ExpToxicol*, 16(9): 501-504.

BAMAC Y, COLAK T, BAMAC B (2005) Comparative study on apoptosis in the testes of normal and alcoholic rats. *Saudi Med J*, 26: 928-933.

BANNISTER P, LOWOSKY M (1987) Ethanol and hypogonadism. *Alcohol*, 73: 86-93.

BERIHU BA (2015) Histological and functional effect of aluminium on male reproductive system. *Int J Pharma Sci Res*, 6: 8.

BLANCO AM, VALLES SL, PASCUAL M, GUERRI C (2005) Involvement of TLR4/type I IL-1 receptor signaling in the induction of inflammatory mediators and cell death induced by ethanol in cultured astrocytes. *J Immunol*, 175: 6893-6899.

BURAIMOH AA, OJO SA, HAMBOLU JO, ADEBISI SS (2012) Histological study of the effects of aluminium chloride exposure on the testis of Wistar rats. *Am Int J Contemp Res*, 2: 114-122.

CHAMBERLAIN JR, SCHWARZE U, WANG PR, HIRATA RK, HANKENSON KD, PACE JM, UNDERWOOD RA, SONG KM, SUSSMAN M, BYERS PH, RUSSELL DW (2004) Gene targeting in stem cells from individuals with osteogenesis imperfecta. *Science*, 303: 1198-1201.

CHINOY J, SORATHIA P, JHALA D (2005) Flouride + Aluminum induced toxicity in mice testis with giant cells and its reversal by vitamin C. *J Fluride*, 38(2): 109-114.

DOMINIGO JL (1995) Reproductive and developmental toxicity of aluminium: a review. *Neurotoxicol Teratol*, 17: 515-521.

EL SOKKARY GH (2001) Quantitative study on the effects of chronic ethanol administration on the testis of adult male rat. *Neuroendocrinol Lett*, 22: 93-99.

ELAINE NM (2004) Human anatomy and physiology. 6th edn. Retrieved from: http://www.ehow.com/facts.5521847-functionanatomy-human testes.

ELIF E, AYLIN A (2018) Is aluminum exposure a risk factor for neurological disorders? *J Res Med Sci*, 23: 51.

ELIZABETH R, SILVA DO, FOSTER D, HARPER MM, SEIDMAN CE (2000) Alcohol consumption raises HDL cholesterol levels by increasing the transport rate of apolipoproteins A-I and A-II. *Circulation*, 102: 2347-2352.

EMANUELE MA, EMANUELE NV (1998) Alcohol's effects on male reproduction. *Alcohol Health Res World*, 22: 195-201.

FERGUSSON DM, BODEN JM, HORWOOD LJ (2009) Tests of casual links between alcohol abuse or dependence and major depression. *Arch Gen Psychiatry*, 66: 260-266.

FLORA S (1991) Effects of combined exposure to aluminium and ethanol on aluminium body burden and some neuronal, hepatic and haematopoietic biochemical variables in the rat. *Hum Exp Toxicol*, 10: 45-48.

FRASER RB (2006) Alcohol consumption and the outcomes of pregnancy. *RCOG Statement*, 5: 1-10.

GANARAJA B, CRYSTAL D, VIJAYALAKSHMI BM (2008) Use of vitamin C on effect of ethanol induced lipid peroxidation in various tissues, sperm count and morphology in the Wistar rats. *J Chinese Clin Med*, 3: 1-5.

GHORBEL I, AMARA IB, KTARI N, ELWEJ A, BOUDAWARA O, BOUDAWARA T, ZEGHAL N (2016) Aluminium and acrylamide disrupt cerebellum redox states, cholinergic function and membrane bound ATPase in adult rats and their offspring. *Biol Trace Elem Res*, 174: 335-346.

GONZALEZ MUNOZ MJ (2008) Role of beer as a possible protective factor in preventing Alzheimer's disease. *Food Chem Toxicol*, 46(1): 49-56.

GUO C, HUANG CJ, YEH MS, HSU GSW (2005) Aluminum induced suppression of testosterone through nitric oxide production in male mice. *Environ Toxicol Pharmacol*, 19: 33-40.

GUO C, LU Y, HSU GSW (2005) The influence of aluminum exposure on male reproduction and offspring in mice. *Environ Toxicol Pharmacol*, 20: 135-141.

HE Z, FENG L, ZHANG X, PARODI DA, SUAREZ-QUIAN C, DYM M (2005) Expression of Col1a1, Col1a2 and procollagen I in germ cells of immature and adult mouse testis. *Reproduction*, 130: 333-341.

HOVATTA O, VENALAINEN E.R, KUUSIMAKI L, HEIKKILA J, HIRVI T, REIMA I (1998) Aluminum, lead and cadmium concentrations in seminal plasma and spermatozoa, and semen quality in finnish men. *Hum Reprod*, 13: 115-119.

HU JH, JIANG J, MA YH (2003) Enhancement of germ cell apoptosis induced by ethanol in transgenic mice over expressing Fas ligand. *Cell Res*, 13: 361-367.

KARIMPOUR A (2005) Developmental toxicity of aluminium from high doses of AlCl3 in mice. *J Appl Res*, 5: 4.

KAWAHARA M, NEGISHI KM (2011) Link between aluminium and the pathogenesis of Alzheimer's disease: The integration of the aluminium and amyloid cascade hypotheses. *Int J Alzheimer's Dis*, 276393: 17.

KHATTAB FKI (2007) Histological and ultrastructural studies on the testis of rat after treatment with aluminium chloride. *Australian J Basic Appl Sci*, 1: 63-72.

KHATTAB HA, ABDALLAH IZ, KAMEL GM (2010) Grape seed extract alleviate reproductive toxicity caused by aluminium chloride in male rats. *J Am Sci*, 6(12): 1200-1209.

KIESSLING KH, TOBE U (1964) Degeneration of liver mitochondria in rats after prolonged alcohol consumption. *Exp Cell Res*, 33: 350-364.

KOPPES LJ (2005) Moderate alcohol consumption lowers the risk of type 2 diabetes. **Diabetes Care**, 28: 719-725.

KUTLUBAY R, OGUZ EO, CAN B, GUVEN MC, SINIK Z AND TUNCAY OL (2007) Vitamin E protection from testicular damage caused by intraperitoneal aluminium. *Int J Toxicol*, 26: 297-306.

KUZMIN A, CHEFER V (2013) Upregulated dynorphin opioid peptides mediate alcohol-induced learning and memory impairment. *Transl Psychiatry*, 3: 72.

LIBET J, COLOMINA M, SIRVENT J, DOMINGO J, CORBELLA J (1995) Reproductive toxicology of aluminium in male mice. *Fundam Appl Toxicol*, 25(1): 45-51.

NAYAK P, DAS SK, VASUDEVAN DM (2006) Role of ethanol on aluminum induced biochemical changes on rat brain. *Indian J Clin Biochem*, 21(2): 53-57.

NAYAK P, SHARMA SB (2010) Augmentation of aluminum-induced oxidative stress in rat cerebrum by presence of pro-oxidant (graded doses of ethanol) exposure. *Neurochem Res*, 35: 1681-1690.

NAYAK P, SHARMA SB, CHOWDARY NV (2013) Aluminum and ethanol induce alterations in superoxide and peroxide handling capacity (SPHC) in frontal and temporal cortex. *Indian J Biochem Biophys*, 50(5): 402-410.

PAJARINEN J, KARHUNEN PJ, SAVOLAINEN V (1996) Moderate alcohol consumption and disorders of human spermatogenesis. *Alcohol Clin Exp Res*, 20: 332-337.

PENA A, MESEGUER I (2007) Influence of moderate beer consumption on aluminium toxico-kynetics: acute study. *Nutr Hosp*, 22(3): 371-376.

REGAN TJ (2000) Moderate alcohol consumption and risk of coronary heart disease among women with type 2 diabetes mellitus. *Circulation*, 102: 487-488.

REUSCHE E, LINDNER B, ARNHOLDT H (1994) Widespread aluminum deposition in extracerebral organ systems of patients with dialysis associated encephalopathy. *Virchows Arch*, 424: 105-112.

SABERZADEH J, OMRANI M, TAKHSHID MA (2016) Protective effects of nimodipine and lithium against aluminum-induced cell death and oxidative stress in PC12 cells. *Iran J Basic Med Sci*, 19(11): 1251-1257.

SCOTT FG (2000) Developmental biology online textbook, 6th edn. Sinauer Associates, Inc. of Sunderland (MA).

SUN H, ZHAO H, SHARPE GM, ARRICK DM, MAYHAN WG (2008) Effect of chronic alcohol consumption on brain damage following transient focal ischemia. *Brain Res*, 1194: 73-80.

TALEBI AR, SARCHESHMEH AA, KHALILI MA, TABIBNEJAD N (2011) Effects of ethanol consumption on chromatin condensation and DNA integrity of epididymal spermatozoa in rat. *Alcohol*, 45: 403-409.

THIRUNAVUKKARASU SV, VENKATARAMAN S, UPADHYAY L (2010) Effect of aluminium chloride on testicular function under the influence of manasamitra vatakam an indigenous drug formulation. *Pharmacology online*, 1: 236-242.

TURNER TT, LYSIAK JL (2008) Oxidative stress: A common factor in testicular dysfunctions. *J Androl*, 29: 488-498.

VAN THIEL DH, GAVALER JS, LESTER R, GOODMAN MD (1975) Alcohol induced testicular atrophy: an experimental model for hypogonadism occurring in chronic alcoholic men. *Gastroenterology*, 69: 326-332.

WALLOCK MONTELIUS LM, VILLANUEVA JA, CHAPIN RE (2007) Chronic ethanol perturbs testicular folate metabolism and dietary folate deficiency reduces sex hormone levels in the Yucatan micropig. *Biol Reprod*, 76: 455-465.

YOUSEF M I, SALAMA AF (2009) Propolis protection from reproductive toxicity caused by aluminium chloride in male rats. *Food Chem Toxicol*, 47: 1168-1175.

YOUSEF MI, EL-MORSYAMA, HASSAN MS (2005) Aluminium induced deterioration in reproductive performance and seminal plasma biochemistry of male rabbits: protective role of ascorbic acid. *Toxicology*, 215: 97-107.

YOUSEF MI, KAMEL KL, ELGUENDI MI, EL-DEMERDASH FM (2007) An in vitro study on reproductive toxicity of aluminium chloride on rabbit sperm: The protective role of some antioxidants. *Toxicology*, 239: 213-223.

ZHU Q, MEISINGER J, EMANUELE NV, EMANUELE MA, LAPAGLIA N, VAN THIEL DH (2000) Ethanol exposure enhances apoptosis within the testes. *Alcohol Clin Exp Res*, 24: 1550-1556.

ZHU YZ, SUN H, FU Y, WANG J, SONG M (2014) Effects of sub chronic aluminium chloride on spermatogenesis and testicular enzymatic activity in male rats. *Life Sci*, 102: 36-40.

Anatomy of the right retro-portal lamina

Sofía Mansilla[1], Andrés Pouy[1], Alejandra Mansilla[1], Mauricio Pontillo[2], Raúl Perdomo[2], Sofía Cerri[3], Gustavo Armand Ugón[1], Eduardo Olivera[1,2]

[1] Departamento de Anatomía, Facultad de Medicina, Universidad de la República, Montevideo, Uruguay

[2] Clínica Quirúrgica 2, Hospital Maciel, Montevideo, Uruguay

[3] Departamento de Histología y Embriología Humana, Facultad de Medicina, Universidad de la República, Montevideo, Uruguay

SUMMARY

Pancreatic cancer is a global health problem because of its high mortality. Local recurrence, rather than metastatic disease, is considered the primary reason for poor prognosis of these patients. Although a consensus has not been established, Cephalic duodenopancreatectomy with "total mesopancreas excision" or right retro-portal lamina resection is suggested to decrease local recurrence, improving patient survival. The right retro-portal lamina was first described in 1959, its anatomical description does not appear in classic anatomical textbooks. The following work aims to perform an anatomical and histological study of the right retro-portal lamina.

A descriptive anatomical study of 30 adult cadavers, fixed in formaldehyde-based solution was performed. The presence of the lamina, limits, dimensions, and macro- and microscopic content was registered.

Right retro-portal lamina was found in 100% of the cases. Its limits were the pancreas uncinate process to the right and the vascular sheath of the superior mesenteric artery to the left. Its dimensions were an average of 20 mm long, 17 mm wide and 3 mm thick. The inferior pancreatic-duodenal artery was identified in 26.6% of the cases. Pancreatic and adipose tissue, as well as vascular and nervous elements, were identified.

The right retro-portal lamina is a constant connective-vasculo-nervous formation. It can be identified with relative ease given its constant insertions. It contains vascular (especially lymphatic) and nervous elements, which argues in favor of its resection in order to avoid local recurrences at this level.

Key words: Right retro-portal lamina – Meso pancreas – Pancreatic cancer – Anatomy – Histology - Cephalic Duodenopancreatectomy

INTRODUCTION

Pancreatic cancer is a global health problem because of its high mortality. It is the seventh cause of cancer deaths worldwide. Our country, Uruguay, ranks 17th in the World and second in America according to the Global Cancer Observatory (GLOBOCAN, 2018). Although the prognosis of this pathology is generally bad, there are certain determining factors that can modify its result. Among them, the margins of resection stand out (Gockel et al., 2007; Perinel and Adham, 2014; Chowdappa and Challa, 2015; Kanhere et

Corresponding author:
Dr. Sofía Mansilla. Departamento de Anatomía, Facultad de Medicina, Universidad de la República, Calle Florencio Sánchez 2746, 11300 Montevideo, Uruguay. Phone: +598 99 349 856. E-mail: sofiamansil-larud@gmail.com. Orcid Id: 0000-0002-5881-9284.

Submitted: June 7, 2020. **Accepted:** January 19, 2021

al., 2015; Xu et al., 2017). Local recurrence due to incomplete resection, rather than metastatic disease, is considered the primary reason for the poor prognosis of these patients (Xu et al, 2017). Although a consensus has not been established, total mesopancreas excision or right retro-portal lamina (RRPL) resection is suggested during Cephalic duodenopancreatectomy (DPC) in order to decrease local recurrence, improving patient survival (Gockel et al., 2007; Gaedcke et al., 2010; Perinel and Adham, 2014; Chowdappa and Challa, 2015; Kanhere et al., 2015; Cao et al., 2015; Xu et al., 2017). This explains why the term mesopancreas was coined, analogous to the mesorectum (Gockel et al., 2007; Agrawal et al., 2010; Kanhere et al., 2015; Peparini et al., 2015; Sharma et al., 2016; Xu et al., 2017).

The RRPL also known as right retro pancreatic lamina, was first described by J.B. Prionton and R. Laux in 1959, as a remnant of the pancreas primitive mesodorsal. The pancreas begins its origin in the 4th week of embryonic development from two primordia: dorsal and ventral. The first origins to the left pancreas, body and tail, while the second to the right pancreas: neck, head and uncinate process. Its fusion occurs at the end of the 6th week (Borghi et al., 1998; Skandalakis et al., 2004). Thus, the primitive mesodorsal of the pancreas is composed of two contingents: a left one, known as the left portal lateral lamina (LPLL), and a right one, which corresponds to the RRPL (Fig. 1) (Champetier et al., 1978; Pissas, 1984). Its anatomical description does not appear in classic anatomical textbooks such as Testut (1950), Patel (1957) or Rouviere (1987). According to classic definitions, it is not a true meso, since it does not contain the main vascular-nervous elements of the organ and lacks the characteristic fibrous envelope or fascia that links to the posterior parietal peritoneum (Gockel et al., 2007; Agrawal et al., 2010; Kanhere et al., 2015; Peparini et al., 2015; Sharma et al., 2016; Xu et al., 2017). Recently, a series of studies involving intra-operative, radiological and cadaveric dissections suggested that the idea that regions of mesentery regress may not be accurate (Kumar et al., 2020).

The RRPL is a dense connective tissue formation, with a rectangular shape, whose limits are: pancreas uncinate process (UP) to the right, superior mesenteric artery (SMA) to the left, right celiac ganglion upwards and duodenum third portion downwards. It contains vascular elements: arterial, venous and lymphatic, as well as nerve fibers (Champetier et al., 1978).

The aim of the following work is to perform an anatomical and histological study of the RRPL.

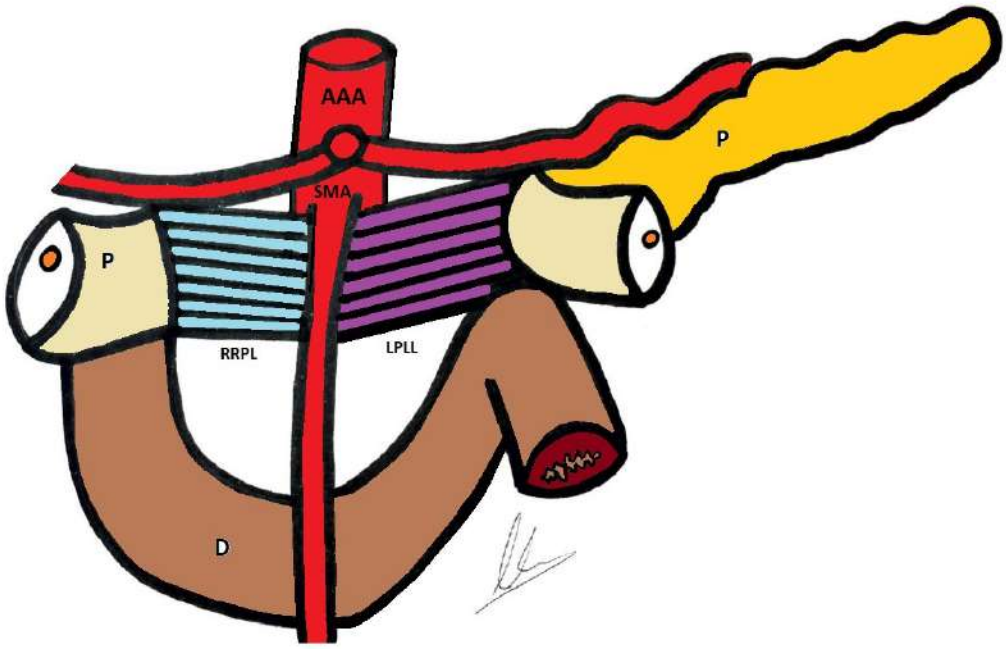

Fig. 1.- Representation of Pancreas (P), Duodenum (D), Abdominal Aortic Artery (AAA), Superior mesenteric artery (SMA), Right retro-portal lamina (RRPL) and Left portal lateral lamina (LPLL).

MATERIALS AND METHODS

Thirty adult cadavers of both sexes (10 men and 20 women), between 40 and 90 years old, fixed in formaldehyde-based solution were used. None of them presented previous abdominal surgery.

The cadaveric material was used following the rules of the Helsinki Declaration regarding prior live donation and informed consent, a sine qua non condition for the anatomy department at the Faculty of Medicine in the Universidad de la República.

Dissection of the duodenum-pancreas and its main vascular pedicles was performed. A medial xiphopubic incision was made. Once inside the peritoneal cavity, we proceeded to disinsert the grastrocolic omentum from its colic insertion, raising the stomach and descending the transverse colon and mesocolon. Subsequently, the right colic flexure was mobilized medially in favor of the pre-duodenal pancreatic fascia, exposing the pancreas anterior surface. Once the UP was identified, its relationship with the superior mesenteric vessels was assessed, and a careful dissection of the RRPL was made (Fig. 2).

The presence of the RRPL, its limits, dimensions, and macroscopic content were registered. All records were made by the same observer with a digital millimeter gauge.

Afterwards, the lamina was resected (Fig. 3 and Fig. 4) and sent to the Histology and Embryology Department. The pieces were embedded in paraffin, and sliced and stained with hematoxylin and eosin. The images were obtained with a Nikon D320 Microscope with digital camera. Microscopic content was registered.

RESULTS

Presence of RRPL, limits and dimensions

The presence of RRPL was found in 100% of the cases (n=30). It extended laterally to the UP (100%, n=30) and medially to the vascular sheath

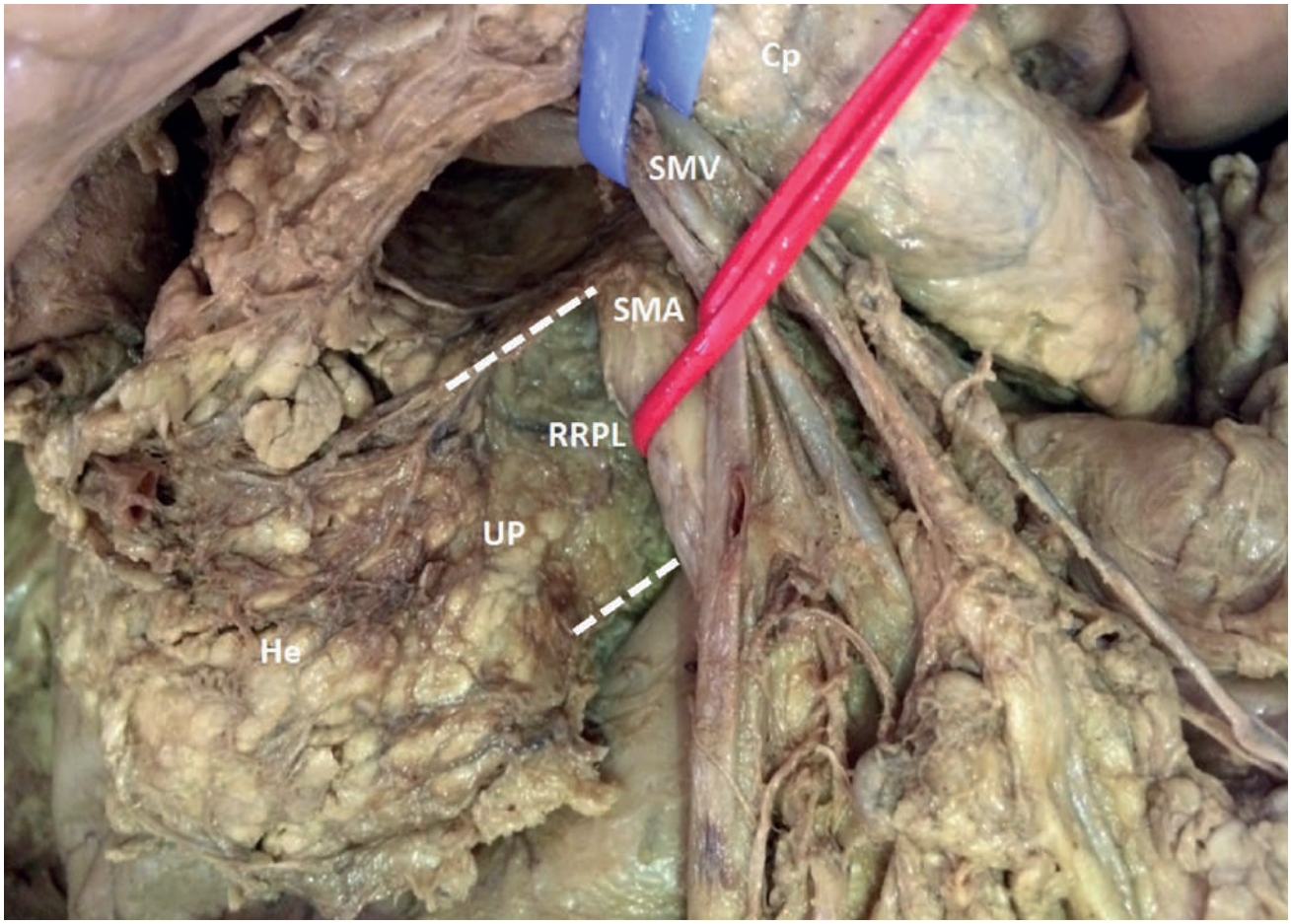

Fig. 2.- Dissection of pancreas uncinated process (UP), head (He) and corp (Cp). The superior mesenteric vein (SMV) and artery (SMA), and the right retro-portal lamina (RRPL) are observed.

of SMA. We emphasize that at the time of the lamina resection a sub-adventitial dissection of the SMA was needed. Its dimensions were 20 mm long, 17 mm wide and 3 mm thick.

Macroscopic content

Vascular and nervous elements were found during dissection. Regarding the arterial content, the inferior pancreatic-duodenal artery was identified in 26.6% of the cases, in which the RRPL extended on the right margin of the SMA below its origin (Fig. 5). We also found the presence of small tributary veins of the superior mesenteric vein, such as inferior pancreatic duodenal veins.

The study of the macroscopic lymphatic content was a real challenge. Only in one of the cases did we find macroscopically evident lymph nodes. In that case, the dissection showed the presence of a

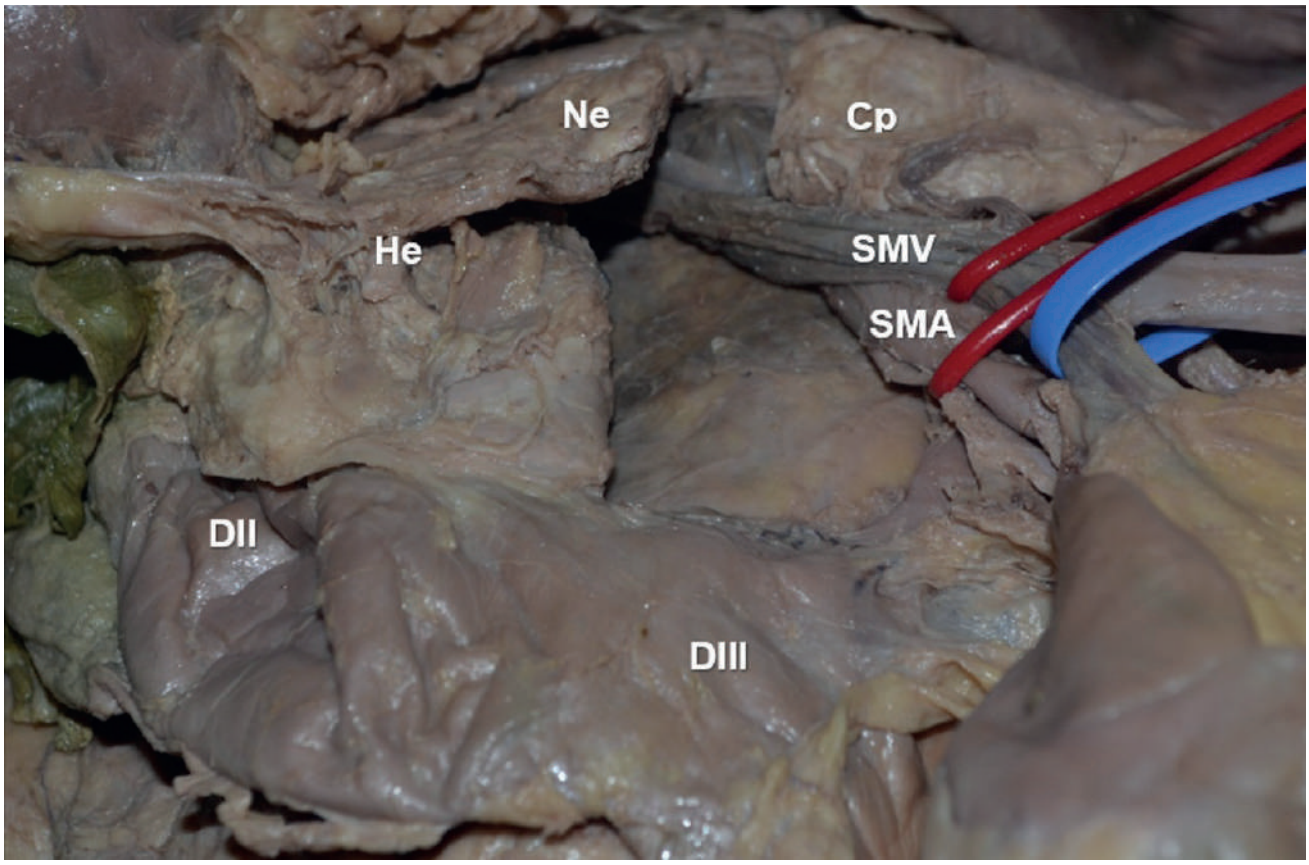

Fig. 3.- Pancreas uncinated process (UP), head (He), neck (Ne) and corp (Cp), superior mesenteric vein (SMV) and artery (SMA). Duodenum portion II (DII), Duodenum portion III (DIII).

Fig. 4.- Right retro-portal lamina. UP: uncinated process margin; SMA: superior mesenteric artery margin, the irregular form is due to the need of artery sub-adventitial dissection.

mass at the cephalo-pancreatic level, suggestive of a cephalo-pancreatic adenocarcinoma, although we did not count with available information to corroborate this hypothesis.

Regarding nervous content, fibers were found entering the medial margin of the UP (Fig. 6), made up of post ganglionic fibers of celiac ganglia, and from superior mesenteric periarterial plexus.

Microscopic content

The microscopic study of the lamina confirmed the presence of vascular elements: arterial, venous and lymphatic, as well as nervous fibers. The findings are illustrated in Fig. 6. We highlight microscopic presence of lymphatic content of the lamina, showing vessels and lymph nodes that could not be identified with the naked eye. In addition, pancreatic parenchyma was found on the right margin of the resected laminas (Fig. 7).

DISCUSSION

The RRPL can be identified with relative ease given its constant limits. To the right of the minor pancreas, the parenchymal sector extends from the head of the pancreas to the left behind the superior-portal mesenteric vascular axis. Also called retro-venous pancreas, it can be divided in three parts, from top to bottom: retro-portal, which hints behind the portal vein; retro-mesenteric, located immediately behind the superior mesenteric vein; and UP, which corresponds to the lower portion of the segment with variable extension to the left (Pissas, 1984).

To the left, its limit is the SMA, which requires a sub-adventitial dissection. The superior mesenteric artery originates from the anterior surface of the abdominal aorta, at the level of the first lumbar vertebra, and is directed down and forward obliquely. It originates in its left margin

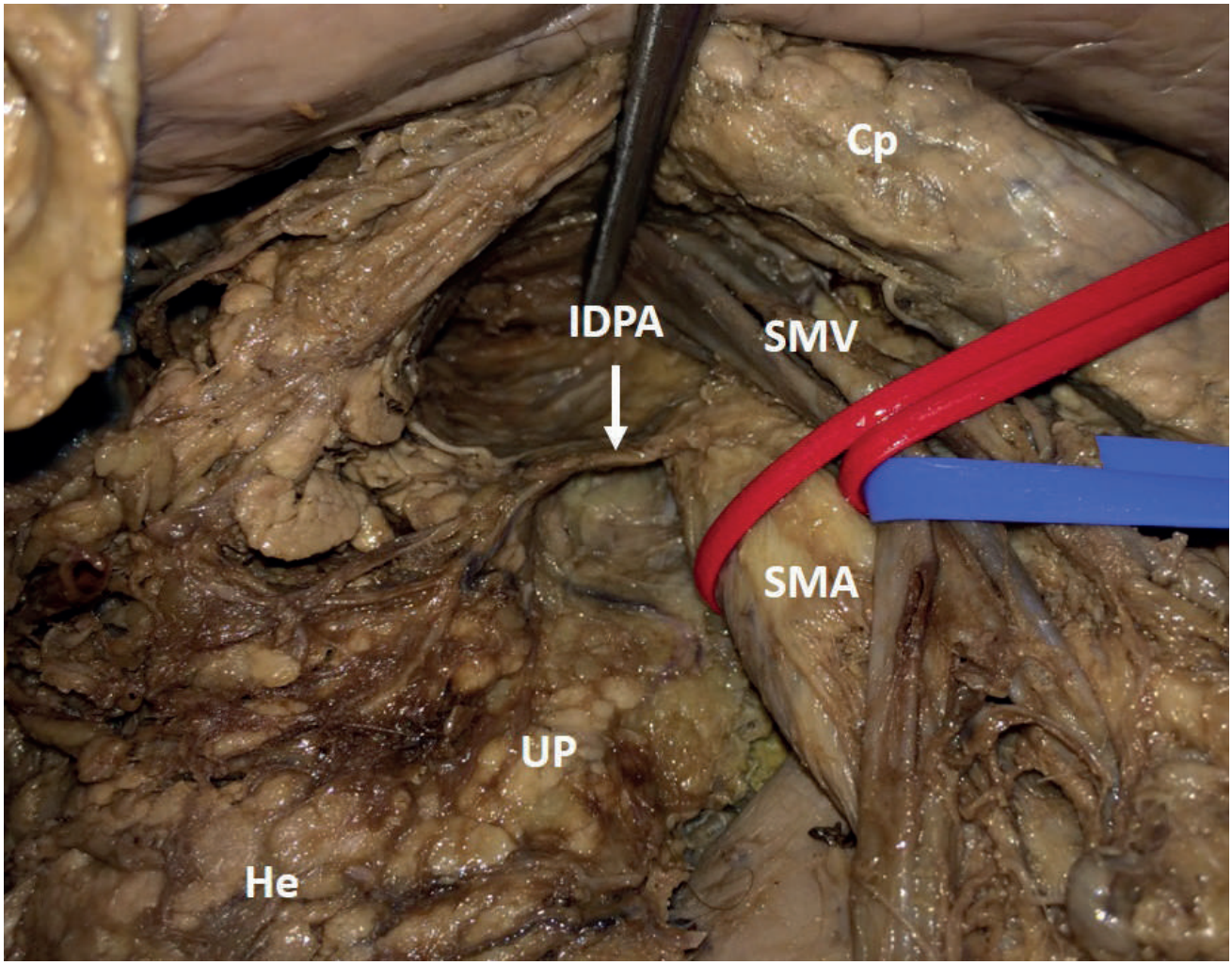

Fig. 5.- Uncinated process (UP), pancreas head (He) and corp (Cp). Superior mesenteric vein (SMV) and superior mesenteric artery (SMA). Inferior duodeno-pancreatic artery (IDPA).

jejunal branches, and in its right margin the inferior pancreatic-duodenal arteries, which run in the thickness of the RRPL and had to be ligated and sectioned at its origin for resection.

As found in our work and in the consulted bibliography, its length ranges from 18.66 mm to 60 mm, a value that depends on the variable extent of the pancreatic parenchyma on the left. Its width and thickness do not exceed 30 mm and 4 mm respectively (Bouassida, 2013).

The content of the RRPL was concordant with the bibliography consulted. The inferior duodenal pancreatic arteries originate from the right margin of the SMA, and run from left to right to the duodenum pancreas. The right hepatic artery, whose incidence has been reported in approximately 14% of cases by different authors, was not found in our work. When present, it originates from the right margin of the superior mesenteric artery, and runs obliquely up and to the right contained in the thickness of the RRPL. Its correct identification and protection are essential in order to avoid catastrophic consequences (Hiatt et al., 1994; Mugunthan et al., 2016).

The dissection of the RRPL shows the presence of small tributary veins of the superior mesenteric vein. Some authors have described the passage of the inferior pancreatic-duodenal veins and small tributaries of the retro-venous pancreas.

The RRPL contains lymphatic vessels of drainage of the UP and posterior surface of the pancreas head, as well as part of the anterior face (Pissas,

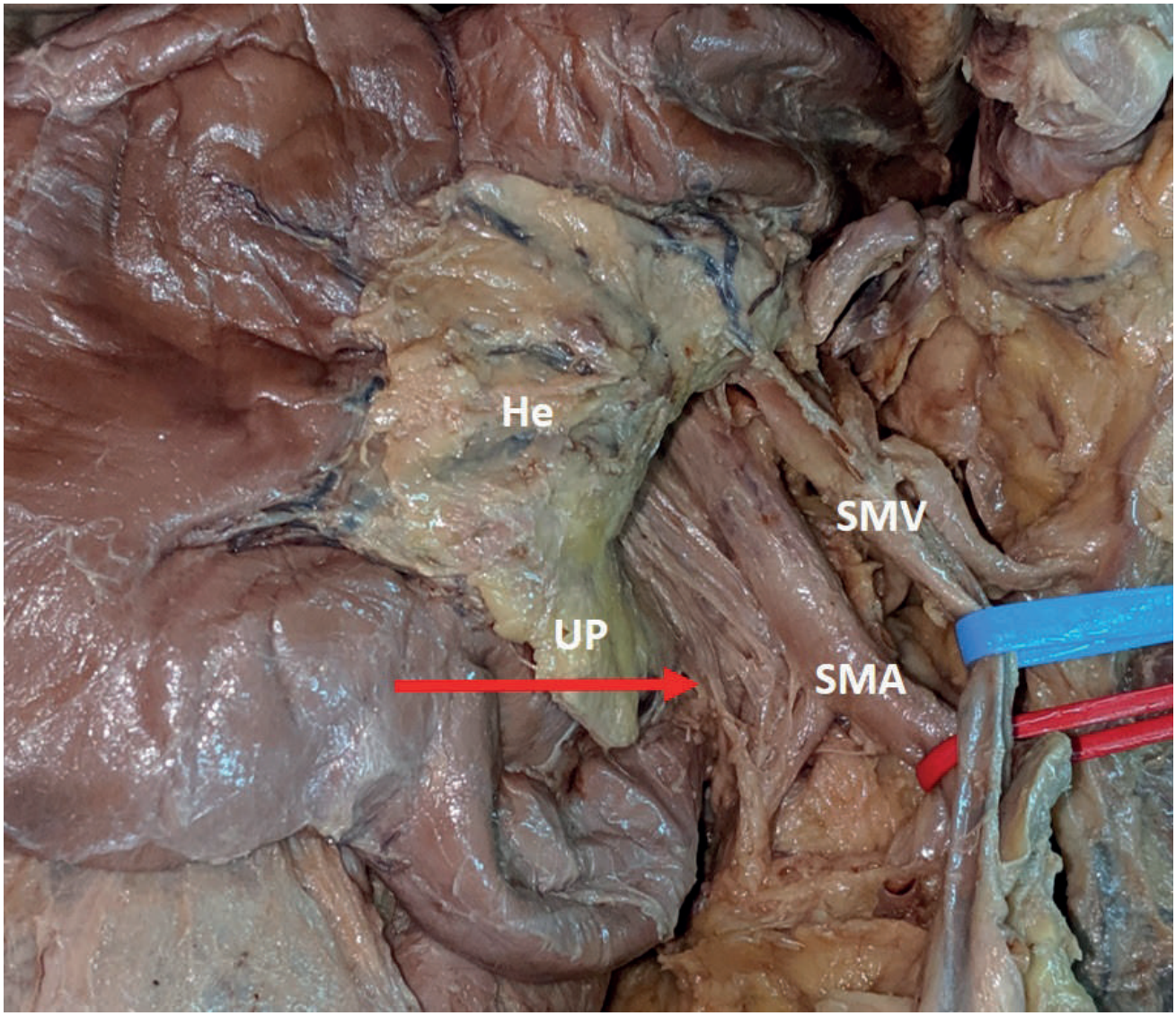

Fig. 6.- Pancreas head (He), Uncinated process (UP), Superior mesenteric vein (SMV), Superior mesenteric artery (SMA). Red arrow shows nerve fibers belonging to the solar plexus.

1984). Pissas (1984) systematized the lymphatic circulation of the pancreas in two currents on both sides of the superior mesenteric artery that drain the right pancreas and left pancreas respectively. The found lymphatic vessels are part of the right current, although we could not identify its origin, distribution and drainage without the use of staining techniques. This is one of the main weaknesses of our work.

The nervous content is of particular interest. It is made up of post ganglionic fibers of celiac ganglia, superior mesenteric plexus and pre aortic plexus, which enter the medial margin of the pancreas hook. It explains possible perineural dissemination pathways of pancreatic head cancer. Yoshioka and Wakabayashi (1950) systemized the aforementioned fibers for the first time under the name of Plexus Pancreaticus Capitalis. According to the origin of its fibers, it can be divided into two portions: an upper one, unco-lunar lamina from the right celiac ganglion; and a lower one, unco-mesenteric, whose fibers come from the superior mesenteric peri-arterial plexus, included on the RRPL (Yoshioka and Wakabayashi, 1950; Yi et al., 2003).

The microscopic findings are the true witnesses of the content of the RRPL, and are consistent with the consulted literature (Bouassida, 2013; Xu et al., 2017).

In summary, the RRPL is a constant connective-vasculo-nervous formation, which constantly involves the proximal portion of the superior mesenteric artery that requires a sub-adventitial dissection. The fact that it contains vascular and nervous elements argues in favor of its resection so as to avoid local recurrences. The lymphatic circulation identification and dissection with staining techniques is one of the aspects to further research in our line of work.

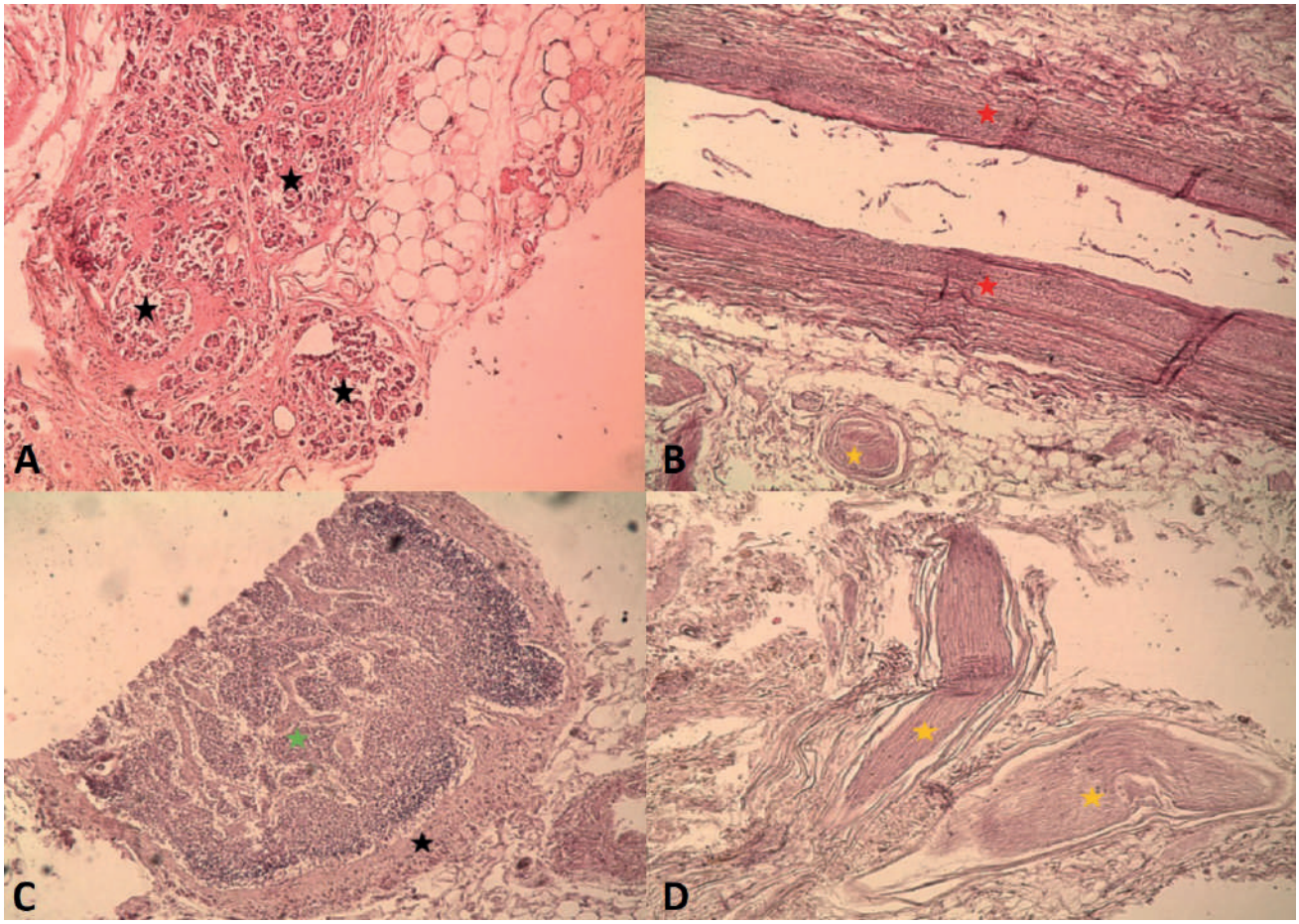

Fig. 7.- A: Pancreas serous acini (black). The organ is surrounded by unilocular adipose tissue (upper right) and loose connective tissue (upper left). **B:** Longitudinal section of a large elastic artery (red). Below it, a cross section of a peripheral nerve (yellow) is distinguished between the connective tissue that surrounds it, surrounded by its perineurium (black arrow). **C:** Lymph node (green), surrounded by its capsule (black) and above it, unilocular adipose tissue. **D:** In yellow, between the loose connective tissue, longitudinal bundles of peripheral nerves are observed surrounded by its perineurium and further out its epineurium. In the upper left, a cross section of a peripheral nerve is distinguished.

ACKNOWLEDGEMENTS

We especially want to thank donors and their families for enabling us to conduct this research.

REFERENCES

AGRAWAL M, THAKUR D, SOMASSHEKAR U, CHANDRAKAR S, SHARMA D (2010) Mesopancreas: Myth or Reality? *J Pancreas,* 5(3): 230-233.

BOUASSIDA M (2013) Retroportal lamina or mesopancreas? Lessions learned by anatomical and histological study of thrty-three cadaveric dissections. *Int J Surg*, 11(9): 834-836.

BORGHI F, GATTOLIN A, GARBOSSA D, BOGLIATTO F, GARAVOGLIA M, CESARE LEVI A (1998) Embryologic bases of extended radical resection in pancreatic cancer. *Arch Surg,* 133: 297-301.

CAO Z, XU J, SHAO Q (2015) Surgical treatment of pancreatic head cancer: concept revolutions and arguments. *Chin J Cancer Res,* 27(4): 392-396.

CHAMPETIER J, LETOUBLON C, DURAND A (1978) Bases anatomiques de la duodéno-pancréatectomie céphalique (DPC). *Anat Clin*, 1: 189-197.

CHOWDAPPA R, CHALLA V (2015) Mesopancras in pancreatic cancer: where do we stand. *Indian J Surg Oncol*, 6(1): 69-74.

GAEDCKE J, GRADE M, SZOKE R, LIERSCH T, BECKER H, GHADIMI B (2010) The mesopancreas is the primary site for R1 resection in pancreatic head cancer: relevance for clinical trials. *Langenbecks Arch Surg,* 395: 451-458.

GLOBOCAN (2018) Cancer incidence. Global cancer observatory. Available in: http://www. https://gco.iarc.fr/databases.php.

GOCKEL I, DOMEYER M, WOLLOSCHECK T, KONERDING M, JUNGINER T (2007) Resection of the mesopancreas (RMP): a new surgical classification of a known anatomical space. *World J Surg Oncol*, 5(44): 1-8.

HIATT J, GABBAY J, BUSUTTIL R (1994) Anatomy of the hepatic arteries in 1000 cases. *Ann Surg*, 220(1): 50-52.

KANHERE H, TROCHSLER M, MADDERN G (2015) The "mesopancreas" dissection - A new surgical paradigm: An anatomical "reflection" of surgical and prognostic importance? *J Pancreas*, 16(5): 514-516.

KUMAR A, FAIQ MA, KISHAN V, RAJ GV, COFFEY JC, JACOB TG (2020) Development of a novel technique to dissect the mesentery that preserves mesenteric continuity and enables characterization of the ex vivo mesentery. *Front Surg*, 6(80): 1-7.

MUGUNTHAN N, KANNAN R, JEBAKANI CM, ANBALAGAN J (2016) Variations in the origin and course of the right hepatic artery and its surgical significance. *J Clin Diagn Res,* 10(9): 11-14.

PATEL J (1957) *Nuevo manual de patologia quirurgica*. Editorial Científico Médica, Barcelona.

PEPARINI N, CARONNA R, CHIRLETTI P (2015) The "meso" of the rectum and the "meso" of the pancreas: similar terms but distinct concepts in surgical oncology. *Hepatobiliary Pancreat Dis Int,*14(5): 548-551.

PERINEL J, ADHAM M (2014) Le mésopancréas: una réalité anatomique ou une assimilation hasardeuse? *E-mémories l'Académie Natl Chir,* 13(2): 89-92.

PISSAS A (1984) Anatomoclinical and anatomosurgical essay on the lymphatic circulation of the pancreas. *Anat Clin*, 6: 255-280.

ROUVIERE H, DELMAS A (1987) *Anatomía Humana Descriptiva, Topográfica y Funcional*. Masson, Barcelona.

SHARMA D, ISAJI S (2016) Mesopancreas is a misnomer: time to correct the nomenclature. *J Hepatobiliary Pancreat Sci*, 23(12): 745-749.

SKANDALAKIS J, COLBORN G, WEIDMAN T, FOSTER R, KOINGSNORTH A, SKANDALAKIS L (2004) Pancreas. In: Skandalakis JE (ed.). *Skandalakis's Surgical Anatomy: The embryologic and anatomic basis of modern surgery*. Broken Hill.

TESTUT L (1902) Tratado de Anatomía Humana. Salvat, Barcelona.

XU J, TIAN X, CHEN Y, MA Y, LIU C, TIAN L (2017) Total mesopancreas excision for the treatment of pancreatic head cancer. *J Cancer,* 8(17): 3575-3584.

YOSHIOKA H, WAKABAYASHI T (1958) Therapeutic neurotomy on head of pancreas for relief of pain due to chronic pancreatitis: a new technical procedure and its results. *AMA Arch Surg*, 76: 546-554.

YI SQ, MIWA K, OHTA T, KAYAHARA M, KITAGAWA H, TANAKA A (2003) Innervation of the pancreas for the perspective of perineural invasion of pancreatic cancer. *Pancreas,* 27(3): 225-229.

Ultrastructure of the anterior lens capsule and epithelium in cataracts associated with granulomatosis with polyangiitis

Ozlem Dikmetas[1], Yasemin Kapucu[1], Aysegul Firat[2], Mustafa F. Sargon[3], Sibel Kocabeyoglu[1]

[1] Department of Ophthalmology, Hacettepe University Faculty of Medicine, Ankara, Turkey
[2] Department of Anatomy, Hacettepe University Faculty of Medicine, Ankara, Turkey
[3] Department of Anatomy, Lokman Hekim University Faculty of Medicine, Ankara, Turkey

SUMMARY

Our aim was to describe electron microscopic findings of anterior lens capsule (ALC) of a patient with granulomatosis with polyangiitis (GPA). A 73-year-old woman referred to our clinic due to decreased vision. The best-corrected visual acuity was counting fingers in 3 m distance with her right eye and in 2 m distance with her left eye. Slit-lamp examination revealed grade-4 nuclear sclerosis in both eyes. An operation was planned for each eye one month apart. The ALCs were obtained during cataract surgery from each eye. Ultrathin sections of ALCs were stained with uranyl acetate and lead citrate and examined under the transmission electron microscope. The lens epithelium was found to be thin and there were some small vacuoles in the cytoplasm. The epithelial surface showed irregularities. There was subepithelial and intercellular oedema, and in some focal areas the lens epithelium was detached from the capsule. ALC obtained from cataract surgery of a subject without any systemic disease showed intracellular vacuoles in some areas with a normal basement membrane. This report showed that the ALC in GPA have significant and demonstrative changes, especially in the epithelial level compared to normal eye. Our findings may have a guiding effect on the pathogenesis of GPA. However, there is still no clear evidence about the existence and pathogenesis of GPA on lens epithelium, and additional studies are needed.

Key words: Granulomatosis with polyangiitis – Electron microscopy – Cataract – Lens capsule

INTRODUCTION

Granulomatosis with polyangiitis (GPA), formerly known as Wegener's granulomatosis (WG), is a multisystem autoimmune disorder, which is characterized by the classic triad of necrotizing granulomatous vasculitis of the respiratory tract, focal segmental glomerulonephritis and necrotizing vasculitis of small arteries and veins (Greco et al., 2016).

Involvement of the paranasal sinuses is the most characteristic clinical feature, followed by pulmonary and renal disease (Jennette et al., 1994). A limited form of the disease, which consists of granulomatous inflammation in the respiratory tract without overt involvement of

Corresponding author:
Ozlem Dikmetas, MD. Department of Ophthalmology, Hacettepe University, Faculty of Medicine, Sihhiye/Ankara 06100, Turkey. E-mail: ozlemdikmetas@gmail.com

Submitted: October 22, 2020. **Accepted:** January 22, 2021

the kidneys, has been described (Tarabishy et al., 2010). Ocular and orbital involvement can occur in patients with GPA, and may affect every structure of the eye from the eyelid to the optic nerve with a wide range of severity. Ocular or orbital involvement is found in 15% of patients at presentation, and in up to 50% of patients during the disease's course (Tarabishy et al., 2010). Some case reports of the ultrastructural appearances are subepithelial basement membrane densities resembling immune complex deposits of renal biopsies (Horn et al., 1974). To the best of our knowledge, this is the first study in the literature evaluating ultrastructural findings of the anterior lens capsule in GPA.

MATERIALS AND METHODS

A 73-year-old woman referred to our clinic due to decreased vision. In ophthalmological examination, the best-corrected visual acuity was counting fingers in 3 m distance with her right eye and in 2 m distance with her left eye. Slit-lamp examination revealed grade-4 nuclear sclerosis in both eyes. Intraocular pressures were in the normal range, and dilated fundus examination revealed no pathological findings. Her medical history included granulomatosis with polyangiitis for five years. She was under intravenous immunoglobulin (IVIG) therapy monthly with systemic 5 mg prednisolone per day. She underwent phacoemulsification and intraocular lens implantation in the left eye, and then the right eye in a second operation one month later. Anterior lens capsules (ALCs) were obtained during the surgery. The specimens were immediately put into 2.5% glutaraldehyde (25% glutaraldehyde E.M. Grade - R 1010, Agar Scientific Ltd., Essex, UK- in phosphate buffer pH: 7.4) in the surgery room for fixation. After fixation for 24 hours, samples were washed in phosphate buffer solution (pH: 7.4) and dehydrated in increasing ethanol concentrations.

Tissue samples were embedded in fresh epoxy resin (Epoxy embedding medium, 45345, Merck KGaA, Germany) and polymerized for 48 h at 60°C. Semi-thin sections (approximately 2 µm thick) were cut with a glass knife on a LKB-Nova ultramicrotome (LKB-Produkter AB, Bromma, Sweden). Freshly prepared and filtered 1% methylene blue solution was dropped onto the tissue section. The slide was left on the 100–110°C hot plate for 40–45 seconds, and then rinsed carefully under tap water. Stained sections were examined and captured under the camera of a light microscope for a descriptive analysis (Firat et al., 2019). When the area was determined by examining the semi-thin sections, tissue blocks were trimmed to prepare the ultra-thin sections of the predetermined area by LKB-Nova ultramicrotome (LKB-Produkter AB, Bromma, Sweden). 70 nm ultra-thin sections were double stained with uranyl acetate and lead citrate (Leica EM AC 20, Wetzlar, Germany). These sections were examined in a Jeol JEM 1200 EX (Japan) transmission electron microscope and the micrographs were digitalized by Veleta side-mounted TEM CCD camera using RADIUS 2.0 imaging software (EMSIS GmbH, Germany).

RESULTS

The lens epithelium was found to be thin and some small vacuoles were observed in the cytoplasm. The epithelial surface showed irregularities. There was subepithelial and intercellular oedema and in some focal areas the lens epithelium was detached from the capsule (Figs. 1A, B, C). Basement membrane showed discontinuations at these oedematous and detached areas (Fig. 1B). In addition, the ALCs of a normal patient who was 65 years old without any systemic diseases was obtained during cataract surgery and this sample was examined to compare with the results of WG patient. The only finding in this sample was a few intracellular vacuoles with a normal basement membrane (Fig. 1D).

DISCUSSION

This report showed demonstrative anterior lens capsule changes in GPA, which was previously evaluated in many aspects, but with limited studies at the lens capsule level. Circulating immune complexes have been demonstrated in the blood of some patients with GPA (Chaudhuri and Davis, 2016). Immunoglobulins, complement and electron-dense deposits have been found in glomeruli of patients with GPA. A pathogenetic

which is well known that circulating immune complexes and the vasculitis in the respiratory tract is raised by IgG and IgM in pulmonary alveolar walls and of IgM in maxillary sinus arteries (Chaudhuri and Davis, 2016). Electron microscopic study of the lung and maxillary sinus showed intravascular fibrin, and demonstrated electron dense deposits in the blood vessel walls (Hui et al., 1981). The light microscopic lesions seen with cases of generalized WG were the characteristic lesion: a focal and segmental glomerulitis in the renal tissues (Antonovych et al., 1989). The electron microscopic findings of dense deposits on the epithelial side of the glomerular basement membrane patients with active generalized GPA provide substantial evidence that the renal injury is a manifestation of immune-complex deposition (Hui et al., 1981; Antonovych et al., 1989). The observations of dense material resembling immune complexes within the capillary wall provide supporting evidence that GPA is a disease of disordered

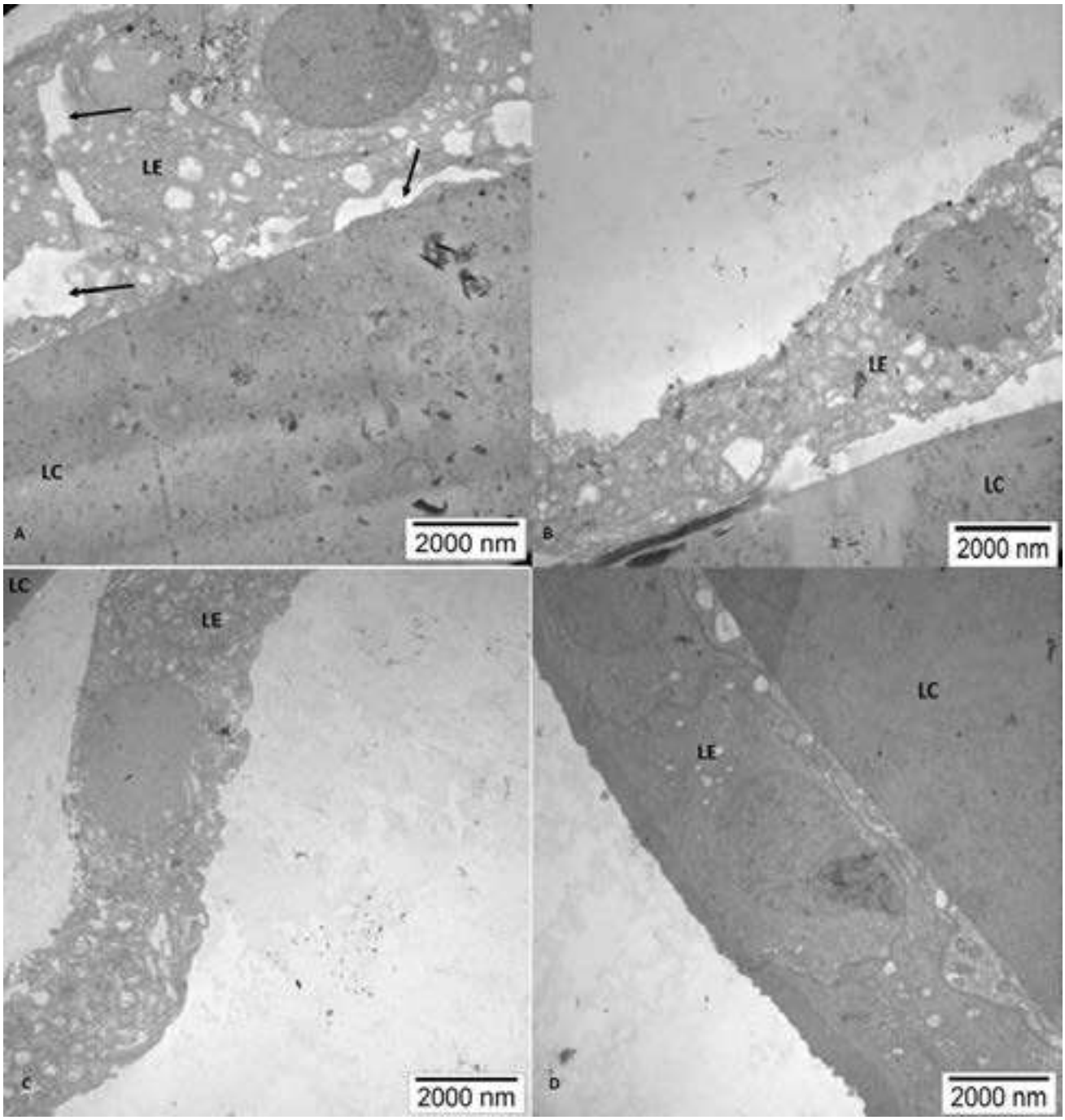

Fig. 1.- Electron micrographs of the specimen. **A:** Focal areas with detached capsule and vacuoles in the cytoplasm, **B:** Lens epithelial detachments from the capsule and vacuoles in the cytoplasm together with discontinuations of the basement membrane, **C:** Epithelial detachment from the lens capsule, **D:** Normal cataractous lens without GPA. (LC: Lens capsule, LE: Lens epithelium).

immunity, and further suggest that the immune injury to the kidney is mediated, at least in part, by the deposition of immune complex (Hui et al., 1981; Antonovych et al., 1989). The lens capsule also has a kidney-like capsule, and before that it mainly consists of three different structures. These structures are capsule, epithelium and lens fibers. The lens is in place in the normal optic system, supported by the iris and vitreous body, with the zonular fibers adhering to the lens capsule. The lens capsule is a modified, transparent basement membrane that envelops the ocular lens completely. Embryologically, the surface originates from the ectoderm, after the intussusception of the surface ectoderm, the apical surface faces the lens vesicle and its basal surface turns outward, forming the basement membrane of the lens capsule (Danysh and Duncan, 2009). In ultrastructural studies of senile cataracts, intra and intercellular vacuoles were found in the lens epithelium. In our case report, a senile cataract patient without GPA was included to make this distinction. In the optic microscopy study of Rahim et al., they detected proliferation and change in the layers of lens epithelial cells in people with senile cataracts (Rahim and Iqbal, 2011). Tekin et al. (2018)examined the lens anterior capsules belonging to congenital cataract patients with electron microscopy, and it was observed that the lens epithelial cells were locally cuboidal. Apparently, vacuoles of different diameters were detected in the cell. These changes are different and more pronounced than normal cataract patients.

As a result, it has been shown with this study that the eyes with GPA have significant changes especially in the epithelial level compared to normal eyes, and that the basement membrane showed discontinuation. The presence of these formations has a guiding effect on the structure from which the pathogenesis of GPA originates. However, there is still no clear evidence about the existence and pathogenesis of GPA, and additional studies are needed.

ACKNOWLEDGEMENTS

Informed consent was taken from the patient.

REFERENCES

ANTONOVYCH TT, SABNIS SG, TUUR SM, SESTERHENN IA, BALOW JE (1989) Morphologic differences between polyarteritis and Wegener's granulomatosis using light, electron and immunohistochemical techniques. *Mod Pathol,* 2(4): 349-359.

CHAUDHURI AA, DAVIS JT (2016) Concomitant granulomatosis with polyangiitis and C3 glomerulonephritis causing renal failure. *Cureus,* 8(2): e482.

DANYSH BP, DUNCAN MK (2009) The lens capsule. *Exp Eye Res*, 88(2): 151-164.

FIRAT A, ONERCI-CELEBI O, TUNCEL A, ERGUN M, HAYRAN M (2019) Microscopic study of human nasal cavity microanatomy using semi-thin resin embedding and methylene blue staining. *J Histotechnol,* 42(1): 13-18.

GRECO A, MARINELLI C, FUSCONI M, MACRI GF, GALLO A, DE VIRGILIO A, G. ZAMBETTI G, DE VINCENTIIS M (2016) Clinic manifestations in granulomatosis with polyangiitis. *Int J Immunopathol Pharmacol,* 29(2): 151-159.

HORN RG, FAUCI AS, ROSENTHAL AS, WOLFF SM (1974) Renal biopsy pathology in Wegener's granulomatosis. *Am J Pathol,* 74(3): 423-440.

HUI AN, EHRESMANN GR, QUISMORIO FP, BOYLEN CT Jr, MAYBERG H, KOSS MN (1981) Wegener's granulomatosis. Electron microscopic and immunofluorescent studies. *Chest,* 80(6): 753-756.

JENNETTE JC, FALK RJ, ANDRASSY K, BACON PA, CHURG J, GROSS WL, HAGEN EC, HOFFMAN GS, HUNDER GG, KALLENBER CG, et al. (1994) Nomenclature of systemic vasculitides. Proposal of an international consensus conference. *Arthritis Rheum*, 37(2): 187-192.

RAHIM A, IQBAL K (2011) To assess the levels of zinc in serum and changes in the lens of diabetic and senile cataract patients. *J Pak Med Assoc,* 61(9): 853-855.

TARABISHY AB, SCHULTE M, PAPALIODIS GN, HOFFMAN GS (2010) Wegener's granulomatosis: clinical manifestations, differential diagnosis, and management of ocular and systemic disease. *Surv Ophthalmol,* 55(5): 429-444.

TEKIN K, EROL YO, INANC M, M. SARGON MF, CAN CU, POLAT S, YILMAZBAS P (2018) Electron microscopic evaluation of anterior lens epithelium in patients with idiopathic congenital cataract. *Int Ophthalmol,* 38(5): 2127-2132.

Following Michelangelo's art and the power of clinical observation: David sign and David goiter

M. Planells Roig[1], P. Moreno Lorente[2], Alba Coret Franco[3], S. Navarro[1], M. Duran[1], D. Navarro Ortega[4]

[1] *Department of Surgery, General Surgery, University Hospital Dr Peset, Valencia, Spain*
[2] *Endocrine Surgery, Bellvitge University Hospital, Barcelona, Spain*
[3] *University Jaime I, Specialists in General Surgery, Castellon, Valencia, Spain*
[4] *Department of Microbiology, University Hospital Dr Peset, Valencia, Spain*

Key words: David sign – External jugular vein – Nodular goiter

In December 2019, Dr. Gelfman published a very interesting article in Jama Cardiology entitled *The David sign* (Gelfman, 2020), explaining his observation in Michelangelo's David's neck, in the Accademia Galleria. We read with great interest this paper, in which he affirmed the external jugular vein on the right side of David's neck was distended well above his clavicle, a fact that led him to observe the same finding in the sculpture of Moses at the tomb of Pope Julius the Second. He realized, based on careful clinical observation, a temporary jugular venous distention must be noticed in healthy individuals when they are excited, and the fact that Michelangelo tried to transmit a message about the capacity of the artist understanding clinical signs and expressing them in his artwork. Inspired by his reflection, we started further investigations that led us to discover a possible nodular goiter in David's neck, which would explain his distended external jugular vein.

We reviewed multiple pictures of David's neck, from multiple angles and perspectives, and we observed, as Dr. Gelfman claims, a young and extremely muscled healthy man, without any external sign of disease, excitation or violent expression on his face. At first look, we saw this patent and normally sized EJV, but with a more careful observation, we also discovered a possible nodular goiter just below Adam's apple. That moved us to investigate about that EJV and the nodular goiter in David's neck, that had not been previously described.

David's EJV can be considered as normal, especially in muscled necks in case of heavy efforts or angry expression. In fact, we are used to seeing it in Djokovic's or Nadal's necks (Fig. 1) and we dare say they are not cardiac patients.

A different finding is a distended, dilated or tortuous EJV, which indicates chronic high central venous pressure (CVP) as an indirect sign of cardiac disfunction or intrathoracic goiter, similar to the left EJV from God's neck in the Sistine Chapel (also painted by Michelangelo), which has never been reported before (Fig. 2).

Corresponding author:
Alba Coret Franco. University Jaime I, Specialists in General Surgery, Castellon, Valencia, Spain. E-mail: coretalb@gmail.com

Submitted: August 24, 2020. **Accepted:** December 17, 2020
Not final proof's revision by the authors

Fig. 1.- Djokovic's and Nadal's necks.

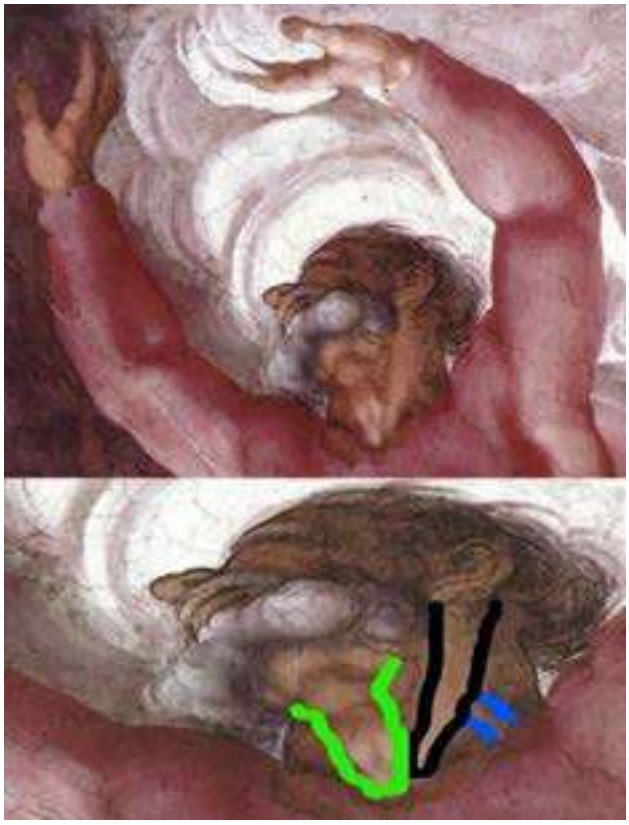

Fig. 2.- Left EJV from God's neck in the Sistine Chapel.

Gelfman exposes that David sign is useful to evaluate central venous pressure (CVP), not only in pathological situations, but in healthy patients in an excited state.

Sankoff and coworkers (Sankoff and Zidulka, 2008) described a method to determine CVP indirectly explaining the meaning of the incomplete emptying of the EJV due to three reasons: 1) sclerotic valves, which prevent emptying in a patient with normal CVP, 2) venous occlusion by a fascial flap at the distal end (resembling the muscle contraction during an excited or angry expression), and finally (3) a really elevated CVP. The relevance of CVP pressure is an indirect marker for intravascular volume. In Sankoff's series, the EJV was easily identifiable in nearly 70% of the patients, corresponding: 11 cases to high CVP and 17 cases to normal CVP. Therefore, a visible EJV should not always be considered a synonym of cardiac dysfunction: a distended EJV may be a consequence of a physiological, positional (muscle contraction) or pathologic condition (as a result of cardiac disfunction or as a consequence of an intrathoracic goiter).

Moreover, normal diameter of EJV investigation in thirty adult cadavers dissection, found an average EJV median diameter of 5.6 +/- 1.9 mm at the crossing line of the laryngeal prominence (Lee et al., 2019), and this should be considered a normal EJV diameter in healthy individuals as the one in David's neck.

As Gelfman explained, the David was completed by 1504, while the mechanism and structure of the circulatory system was described by William Harvey (1578-1657) on 1628. Although it was preceded by the publication of Miguel Servet (1509-1553), this was never mentioned or recognized in physiology texts. Later, in 1924, the Egyptian physician Dr. Muhyo AlDeen Altawi discovered a writing from Ibn al-Nafis, entitled *Commentary of Anatomy in the Cannon of Avicenna*, where the description of pulmonary circulation was based on Galen's speculations (IIAC) (Hajar Albanali, 2005), but not in anatomic dissections.

Dr. Gelfman argues that, before the battle with Goliath, the sculpture shows tension. In the author's opinion, it is not clear that any tension can be found in David's countenance, but clearly his eyes show a definitive sadness.

This fact contrasts clearly with Moses's regard (with an angry mien) at the tomb of Pope Julius the Second. From our point of view, the EJV from David should not be correlated with any expression of anger or temperament. Moreover, when we reviewed Michelangelo's portraits, we could recognize David's sad look as Michelangelo's usual expression in portraits (Fig. 3).

It is, therefore, a brilliant finding to discover that he was able to capture a clinical sign as a single frame that would convey the future situation of the battle, but it would also be a very interesting discovery that Michelangelo may have represented the David with a nodular goiter. He had anatomic training (Sterpetti, 2019), and was a perfectionist, obsessed with anatomy. As a native young Tuscan, where goiter was endemic, he was familiar with its clinical appearance. Moreover, he also saw goiter from an anatomical context, as he had his very own dissecting room at the Church of Santo Spirito in Florence, where a friendly prior provided him with corpses for studies of anatomy (Condivi, 1976; Vasari et al., 1998). Related to this idea, a distended EJV may be associated to nodular or intrathoracic goiter, although not visible. A plurifactorial origin of David's EJV may be explained by a positional factor, with his neck turned left, his nodular goiter, and the tension of his body secondary to the contrapposto performance of the sculpture, a technique which gives a feeling of movement: his left arm up, right arm down and backward, and a Valsalva secondary to the different position in his legs (one on the back and one in the front with all his abdominal wall contracted). Michelangelo's David is captured in movement like in a photogram, and frozen at the moment before lifting the stone. And we could not find previous any mention to or writing about the theory of a distended EJV secondary to a nodular goiter in Michelangelo David's neck.

As Dr. Gelfman comments in the article that led us to write this paper, careful observation is one of

Fig. 3.- David's sad look as the usual Michelangelo appearance in the portraits.

the main tools of medicine. It was in 1504, and it is still today, as it remains the mainstay contribution to early diagnosis avoiding unnecessary explorations. From now on, we will remember David sign (by Gelfman) in patients with a patent or distended EJV, mainly in individuals in an excited state preparing to face their own Goliaths (Gelfman, 2020).

Another comment of Dr. Gelfman includes the Sistine Chapel, painted during the winter of 1511 and October 1512 (after David), and the concealed anatomical image in God's neck in the *Separation of Light from Darkness* (the Big Bang of the Renaissance universe), which has been interpreted as a goiter (Bondeson and Bondeson, 2003) in God's neck. God's huge EJV is clearly different from the normal caliber EJV of the sculptured David called by Dr Gelfman "The David Sign", although he did not realize as previous author the pathologic left EJV of God from the Sistine Chapel.

This interpretation has been challenged by Suk and Tamargo (2010). Whether goiter is visible (Grade 3 OMS classification) or not (Grade 2), both may be associated with a retrosternal extension. In these cases, the Marañón maneuver published in 1926 comprises a hyperextension of the neck associated to upright arms in a U-like fashion round the neck (as God was painted by Michelangelo). If there is a retrosternal goiter, the chronic ingurgitated external jugular vein refills fully with blood: it may not be easily palpable during clinical exploration. That would explain the huge EJV in God's neck, which has never been noticed by other authors and shows the result of the Marañón/Pemberton's maneuver.

Pemberton's sign was described in 1946, but preceded by G. Marañón's description in Spain in 1926. Pemberton's sign (Pemberton, 1946; Basaria and Salvatori, 2004) extended in the medical literature since his letter in *The Lancet* entitled "Sign of Submerged Goiter". In his own words: "That is a useful sign given by an intrathoracic goiter, which has been used and taught for many years. Doubtless the sign has been described before and even bears a name, but we are unaware of it" (he didn't remember/know Marañón).

In conclusion, we want to thank Dr. Gelfman for his observational clinical note on David sign, which triggered our commentaries and investigation. In his article, Gelfman argues that, by means of David's sculpture, Michelangelo tried convey a message about the capacity of the artist for understanding clinical signs and expressing them in his artwork. It led us to think that, in David sign, the EJV was normal, David's expression was sad but not angry, and we have discovered a possible nodular goiter never described before in association to the contrapposto, which helped to fill his normal EJV. We have also discovered the pathological distorted EJV of God in the Sistine Chapel, which could indicate a not visible intrathoracic goiter never previously commented. Finally, we have dusted off from libraries and memories the real owners of pulmonary circulation description, mainly Miguel Servet and Ibn al-Nafis, and also the first report of Pemberton maneuver by Dr. Marañón, who anticipated Pemberton in 20 years.

REFERENCES

BASARIA S, SALVATORI R (2004) Pemberton's Sign. *N Engl J Med*, 350(13): 1338-1338. [cited 2020 Apr 16] Available from: http://www.nejm.org/doi/abs/10.1056/NEJMicm990287

BONDESON L, BONDESON AG (2003) Michelangelo's divine goitre. *J R Soc Med*, 96(12): 609-611.

CONDIVI A (1976) The life of Michel-Angelo. H. Wohl, London Phaidon, editor. *Penn State Press*, p 154.

GELFMAN DM (2020) The David sign. *JAMA Cardiol*, 5(2): 124-125.

HAJAR ALBINALI H (2005) Chairman's reflections : Blood-letting. *Hear Views*, 5(2): 74-85.

LEE HJ, RYU SY, CONG L, AHN HJ, PARK MK, KIM HJ, HU KS (2019) Anatomy of the superficial venous structures of the neck: a cadaveric study to guide superficial injections. *Dermatologic Surg*, 45(2): 203-209.

MARAÑÓN G (1926) Diagnosis or retroesternal goiter. *Ann R Acad Med*.

PEMBERTON HS (1946) Sign of submerged goitre. *Lancet*, 248(6423): 509.

SANKOFF J, ZIDULKA A (2008) Non-invasive method for the rapid assessment of central venous pressure: description and validation by a single examiner. *West J Emerg Med*, 9(4): 201-205.

STERPETTI AV (2019) Cardiovascular physio-pathology by Leonardo Da Vinci (1452-1519). *Circ Res*, 124(4): 472-474.

SUK I, TAMARGO RJ (2010) Concealed neuroanatomy in Michelangelo's separation of light from darkness in the Sistine Chapel. *Neurosurgery*, 66(5): 851-861.

VASARI G, BONDANELLA JC, BONDANELLA P (1998) The lives of the artists. *Oxford University Press*, p 586.